SCUOLA DI DOTTORATO
UNIVERSITÀ DEGLI STUDI DI MILANO-BICOCCA

Department of

PHYSICS “G. Occhialini”

PhD program PHYSICS AND ASTRONOMY Cycle XXXV

Curriculum in Applied Physics

New advances in neutron imaging techniques and a quantitative development of Neutron Resonance Transmission Imaging

Surname MARCUCCI Name GIULIA

Registration number 778407

Tutor: Prof. Cremonesi Oliviero

Supervisor: Dr. Di Martino Daniela

Coordinator: Prof. Ragazzi Stefano

ACADEMIC YEAR 2021/2022

Table of contents

Abstract

In recent years, neutron imaging established its strengths and extraordinary versatility for non-destructive investigation of many kinds of morphological and microstructural properties of materials expanding its availability at neutron sources worldwide. The rapid development of neutron imaging methods and detection systems has led to a striking improvement of both spatial and time resolution as well as of techniques based on a broad range of contrast mechanisms, making imaging with neutron beams indispensable in modern research.

Due to its intrinsic properties, neutron interacts with matter in a strongly different way from electrons, protons or X-rays, making neutron-based techniques fully complementary with these probes: the high penetrating power in dense matter is exploited to achieve bulk properties information of the analysed material in a completely non-invasive way. Moreover, neutrons are an optimum probe for observing light atoms, such as hydrogen, as well as for distinguishing neighbour elements in the periodic table and analogously between isotopes, allowing to obtain a different contrast for metals and light elements and they are the only scattering probe to provide isotopic contrast. The neutron magnetic moment makes them appealing for the study of magnetism. Since the interaction of neutrons can be exactly calculated, they can be used for precise quantitative analysis.

The current state-of-art of neutron imaging techniques is particularly advanced. This thesis, therefore, aims to provide further advances in this sector with the following activities: the implementation of the first Italian neutron tomography facility at the LENA research reactor of the University of Pavia and the development of a reliable protocol of analysis for resonant transmission imaging experiments conducted at the INES beamline of the ISIS spallation source (UK), with a particular focus on a first approach for a quantitative calibration of this imaging technique.

Neutron tomography is a well-optimised imaging technique that can provide the three-dimensional map of neutron attenuation coefficients inside an object. Therefore, based on the knowledge in the field of neutron tomography shared by researchers, the design and installation of the first Italian neutron tomography facility at the TRIGA reactor of the LENA laboratory have been carried out within the CHNet-NICHE (Neutron Imaging for Cultural HEritage), an INFN (Italian National Institute of Nuclear Physics) project, aiming

to specifically design the imaging beamline for conducting Cultural Heritage analyses. My contribution to the NICHE project consists of Monte Carlo simulations of the entire TRIGA MARK II Reactor and in particular the reconstruction of the main characteristics of the B Channel. I contributed to the installation of the facility and to the reconstruction of the tomographic acquisitions using a Python-based software developed in a previous PhD project of the Physics Department of the Milano Bicocca University.

For well-established analytical techniques, it may be natural to extend their potentiality to imaging applications. This is the case of the Neutron Resonance Transmission Analysis method, which was recently optimised for adding space-resolved information resulting in the now-called Neutron Resonance Transmission Imaging (NRTI) technique. During this 3-years Ph.D. research, my personal contribution to the NRTI improvement started from planning the experimental activities with the instrument scientist of the INES beamline, followed by the definition of a reliable normalisation strategy of the transmission data based on well-known procedures of neutron imaging adapted to the time-of-flight and spallation physics. The definition of ad-hoc Python codes for data processing and normalisation is an integral part of the work personally conducted within this thesis. The final goal of this project is to identify a protocol towards quantitative imaging, making the NRTI technique a particularly advanced imaging compared to standard tomography, which currently offers only qualitative investigations.

NRTI exploits the epithermal portion of the neutron flux - not yet widely used in neutron imaging - combining the elemental/isotopic sensitivity due to the resonant absorption of neutrons with morphological details obtained by the employment of a time and space-resolved detection system. What makes NRTI different from standard neutron radiography is the possibility of not only localising specific features inside the volume of an object but also identifying and localising specific elements and isotopes with enhanced contrast with respect to others, without the need for sampling. Each detector pixel contains the full transmitted spectrum which is not integrated over the energy range, in contrast with neutron tomography where it is a typical process done by the neutron camera. Therefore, NRTI allows to analyse the resonant dips in the transmission spectrum to perform resonance-selection imaging, *i.e.* the resonant dips of a specific element or even isotope can be selected to increase its transmission contrast in the 2D map for better visualise its spatial distribution. Moreover, the analysis of resonant dip areas can provide quantitative details of the object composition, extending the potential of neutron imaging to quantitative investigations.

It should also be mentioned that the advancement of NRTI experimental activities has been challenging in this period due to the unforeseen Covid-19 pandemic, which extended the already planned long-shutdown (from late summer 2020 to the end of 2022) of the

ISIS spallation source, severely limiting the progress of the quantitative calibration of the technique. However, future steps needed to pursue this goal have been identified on the basis of the deep analysis conducted on the acquired data.

This Thesis gives particular account to the application of neutron imaging in the field of Cultural Heritage. As already mentioned, the range of current and potential applications is broad and the non-destructiveness and complementarity of neutron imaging make it an invaluable tool to analyse precious archaeological objects revealing structures at the microscopic scale, and chemical composition and providing 3D images of the inner parts of the artefacts, notwithstanding the facts that neutrons are not the first chosen technique in the archaeometric field, because they are not in-situ analysis but archaeological objects have to be taken to a neutron source.

This Thesis comprises seven chapters:

Chapter 1 recalls the fundamental physical properties of neutrons and summarises the principles of neutron-matter interaction. In particular, the concept of neutron cross-section and resonant interaction is briefly discussed, as its mechanism is at the bases of the NRTI imaging technique explored in this work. Subsequently, an overview of the main neutron sources is provided, with particular focus on the mechanism of neutron production by spallation reaction and nuclear fission.

Chapter 2 is dedicated to the description of the ISIS spallation source (UK) and the INES beamline, where the main work of this thesis was conducted, including the experimental data acquisition, dedicated to the advancement of the NRTI technique.

Chapter 3 is structured similarly to Chapter 2: general details of the Triga Mark II reactor of the Applied Nuclear Energy Laboratory (LENA, Pavia) are presented, with particular focus on the thermal channel where the CHNet-NICHE project was conducted, the latter dedicated to the implementation of the first Italian neutron imaging facility for applications to Cultural Heritage.

Chapter 4 intends to provide an overview of the fundamental principles and current state-of-art of resonant neutron absorption spectroscopy techniques and neutron tomography.

In Chapter 5 the CHNet NICHE project is presented with the technical characteristics of the facility achieved by the NICHE working group. The contribution of this Thesis is outlined, describing the results obtained by Monte Carlo simulation of the neutron flux characteristics and by tomographic data reconstruction performed after a specific training session experienced in the first year of the PhD.

Chapter 6 is devoted to describe in detail the Neutron Resonance Transmission Imaging technique, focusing on the instrumentation, the data acquisition and processing and the

main explored applications of the technique. Finally, an attempt to define and overcome the principal issues for the quantitative calibration of NRTI is presented.

In Chapter 7 general conclusions about the research work presented in this doctoral thesis are discussed.

Acknowledgements

This work was partially supported within the CNR-STFC Agreement (No. 2014–2020 and No. 2020-2027), concerning collaboration in scientific research between the ISIS Neutron and Muon Source (UK) of STFC and CNR (Italy). The INFN V committee and the CHNet INFN network are gratefully acknowledged for the technical and economic support to the development of the CHNet-NICHE activity, as well as the LENA facility for providing beamtime. Financial support by the Access to Research Infrastructures activity in the Horizon 2020 Programme of the EU (IPERION CH Grant Agreement No. 654028) is gratefully acknowledged (FIXLAB: AGLAE, France).

This journey has been filled with wonderful people who I am grateful to have been able to travel with. I would like to express my deepest gratitude to my PhD Supervisors, Dr. Daniela Di Martino and Prof. Oliviero Cremonesi for their invaluable supervision, precious help and advice that improved my scientific knowledge and enriched my research experience during the course of my PhD degree.

I also could not have undertaken this research experience without the superivision of Dr. Antonella Scherillo, who generously provided knowledge and expertise as the instrument scientist of the INES beamline. Words cannot express my gratitude for her invaluable patience and feedback during our countless discussions regarding every detail and result of the experimental measurements conducted at the ISIS facility. This endeavour would not have been possible without Dr. Massimiliano Clemenza, for his treasured support which was really influential in shaping my experiment methods and critiquing my results.

I would like to extend my sincere thanks to Dr. Carlo Cazzaniga and Dr. Lina Quintieri for sharing with me their precious knowledge in simulation programming and other vital aspects of neutron physics; Prof. Maria Pia Riccardi and Prof. Costanza Cucini for introducing me to one of their case study related to Cultural Heritage and for their trust in me to personally conduct analyses on their samples.

I had the pleasure to collaborate with several other researchers involved in the INFN CHnet-NICHE project, whom I thank for the pleasant exchange of knowledge and for improving my approach to experimental activity.

Thanks are due to many other people met abroad during my research studies at the ISIS Neutron and Muon source (UK) and have made this journey unique in many ways. I am also grateful to my office mates, PhD colleagues and my friends, for their moral support, especially during the unforeseen Covid-19 pandemic and the long ISIS shutdown, and for creating an inspiring working group.

Chapter 1

Neutron Physics and Sources

The neutron is a subatomic particle made of three valence quarks: two down quarks and one up quark. Consequently, the interaction of neutrons with matter is dominated by the strong nuclear force and involves the nuclei of the absorbing material. Neutrons provide a unique and excellent probe for the atomic properties of condensed matter, as their neutral charge and the short range of interaction ($\sim 10^{-15}\ m$) ensure weak but not negligible interactions with the nucleus of an atom, resulting in a highly penetrating capability of neutrons (of the order of centimetres). This feature has three important advantages:

1. neutrons can be used to investigate microscopic properties of matter non-destructively;
2. neutrons are a bulk probe of matter, not sensitive to surface effects/structures;
3. neutrons can be used to investigate objects in complex sample environments.

Quantum mechanics associated with neutrons the wave-particle duality: as (moving) particles, they can be described by momentum and kinetic energy; on the other hand they present wave characteristics as wavelength and frequency. The link between these two properties is provided by the De Broglie wavelength[1] (Eq.1.1) and by the Planck-Einstein equation (Eq.1.2):

$$\lambda = h/p \tag{1.1}$$

$$E = \lambda \nu \tag{1.2}$$

where $h = 6.626 \cdot 10^{34}\ Js$ is the Planck's constant, p the neutron linear momentum, E the neutron kinetic energy and ν the neutron frequency.

[1] Louis De Broglie won the Nobel prize for Physics in 1929 for his hypothesis that all matter has wave properties.

A further outstanding property of the neutron is its magnetic moment ($\mu = -9.66 \cdot 10^{-27}\ J\ T^{-1}$, antiparallel to the internal angular momentum of the neutron), which makes neutrons very sensitive to magnetic fields and allows for resolving bulk magnetic properties in samples and studying basic phenomena in condensed matter. The basic properties of a neutron are summarised in Table 1.1.

Table 1.1 Main properties of a free neutron [7].

Mass	$939.57\ \mathrm{MeV}/c^2$
Charge	0
Spin	$1/2$
Magnetic Dipole Moment	$-1.913\ \mu_N$
Mean lifetime	$880\ s$
Quark composition	*uud*

1.1 Neutron interaction with matter

If neutrons interact with atomic nuclei, they can produce a variety of nuclear reactions, depending on their energy (Table 1.2) and the type of nucleus. Generally, the neutron may either totally be absorbed and replaced by one or more secondary radiations, or else undergoes a direct scattering process (elastic or inelastic) in which the energy and/or direction of the neutron changes significantly.

Table 1.2 Schematic subdivision of the various types of neutrons based on their kinetic energy and corresponding wavelength. Thermal neutrons are often referred to as standard energy of 25 meV (1.8 Å) which corresponds to room temperature of 293.59 K.

Neutrons	**Energy range**	**Wavelength range (Å)**
Ultracold and cold	< 0.01 eV	> 2.86
Thermal	$0.01 - 0.5$ eV	$2.86 - 0.41$
Epithermal	0.5 eV - 10 keV	$0.41 - 2.86 \cdot 10^{-3}$
Fast	10 keV - 20 MeV	$2.86 \cdot 10^{-3} - 6.40 \cdot 10^{-5}$
Ultrarelativistic / high energy	> 20 MeV	$< 6.40 \cdot 10^{-5}$

The probability of neutron interaction is described by the physical quantity called *cross-section*, which has the dimension of an area. The total cross-section is the sum of two terms,

the scattering cross-section σ_S and the absorption cross-section σ_A:

$$\sigma_{TOT} = \sigma_S + \sigma_A \tag{1.3}$$

As a measure for cross-sections, the unit barn is used ($1\ barn = 10^{-24}\ cm^2$). Neutron absorption processes are also referred to as compound nucleus reactions, due to the formation of a relatively long-lived ($\geq 10^{-17}\ s$) compound nucleus, which may decay in various ways [7]:

- by emitting a neutron with the same energy as the originally captured neutron. This process is called compound elastic scattering or sometimes resonance scattering;
- through inelastic scattering, when a neutron with a kinetic energy smaller than that of the incident neutron is emitted. In this case, the residual nucleus remains in an excited state which subsequently decays by y-ray emission;
- by emitting charged particles ($(n,\alpha)-$, $(n,p)-$ reactions), two neutrons ($(n,2n)-$reactions), or one or more gamma-rays (radiative capture or $(n,\gamma)-$reactions);
- by fission in the heaviest nuclei ($A > 80$) induced by slow neutrons.

Resonance scattering and radiative capture are possible for all neutron-induced compound nucleus reactions, while $(n,p)-$, $(n,\alpha)-$reactions in most cases and the $(n,2n)-$reaction and inelastic scattering in all cases are threshold reaction, *i.e.* they occur above a particular energy of the incident neutron.

For thermal and cold neutrons the absorption cross-section linearly decreases with the neutron energy $(1/E)$. However, the neutron absorption cross-sections vary greatly even amongst isotopes of the same element, and some isotopes are strong absorbers of neutrons of epithermal energies due to the presence of very intense resonances in their cross-section. Fig.1.1 shows the resonances of different nuclides; these structures are strong sharp maxima which appear at specific energy for each nuclide. Creating a compound nucleus is a resonance reaction, *i.e.*, the incident neutron must have a combined binding and kinetic energy that corresponds to an excited state of the nucleus.

Nearly all light nuclei (with atomic weight $A < 25$) have only a few, widely spaced excited states; thus, their cross-section shows only single, widely spaced resonances such as ^{1}H or ^{16}O in Fig.1.1. The resulting predominant reaction for slow and intermediate energy neutrons (up to a few hundred of keV) is potential scattering.

Intermediate nuclei ($25 < A < 80$) as manganese or iron (Fig.1.1) typically exhibit well-separated resonances for an average interval of several keV up to high energies, whilst in the

case of heavy nuclei ($A < 80$), such as indium, the resonances lie very close together and at energies as low as several keV they already overlap forming a continuous variation of the cross-section with energy. Fig.1.2 summarises the distribution of resonances over neutron energies and nuclei atomic mass.

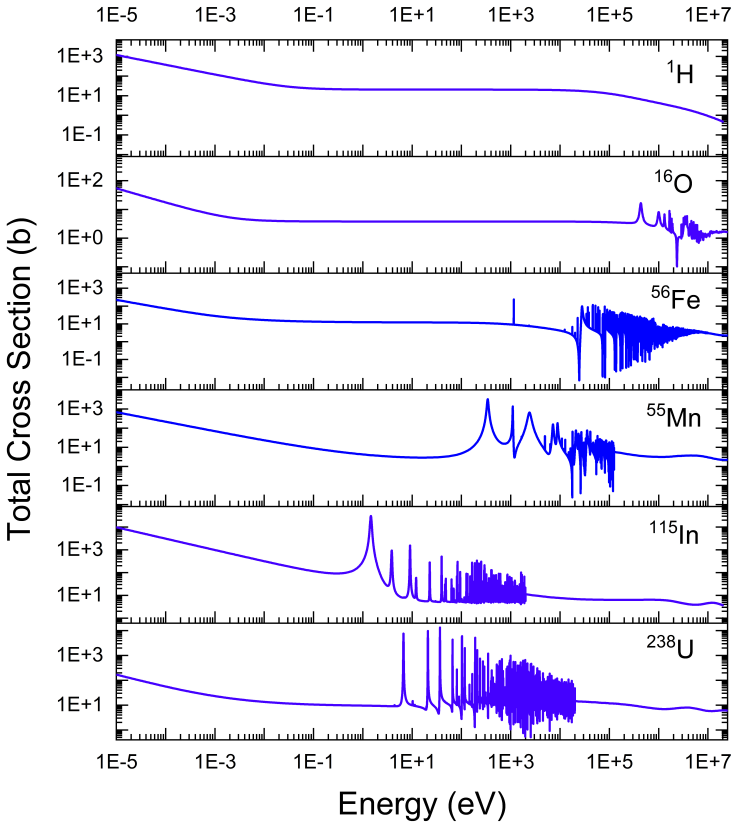

Fig. 1.1 Total cross-section as a function of neutron energy of ^{1}H, ^{16}O, ^{56}Fe, ^{55}Mn, ^{115}In and ^{238}U. The cross sections are taken from the KAERI database [2].

Alternatively, nuclear reactions can proceed without the compound nucleus formation, following direct elastic or inelastic collisions. Direct elastic scattering is frequently identified with the term potential scattering and describes the neutrons deflection due to their interaction with the (real) nuclear potential [7]. Elastic scattering with nuclei is a significant interaction for slow neutrons, because of their small kinetic energy and therefore the very negligible amount of energy transferred to the nucleus. Instead, the relative probability of inelastic scattering increases with neutron energy.

Fast neutrons can transfer an appreciable amount of energy in a single collision, producing secondary radiations in the form of energetic recoil nuclei. After each collision, the neutron

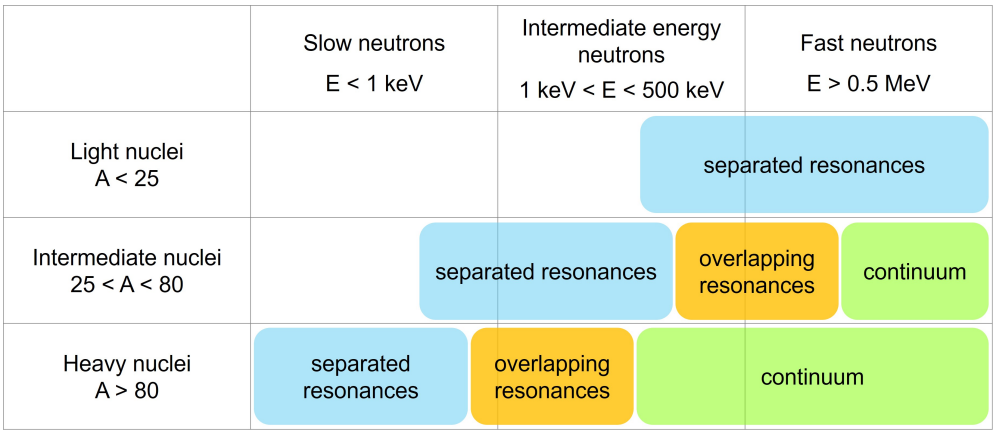

Fig. 1.2 Resonances distribution as a function of neutron energy for light, intermediate and heavy nuclei.

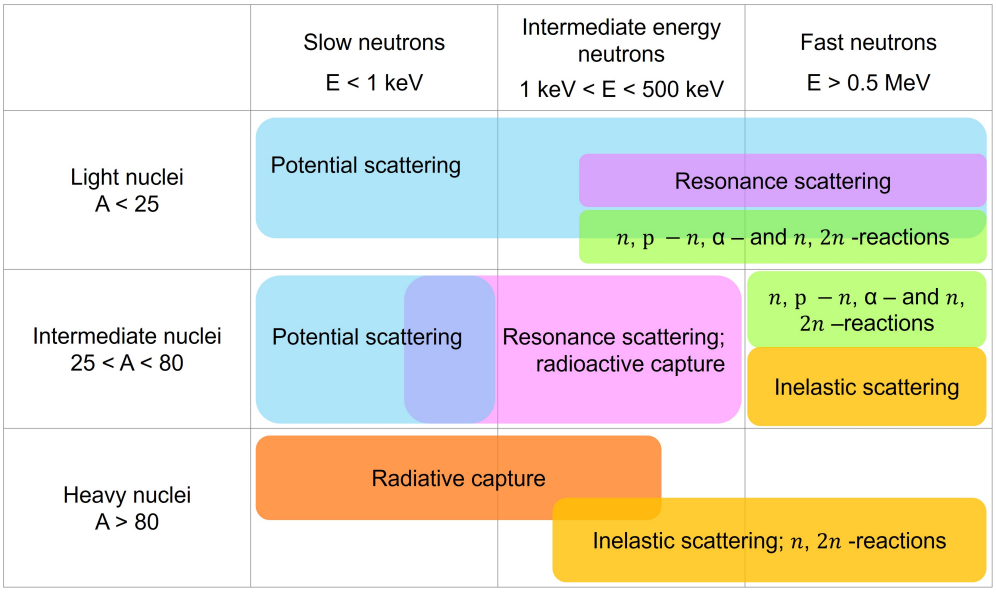

Fig. 1.3 A systematic review of reactions associated with neutrons in relation to neutron energy and nuclei weight.

loses energy and is thereby slowed down (or moderated) to lower energy. Hydrogen is the most efficient moderator because the neutron can lose up to all its energy in a single collision with its nucleus.

However, the amount of scattering or absorption of neutrons varies in an apparently random way through the periodic table and even significantly between isotopes, instead of following a precise relation as for X-rays and electrons, for which the scattering power increases in proportion to the number of electrons in the atom. Fig.1.4 clarifies this fundamental difference, highlighting also the sensitivity of (thermal) neutrons to light atoms

such as H, Li and B which therefore provides a good contrast to heavy atoms. This feature makes for example neutron imaging complementary to X-ray imaging, as shown in Fig.1.5. Furthermore, a remarkable discrimination between certain isotopes of a nuclide can be obtained by exploiting neutrons as a probe.

To summarise, the intrinsic properties of neutrons provide a wide range of advantages for non-invasive investigations of materials, ranging from massive objects to the fine structure of a crystal or a biological organism. A detailed description of the most frequently employed neutron-based techniques for material characterisation will be given in Chapter 5.

Attenuation coeffitients for thermal neutrons [cm^{-1}]

1a	2a	3b	4b	5b	6b	7b	8			1b	2b	3a	4a	5a	6a	7a	0
H																	He
3.44																	0.02
Li	Be											B	C	N	O	F	Ne
3.30	0.79											101.60	0.56	0.43	0.17	0.20	0.10
Na	Mg											Al	Si	P	S	Cl	Ar
0.09	0.15											0.10	0.11	0.12	0.06	1.33	0.03
K	Ca	Sc	Ti	V	Cr	Mn	Fe	Co	Ni	Cu	Zn	Ga	Ge	As	Se	Br	Kr
0.06	0.08	2.00	0.60	0.72	0.54	1.21	1.19	3.92	2.05	1.07	0.35	0.49	0.47	0.67	0.73	0.24	0.61
Rb	Sr	Y	Zr	Nb	Mo	Tc	Ru	Rh	Pd	Ag	Cd	In	Sn	Sb	Te	I	Xe
0.08	0.14	0.27	0.29	0.40	0.52	1.76	0.58	10.88	0.78	4.04	115.11	7.58	0.21	0.30	0.25	0.23	0.43
Cs	Ba	La	Hf	Ta	W	Re	Os	Ir	Pt	Au	Hg	Tl	Pb	Bi	Po	At	Rn
0.29	0.07	0.52	4.99	1.49	1.47	6.85	2.24	30.46	1.46	6.23	16.21	0.47	0.38	0.27			
Fr	Ra	Ac	Rf	Ha													
	0.34																

	Ce	Pr	Nd	Pm	Sm	Eu	Gd	Tb	Dy	Ho	Er	Tm	Yb	Lu
*Lanthanides	0.14	0.41	1.87	5.72	171.47	94.58	1479.04	0.93	32.42	2.25	5.48	3.53	1.40	2.75
	Th	Pa	U	Np	Pu	Am	Cm	Bk	Cf	Es	Fm	Md	No	Lr
**Actinides	0.59	8.46	0.82	9.80	50.20	2.86								

Attenuation coeffitients for X-ray [cm^{-1}] (150kV)

1a	2a	3b	4b	5b	6b	7b	8			1b	2b	3a	4a	5a	6a	7a	0
H																	He
0.02																	0.02
Li	Be											B	C	N	O	F	Ne
0.06	0.22											0.28	0.27	0.11	0.16	0.14	0.17
Na	Mg											Al	Si	P	S	Cl	Ar
0.13	0.24											0.38	0.33	0.25	0.30	0.23	0.20
K	Ca	Sc	Ti	V	Cr	Mn	Fe	Co	Ni	Cu	Zn	Ga	Ge	As	Se	Br	Kr
0.14	0.26	0.48	0.73	1.04	1.29	1.32	1.57	1.78	1.96	1.97	1.64	1.42	1.33	1.50	1.23	0.90	0.73
Rb	Sr	Y	Zr	Nb	Mo	Tc	Ru	Rh	Pd	Ag	Cd	In	Sn	Sb	Te	I	Xe
0.47	0.86	1.61	2.47	3.43	4.29	5.06	5.71	6.08	6.13	5.67	4.84	4.31	3.98	4.28	4.06	3.45	2.53
Cs	Ba	La	Hf	Ta	W	Re	Os	Ir	Pt	Au	Hg	Tl	Pb	Bi	Po	At	Rn
1.42	2.73	5.04	19.70	25.47	30.49	34.47	37.92	39.01	38.61	35.94	25.88	23.23	22.81	20.28	20.22		9.77
Fr	Ra	Ac	Rf	Ha													
	11.80	24.47															

	Ce	Pr	Nd	Pm	Sm	Eu	Gd	Tb	Dy	Ho	Er	Tm	Yb	Lu
*Lanthanides	5.79	6.23	6.46	7.33	7.68	5.66	8.69	9.46	10.17	10.91	11.70	12.49	9.32	14.07
	Th	Pa	U	Np	Pu	Am	Cm	Bk	Vf	Es	Fm	Md	No	Lr
**Actinides	28.95	39.65	49.08											

Fig. 1.4 Comparison of the linear attenuation coefficients, expressed in cm^{-1}, for thermal neutrons (top) and 150 *keV* X-rays (bottom) for each element of the periodic table [3]. The amount of attenuation is indicated by the greyscale, where darker grey indicates a stronger attenuation strength.

Fig. 1.5 X-rays (left) and neutron (right) radiography of an analogue camera [4]. X-rays are more attenuated by heavier materials, like the metallic parts of the camera, whilst neutrons are more sensitive to light atoms, such as hydrogen, making possible the visualisation of plastic details of the photo apparatus with high contrast.

1.2 Production of neutrons

Because of their short lifetime, free neutrons do not occur in nature and must be artificially produced. In ordinary condensed matter, neutrons are bound in the nucleus of atoms. Several nuclear reactions can be exploited to release neutrons from the nuclei. The 1935 Nobel Prize was awarded to James Chadwick for his discovery of the neutron [5] through the (α, n) reaction by firing α particles, produced from the radioactive decay of polonium, to a target of beryllium:

$$^{9}Be + \alpha \rightarrow ^{12}C + n \tag{1.4}$$

Today, there are four main kinds of neutron sources, depending on the reaction used for producing neutrons:

- spallation sources;
- reactor sources;
- compact accelerator-driven sources;
- fusion sources.

However, to produce high neutron fluxes useful for contemporary neutron scattering and imaging research, the first two sources are employed, respectively based on nuclear fission and nuclear spallation reactions. For the purposes of this thesis, a brief description of (research) reactors and spallation sources will be provided separately in the following Sections 1.2.1 and 1.2.2. In many cases, these two types of sources are complementary because of the different neutron spectrum (in terms of energy and time shape) and the brilliance they provide.

Both types of sources generate fast, highly penetrating neutrons with energies between MeV and GeV at the time of generation, while material science analyses require sub-eV energies. The slowing down of fast neutrons is achieved by using hydrogenous moderators held at different temperatures. The presence of different moderators in one neutron source provides extraordinary flexibility for conducting different experiments matched to the needs of the scientific application. Regardless of how they are produced, slow neutrons are particularly versatile in exploring matter through neutron scattering or imaging experiments, as pointed out in the previous section: their velocities correspond to both a wavelength and energy adapted to the scale of interatomic distances and to magnetic, molecular and crystal vibrations. A detailed overview of the current situation on European neutron facilities can be found in [6].

1.2.1 Spallation sources

Accelerator-driven spallation sources attract a vast number of multidisciplinary users, from industrialists to basic researchers and, compared to nuclear research reactors, spallation sources are "environmentally friendly".

Nuclear spallation is a reaction by which neutrons are produced bombarding a heavy metal target (often made of Ta or W alloy) with protons or other subatomic particles with energies above 100 MeV. The high energies of the projectile particles mean their De Broglie wavelength is short enough ($\lambda = \sqrt{h^2/2mE} \leq 1\ fm$) to interact with individual nucleons inside the nucleus, causing an intranuclear cascade with a twofold effect (see Fig.1.6): first, the collision release energy to the nucleus placing it in a highly excited state; secondly, a few energetic particles or clusters of particles may be knocked out of the nucleus and trigger another internuclear cascade or escape from the target. The excited nucleus left behind will de-excite by evaporating low-energy particles, such as neutrons with energies of the order of 1 MeV.

As a figure of merit, a 1-GeV proton can produce on average 25 neutrons from a lead target 60 *cm* thick [7]. The resulting neutron spectrum (Fig.1.7) produced by spallation extends to a small fraction of neutrons with energies up to nearly the same order as the incident protons. Still, the maximum component is around 2 MeV due to the evaporating neutrons.

The time distribution of spallation neutrons is exclusively determined by the distribution of the driving particle pulse as the release of spallation neutrons takes place within less than $10-15\ s$ after the collision with the nucleus.

Spallation neutron sources are mainly divided into three groups: short-pulse sources, long-pulse sources and continuous sources. The first typically deliver 1 μs width proton

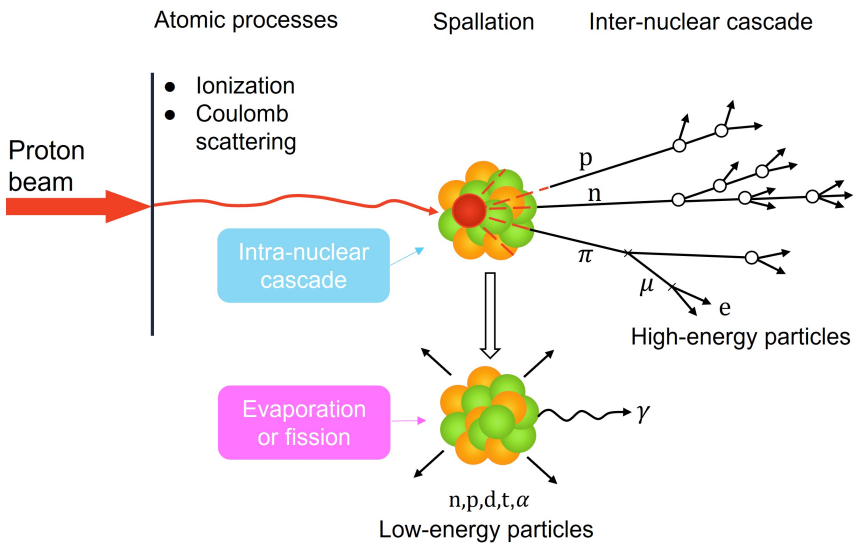

Fig. 1.6 Nuclear spallation process induced by high-energy protons hitting a heavy metal target.

pulses and are currently predominating because of their good timing resolution for Time-Of-Flight measurements of the neutron energy, which is dominated by the neutron slowing-down process in the moderators. Long-pulse sources typically produce 1 *ms* proton pulse widths and are another option for experiments not requiring high timing resolution. Finally, continuous spallation sources are characterised by no macro-time structure and the optimization goal is the high-time average flux [9]. The currently only existing continuous spallation source in the world is the SINQ at the Paul Scherrer Institut (PSI) in Switzerland [10], whilst pulsed spallation sources are more widespread worldwide: the most powerful of this kind is the Spallation Neutron Source (SNS) in the United States (Fig.1.8) [11, 12], in expectation of the completion of the European Spallation Source (ESS) [13].

1.2.2 Reactor sources

Reactor technology is highly developed and has not changed significantly for many years.

Historically, nuclear reactors have been the source with the highest neutron flux (even up to 10^{15} cm^{-2}s^{-1}), then pulsed reactors and spallation sources have begun to be competitive yielding results in scattering measurements.

Nuclear reactors exploit the thermal induced fission to produce neutrons. Following the discovery of the neutron, the realisation of first fission experiments was a natural step after Fermi (Nobel Prize in 1938) and co-workers studies on β-decays following neutron capture reactions.

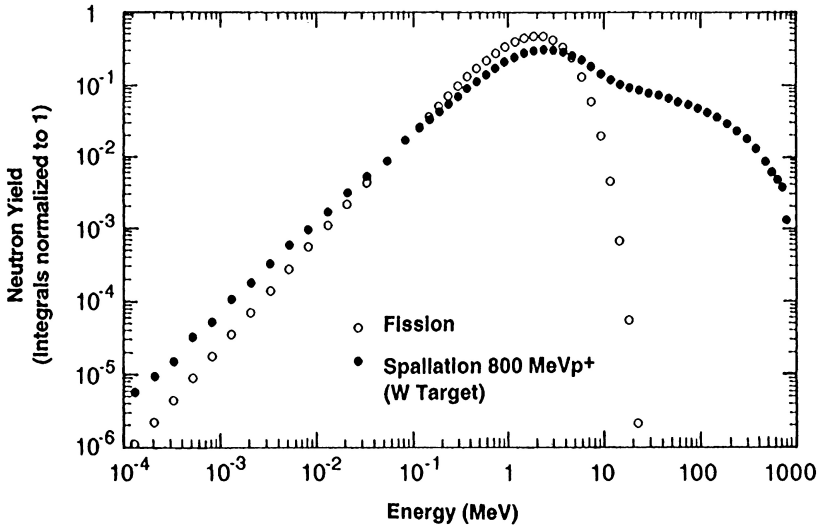

Fig. 1.7 Calculated spallation neutron spectrum resulting from the bombardment of 800 MeV protons to a tungsten target, compared to the neutron spectrum from thermal neutron fission of ^{235}U [8].

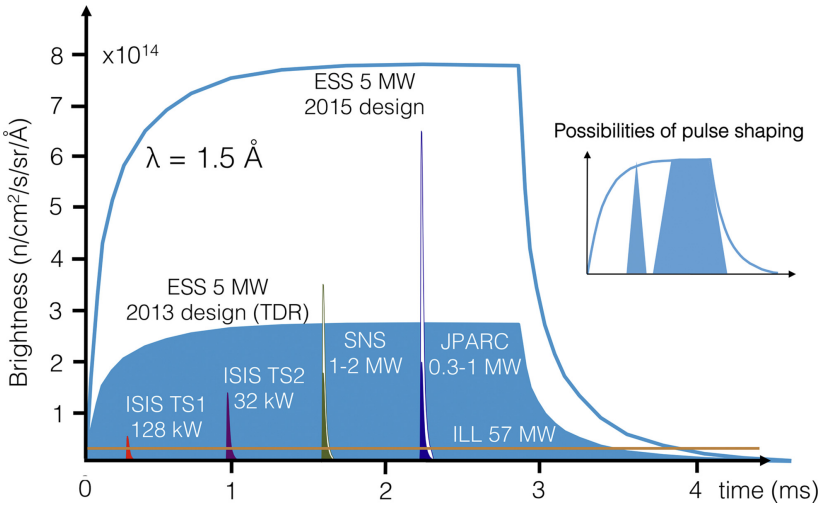

Fig. 1.8 Comparison of the brightness and time structure of the neutron beams provided by principal existing and planned spallation sources and the ILL research reactor [image credit: ESS].

A typical fission reaction induced by thermal neutrons nuclei involves a critical mass of fissile ^{235}U:

$$n_{th} + {}^{235}U \rightarrow {}^{93}Rb + {}^{141}Cs + 2n + Q \tag{1.5}$$

where Q is the energy released during the nuclear process in the form of kinetic energy, fission fragments, γ-rays and neutrons and is around $180 - 200$ MeV.

More generally, a fission reaction induced by thermal neutrons can be represented as:

$$n_{th} + {}^{A}_{Z}X \rightarrow X_1 + X_2 + \nu n + Q \tag{1.6}$$

where ν is the mean number of prompt neutrons emitted per reaction. This mean number is characteristic of the particular fission process: the greater the energy of the incident neutron, the greater the mean number of neutrons produced. Similarly, the heavier the fissioning nucleus, the more neutrons it will produce on average. In the case of a fission reaction involving a ^{235}U nucleus, is around 2.45 (Fig.1.9).

Prompt neutrons are produced practically instantaneously after fission of the nucleus, within less than $10-15$ *s* following the reaction [15].

The mean energy of prompt neutrons following fission of ^{235}U is about 2 MeV. Prompt neutrons make up over 99% of the produced neutrons by fission. The 1% are delayed neutrons, which may be emitted a significant time after fission ($\sim s$) by beta-decay of fission fragments produced in an excited state. Although thermal-induced in very small quantities, delayed neutrons are crucial in achieving kinetic control of a reactor, as no mechanical system could respond rapidly enough to prevent the statistical variations of the prompt neutron emission.

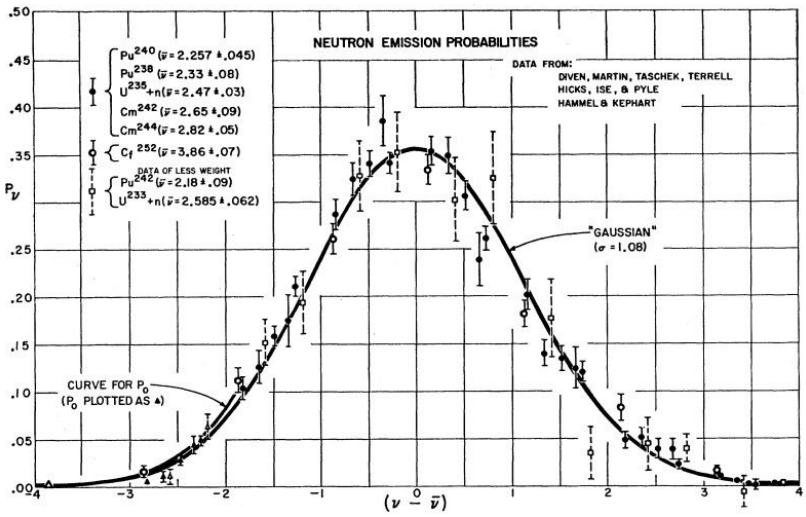

Fig. 1.9 Probability distribution of fission neutrons for different fissioning nuclei [16].

The fission fragments X_1 and X_2 (Eq.1.6) are not uniquely determined but follow a mass distribution of the form shown in Fig.1.10. The distribution is symmetric about the centre and the production of a heavier fragment ($A_1 \simeq 140$) and a lighter fragment ($A_2 \simeq 95$) is more probable (by a factor of 600 [7]) than the production of fragments with (nearly) equal masses.

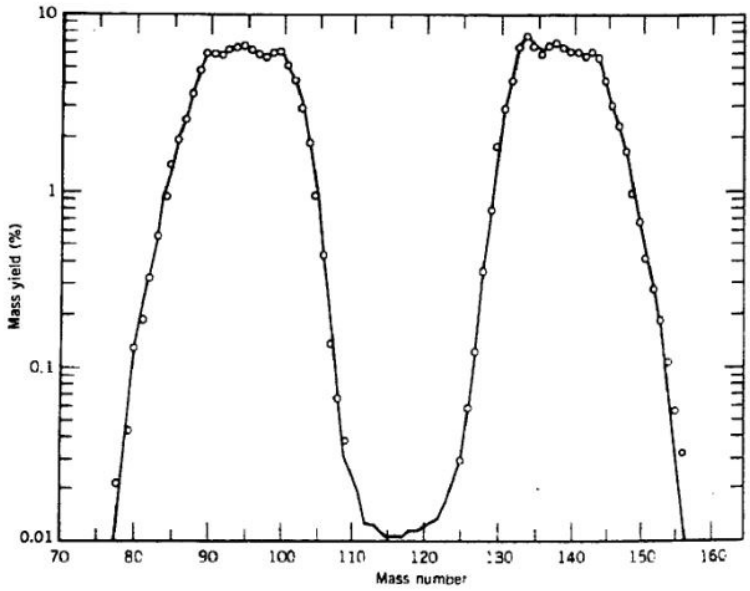

Fig. 1.10 Mass distribution of fission fragments from thermal fission of ^{235}U [17].

The basic classification of nuclear reactors can be made on the use for which they are intended: power generation, research and conversion of fissionable materials. However, all reactors consist of the same essential elements:

- the fuel, *i.e.* the fissile material;
- the moderator, mandatory for thermalising fast neutrons produced by fission;
- the reflector surrounding the reactor core to reduce neutron leakage and the critical size of the reactor;
- a containment vessel, designed to prevent the escape of radioactive steam and fission products;
- the shielding block, to avoid biological hazards related to neutrons and γ-rays emission;
- the cooling system, to absorb heat produced in the core;
- emergency and control systems, to control the power level keeping it constant.

Some leading research reactor sources for scattering applications are HFIR at the Oak Ridge National Laboratory [18] with thermal power of 85 MW; ILL in Grenoble (FR) [19, 20] is the most powerful reactor in Europe; OPAL (ANSTO, Australia) [21] and HANARO (KAERI) in South-Korea [22].

References

[1] Beckurts, K.H. and Wirtz, K. (1964) *Neutron Phyiscs*, Springer Berlin, Heidelberg. doi: 10.1007/978-3-642-87614-1.

[2] https://atom.kaeri.re.kr. Accessed 25th Jan 2023.

[3] The Paul Scherrer Institute (PSI) - Neutron Imaging and Activation Group (NIAG). https://www.psi.ch/niag/comparison-to-x-ray.

[4] The Paul Scherrer Institute (PSI) - Neutron Imaging and Activation Group (NIAG). https://www.psi.ch/en/niag/what-is-neutron-imaging.

[5] Chadwick, J. (1932) “Possible Existence of a Neutron", *Nature: International weekly journal of science*, 129(3252), pp. 312–312. doi: 10.1038/129312a0.

[6] National Research Council (U.S.). Panel on Neutron Scattering and Rossi, G. (2016) "Neutron scattering facilities in europe: present status and future perspectives". Italy: University of Milan.

[7] Bilheux, H.Z., McGreevy, R.L., and Anderson, I.S. (2009) *Neutron Imaging and Applications: A Reference for the Imaging Community*, Springer New York, NY. doi: 10.1007/978-0-387-78693-3.

[8] Russell, G.J. (1991) "Spallation physics – an overview", *Proceedings of ICANS-XI, Tsukuba, KEK-Report*, 90(25), pp. 291–299.

[9] Bauer, G.S. (2001) "Physics and technology of spallation neutron sources", *Nuclear Instruments and Methods in Physics Research A: Accelerators, Spectrometers, Detectors and Associated Equipment*, 463, pp. 505–543.

[10] Wagner, W. et al. (2006) “The Swiss Spallation Neutron Source Sinq—developments and Upgrades for Optimized User Service”, *Physica B: Physics of Condensed Matter*, 385-386, pp. 968–971. doi: 10.1016/j.physb.2006.05.285.

[11] Mason, T.E. et al. (2006) “The Spallation Neutron Source in Oak Ridge: A Powerful Tool for Materials Research”, *Physica B: Physics of Condensed Matter*, 385-386, pp. 955–960. doi: 10.1016/j.physb.2006.05.281.

[12] Gabriel, T.A., Haines, J.R. and McManamy, T.J. (2003) “Overview of the Spallation Neutron Source (SNS) with Emphasis on Target Systems”, *Journal of Nuclear Materials*, 318, pp. 1–13. doi: 10.1016/S0022-3115(03)00010-2.

[13] Richter, D. (2002) “The European Spallation Source”, *Applied Physics A : Materials Science and Processing*, 74(1), p.22. doi: 10.1007/s003390201809.

[14] https://europeanspallationsource.se/. Accessed 25th Jan 2023.

[15] Salvatore Esposito and Ofelia Pisanti (2010) *Neutron Physics For Nuclear Reactors: Unpublished Writings By Enrico Fermi.* Singapore: World Scientific.

[16] Terrell, J. (1957) "Distributions of Fission Neutron Numbers", *Phys.Rev.*, 108(3), pp. 783-789.

[17] Diiorio, G.J. (1976) "Direct physical measurement of mass yields in thermal fission of uranium-235", PhD Dissertation, University of Illinois Urbana-Champaign, United States.

[18] Nagler, S.E. and Mook, H.A. (2008) "A brief history of neutron scattering at the Oak Ridge High Flux Isotope Reactor", Correspondent’s Report, Neutron News, 19(2), pp. 12-13. doi: 10.1080/10448630801975668.

[19] Drexel, W.J. (1982) "Instrument Control and Data Acquisition System of the ILL High Flux Reactor Neutron Beam Instruments", In *IEEE Transactions on Nuclear Science*, 29(1), pp. 123-126. doi: 10.1109/TNS.1982.4335809.

[20] Carlile, C.J. (2006) "ILL in the changing international context", *Physica B: Condensed Matter*, 385–386, pp. 961-965, ISSN 0921-4526. doi: 10.1016/j.physb.2006.05.283.

[21] Kennedy, S.J. (2006) "Construction of the Neutron Beam Facility at Australia’s Opal Research Reactor", *Physica B: Physics of Condensed Matter: Part 2*, 385, pp. 949–954. doi: 10.1016/j.physb.2006.05.280.

[22] Heonil Kim, Hark Rho Kim and Kye Hong Lee (1996) “Design Characteristics and Startup Tests of Hanaro–The Newly In-Service Korean Research Reactor”, *Journal of Nuclear Science and Technology*, 33(7), pp. 527–538.

Chapter 2

ISIS Facility and the INES beamline

The ISIS Neutron and Muon Source is a world-leading research centre in the physical, life and engineering sciences owned by the Science and Technology Facility Council (STFC) at the Rutherford Appleton Laboratory (Oxfordshire, UK - Fig.2.1). A schematic layout of ISIS is shown in Fig.2.2.

ISIS is a synchrotron-driven source designed to operate with an 800 MeV pulsed protons beam, with a repetition rate of 50 Hz: 40 pulses per second (pps) are received by the Target Station 1 (TS1), whilst 10 pps by the Target Station 2 (TS2). A Penning ion source delivers negative H^- ions to a Linac accelerator, which accelerated the beam up to 70 MeV and produces 200 μs long, 22 mA H^- pulses which are transported to the synchrotron. On entry to the synchrotron, the H^- beam is stripped of its two electrons by a 0.3 μm thick aluminium oxide stripping foil. The resulting protons are accumulated in the synchrotron into two bunches which are accelerated to 800 MeV. Immediately prior to extraction, the proton pulses are 100 *ns* long with a peak-to-peak separation of 230 *ns*. The entire acceleration process is repeated 50 times per second, so an overall mean current of 225 A is delivered to the targets, where the spallation process takes place for neutron production [1].

The mean protons currents delivered to the tungsten targets of TS1 and TS2 are 180 A and 45 A respectively A. However, each pulse received by both targets has a charge of $2.8 \cdot 10^{13}$ protons (45 C).

At TS1, muons are also produced using a thin carbon target located directly in the proton beam upstream of the neutron target. Neutrons and muons are channelled into more than 30 instruments, each of which is optimised for a specific scientific purpose.

Fig. 2.1 Aerial view of the Harwell Campus (Oxfordshire), where is based the ISIS Neutron and Muon Source [image credit: STFC].

2.1 The Italian Neutron Experimental Station Beamline

The Italian Neutron Experimental Station (INES) is built and managed by the Italian National Research Council (CNR) within the cooperation agreement with STFC, and is operative since the beginning of 2006 [2].

The INES beamline consists of a general-purpose neutron diffractometer employed to investigate a wide range of microscopic information inside dense matter. In particular, INES is a powerful instrument optimised for archaeological application, especially for studying metallic specimens. The available large sample volume allows the placement of non-standard samples in the neutron beam, through the use of aluminium frames when needed. Recently updates to the instrument resulted in the removal of the sample vacuum container. Thus, experimental measurements are now conducted in air, at standard pressure and temperature conditions, in an absolutely non-invasive way.

The neutrons ejected from the TS1 target are slowed down to thermal-epithermal energies in an ambient water moderator before arriving at the INES beamline, which is at a 22.8 m distance from the moderator and is located downstream of the spectrometer TOSCA. The limited dimension/size of the moderator results in an under-moderated beam, favouring the formation of a high fraction of epithermal neutrons in the INES spectrum, shown in Fig.2.4. Moreover, at 9.60 m far from the moderator a nimonic chopper is placed to filter out the high-energy neutrons. The measurements of the INES flux have been carried out with a Time-Of-Flight spatially resolved neutron monitor, described in Chapter 5, at a distance of 23.44 m from the moderator.

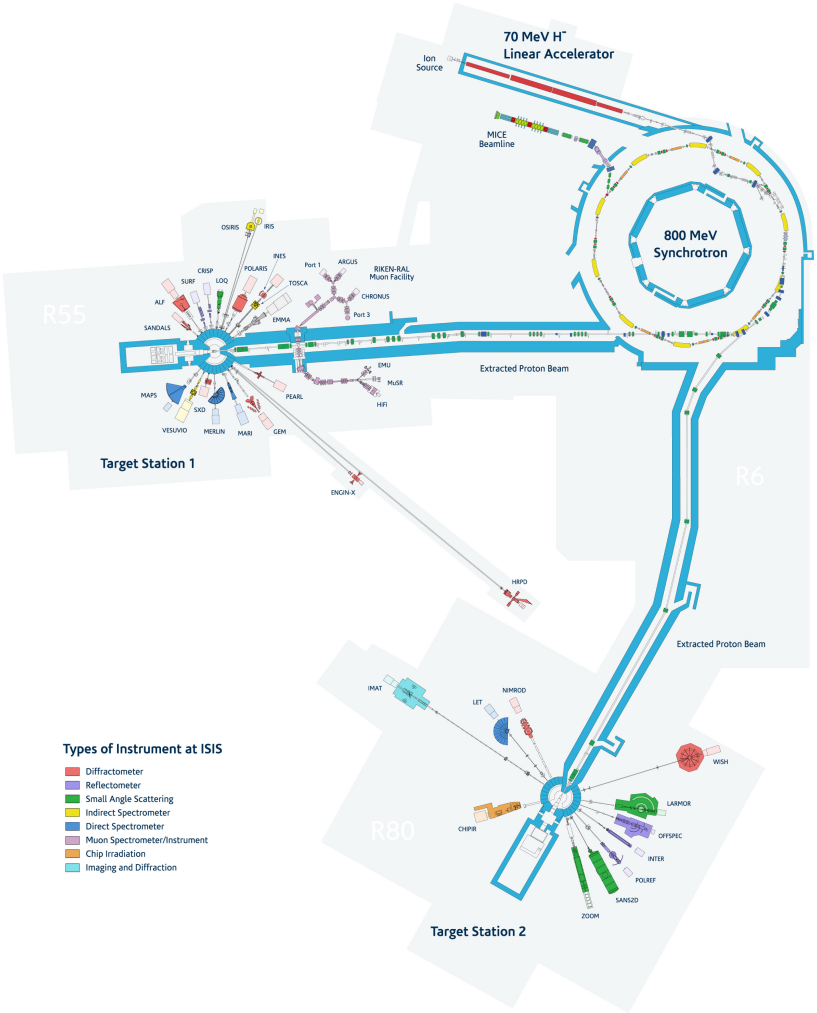

Fig. 2.2 Schematic representation of the physical layout of ISIS. The type of instrument (diffractometer, reflectometer, etc.) is highlighted for both the target stations TS1 and TS2. The light grey areas are the footprints of the buildings [image credit: STFC].

The neutron beam emerging from INES is collimated to give an almost entirely uniform square transverse section of about 3.2×3.2 cm^2, as shown in Fig.2.5. The vertical and horizontal beam profiles selected from the central position and displayed in Fig.2.6 show a slight non-uniformity of the beam intensity along the vertical direction.

A system of motor-adjustable jaws is installed at INES to change the side length of the beam and select the appropriate gauge volume of interest for the analysis of a sample, even in the millimetric range.

A beam shutter is present at INES, allowing the data acquisition almost independently from TOSCA. On average, a sample on TOSCA removes between 5 and 10% of the primary beam neutrons [3].

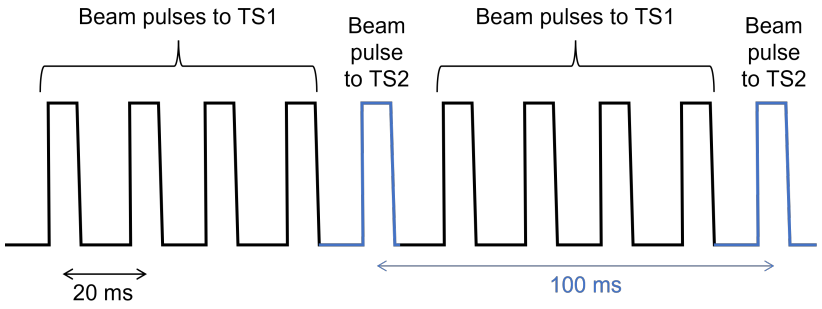

Fig. 2.3 Time structure of the proton beam pulses delivered to the Target Stations TS1 (in black) and TS2 (in blue) with a repetition rate of 50 Hz. Each pulse is composed of two proton bunches.

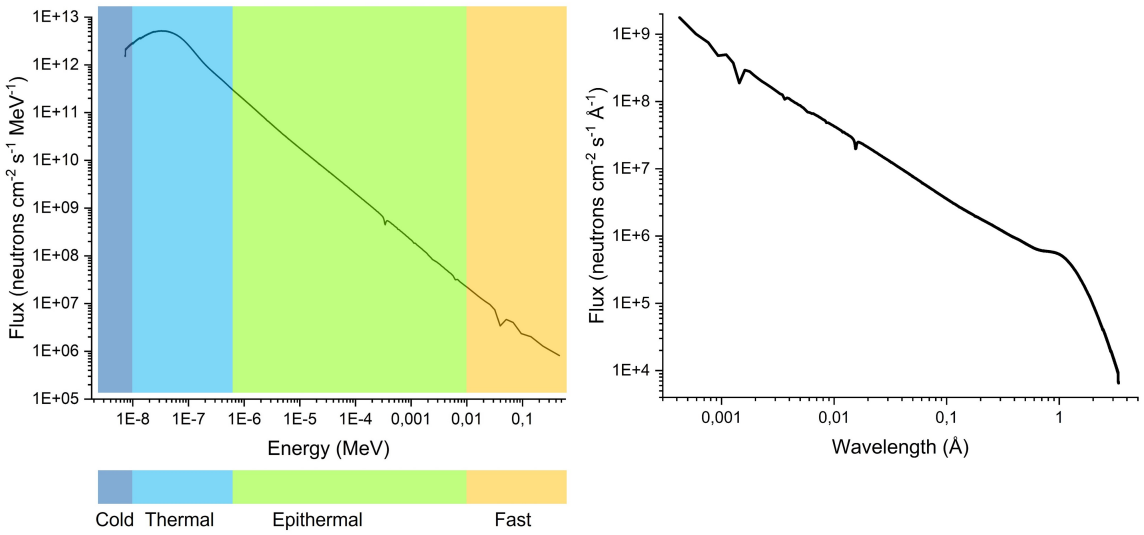

Fig. 2.4 On the left: INES energy neutron spectrum measured during INES commissioning experiment in Cycle 2021/01 (May 2021) at transmission position of 23.44 m from the moderator. The energy range subdivision is highlighted according to Table 1.2 (Chapter 1). On the right: the INES spectrum in wavelength scale.

The energetic structure of the INES neutron beam and its setup configuration allows to perform a wide range of neutron-based analyses, such as Time-Of-Flight Neutron Diffraction (TOF-ND), Neutron Resonance Capture Analysis (NRCA) and Neutron Resonance Transmission Imaging measurements (NRTI) (Fig.2.7-2.9). A detailed description of NRCA and NRTI techniques is provided in Chapter 5, whilst the set-up configuration currently available at INES is provided below.

The detection system for ToF-ND measurements consists of 144 ^{3}He detectors, grouped into 9 banks at a 1-meter distance from the sample position (22.804 m from the moderator),

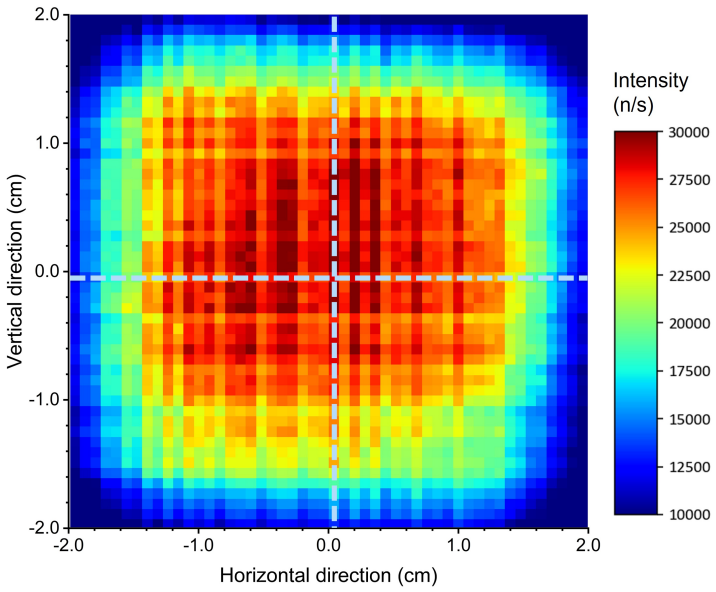

Fig. 2.5 Transverse intensity map of the INES neutron beam measured at a distance of 23.44 m from the moderator, coincident with the position of NRTI acquisitions (original data collected during INES commissioning experiment RB2030016.

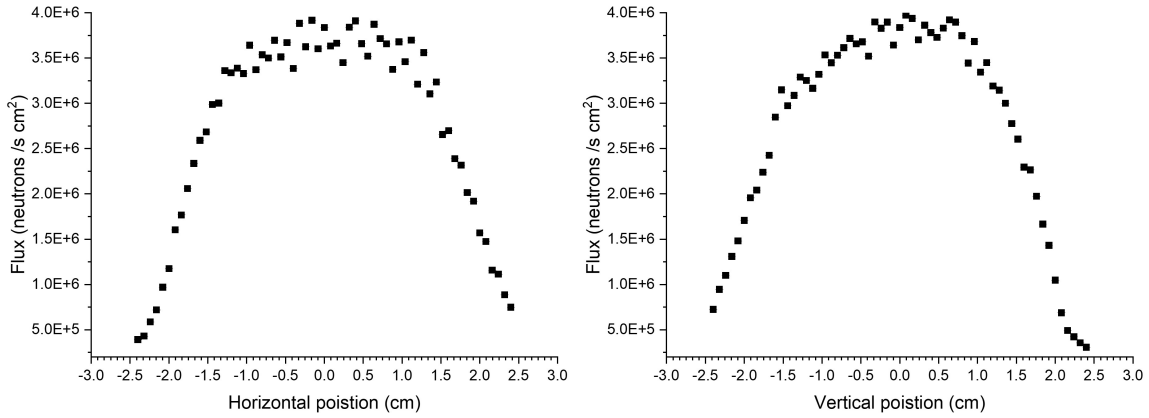

Fig. 2.6 The experimental INES neutron beam profile projected along the central horizontal and vertical shown in Fig.2.5.

covering a scattering angular range between 11.6° and 170.6°. Each of the 144 detectors produces a whole diffraction pattern as a function of the neutron time-of-flight, leading to different ranges of d-spacing depending on the scattering angle. The whole d-spacing range covered by the detection system extends from 0.1 to 16 Å (corresponding to a Q-range of 0.4 - 60 $Å^{-1}$). For each bank, the ToF spectra are usually converted in wavelength and averaged over the 16 detectors. The long primary flight path available for ToF measurements at INES

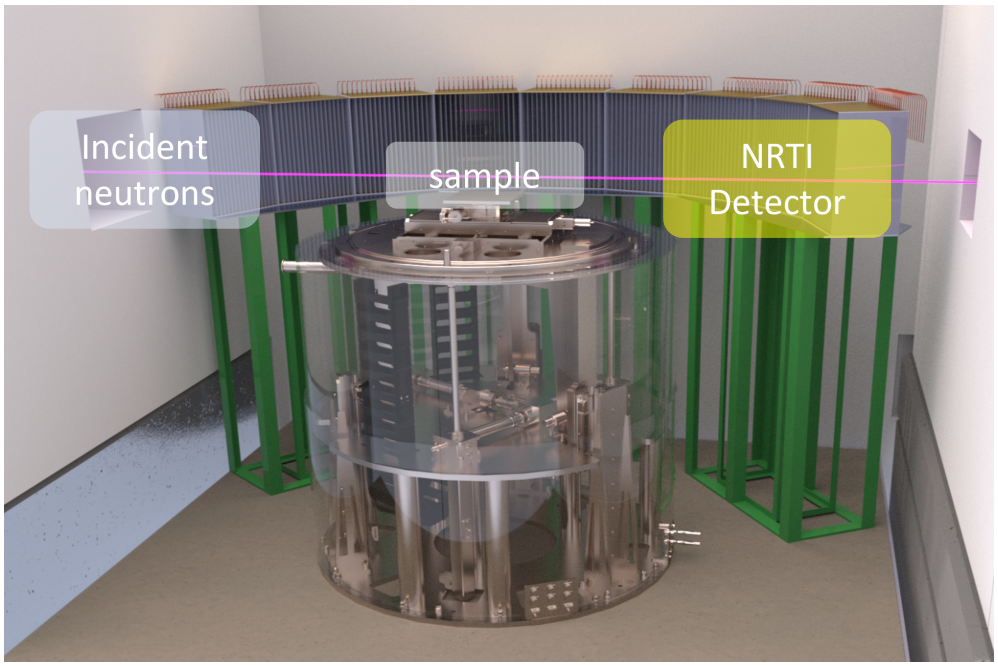

Fig. 2.7 A schematic layout of the INES beamline.

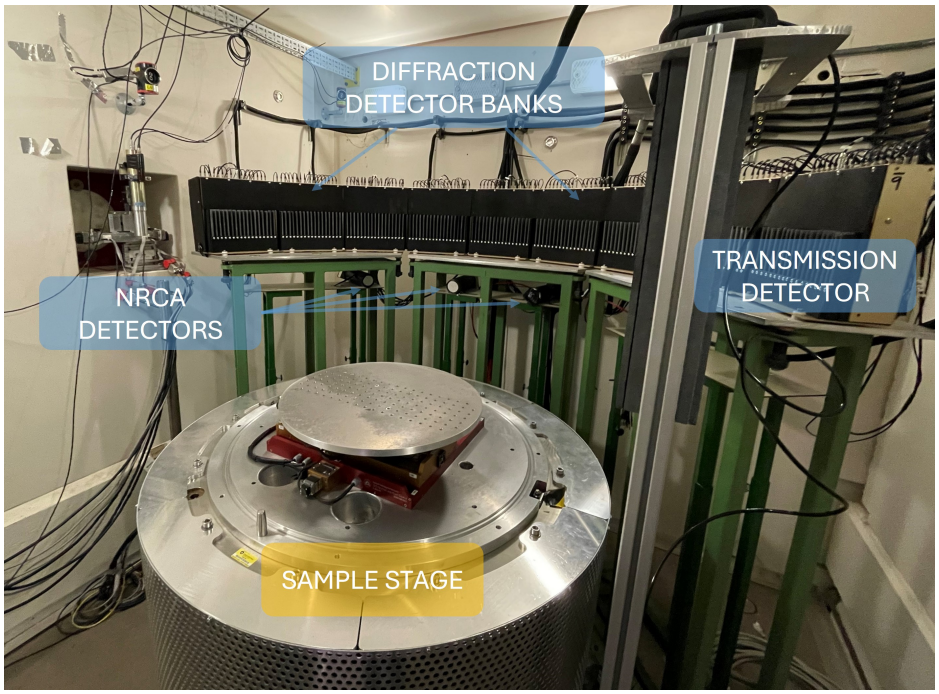

Fig. 2.8 Image of the INES beamline showing the different detectors employed for NRCA, ToF-ND and NRTI measurements. The XYZ movable stage for placing a sample is at the center of the image.

Fig. 2.9 On the left: front view of the detector used for transmission measurements. On the right: the detector used for monitoring the incident neutron flux coming to the sample under analysis in the beamline.

(22.804 m) results in a good resolving power of the instrument: the percentage resolution in backscattering is $\Delta d/d$=0.1%, whilst forward scattering reaches 1.3%.

NRCA experiments can be performed at INES, simultaneously with the ToF-ND measurements, by means of 3 Yttrium Aluminium Perovskite (YAP) scintillator crystals, with a surface area of 1 cm^2 and 0.6 cm thick, coupled to silicon photomultipliers and positioned above the sample stage at about 1 m distance from the sample position.

A diode laser device is available to visualise the centre of the incident neutron beam and therefore to centre the gauge volume of objects of irregular shapes with respect to the beam. Moreover, an XYZ movable stage is installed to facilitate the sample alignment.

References

[1] https://www.isis.stfc.ac.uk/Pages/Characteristics-of-a-pulsed-source.aspx

[2] Bartoli, L. et al. (2008) "Neutron Diffraction in Archaeometry: The Italian Neutron Experimental Station Ines@Isis", *Metallurgia Italiana*, 100(8), pp. 33–39.

[3] Imberti, S. et al. (2008) "Neutron Diffractometer Ines for Quantitative Phase Analysis of Archaeological Objects", *Measurement Science and Technology*, 19(3). doi: 10.1088/0957-0233/19/3/034003.

Chapter 3

LENA Reactor and the thermal neutron beamline

The Laboratory of Applied Nuclear Energy (LENA, Pavia - Italy) hosted a steady-state 250 kW TRIGA (Training Research and Isotope production General Atomics) Mark II Research Reactor, which offers in- and out-core neutron irradiation channels with various type of neutron spectrum. Since the first criticality of the reactor led in 1965 [1], several scientific and technical applications have been carried out [2], such as - just to cite a few - Boron Neutron Capture Therapy (BNCT), Neutron Activation Analysis (NAA) for trace elements determination in materials and environmental samples, neutron irradiation hardness studies on electronic components and production of radio-labelled pharmaceuticals for medical diagnosis.

The LENA reactor is characterised by a right-cylindrical core, cooled and partly moderated by light water [3]. 90 cylindrical elements located on 5 concentric rings around the Central Thimble (CT) channel compose the lattice of the core. These elements have different purposes: 81 of them are moderator-fuel elements (uranium enriched at 20% with ^{235}U mixed with zirconium hydride); 3 rods made of boron carbide and borated graphite control the reactivity of the reactor by regulating the power level and ignition/shutdown of the reactor; one radium–beryllium source is employed to trigger off the chain reaction during reactor ignition; 3 are vertical irradiation channels which penetrate inside core allowing irradiation of small samples into the maximum flux region; the remaining elements are graphite elements (dummy elements). Fuel elements on the first, second and third rings have stainless steel cladding, while those on the fourth and fifth rings have aluminium cladding [4]. A uniform mixture of uranium (8% weight, enriched to 20% in ^{235}U), zirconium (91% weight) and hydrogen (1% weight) constitutes the fuel.

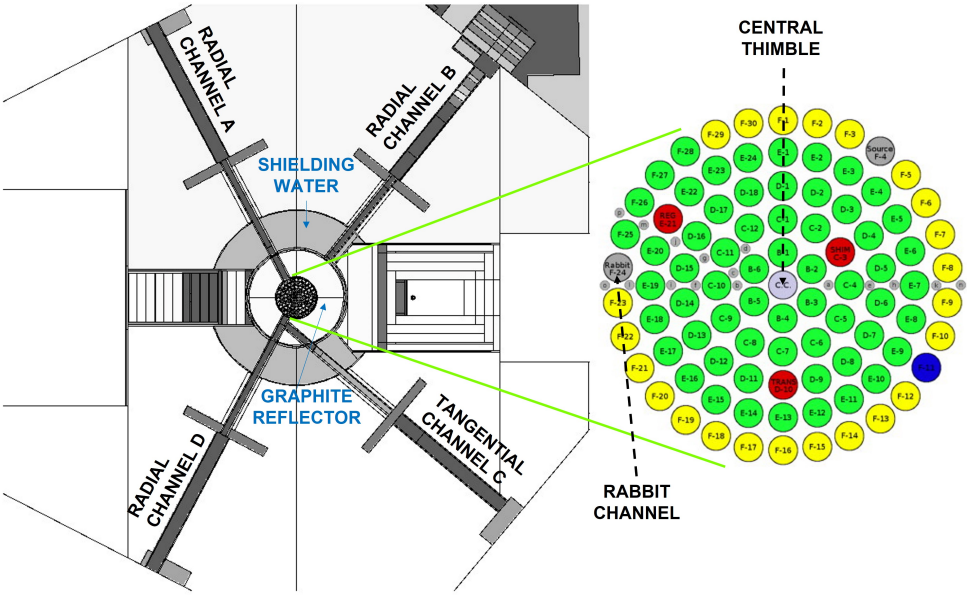

Fig. 3.1 Top view of the LENA reactor. The horizontal irradiation channels are indicated, as well as the position of the water tank and the graphite reflector surrounding the reactor core. On the right, an enlargement of the core configuration [1]. Fuel elements are represented in green, graphite rods in yellow, control rods in red and the empty slot in blue. The smaller grey circles represent holes on the top core grid. The position of the two vertical irradiation channels is indicated (Central Thimble and Rabbit Channel).

The core is surrounded by a 30 cm thick radial graphite reflector. Moreover, the fuel elements themselves have the effect of an axial reflector due to the allocation of two 10 cm thick graphite cylinders at the ends of the rod. The light water in the reactor tank also acts as a reflector.

The LENA reactor provides both vertical and horizontal irradiation channels (Fig.3.1). Along the vertical axis of the core, the neutron flux is maximum. Here, 4 vertical channels are installed: the Central Thimble, the Pneumatic Transfer Tube (Rabbit), the Rotary Specimen Rack (Lazy Susan) and the Thermal Channel. These irradiation channels are mainly employed for Instrumental Neutron Activation Analysis and isotope production. The Central Thimble is a dry tube which can host up to 3 samples in cylindrical containers (130 mm-height; 30 mm-diameter made by polyethene or aluminium) and its position in the core can be conveniently adjusted according to irradiation needs. The Rabbit channel is positioned in the outer core ring and can be operated remotely by a pneumatic sample transfer system, through which samples are sent and received directly from the dedicated hood in a radiochemical laboratory. The Lazy Susan is an aluminium channel provided with 40 holes (38 mm of inner diameter) arranged in an annular groove in the upper section of the reactor core, which can load up to 80 samples in cylindrical containers (130 mm-height, 30 mm-diameter). Just out

the reactor is placed the Thermal Channel, made of an aluminium cylinder (38 cm-height; 7 cm-diameter).

The LENA TRIGA Mark II is equipped with 4 horizontal irradiation channels: two of them are radial irradiation channels (A and B) which extend to the reflector outer edge; the channel C is tangential to the core, whilst the radial piercing channel D runs through the graphite reflector. For the purpose of this thesis, a detailed description of the horizontal radial channel B is provided in the following section.

Table 3.1 Main features of LENA TRIGA Mark II based on details described in [5].

Maximum steady-state power	250 kW
Fuel	Uranium zirconium hydride fuel enriched 20% wt. in ^{235}U
Reflector	Graphite
Moderator	Demineralized light water
Control rods	2 containing boron carbide + 1 containing boron enriched graphite
Maximum neutron flux	$\sim 2.0 \cdot 10^{13}$ cm^{-2} s^{-1}
Vertical irradiation channels	4 (Central Thimble, Rabbit, Lazy Susan and Thermal Channel)
Horizontal irradiation channels	4 (3 radial channels and 1 tangential channel)

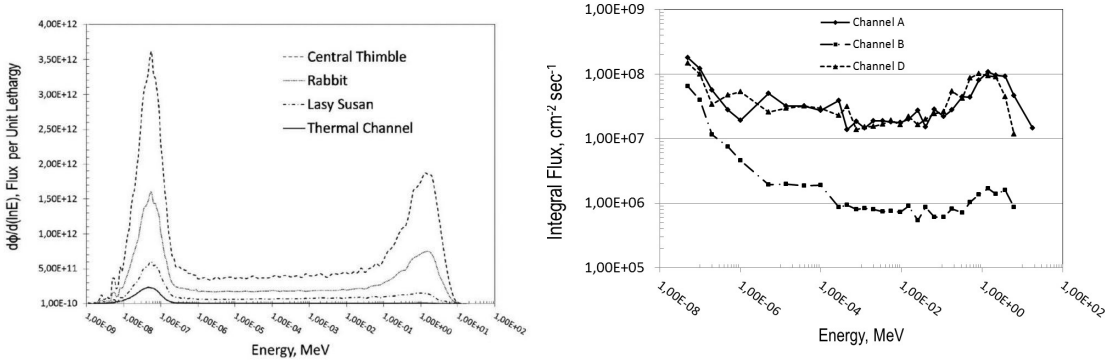

Fig. 3.2 On the left: fluxes per unit lethargy spectra calculated with Monte Carlo code MCNP in the vertical channels [3]. On the right: integral flux spectra calculated with Monte Carlo code MCNP for horizontal channels A, B and D [2]. The presence of the graphite reflector causes a lower flux for channel B.

3.1 The horizontal thermal channel B

A thermal neutron beamline is available at channel B (CHB) of the LENA reactor, where a 5.55 m long cylindrical collimator, with a 100 mm thick sapphire (Al_2O_3) filter and a 70 mm thick bismuth filter, is placed (Fig.3.3).

The actual configuration of the CHB results from a previous two-years work within the framework of the INFN-CHNet TANDEM project and co-founded by LENA Laboratory aiming at implementing a Prompt Gamma Neutron Activation Analysis (PGNAA) facility in this channel [2]. PGNAA is usually conducted with thermal or cold neutron flux (10^6 - 10^9 cm^{-2} s^{-1}) to study the elemental composition of the samples of interest in different fields like materials science or Cultural Heritage. To install the PGNAA setup at the TRIGA Mark II research reactor, the horizontal channel B was chosen due to the higher thermal-to-fast neutron flux ratio investigated through MNCP simulations with respect to other channels and for logistic reasons. An experimental hutch made of baryte concrete was designed and installed around the exiting of beam port B to house the HPGe detector employed for the PGNAA measurements. Moreover, to produce a collimated thermal neutron beam with enhanced thermal-to-fast neutron ratio, a sapphire (Al_2O_3) cylinder as a fast neutron filter, a Bi disk to attenuate the γ background coming from the reactor core and a collimator were installed in the CHB.

After the filters, an alternating layer of iron and lithiated polyethylene rings (50 mm of inner diameter) were placed to slow down fast neutrons through inelastic scattering with iron and thermalise them through hydrogen. ^{6}Li is used to capture thermal neutrons diverging from the propagation direction (^{10}B as a thermal neutron absorber was not used because of its 478 keV-γ emission from neutron capture reaction). The beam exiting these rings is therefore thermalised and collimated with a diameter of 50 mm at the exit of the collimator.

An internal horizontal and an external vertical shutter systems were installed at the CHB (Fig.3.4), both made of alternating iron and lithiated polyethylene layers as well. A beam catcher was then positioned at the end of the concrete shielding to stop the neutron beam. The dimensions of each component of the beamline are listed in Table 3.2.

Table 3.2 Description of materials and dimensions characterising the CHB components.

Component	**Materials**	**Dimensions (cm)**
Sapphire	Al_2O_3	Diameter: 7 Thickness: 10
Bismuth disk	Bi	Diameter: 10 Thickness: 7
Internal collimator	Lithiated polyethene + Fe	Internal diameter: 5 External diameter: 20 Polyethene rings thickness: 10+10 = 20 Fe rings thickness: 5+8 =13 Total thickness: 33
Horizontal shutter	Boral + lithiated polyethene + Fe	Boral thickness: 0.5 Lithiated polyethene thickness: 4 Fe thickness: 17 Total thickness: 21.5 Length: 30, height: 22
Vertical shutter	Lithiated polyethene + Fe	Lithiated polyethene thickness: 7.5+7.5+10 = 25 Fe thickness: 10+5+5 = 20 Total thickness: 45 Length: 15, height: 41
Beam Stopper	Lithiated polyethene + Fe + Ba. concrete	Lithiated polyethene thickness: 20 Fe thickness: 15 Ba concrete: 40 Total thickness: 75 Length: 15, height: 15

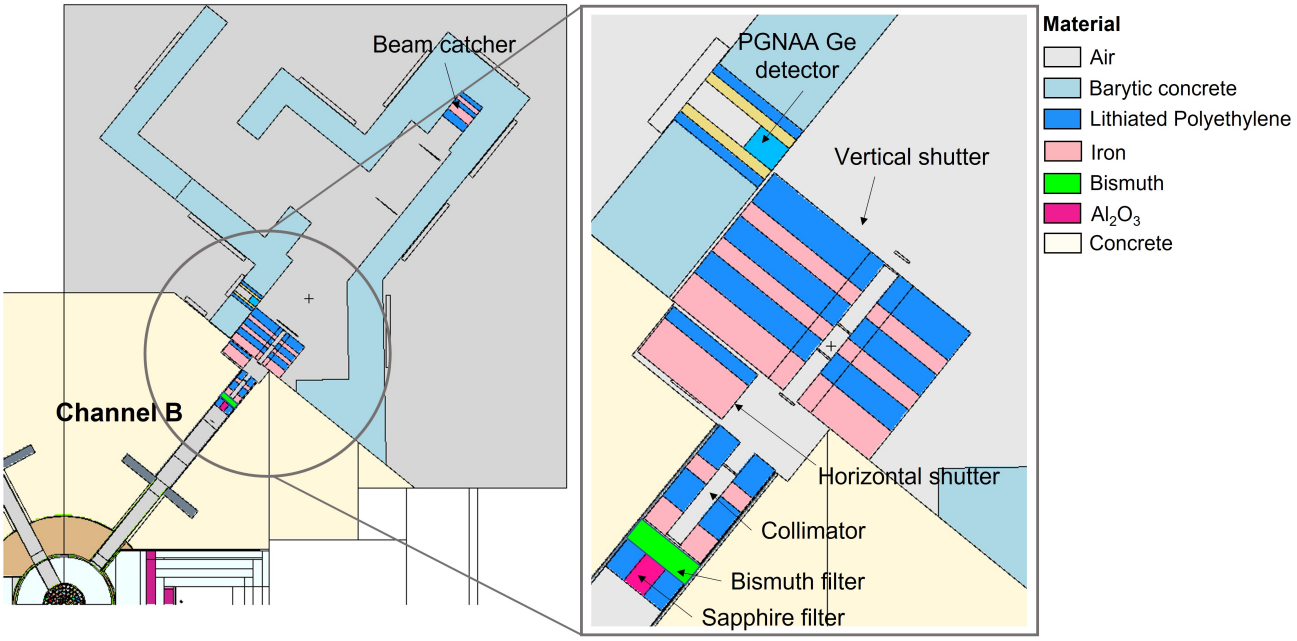

Fig. 3.3 On the left: horizontal view of the thermal channel B in the LENA reactor with the hutch installed for the PGNAA facility. On the right: the collimator with the sapphire and bismuth filters, the two shutters and Ge detector employed for PGNAA measurements.

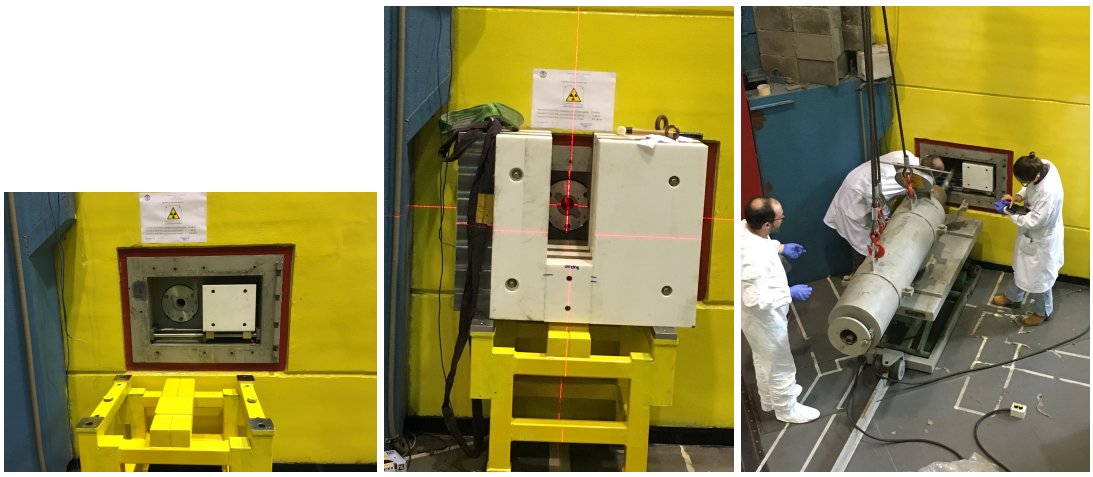

Fig. 3.4 (left): the horizontal shutter installed at the beam port B within the TANDEM project. (central): the vertical shutter. (right:) the collimator placed inside the thermal channel B during the TANDEM project.

References

[1] Alloni, D. et al. (2014) “Final Characterization of the First Critical Configuration for the Triga Mark II Reactor of the University of Pavia Using the Monte Carlo Code MCNP”, *Progress in Nuclear Energy*, 74, pp. 129–135. doi: 10.1016/j.pnucene.2014.02.022.

[2] https://lena.unipv.it/. Accessed 6th April 2023.

[3] Borio di Tigliole, A. et al. (2014) “Triga Reactor Absolute Neutron Flux Measurement Using Activated Isotopes”, *Progress in Nuclear Energy*, 70, pp. 249–255. doi: 10.1016/j.pnucene.2013.10.001.

[4] Alloni, D. et al. (2015) “Neutron Flux Characterisation of the Pavia Triga Mark II Research Reactor for Radiobiological and Microdosimetric Applications”, *Radiation Protection Dosimetry*, 166(1-4), pp. 261–265. doi: 10.1093/rpd/ncv291.

[5] Prata, M. et al. (2014) “Italian Neutron Sources”, *The European Physical Journal Plus*, 129(11), pp. 1–15. doi: 10.1140/epjp/i2014-14255-3.

[6] Salvini, A., Alloni, D., Clemenza, M. (2019) "Design and Safety of the PGNAA Facility at the TRIGA Research Reactor of the University of Pavia – Lena", Proceedings of the International Conference Nuclear Energy for New Europe, Portorož, Slovenia, September 9-12.

Chapter 4

Neutron techniques for material characterization: an overview

Several intrinsic properties of neutrons allow the investigation of a wide range of objects, from a microscopic to a centimetre scale, providing different kinds of information such as the chemical composition in terms of elements and isotopes, phase-specific and microstructural analysis and morphological features of large objects.

Moreover, the non-destructiveness of the neutron as a probe makes neutron-based techniques unique and of great benefit for Cultural Heritage examinations, being in most cases complementary to the more conventional methods usually employed for the analysis of archaeological objects. Neutron analyses are characterized by a beam size of several centimetres, providing bulk averaged information. Moreover, the penetration power of these neutral particles makes them a powerful tool for visualizing the internal properties of materials without sampling the objects, in contrast with X-rays and charged particles. An additional striking feature of neutrons is their high sensitivity to specific light elements (*e.g.* H), providing good contrast for light atoms in the presence of heavy atoms, making for example neutron imaging complementary to the "traditional" X-ray imaging.

A wide extensive range of neutron absorption and scattering reactions including diffraction, refraction, magnetic interactions, and, potentially, vibrations are exploited for material characterisation. Some of these reaction mechanisms are at the basis of the most common neutron-based techniques actually explored in the scientific research and introduced in this Chapter, which are: neutron resonance absorption spectroscopy (comprising Neutron Resonance Capture Analysis (NRCA) and, Neutron Resonance Transmission Analysis (NRTA)) and Neutron Tomography (NT). Fig.4.1 schematically represents the nuclear processes exploited for the most-common neutron-based techniques employed for material characterisation. The following sections aim to give basic notions of NRCA, NRTA and NT

supporting the research conducted in this Thesis. A more detailed overview of neutron-based methods is reported in the books of Kardjilov N. and Festa G. [1], Anderson I.S. et al. [2, 3], Schillebeeckx P. and Postma H. [5].

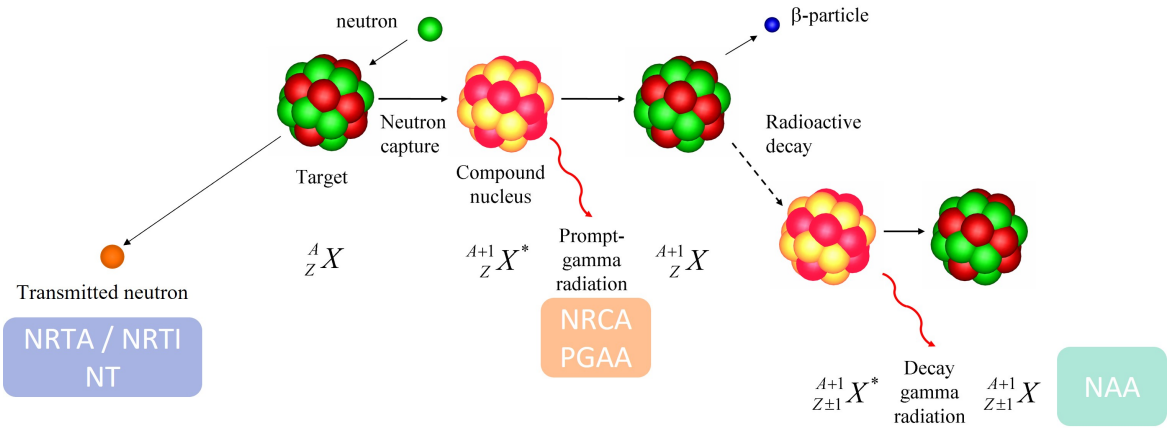

Fig. 4.1 A schematic representation of the neutron reactions used for neutron-based techniques commonly employed for material characterisation [5].

It is worth mentioning some weaknesses of neutron techniques, which are the potential activation of objects for short or long times, the longer acquisition time and lower spatial resolution with respect to X-rays analysis, and the high cost of neutron production. For this reason, previous characterisations with common methods are useful and quite often necessary for accessing neutron beamtime.

4.1 Neutron resonance absorption spectroscopy

The analytical approach of neutron resonance absorption spectroscopy is based on the presence of sharp peaks, known as resonances, at which the neutron-induced reaction cross-sections increase by several magnitudes.

For each nuclide, resonance structures appear at specific energies univocally determining a fingerprint for the presence of an element and/or an isotope in the material.

In the field of resonance absorption spectroscopy with neutrons for elemental and isotopic composition determination, two methods have been currently explored being powerful non-destructive analyses: they are known as Neutron Resonance Transmission Analysis

(NRTA) and Neutron Resonance Capture Analysis (NRCA). Both NRTA and NRCA are usually performed at neutron spallation sources exploiting the high epithermal neutron fluxes available there, which is a profitable energy range for elemental and isotopic material characterisation due to the fact that the intense and well-separated resonance structures in the neutron-induced reaction cross-sections lie in this energy region.

Fig.4.2 shows the total neutron cross-section for some elements of interest for composition analysis of archaeological metallic artefacts. Here, the epithermal neutron energy region is highlighted, in order to focus on the main resonances useful for NRCA and NRTA analysis.

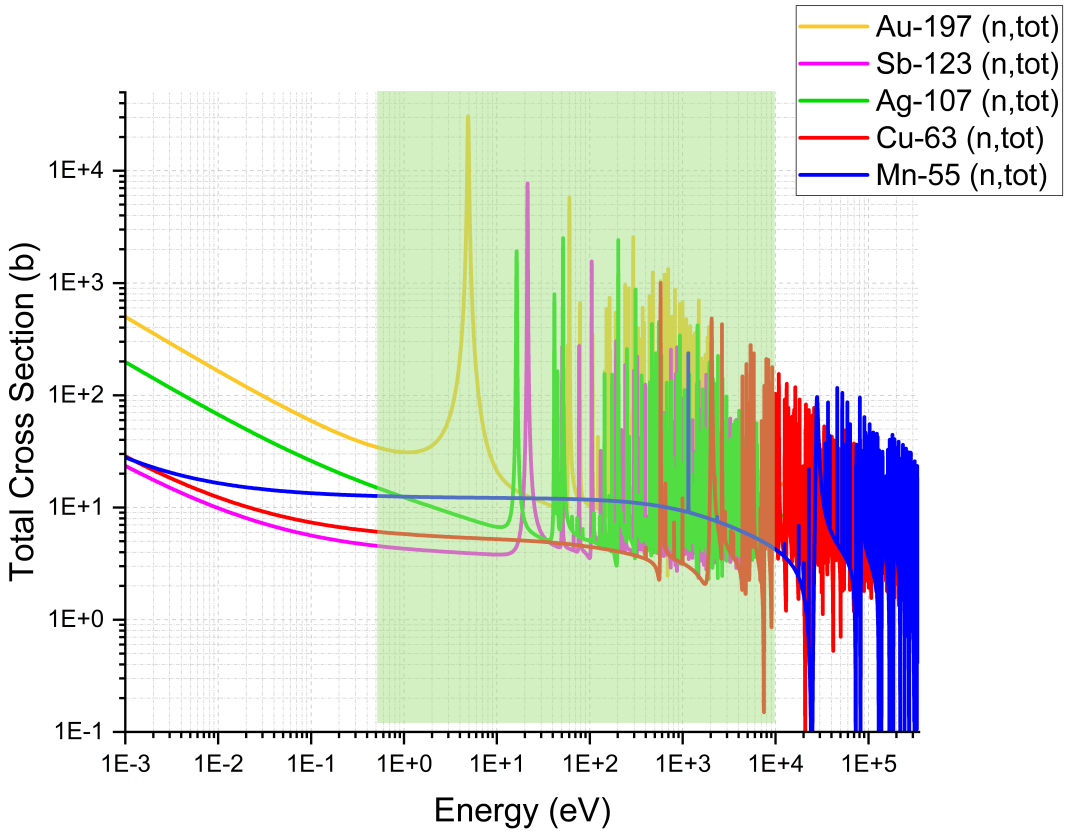

Fig. 4.2 Neutron total cross-section of ^{197}Au, ^{123}Sb, ^{107}Ag, ^{63}Cu and ^{55}Mn. The green region delimits the epithermal energy region where the main resonances of these elements are more intense and well resolved [6].

A brief discussion of the fundamentals of neutron resonance can be found in the following sections, along with a description of NRTA and NRCA methods.

4.1.1 General description of resonances

As previously mentioned in Chapter 1, resonances in neutron-induced reaction cross-sections correspond to compound states, which can be described by a finite lifetime and by an energy uncertainty (or width) $\Gamma = \hbar/\tau$ (Fig.4.3). The quantity $\Gamma/\hbar = 1/\tau$ represents the decay probability per second of the compound state and it is composed of different contributions, depending on the various possible decay channel (such as γ-emission, re-emission of a neutron, emission of charged particles, etc.):

$$\Gamma = \Gamma_\gamma + \Gamma_n + \Gamma_\alpha + ... \tag{4.1}$$

where Γ_γ is called the radiation width, Γ_n the neutron width, etc. Generally, for each reaction i, Γ_i varies between resonances and among nuclei. Some general patterns do, however, exist: the radiation width Γ_γ, for example, changes only slightly among resonances of the same nucleus (around 0.2 eV for intermediate nuclei; for heavy nuclei, it decreases to some 30 meV [7]). The neutron width Γ_n involves some more degrees of complexity, but on average it increases with neutron energy (light nuclei are characterised by a Γ_n of the order of keV, for intermediate nuclei Γ_n is of the order of eV, and for heavy nuclei of the order of meV).

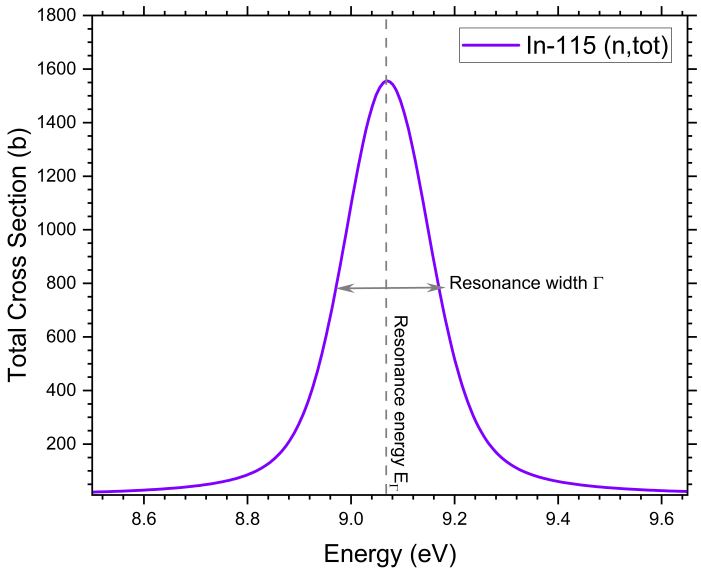

Fig. 4.3 Total resonance cross section of ^{115}In in the vicinity of the 9.07 eV resonance, at 300 K [6].

From quantum mechanics, the incident neutron, the target nucleus and both resulting reaction products may be described by ingoing and outgoing wavefunctions. The neutron is characterised by a spin $s = 1/2$; the target nucleus has a spin quantum number I which can be zero or a multiple of $1/2$. These two spins combine to the so-called channel spin $s = I + 1/2$. Angular moments of the ingoing wave are useful for representing the relative motion of the neutron, where l is zero or a positive integer. It is possible to classify resonances according to the partial wave that contributes to the resonance: $s-$, $p-$, $d-$, $f-$resonances correspond to moments of 0, 1, 2, 3, respectively. Most resonance reactions for slow and intermediate neutrons do not involve an exchange of orbital angular momentum from the captured neutron to the compound states. These resonances are called $s-$wave resonances and can be parameterised through an energy-independent reduced neutron width Γ_{n0} as follows:

$$\Gamma_n = \Gamma_{n0}\sqrt{E/E_0} \tag{4.2}$$

with E_0 = 1 eV. Reduced neutron width for $p-$, $d-$, etc. wave resonances have a more complex definition.

Denoting with the incident (c) and exit (c') channels the incident and emerging particles, respectively, the transition probability from a specific incident channel to an exit channel, which is the partial cross-section $\sigma_{cc'}$, can be parameterised through the R-matrix formalism [8] as follows:

$$\sigma_{cc'} = \pi\lambda\!\!\!^{-}{}_{cc'}{}^2 g_c |\delta_{cc'} - U_{cc'}| \tag{4.3}$$

where $\lambda\!\!\!^{-} = \lambda/2\pi$ is the reduced de Broglie wavelength of the neutron, $g_c = (2J+1)/2(I+1)$ describes the probability of combination of the neutron angular moment I and the target spin giving the total spin quantum number J, $\delta_{cc'}$ is the Kronecker delta and $U_{cc'}$ is the collision matrix containing the probability combinations between the incident channels and the outgoing channels. Different formalism can be used to describe this collision matrix [9–11], such as the Single-Level Breit-Wigner (SLBW) approximation, the Multi-Level Breit-Wigner approximation, the Adler-Adler approximation or the Reich-Moore formalism.

In this dissertation, the simplest model for describing the resonance shape is discussed, which is given by the SLBW formalism. It applies only to resonances that are well separated and do not interfere with one another.

In the neighbourhood of an isolated single-state resonance of a nucleus, with an orbital momentum of the neutron-nuclear system, the total cross section can be described through the Breigt-Wigner formula [9] as the sum of a resonance term, a potential scattering term and

an asymmetric term resulting from the interference between potential and resonance elastic scattering:

$$\sigma_{TOT}(E) = \pi\lambda\!\!\!^{-2} g_J \frac{\Gamma\Gamma_n}{(E-E_\Gamma)^2+(\Gamma/2)^2} + 4\pi\lambda\!\!\!^{-2} g_J \frac{\Gamma_n(E-E_\Gamma)R'}{(E-E_\Gamma)^2+(\Gamma/2)^2} + 4\pi R' \qquad (4.4)$$

where $g_J = (2J+1)/2(I+1)$ describes the probability of combination of the neutron angular moment I and the target spin giving the total spin quantum number J, E_Γ is the resonance energy and R' is the effective scattering radius. Upon the resonance, the neutron width is not affected by an energy dependence, resulting in a symmetric Lorentzian shape $1/(1+x^2)$, with $x = 2(E-E_\Gamma)/\Gamma$ for the resonance cross-section in Eq.4.4.

In the low energy region far from the resonance ($E \ll E_\Gamma$ and $E \ll \Gamma$), the capture cross-section varies with $\sqrt{E}$, that is inversely proportional to the neutron velocity v. The area under the resonance term of the total cross section in Eq.4.4 is:

$$A_{TOT} = 2\pi\lambda\!\!\!^{-2} g_J \Gamma_n \qquad (4.5)$$

As a further explanation, Fröhner (2000) gives a more detailed analysis of resonance structured in neutron-induced reaction cross-sections.

From experimental measurements of neutron cross sections, the observed resonance profiles result broadened due to the statistical thermal motion of the atomic nuclei. This effect is known as Doppler broadening and causes a shift of the relative kinetic energy in the neutron-nucleus system. The mathematical description of the Doppler broadened cross-section σ^D can be obtained through the convolution of the cross-section σ for a target nucleus at rest and an energy transfer function $S(E,E')$. According to the Free Gas Model, for $E \gg \Delta_D$ (Δ_D is the Doppler width), σ^D can be approximated by a convolution of $\sqrt{E'/E}\sigma(E')$ with a Gaussian [12]:

$$\sigma^D \simeq \frac{1}{\sqrt{\pi}\Delta_D} \int_{-\infty}^{\infty} dE' e^{\left(\frac{E-E'}{\Delta_D}\right)^2} \sqrt{\frac{E'}{E}} \sigma(E') \qquad (4.6)$$

where the Doppler width at sample temperature T is given by $\Delta_D = \sqrt{\frac{4EK_BT}{M/m}}$ with M and m the rest mass of the target nucleus and neutron respectively and K_B the Boltzmann constant.

In the case of a crystalline solid, the sample temperature can be approximated to an effective temperature related to the Debye temperature following the Free Gas Model:

$$T_{eff} \simeq \frac{3}{8}\Theta_D \coth\left(\frac{3}{8}\frac{\Theta_D}{T}\right) \qquad (4.7)$$

For single-element crystalline solids at room temperature T=300 K and elements like lead occurring as clusters in a solid solution such as bronze, the effective temperature is only a few per cent higher than T and the Debye temperature is their elemental D value. However, in dissolved or compounded elements the Debye temperatures will differ and can be evaluated through a simple interpolation model.

Regarding only the capture cross-section $\sigma_\gamma(E)$, of interest for the NRCA technique, it can be handled similarly to the total cross-section above mentioned within the Single-Level Breit-Wigner formalism:

$$\sigma_\gamma(E) = \pi\lambda\!\!\!^{-2} g_J \frac{\Gamma_\gamma \Gamma_n}{(E-E_\Gamma)^2 + (\Gamma/2)^2} \tag{4.8}$$

Only a resonance term is included in this capture cross-section. The radiation width Γ_γ is the sum of the partial widths related to all primary γ-rays emitted from the capture state. At the resonance centre E_Γ, the capture cross-section reaches its maximum:

$$\sigma_{\gamma,MAX}(E-E_\Gamma) = 4\pi\lambda\!\!\!^{-2} g_J \frac{\Gamma_\gamma \Gamma_n}{\Gamma^2} \tag{4.9}$$

and the resonance area is given by $A = 2\lambda\!\!\!^{-2} g_J \frac{\Gamma_\gamma \Gamma_n}{\Gamma}$.

As an approximation to the Doppler broadened capture cross-section around a single resonance, the following formula may be used:

$$\sigma^D{}_\gamma(E) \simeq \sigma_{\gamma,MAX} \Psi(\beta, x) \tag{4.10}$$

where $\Psi(\beta, x)$ is the Voigt function:

$$\Psi(\beta, x) = \frac{1}{\beta\sqrt{\pi}} \int_{-\infty}^{\infty} dy \frac{1}{1+y^2} e^{-\frac{(x-y)^2}{\beta^2}} \tag{4.11}$$

with the following variables:

$$\beta = 2\Delta_D/T \;\;,\;\; x = 2(E-E_\Gamma)/\Gamma \;\;,\;\; y = 2(E-E')/\Gamma \tag{4.12}$$

The Voigt function is characterised by a Gaussian shape around the resonance centre E_Γ and by a Lorentzian shape in the lateral broadened tails. Despite the convolution, the resonance curve remains the same in the area while being lowered and widened. The resonance peak maximum is reduced by a factor:

$$\Psi(\beta, E = E_\Gamma) = \frac{\sqrt{\pi}}{\beta} e^{1/\beta^2} erfc(1/\beta) \tag{4.13}$$

in which erfc is the complementary error function.

4.1.2 Time-Of-Flight spectroscopy

Neutron resonance spectroscopic measurements are carried out by NRTA and NRCA using the Time-Of-Flight (TOF) method typically at a white neutron source. An accelerator-driven neutron source running in pulse mode or a continuous neutron source using a chopper can achieve this type of spectroscopy.

The TOF technique relies on the determination of the time t needed for a neutron to travel a given distance L. A schematic representation of a basic TOF setup is shown in Fig.4.4. Using the measure of the time-of-flight t and knowing the distance L, the energy of the neutron can be determined, under the assumption of non-relativistic velocities of the particle:

$$E = 1/2m(L/t)^2 \tag{4.14}$$

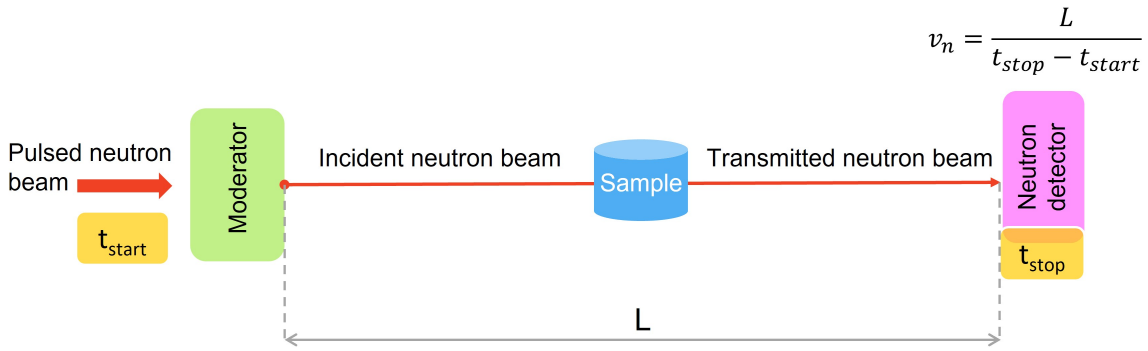

Fig. 4.4 Schematic representation of the TOF technique in case of a transmission measurement. Spectroscopy measurements are possible by tracing back the neutron velocity (and therefore energy) using the known neutron flight-path L and its time of flight.

From a practical approach, the time-of-flight t is derived from the difference between a stop signal t_{stop} provided by the detection system and a start signal t_{start} delivered by the source. More specifically, different contributions can be distinguished, which sum up providing the observed time-of-flight and its overall uncertainty [13]: the time difference between the moment the neutron leaves the target-moderator assembly and its time of creation; the time (t_m) that a neutron, leaving the target-moderator assembly with a velocity v, needs to travel the distance L; the time difference (t_d) between the time of detection and the moment the neutron enters the detection system or the sample. Usually, the total TOF uncertainty is dominated by the moderation process t_m (few hundreds of ns [5, 4]), whose probability distribution strongly depends on the neutron energy. However, a variable

transformation can be operated by introducing an equivalent distance $L_m = vt_m$. As a result, the distribution L_m is less dependent on neutron energy [13].

The total energy resolution characterising a Time-Of-Flight spectroscopy set-up can be approximated by:

$$\frac{\delta E}{E} = 2\frac{\delta v}{v}\sqrt{\left(v\delta t_{start}\right)^2 + \left(\delta t_{stop}\right)^2 + \delta {L_m}^2 + \delta {L_d}^2} \tag{4.15}$$

where each component is not correlated to the others, follows a Gaussian distribution and in first approximation is independent of the neutron energy.

Under these assumptions, with increasing distance, energy resolution improves for fixed energy. However, the $1/L^2$ dependence of the neutron intensity must be considered as well, and thus a compromise has to be usually made between resolution and intensity. Moreover, the Doppler broadening is dominant at low energies, which needs to be taken into account when defining an optimum distance [15].

4.1.3 Neutron Resonance Capture Analysis

Through NRCA the elemental composition of an object can be disclosed, providing insight into the origin of the sample, the fabrication methods, trade relations and the usage of the objects. NRCA is particularly useful for detecting impurities whose capture cross sections are very intense at low energies: even parts per million (ppm) of elements with resonances between 1 and 10 eV region can be detected [1]. Other main advantages of the technique are the direct availability of results after the measurement and the detection geometry that allows the investigation of large objects.

The technique is based on TOF measurement of prompt γ-rays emitted after neutron capture reactions in the material under investigation [15, 16]. The arrival time of the γ cascade following the neutron capture reaction is recorded on the detector instead of performing standard energy spectroscopy. Thus, the time of flight (and therefore energy) of the neutron captured by the sample is determined. The resulting TOF spectrum is characterised by resonance peaks induced by (n,γ) resonance absorption, which are analysed for determining qualitative (from their time position) and quantitative (from their content) information about the sample elemental composition (Fig.6.23).

The optimum detection system for NRCA applications should have, therefore, a very good time resolution and low sensitivity to scattered neutrons.

The observable of interest is the capture yield, which is the fraction of the incident neutron beam undergoing a capture reaction in the sample. Nuclide-specific capture yields $Y_{\gamma,k}$ can be expressed as the sum of primary $Y_{0,k}$ and multiple interaction events $Y_{m,k}$, *i.e.* capture

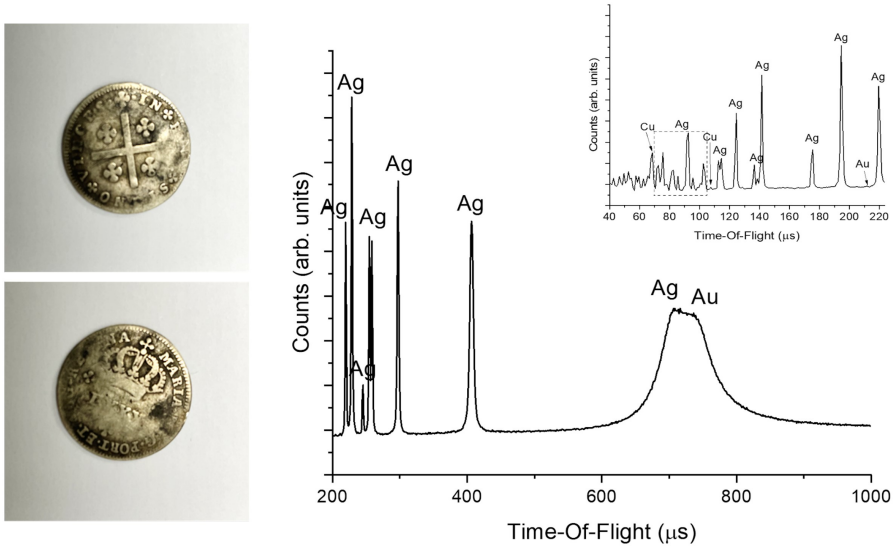

Fig. 4.5 The NRCA spectrum of an 18th-century silver Portuguese coin (images on the left). The identified peaks are related to the presence of silver, copper and gold in the coin bulk (original NRCA data collected during the experiment "Combination of neutron-based techniques to derive the composition of an 18th-century coin": https://doi.org/10.5286/ISIS.E.RB2010534).

reactions after at least one neutron scattering event in the sample. Each $Y_{\gamma,k}$ contributes to the total capture yield of the material [15]:

$$Y_\gamma = \sum_k Y_{\gamma,k} = \sum_k Y_{0,k} + Y_{m,k} \tag{4.16}$$

In the assumption of a parallel uniform neutron beam impinging on a homogeneous slab of material perpendicular to the beam, the primary capture yield $Y_{0,k}$ resulting from a capture reaction by nuclide k is directly proportional to the product of the areal density n_k and the Doppler broadened capture cross-section ${\sigma^D}_{\gamma,k}$ only in case of thin samples and/or small total cross sections:

$$Y_{0,k} = n_k {\sigma^D}_{\gamma,k} F \tag{4.17}$$

It is necessary to consider the impact of multiple collision events on relatively thick samples. The factor F takes into account the self-shielding caused by the attenuation of the neutron beam in the sample:

$$F = \frac{1 - e^{-\sum_j n_j {\sigma^D}_{TOT,j}}}{\sum_j n_j {\sigma^D}_{TOT,j}} \tag{4.18}$$

Experimentally, the measured capture yield is related to the theoretical Y_γ and it is defined by several experimental parameters:

$$Y_{exp} = \frac{C_\gamma - B_\gamma}{\varepsilon \Omega P A \phi} \tag{4.19}$$

where C_γ and B_γ are the observed sample and background spectra, both corrected from dead time effects; ϕ is the incident neutron flux; A is the effective area of the sample irradiated by the neutron beam; P is the escape probability of the prompt gamma rays from the sample; Ω is the solid angle between sample and detector and ε is the detection efficiency. Eq.4.19 clearly shows that Y_{exp} can be determined only if every contribution related to the detection of gamma-rays is known. In many cases, only Ω and A are independent from the energy of the incident neutron beam [15]. As a reference, a detailed discussion of the background evaluation is given by Borella et al. [17] and a method for the determination of the energy-dependent neutron flux is given by Carlson et al. [18].

In the course of several years, NRCA has been widely employed in various neutron sources to study many metallic archaeological artefacts non-destructively, which are mainly composed of elements with neutron absorption resonances in the epithermal energy region. Bronze or more generally copper-based objects have been extensively studied through NRCA, including bronze Etruscan statuettes [19], Roman metal objects like parts from water taps [20], Bronze-Age swords [21] and prehistoric bronze axes [22]. In ancient bronzes, impurities such as arsenic, antimony, cobalt, and nickel may be present in considerable amounts; these elements typically present strong capture resonances and therefore are easy to identify with relatively short NRCA measurements, which in some cases are combined with TOF-ND experiments.

At the ISIS spallation source, NRCA experiments are routinely performed at the INES beamline (Chapter 2), whose neutron spectrum is suitable for conducting NRCA analysis of archaeological objects. The resonant capture experimental setup is optimized for providing a qualitative and semi-quantitative evaluation of the composition of an object and relative isotopic concentration, with a low limit for the sensitivity for almost-in-traces elements. At INES, NRCA is usually conducted in multi-technique investigations, as reported in recent studies involving also non-metallic archaeological objects [23, 24].

As a drawback, NRCA is not very suitable to detect small amounts of light elements and elements with neutron and/or proton numbers close to a magic shell (such as lead). A better alternative for such elements can be prompt γ-ray activation analysis (PGAA), which is very complementary to NRCA [25].

4.1.4 Neutron Resonance Transmission Analysis

During an NRTA experiment, neutrons of the incident beam with the same energy of the nuclear resonances of the nuclide cross-sections constituting the sample are absorbed and therefore removed, resulting in an attenuated transmitted neutron beam. The typical structure of the transmitted neutron beam presents negative dips (Fig.4.6) whose positions in time/energy correspond to the absorption resonances responsible for neutron removal [15, 16]. By indexing the position of these dips, elemental and isotopic identification can be achieved through comparison with the total cross-sections of elements available in a nuclear database.

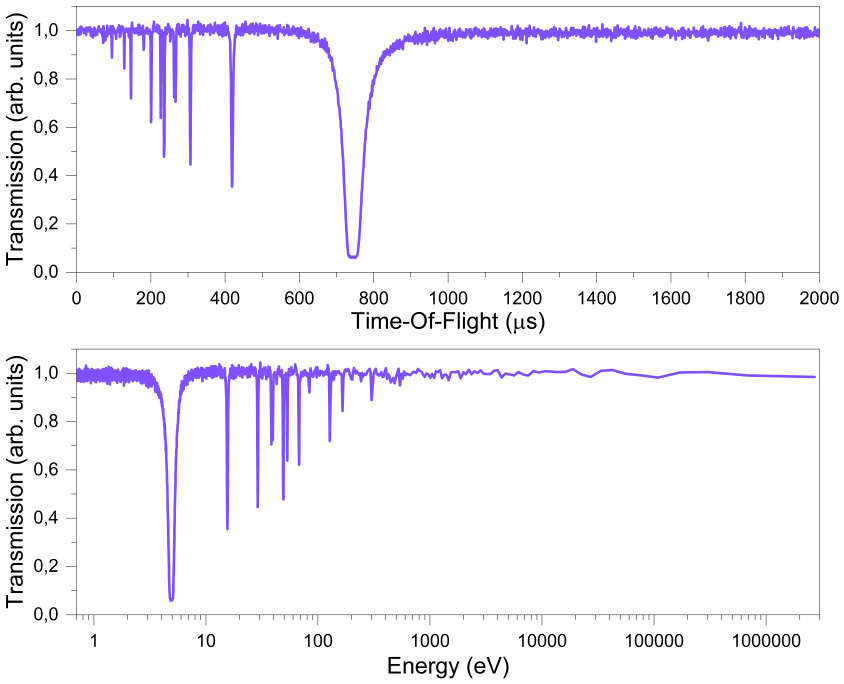

Fig. 4.6 Neutron resonance transmission spectrum of a 99.99% pure silver foil in time-of-flight (μs) and energy (eV) coordinates, with the negative dips characterising the neutron resonant absorption due to the silver atoms. The transmission spectrum is taken from original data collected during INES commissioning experiments (ISIS experiment RB number 2030016).

The measured transmitted beam is directly related to the theoretical transmission, representing the fraction of the neutron beam traversing the sample without any interaction, which, under the condition of a good transmission geometry, is given by:

$$T = e^{-\Sigma_k n_k \sigma^D{}_{n,k}} \tag{4.20}$$

where ${\sigma^D}_{n,k}$ is the Doppler broadened total cross-section and n_k is the number of atoms per unit area of nuclide k.

To perform an optimum transmission experiment, the following conditions must be satisfied:

- the sample has a constant homogeneous spatial distribution of the material and it is placed perpendicularly to a parallel incoming neutron beam;
- all detected neutrons have passed through the sample;
- scattered neutrons are not detected.

These conditions can be accomplished by collimating the neutron beam at both the sample and detector position, as explored in [26].

By measuring the transmitted neutron beam with (C_{in}) and without the sample (C_{out}), the experimental transmission can be derived, after background correction and normalisation to the neutron intensity for both detected spectra (B_{in} and B_{out}):

$$T_{exp} = \frac{C_{in} - B_{in}}{C_{out} - B_{out}} \tag{4.21}$$

An alternating measure of samples-in and samples-out transmission spectra can reduce the uncertainty due to the normalisation to less than 0.25% [15]. This sequence avoids systematic effects due to slow variations in beam intensity and detector efficiency over time [1]. According to Eq.4.21, indeed, the experimental transmission computed as the ratio of counting spectra is independent of the detector efficiency and incoming neutron flux. Therefore, no additional calibration measurements for the detection efficiency or absolute measurements of neutron flux are necessary.

4.2 Neutron Tomography

In 1935, Kallmann H. and Kuhn E. successfully carried out the first neutron radiography experiment [27], giving an insight into the possibility of conducting non-destructive inspection investigations by means of neutrons beams.

However, with the limited technology of the time, quite poor images were achieved owing to the weak beam produced by a small neutron generator. Significant advances in nuclear reactor technology were realised during World War II and the increase of several orders of magnitudes in the neutron fluxes intensity was achieved, demonstrating the potential of neutron radiography: in 1956, J. Thewlis and R.T.P. Derbyshire conducted the first

radiography with better quality using a thermal neutron beam produced by the BEPO reactor at Harwell, in England [28].

From the 1960s to the mid-1980s, the technique developed at different laboratories and reactors in Europe and America, together with the advances in data storage and digitization, opening the possibility of quantitative analysis of neutron images via imaging processing techniques. During the last decades, researchers in neutron imaging have been working to enhance the resolution of the imaging system, focusing for example on improvements in the detection field.

In the broad sense of neutron imaging, this technology is now routinely used in a variety of applications which mainly focus on the non-destructive evaluation of a sample morphology. Several neutron properties can be exploited for imaging experiments, such as the scattering or absorption cross-sections or its magnetic moment. Fig.4.7 summarised the different contrast mechanisms actually explored in the field of neutron imaging.

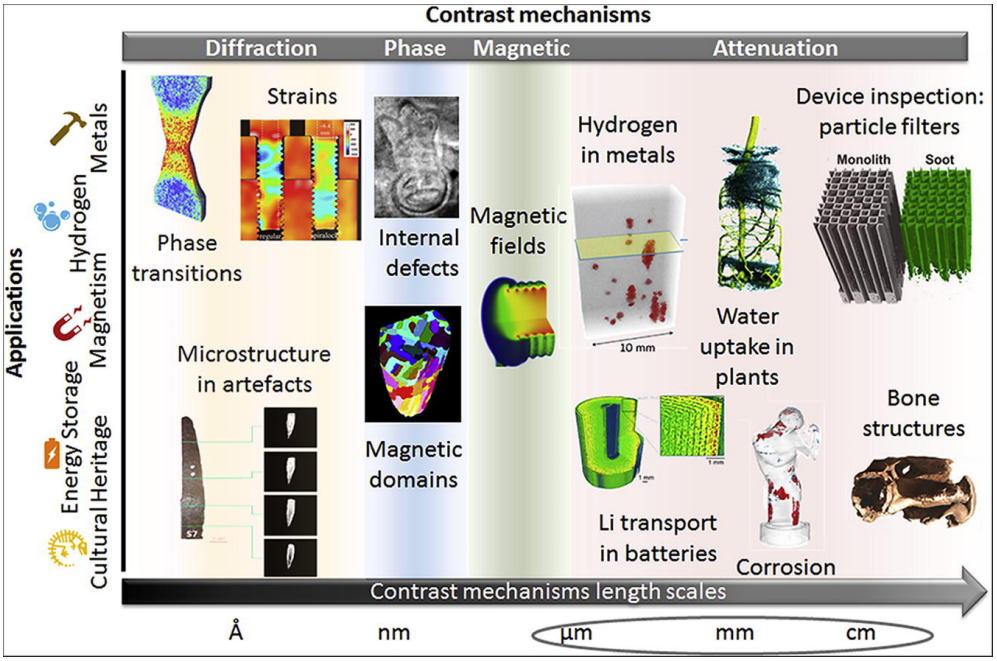

Fig. 4.7 Different contrast mechanisms explored for studying materials properties and related processes at various length scales. The relation between the contrast mechanism and its application is indicated along the vertical axis [29].

As with other tomographic techniques, Neutron Tomography (NT) provides a three-dimensional map of an object neutron attenuation coefficient, and the object interior can be viewed in planar sections. The linear attenuation coefficient μ (cm^{-1}) is an energy-dependent characteristic of the material. The transmitted neutron beam passing through the sample is detected, resulting attenuated by the different reactions that may occur with the material

(mainly absorption and scattering). If the sample contains several elements or even different isotopes each with number density N_i, the linear attenuation coefficient can be expressed as the sum of an absorption and a scattering contribution as follows:

$$\mu(E) = \sum_i N_i\left(\sigma_i{}^{abs}(E) + \sigma_i{}^{scatt}(E)\right) = \sum_i N_i\left(\sigma_i{}^{TOT}(E)\right) \tag{4.22}$$

where $\sigma_i{}^{abs}$, $\sigma_i{}^{scatt}$ and $\sigma_i{}^{TOT}$ are the associated microscopic absorption, scattering and total cross-section, respectively. $\mu(E)$ is also called the macroscopic cross-section.

For a collimated monoenergetic beam propagating in the z-direction of a reference system and crossing a sample, the linear attenuation coefficient is a constant and the attenuation of neutrons obeys the exponential Beer–Lambert law (as that of X-rays) assuming that absorption is the dominant process during NT experiments:

$$I = I_0 e^{-\int_l \mu(x,y)ds} \tag{4.23}$$

In Eq.4.23 I and I_0 are the transmitted and the incident neutron beam, respectively, ds is the differential element in the path l, and $\mu(x,y)$ is the material linear attenuation coefficient at a point (x,y). At first approximation multiple scattering and beam hardening effects or energy-dependent detector response can be neglected.

However, neutron sources used in NT are usually characterised by a broader energy spectrum. In this case, the Beer-Lambert law has to take into account the dependence of the attenuation coefficient of the material on neutron energy:

$$I(E) = I_0(E) e^{-\int_l \mu(x,y,E)ds} \tag{4.24}$$

and the total intensity passing beyond the sample of thickness t is given by:

$$I_{TOT} = \int_0^{E_{MAX}} dE I_0(E) e^{-\mu(E)t} \tag{4.25}$$

Radiographic and tomographic investigations can be conducted within a maximum sample thickness, determined by:

$$t_{MAX} = -\frac{\ln(0.02)}{\mu} = \frac{3.91}{\mu} \tag{4.26}$$

assuming that the sensitivity limit and dynamics of the detection system define a minimum transmission of 2%.

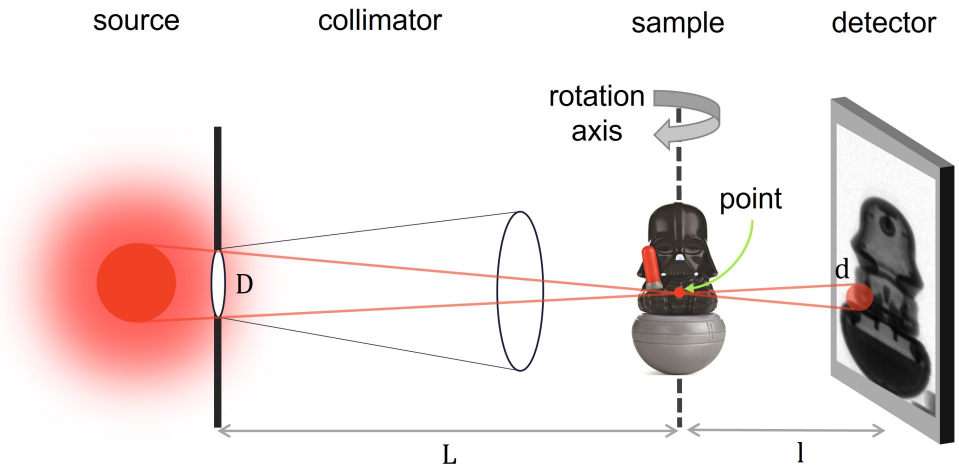

Fig. 4.8 Schematic representation of a standard tomographic experimental setup. The symbols are clarified in the text.

Data acquisition in NT consists in acquiring a series of transmission radiographies at different angular steps by rotating the object over 180° or 360° degrees, whilst the detection system is kept fixed. A schematic view of a typical tomographic setup is shown in Fig.4.8.

The neutrons exiting from the source are usually collimated by slits, apertures or collimator systems to produce a well-defined neutron beam used to illuminate objects and to obtain shadow images on a two-dimensional detector screen. In fact, the finite size of the source and the beam divergence result in the enlargement (or blurring) of the sample image at the detector position. The maximum blur d observed in the image for a point of the sample is determined by the source dimension D and by the source-to-sample (L) and the sample-to-detector (l) distances:

$$d = D\frac{l}{L} \tag{4.27}$$

Hence, for neutron tomography the beam geometry should be as close as possible to a point-source configuration in order to obtain a well-defined image, *i.e.* the source size D should be small in comparison to the source-to-sample distance L.

The figure of merit 'L/D ratio' gives an estimation of how close is the beam geometry to the ideal point-source configuration, being the main parameter to characterize the performance and quality of an imaging facility.

To improve the spatial resolution, a larger L/D ratio is required. However, by acting on one of the two parameters (reducing D or increasing L), the reduction of the neutron flux is encountered in both cases (it is sufficient to consider the $1/L^2$ dependence of the neutron flux), which means a lower image signal-to-noise ratio and longer exposure time. Therefore,

a suitable L/D ratio can be selected for a particular experimental situation depending on its experimental requirements - high flux or high resolution [30].

Regarding the sample-to-detector distance, it is influenced by the sample size and by the pixel size of the detector. The achievable higher spatial resolution, which corresponds to the smaller pixel size, requires a smaller integrated flux at the pixel. For conventional NT, this issue can be partially resolved by using a white beam to get acceptable results in short times. However, scattering effects are also responsible for image blurring. A white neutron beam comprises a fraction of fast neutrons, for which scattering reactions are the most frequent. Therefore, to improve the tomographic resolution, cold or thermal neutrons are usually used, for which the main attenuation reactions occur by absorption.

The procedure of acquisition and processing of neutron tomography data is now standardized in accordance with the following main steps:

1. to reduce the geometrical blurring, the object is placed on a rotating sample-stage as close as possible to the detector.

2. A finite number of radiographs, also called projections, is acquired by rotating the object with equal angular steps over 180°. The necessary number of radiographs that should be collected for a sample of a given dimension can be deduced by the Nyquist-Shannon theorem [31]. For an angular scan $[0, 2\pi)$ it can be expressed as

$$N = \frac{\pi}{2} N_{obj} \tag{4.28}$$

   where N is the number of projections and N_{obj} is the number of pixels taken by the widest horizontal dimension of the object imaged.

3. For normalisation purposes, some radiography without the sample (open-beam images) and with beam-off condition (dark-current images) are acquired before and/or after the tomographic scan of the object.

4. T1he projections are normalised using the following formula:

$$p = -\log\left(\frac{D_{flat}}{D}\frac{I - I_{dark}}{I_{flat} - I_{dark}}\right) \tag{4.29}$$

   where I is the raw projection image, I_{dark} and I_{flat} are the mean of the dark and flat images, respectively, while D and D_{flat} are the median computed within a ROI free of sample in the projections and flat images, respectively [32].

5. By means of a reconstruction algorithm for parallel beam geometry, the 2D map of the attenuation coefficient is computed for each slice of the object volume. Usually, the Filtered Back Projection is used as a reconstruction method. Further details on image reconstruction and algorithms can be found for example in [30, 31].

The real and non-ideal acquisition system leads, however, to reconstructed images not immediately equal to the true images due to the presence of artifacts, which need to be corrected. Image artifacts most commonly associated with NT include the zinger artifact, ring artifact, and scattering artifact. Zinger artifacts refer to bright pixels resulting from gamma-rays hitting the detector and occurring at random positions in a projection. In the reconstructed image, a spot of bright pixels causes a line artifact due to back-projection process.

Ring artifacts are caused by outlier pixels occurring at the same coordinates in almost all projections. Generally, a camera with bad pixels or a detector with a non-linear response usually produces such artifacts Rings are partially suppressed by data normalisation and outlier removal, but additional filtering is often needed. For suppression of the zinger and ring artifacts, several specific filters can be found in literature [33–36]. An example of zinger and ring artifacts is shown in Fig.4.9.

Tomographic reconstruction is based on the assumption that neither absorbed nor scattered neutrons are measured in the detector. However, in practice scattered neutrons do have a chance of reaching the detector and contributing to the estimated transmission, leading to strong distortion in the reconstructed images of samples containing high neutron scattering materials. Despite modern advances in reconstruction algorithms (e.g., [37, 38]), the correction of scattering artifacts remains a challenging issue.

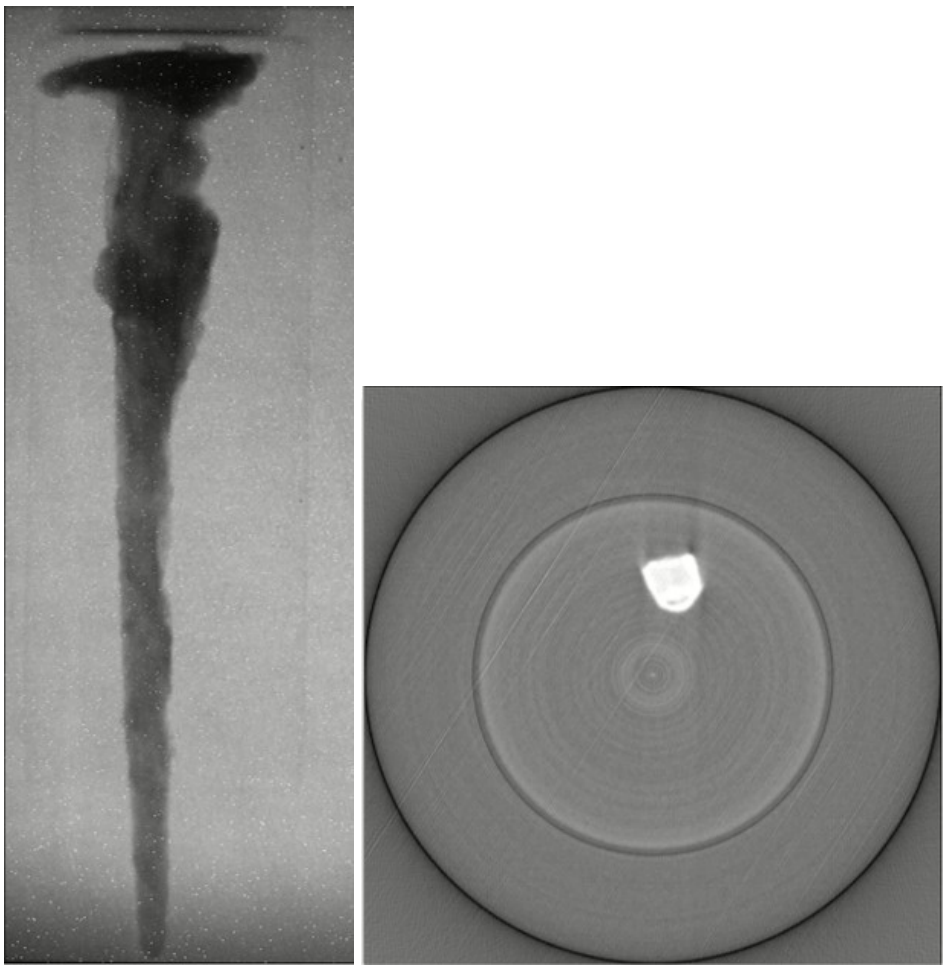

Fig. 4.9 On the left, a neutron radiography of an iron nail affected by several bright outliers. On the right, a reconstructed slice of the nail. Zinger and ring artifacts due to the uncorrected outliers are visible. The normalised and reconstructed images are taken from original data processing of a commissioning imaging experiment conducted at PSI.

References

[1] Kardjilov, N. and Festa, G. (2017) *Neutron methods for archaeology and cultural heritage*. Cham: Springer (Neutron scattering applications and techniques).

[2] Anderson, I.S., Hurd, A.J. and McGreevy, R.L. (2008) *Neutron scattering applications and techniques*. New York, NY: Springer.

[3] Anderson, I.S., McGreevy, R.L. Bilheux, H.Z. (2008) *Neutron imaging and applications: a reference for the imaging community*. New York: Springer (Neutron scattering applications and techniques).

[4] Schillebeeckx, P. and Postma, H. (2022). "Resonance Analysis Methods for Archaeological and Cultural Heritage Applications". In: D'Amico, S., Venuti, V. (eds) *Handbook of Cultural Heritage Analysis*. Springer, Cham. doi: 10.1007/978-3-030-60016-7_7.

[5] https://www.bnc.hu/?q=radiative_neutron_capture. Accessed 6th Apr 2023.

[6] https://atom.kaeri.re.kr/. Accessed 25th Jan 2023.

[7] Beckurts, K.H. and Wirtz, K. (1964) *Neutron Phyiscs*, Springer Berlin, Heidelberg. doi: 10.1007/978-3-642-87614-1.

[8] Lane, A.M. and Thomas, R.G. (1958) "R-Matrix Theory of Nuclear Reactions", *Rev. Mod. Phys.*, 30(2), pp. 257-353.

[9] Breit, G. and Wigner, E.P. (1936) "Capture of Slow Neutrons", *Phys. Rev.* 49(7), pp. 519–531.

[10] Stacey, W.M. (2007) *Nuclear Reactor Physics*, Wiley-VCH, 2nd edition. ISBN 3527406794.

[11] Herman, M. (2005) "ENDF-6 Formats Manual", *Brookhaven National Laboratory*. BNL-NCS-44945-05-Rev.

[12] Fröhner, F.H. (2000) *Evaluation and analysis of nuclear resonance data*, Technical Report, Nuclear Energy Agency, OECD Data Bank, JEFF Report 18.

[13] Schillebeeckx, P. et al. (2012) "Determination of Resonance Parameters and Their Covariances from Neutron Induced Reaction Cross Section Data", *Nuclear Data Sheets*, 113(12). doi: 10.1016/J.NDS.2012.11.005.

[14] Škoro, G., Lilley, S. and Bewley, R. (2018) "Neutronics Analysis of Target, Moderators and Reflector Design for the ISIS TS-1 Project", *Physica B: Physics of Condensed Matter*, 551, pp. 381–385. doi: 10.1016/j.physb.2017.12.060.

[15] Schillebeeckx, P. et al. (2012) "Neutron Resonance Spectroscopy for the Characterization of Materials and Objects", *Journal of Instrumentation*, 7(03), p. 03009. doi: 10.1088/1748-0221/7/03/C03009.

[16] Postma, H. and Schillebeeckx, P. (2009) "Neutron Resonance Capture and Transmission Analysis", *Encyclopedia of Analytical Chemistry*, John Wiley & Sons Ltd, pp. 1-22.

[17] Borella A., et al. (2006) "Determination of the ^{232}Th(n,γ) cross-section from 4 to 140 keV at GELINA", *Nucl. Sci. Eng.*, 152.

[18] Carlson, A.D. et al. (2009) "International Evaluation of Neutron Cross Section Standards", *Nuclear Data Sheets*, 110(12). doi: 10.1016/j.nds.2009.11.001.

[19] Postma, H., Schillebeeckx, P. and Halbertsma, R.B. (2004) "Neutron Resonance Capture Analysis of Some Genuine and Fake Etruscan Copper Alloy Statuettes", *Archaeometry*, 46(4), pp. 635–646. doi: 10.1111/j.1475-4754.2004.00179.x.

[20] Schut, P.A.C. et al. (2008) "Neutron Resonance Capture and Neutron Diffraction Analysis of Roman Bronze Water Taps", *Journal of Radioanalytical and Nuclear Chemistry: An International Journal Dealing with All Aspects and Applications of Nuclear Chemistry*, 278(1), pp. 151–164. doi: 10.1007/s10967-007-7190-3.

[21] Postma, H. et al. (2010) "Non-Destructive Bulk Analysis of the Buggenum Sword by Neutron Resonance Capture Analysis and Neutron Diffraction", *Journal of Radioanalytical and Nuclear Chemistry: An International Journal Dealing with All Aspects and Applications of Nuclear Chemistry*, 283(3), pp. 641–652. doi: 10.1007/s10967-009-0405-z.

[22] Postma, H., Schillebeeckx, P. and Kockelmann, W. (2011) "The Metal Compositions of a Series of Geistingen-Type Socketed Axes", *Journal of Archaeological Science*, 38(8), pp. 1810–1817. doi: 10.1016/j.jas.2011.03.015.

[23] Marcucci, G. et al. (2021) “Historical Glass Mosaic Tesserae: A Multi-Analytical Approach for Their Characterization”, *The European Physical Journal Plus*, 136(7). doi: 10.1140/epjp/s13360-021-01696-2.

[24] Rossini, R. et al. (2023) “A New Multidisciplinary Non-Destructive Protocol for the Analysis of Stony Meteorites: Gamma Spectroscopy, Neutron and Muon Techniques Supported by Raman Microscopy and Sem-Eds”, *Journal of Analytical Atomic Spectrometry*. doi: 10.1039/D2JA00263A.

[25] Postma, H. and Schillebeeckx, P. (2005) “Non-Destructive Analysis of Objects Using Neutron Resonance Capture”, *Journal of Radioanalytical and Nuclear Chemistry : An International Journal Dealing with All Aspects and Applications of Nuclear Chemistry*, 265(2), pp. 297–302. doi: 10.1007/s10967-005-0824-4.

[26] Sirakov, I. et al. (2013) “Results of Total Cross Section Measurements for ^{197}Au in the Neutron Energy Region from 4 to 108 Kev at Gelina”, *The European Physical Journal A: Hadrons and Nuclei*, 49(11), pp. 1–10. doi: 10.1140/epja/i2013-13144-2.

[27] Kallmann, H. (1948) “Neutron radiography”. In: Research; a journal of science and its applications 1, pp. 254–260.

[28] Thewlis J. and Derbyshire R.T.P. (1956). Report AERE M/TN 37, U. K. Atomic Energy Research Establishment.

[29] Kardjilov, N. et al. (2018) “Advances in Neutron Imaging”, *Materials Today*, 21(6), pp. 652–672. doi: 10.1016/j.mattod.2018.03.001.

[30] Banhart, J. (2008) *Advanced Tomographic Methods in Materials Research and Engineering*, Monographs on the Physics and Chemistry of Materials, Oxford, online edn, Oxford Academic. doi: 10.1093/acprof:oso/9780199213245.001.0001.

[31] Kak, A.C. and Slaney, M. (2001) *Principles of computerized tomographic imaging*, Society for Industrial and Applied Mathematics.

[32] Micieli, D. et al. (2018) “A Comparative Study of Reconstruction Methods Applied to Neutron Tomography”, *Journal of Instrumentation*, 13(6). doi: 10.1088/1748-0221/13/06/C06006.

[33] Rivers, M. (1998) *Tutorial Introduction to X-ray Computed Microtomography Data Processing*, University of Chicago. https://www.mcs.anl.gov/research/projects/X-ray-cmt/rivers/tutorial.html.

[34] Münch, B. et al. (2009) “Stripe and ring artifact removal with combined wavelet-Fourier filtering”, *Optics Express* 17(10) , p. 8567. issn: 1094-4087. doi: 10.1364/OE.17.008567.

[35] Titarenko, S. et al. (2010) “An analytical formula for ring artefact suppression in X-ray tomography”, *Applied Mathematics Letters*, 23(12), pp. 1489–1495. doi: 10.1016/j.aml.2010.08.022.

[36] Mertens, J. C. E., Williams, J. J. and Chawla, N. (2015) “A Method for Zinger Artifact Reduction in High-Energy X-Ray Computed Tomography”, *Nuclear Inst. and Methods in Physics Research, A*, 800, pp. 82–92. doi: 10.1016/j.nima.2015.08.012.

[37] Carminati, C. et al. (2020) "Effect of Scattering Correction in Neutron Imaging of Hydrogenous Samples using the Black Body Approach", In U. Garbe, F. Salvemini, J. J. Bevitt (Eds.), *Materials research proceedings: Vol. 15. Neutron radiography. WCNR-11*, pp. 174-179. doi: 10.21741/9781644900574-27

[38] Raventos, M. et al. (2017) “A Method for Neutron Scattering Quantification and Correction Applied to Neutron Imaging”, *Physics Procedia*, 88, pp. 275–281. doi: 10.1016/j.phpro.2017.06.038.

Chapter 5

The CHNet-NICHE project

In the framework of the Cultural Heritage Network of the Italian National Institute for Nuclear Physics (INFN-CHNet), dedicated to the research and development of analytical techniques for performing advanced diagnostics on Cultural Heritage (CH) artefacts and materials [1], the first Italian neutron imaging facility specifically designed for CH analysis has been installed and implemented at the LENA laboratory of the TRIGA reactor in Pavia as the main focus of the CHNet-NICHE (Neutron Imaging for Cultural HEritage) project.

Recent improvements in the neutron imaging detectors field opened the possibility of exploiting weak neutron sources, such as low-power reactors including the TRIGA in Pavia, to perform imaging experiments with a good resolution.

The design and installation of the NICHE facility took place in 2020 at the thermal beam-port channel B of the LENA reactor, and it was completed in May 2021 making the beamline operational for the first neutron tomographies. In this way, the INFN-CHNet infrastructure could provide network-based applications for national external users at NICHE, enabling for non-destructive morphological characterisation of samples through thermal neutron radiography and tomography, which in most cases provide key details complementary to the well-known and widely-used X-ray tomography.

As previously investigated within the CHNet-TANDEM project [2], the beam-port B of the TRIGA reactor provides the highest thermal-to-fast neutron ratio and therefore it is the most indicated for thermal neutron imaging experiments. The internal components of channel B are described in Chapter 3. Several other experimental activities are usually performed in this channel and an experimental hutch made of baryte and concrete was already built before the NICHE project, strictly limiting the available space for the installation of the imaging setup, as shown in Fig.5.2. The maximum length of the hutch is 2.5 m, the minimum width is 0.6 m and the height is 2.1 m. The hutch is equipped with a set of three guide rails collinear with the neutron beam and connected to the sample holder and the neutron camera

box, allowing to adjust the detector position depending on the L/D collimation power and the neutron flux incident on the sample requested.

Fig. 5.1 View of the LENA TRIGA reactor. The beam port B experimental hutch hosting the NICHE set-up is highlighted in the red box.

The following specifications of the NICHE imaging station are based on [3]. The design of the measuring point and the realisation of the facility setup have been carried out with standard instrumentation and components chosen on the basis of the experience gained in the field at neutron imaging facilities as well as on the basis of the studies carried out by the groups of the network, *e.g.* [2], and available in the literature.

The NICHE detection system is composed of a light-tight camera box housing a 300 μm-thick ^{6}LiF/ZnS(Ag) scintillator screen 200$\times$200 mm wide, followed by a 45° mirror, a 35 mm focusing lens and a ZWO ASI 2600 MM pro-CMOS camera (16 bit). The scintillator pixel size corresponds to 30$\times$30 μm^2, enabling a field-of-view (FOV) of 180$\times$120 mm^2. By using the 45° mirror, the CMOS camera is protected from radiation damage caused by neutrons. Remote control is used for lens focusing, camera operation and sample positioning via ARDUINO Mega, using a software developed internally in the NICHE group through the LabView 2018 environment. A specific code has been implemented to perform sequences of radiographs in different areas of an object and tomographic acquisitions, if necessary.

Generally, the quality of a radiographic image depends on beam properties, such as the neutron flux, the degree of collimation, the beam size, and background noise. A pinhole system made of borated ceramic tiles [6] allows for different collimation configurations

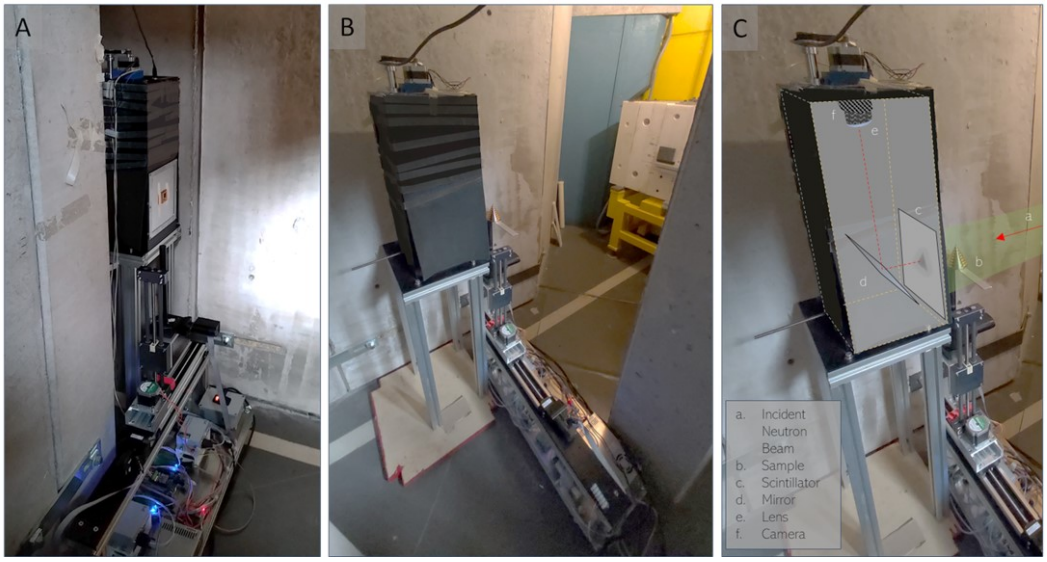

Fig. 5.2 (A,B): Pictures of the detection camera box with the translation and rotation sample-stages, positioned at two different distances from the pinhole. (C): A schematic representation of the optical components within the camera box [3].

depending on the selected pinhole diameter among the available ones: 5, 10, 20, 30, 40, and 50 mm. In particular, it has been studied the dependence of exposure time and resolution on the pinhole diameter, concluding that for the 10 mm size a reasonably short exposure time together with an acceptable resolution can be maintained, while larger pin-hole configurations offer improvement in the flux intensity but do not compensate for resolution loss.

Due to the shape and size of the experimental hutch and sample manipulation system, which needs to safely move the sample out of the neutron beam, there are limitations in the relative distance of the camera and the sample holder with respect to the beam shutter. The effective distance between the shutter and the scintillator ranges between 1100 and 1920 mm, thus determining a minimum and maximum nominal value for the L/D coefficient of 110 and 190 respectively with the pinhole diameter of 10 mm. In order to maximise the flexibility of the NICHE imaging station, two different sample-pinhole distances have been individuated: they can be selected for NT experiments depending on the imaging conditions needed, respectively the highest thermal flux or the highest spatial resolution, as reported in Table 5.1. The resolution power of the imaging system, commonly indicated by means of the L/D ratio (L is the pinhole-to-sample distance, D is the pinhole diameter) and the spatial resolution of the radiographs have been included in Table 5.1 as well. Following the IAEA recommended standard procedure for obtaining a certified evaluation of the resolution of the instrument (IAEA project n. 08CT14309), the spatial resolution has been evaluated by positioning at different distances from the scintillator surface, at 0 mm distance and at

40 mm distance, a Siemens star and a Bar pattern devices (Fig.5.3 and Fig.5.4) produced and distributed by the Paul Scherrer Institut (PSI) and exploiting the radial lines of these reference samples [4, 5].

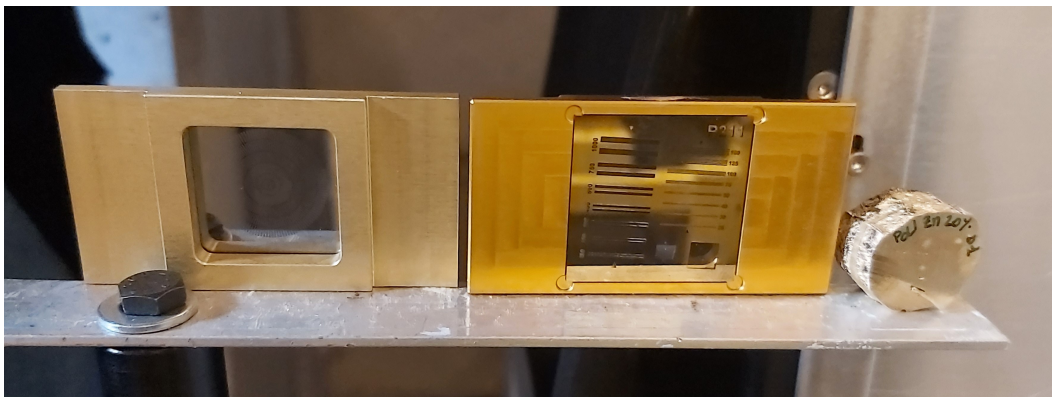

Fig. 5.3 Picture of the Bar pattern and Siemens Star devices used for the experimental evaluation of the spatial resolution of the imaging system.

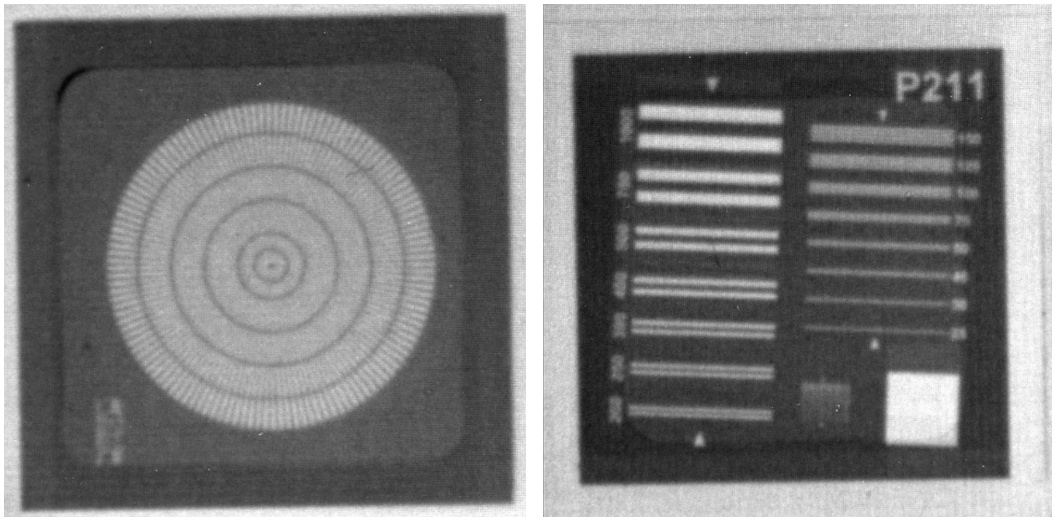

Fig. 5.4 Radiographies of the Bar pattern and Siemens Star devices used for the experimental evaluation of the spatial resolution of the imaging system.

Sample positioning is available through two linear and one rotational stages, enabling the sample translation in the horizontal and vertical directions (*i.e.*, orthogonal to the beam) and sample rotation around a vertical axis. The linear stages motion is remotely controlled by precision stepper motors, while a PI M-060 stage remotely makes the rotation [1]. By means of the linear stages, it is possible to perform neutron radiographies of samples larger than the FOV: partial images at different positions can be acquired by moving the object after each measurement and they can be recombined together by a stitching procedure to reconstruct the

entire object image. the remote control of the linear stages allows for conducting the stitching procedure without introducing artefacts or discontinuities. It is worth mentioning, however, that the experimental hutch size limits this procedure to a maximum object size of 25 cm in the horizontal direction. The rotating stage can be exploited for neutron tomography. The minimum acquisition time of each radiography is about 120 s in order to have an acceptable signal-to-noise ratio, whilst the minimum number of projections required for tomography with good imaging resolution is 300. Therefore a complete tomography requires a minimum of two operational days at LENA. The resulting spatial resolution of tomography at the NICHE beamline has been estimated to be better than 250 μm [3].

Table 5.1 Characteristics of the NICHE imaging set-up in two working positions exhibiting the highest thermal flux and the highest spatial resolution respectively. The best resolution was measured by sticking a Gd bar pattern grid directly on the scintillator. $\varnothing$ is the diameter of the full brightness area of the neutron beam, and S is the side of the inscribed square [3].

Position A: highest neutron flux	**Position B: highest spatial resolution**
Pinhole-to-sample distance: 140 cm	Pinhole-to-sample distance: 190 cm
L/D $\simeq$ 140	L/D $\simeq$ 190
Field of view: $\varnothing$ = 65 mm, S = 45 mm	Field of view: $\varnothing$ = 95 mm, S = 65 mm
Best spatial resolution: 150 μm	Best spatial resolution: 125 μm
Radiography Acquisition time: 300 s	Radiography Acquisition time: 600 s

5.1 Monte Carlo MCNP simulations for the neutron flux characterization

The contribution of this thesis in the NICHE project consists in Monte Carlo simulations of the main characteristics of the neutron flux in the B channel and in the reconstruction of the tomographic acquisitions. The Monte Carlo N-Particle (MCNP) radiation transport code [7, 8] was used to simulate the flux at the shutter beam position, the effect of the sapphire filter and the ratio of the thermal-to-fast neutrons at different positions along the thermal channel and in the experimental hutch. MCNP simulations have been performed by implementing the whole reactor core as the neutron source with the KCODE criticality mode in the code.

The geometry of the radial channel B implemented in the MCNP code is shown in Fig.5.5, with all the components (filters, shutters, etc.) present inside the collimator. The simulated

neutron flux exiting the collimator of the thermal channel B for the whole energy range of the reactor source (from cold neutrons - E $< 10^{-8}$ - to 20 MeV neutrons) is shown in Fig.5.6. The thermal contribution can be noticed as being predominant for this reactor channel due to the presence of the sapphire filter, which reduces the epithermal and fast neutron components. In fact, the main purpose of the sapphire and bismuth filters is to produce thermal neutron beams almost free of fast neutron background and with a high neutron-to-gamma ratio suitable for conducting neutron imaging experiments [9–11].

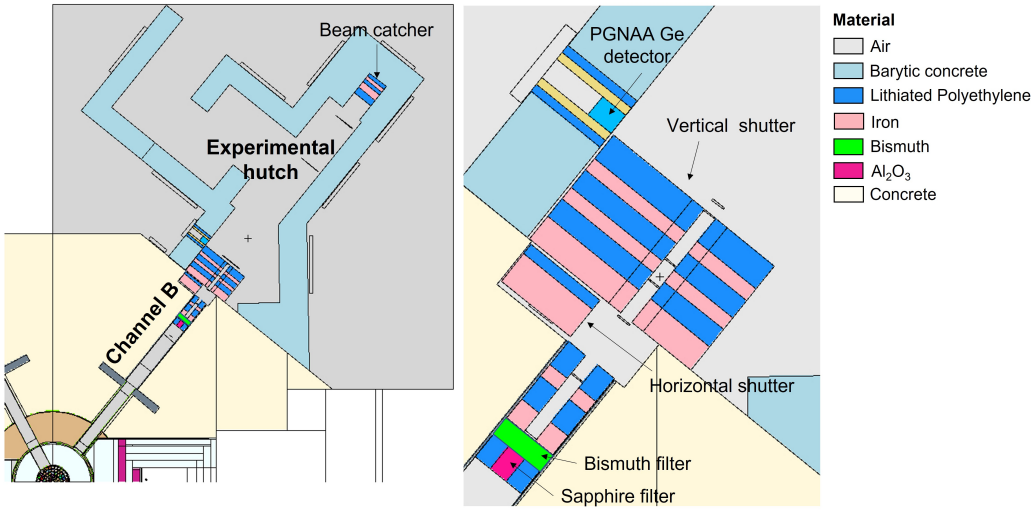

Fig. 5.5 On the left: vertical view of the thermal Channel B and the NICHE experimental hutch in MCNP simulation. On the right: the various components inside the collimator of Channel B.

The filtering effect of the sapphire crystal has been investigated by simulating with the MCNP code the neutron flux before and after the sapphire crystal in the energy range 10^{-9} MeV - 10^{-7} MeV with 1 meV energy binning. The MCNP simulations are based on the Al_2O_3 cross-section given by Cartagi F. et al.[12].

Fig.5.7 shows the thermal neutron spectrum incident on the sapphire filter having a Maxwellian distribution as a result of the thermalisation process encountered through the water shielding around the reactor core. The neutron spectrum exiting the Al_2O_3 filter still has the typical Maxwellian distribution and by fitting both fluxes (before and after the Al_2O_3 crystal) with the distribution function $f(E) = N\frac{4E}{K_BT}\sqrt{\frac{m}{2\pi K_BT}}e^{-E/K_BT}$ (where N is the total number of neutrons, m the neutron mass and K_B the Boltzmann constant), the neutron temperature T has been derived to be 305 ± 14 K and 300 ± 7 K before and after the filter, respectively. These results indicate that the presence of the filters does not alter the distribution of thermal neutrons, although there is an absorption of this component by a factor 2 as can be seen from Fig.5.8 and in Table 5.2. However, this loss in thermal neutrons is

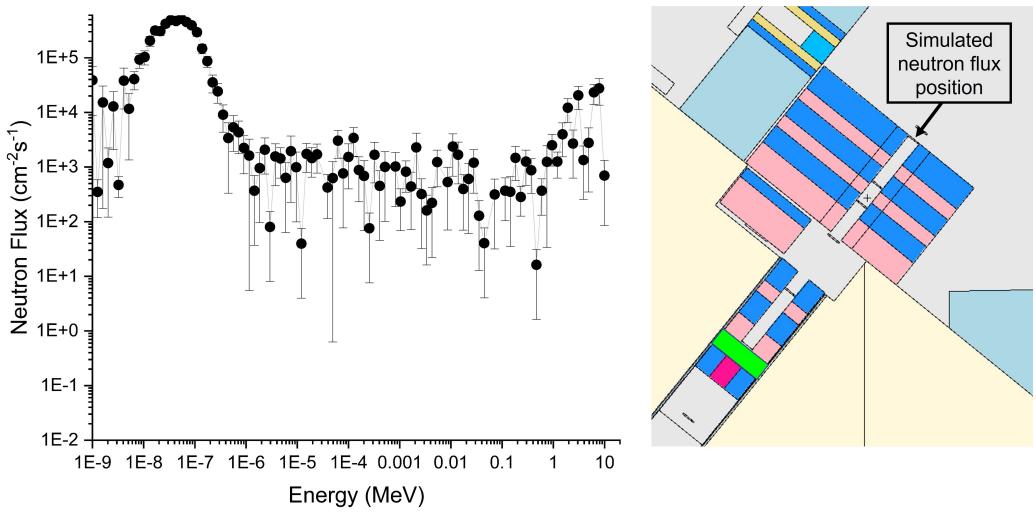

Fig. 5.6 MCNP outcome of the neutron flux as a function of the neutron energy exiting the collimator of the thermal Channel B. The position of the MCNP tally is pointed out on the right.

compensated by a gain of a factor 5 in the decrease of the fast and the epithermal components due to the sapphire filter.

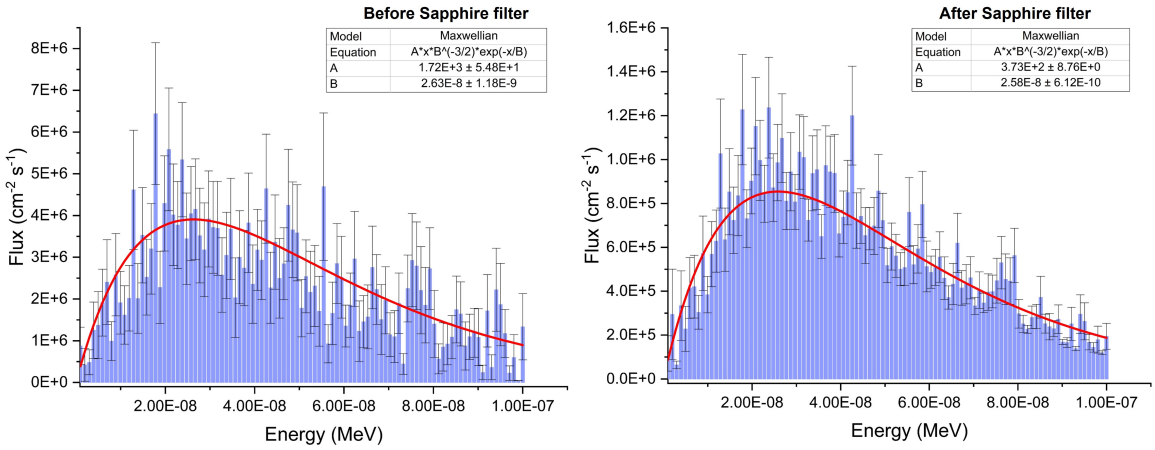

Fig. 5.7 On the left: simulated thermal neutron flux in the energy range 10^{-9} MeV - 10^{-7} MeV with 1 meV energy binning before the sapphire filter. On the right: the simulated thermal neutron flux (10^{-9} MeV - 10^{-7} MeV) after sapphire thermalisation. Both fluxes have been fitted with a Maxwellian distribution as described in the text.

Moreover, the different energetic components of the neutron beam have been simulated along the channel, starting from approximately 30 cm before the filters in the collimator up to different positions in the experimental hutch for performing tomographic acquisition. Fig.5.8 shows the cold (E< 10^{-8} MeV), thermal ($10^{-8} - 5.0 \cdot 10^{-7}$ MeV), epithermal

Table 5.2 The neutron flux integrated over the three energy components- thermal, epithermal and fast- before and after the sapphire and bismuth filters. The distances are relative to the end of the sapphire filter.

Distance from Al_2O_3 filter (cm)	**Integrated neutron flux ($cm^{-2}s^{-1}$) Thermal neutron**	**Epithermal neutron**	**Fast neutron**
-26.5	$1.61 \cdot 10^8$	$5.24 \cdot 10^7$	$4.03 \cdot 10^7$
0	$8.78 \cdot 10^7$	$9.50 \cdot 10^6$	$8.04 \cdot 10^6$
7	$3.98 \cdot 10^7$	$4.45 \cdot 10^6$	$7.19 \cdot 10^6$

($5.0 \cdot 10^{-7} - 0.01$ MeV) and fast ($0.01 - 20$ MeV) components for different positions in the collimator (points 1-7) and in the hutch (points 8-10, A, B). The total neutron flux exiting the collimator turned out to be $5.0 \cdot 10^6$ $cm^{-2}s^{-1}$ and it is mainly composed of thermal neutrons ($4.4 \cdot 10^6$ $cm^{-2}s^{-1}$), whilst the fast component is $9.6 \cdot 10^4$ $cm^{-2}s^{-1}$, the epithermal component is $8.0 \cdot 10^4$ $cm^{-2}s^{-1}$ and the cold component is $4.2 \cdot 10^5$ $cm^{-2}s^{-1}$. The thermal-to-(epithermal and) fast neutrons ratio along these positions (shown in Fig.5.9) indicates a promising suitability of the beam-port B equipped with the sapphire and bismuth filter for conducting thermal neutron imaging experiments, notwithstanding the limited reactor power (250 KW). This parameter is related to the noise affecting neutron radiographies as fast neutrons mainly interact with the material via scattering events with both the neutron detector and the object, causing degradation in spatial resolution.

MCNP simulations outcome shows that point A, characterised by a pinhole-to-sample distance of 140 cm, has the highest thermal-to-fast ratio but experimentally has a lower spatial resolution with respect to the other more distant positions. The highest spatial resolution is reached in point B at 190 cm from the pinhole, notwithstanding the lower thermal-to-fast neutron ratio than point A.

Table 5.3 Simulated neutron flux exiting the collimator of the beam port B integrated over the main energy components (from cold to fast). The total neutron flux evaluated at this position is $5.0 \cdot 10^6$ $cm^{-2}s^{-1}$.

Neutron component	**Energy range (MeV)**	**Integrated neutron flux ($cm^{-2}s^{-1}$)**
Cold	E$< 10^{-8}$	$4.2 \cdot 10^5$
Thermal	10^{-8} - $5.0 \cdot 10^{-7}$	$4.4 \cdot 10^6$
Epithermal	$5.0 \cdot 10^{-7}$ - 0.01	$8.0 \cdot 10^4$
Fast	0.01 - 20	$9.6 \cdot 10^4$

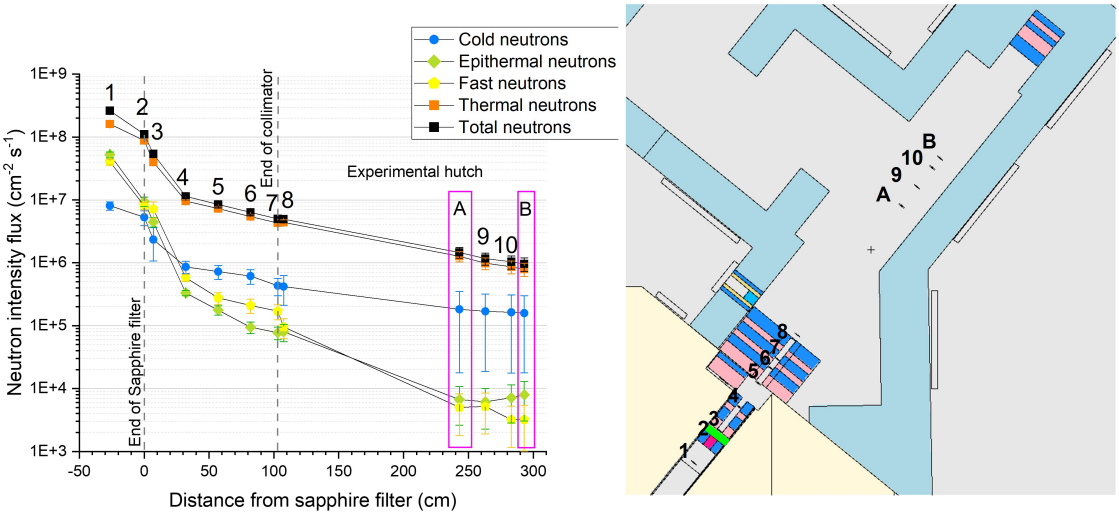

Fig. 5.8 Energy components of the neutron flux along different positions in the collimator and in the experimental hutch. Cold neutrons are defined in the energy range E$<$ 10^{-8} MeV; thermal neutrons: 10^{-8} - $5.0 \cdot 10^{-7}$ MeV; epithermal: $5.0 \cdot 10^{-7}$ - 0.01 MeV; fast neutrons: 0.01 - 20 MeV. The positions A and B explored during NICHE experimental campaigns and described in Table 5.1 are highlighted.

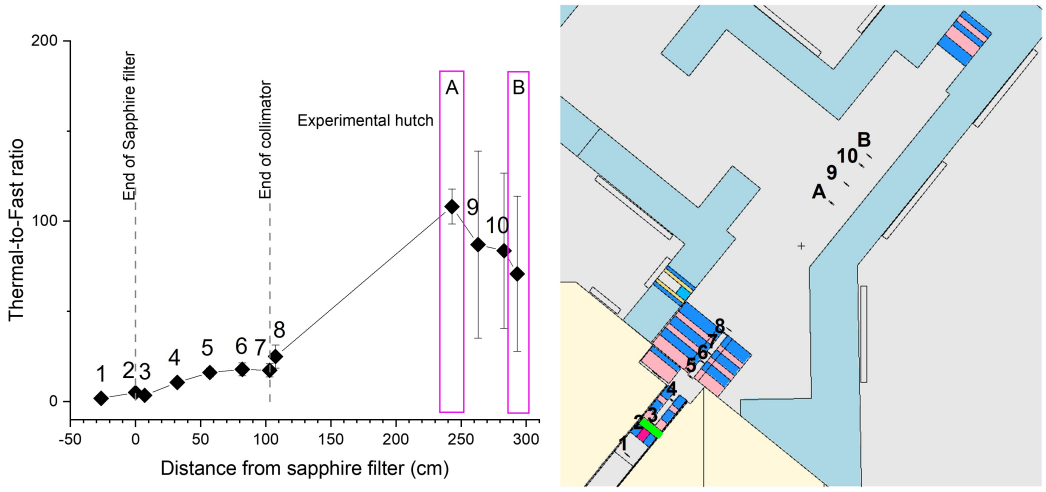

Fig. 5.9 Thermal-to-fast neutrons ratio. The fast component comprises the epithermal flux. The thermal component turned out to be higher than the fast contribution by a factor of 100 exiting the collimator of the B-channel.

5.2 Tomographic data processing and reconstruction

Neutron data acquired during NICHE imaging experiments are reconstructed using the Python NeuTomPy Toolbox [13], specifically developed as a powerful freeware tool to process

neutron tomographic data, and the well-known ImageJ software [14]. The fundamental elements for image reconstruction (Fig.5.10) are:

- raw projections of the object;
- flat projections, *i.e.* the open beam acquisitions;
- dark projections, *i.e.* acquisition without the sample and without the neutron current.

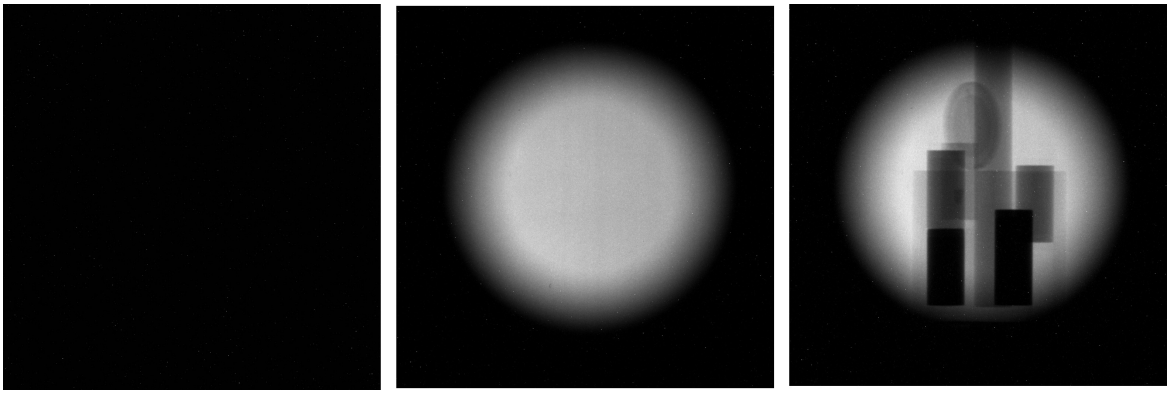

Fig. 5.10 Examples of a dark-field projection, flat (open beam) projection and raw sample radiography (data acquired during CHNet-NICHE tomography experiments in May 2021). Due to the round shape of the pinhole, the beam shape is circular with the diameter increasing with distance, due to beam divergence.

Projections are usually saved and processed as TIFF or TIF files. The reading of the raw dataset, dark-field and flat-field images into the NeuTomPy software is performed through the function `read dataset`, which converts a TIFF stack of images into a numpy array. This function also required the specification of the projection at 180°. The reconstruction of a tomographic dataset can be summarised in the following main steps:

1. normalization;
2. outliers correction;
3. rotational axis correction;
4. 3D reconstruction.

Data are then normalised by log-transformation, flat-fielding and dark subtraction procedures with neutron dose correction, as described in Chapter 5 and performed using the `normalize proj` function:

$$p = -\log\left(\frac{D_{flat}}{D}\frac{I - I_{dark}}{I_{flat} - I_{dark}}\right) \tag{5.1}$$

A radiation dose-normalisation is required if the intensity of the radiation source is not stable [15]. In this case, a region of interest (ROI) corresponding to a background area not covered by the object in all the projections must be specified through three different ways: drawing interactively a rectangular selection, specifying the ROI coordinates or reading a .roi file created using ImageJ.

Before or after normalization, raw, flat and dark projections are corrected from dead pixels and gamma spots (dark and bright outliers) using the NeuTomPy instruction `remove outliers stack`. Bright outliers are due to gammas reaching the CCD chip and depositing energy to form bright spots. Dark outliers are due to pixels uncorrected response. Through this correction function, outliers pixels are replaced by the median of the pixels in the neighbourhood if it deviates from the median by more than a specific value (k$\times$threshold). It is possible to specify the threshold as a global value or to compute it proportionally to the local standard deviation. Misalignment between the rotational axis and the vertical detector

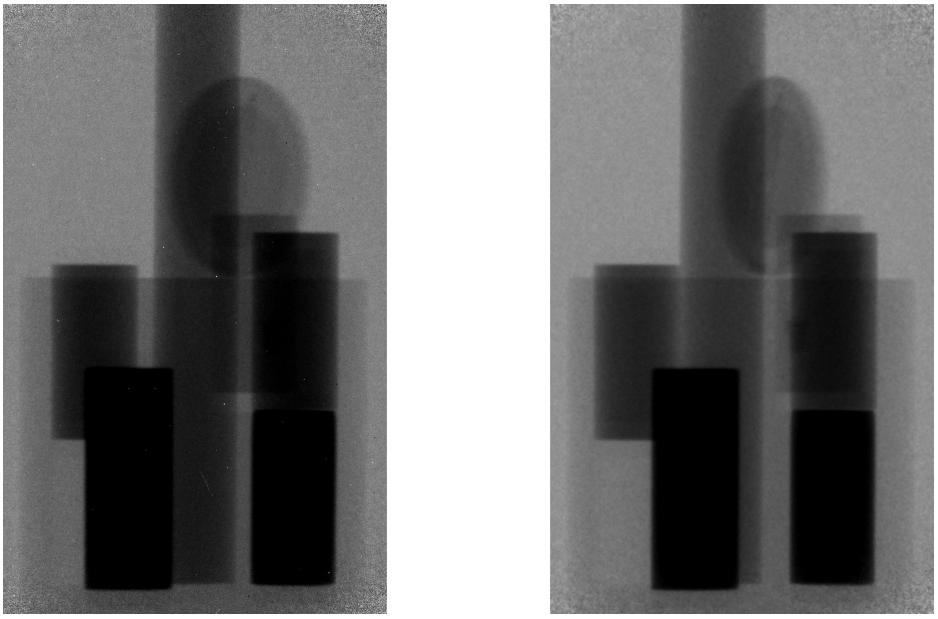

Fig. 5.11 On the left: an example of a normalised sample projection affected by bright and dark outliers. On the right: the same normalised sample projection after outliers correction, performed through the NeuTomPy software.

axis is a common experimental issue in NT. The Python function `correction COR` evaluates the horizontal offset and the tilt angle by minimizing the squared error between two opposite radiographs (*e.g.*, projections at 0° and 180°) computed at different vertical positions, after user interactive specification of different ROIs where the sample is present. An indication of a good correction of the rotational axis can be deduced from the subtraction of the projection at 0° and at 180°-flipped, resulting in an image which shall contain pixel values around

zero and no features of the samples should be visible. A comparison between an inaccurate rotation axis correction and a reliable correction is made in Fig.5.12 and Fig.5.13.

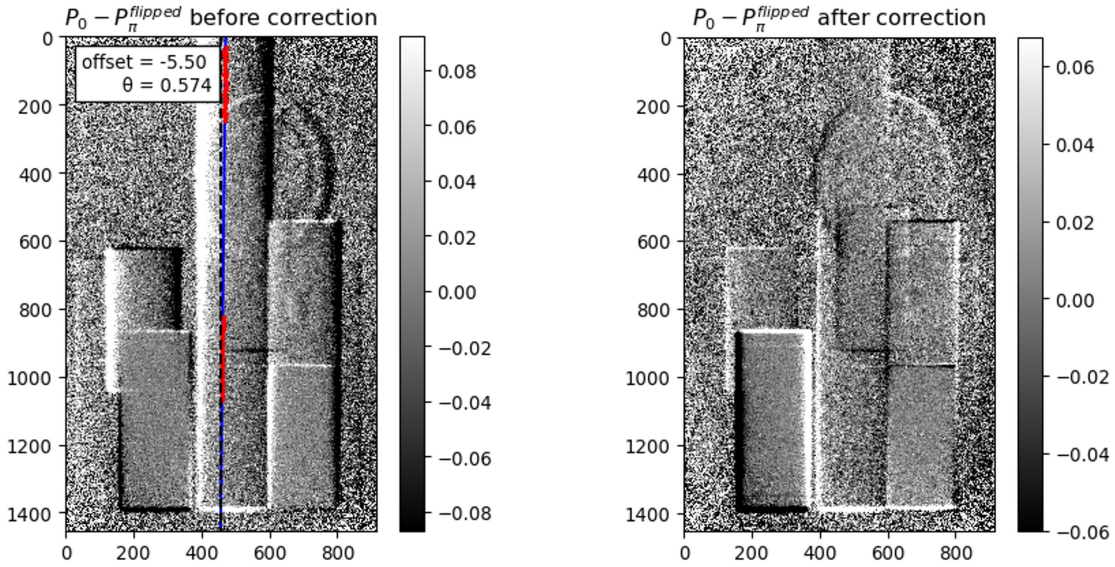

Fig. 5.12 Example of an inaccurate rotational axis correction: some features of the investigated objects still remain visible after the correction and subtracting the projection at 180°, flipped, to the projection at 0° (original data acquired during CHNet-NICHE tomography experiments).

The reconstruction of the volume object can be performed by using both CPU- and GPU-based algorithms for 2D parallel beam geometry, implemented in the ASTRA toolbox [16] and recall through the NeuTomPy instruction reconstruct. The available reconstruction algorithms are listed in [13].

Two examples of NT reconstruction based on data acquired during a NICHE experimental campaign are reported below. The first object is a composite sample named ‘revolver’ and made of an aluminium cylinder with holes filled with bars of different materials (bronze, brass, silver, polyethylene, steel and iron) and a 1€ coin has been sticked between the brass and steel cylinders. Fig.5.14 shows the different components of the ‘revolver’ and its positioning on the sample stage in front of the imaging camera. The normalised reconstructed projections of this object are shown in Fig.5.15. The reconstruction is performed with the GPU-FBP method and the Hamming filter to suppress most of the zinger and ring artifacts. However, the projection containing the polyethylene cylinder is affected by strong noise artifacts due to the high incoherent scattering events induced by the hydrogen content in this kind of material. The 3D volume rendering of the object has been performed through the Avizo software and is shown in Fig.5.16. Also in the 3D reconstruction, the scattering noise

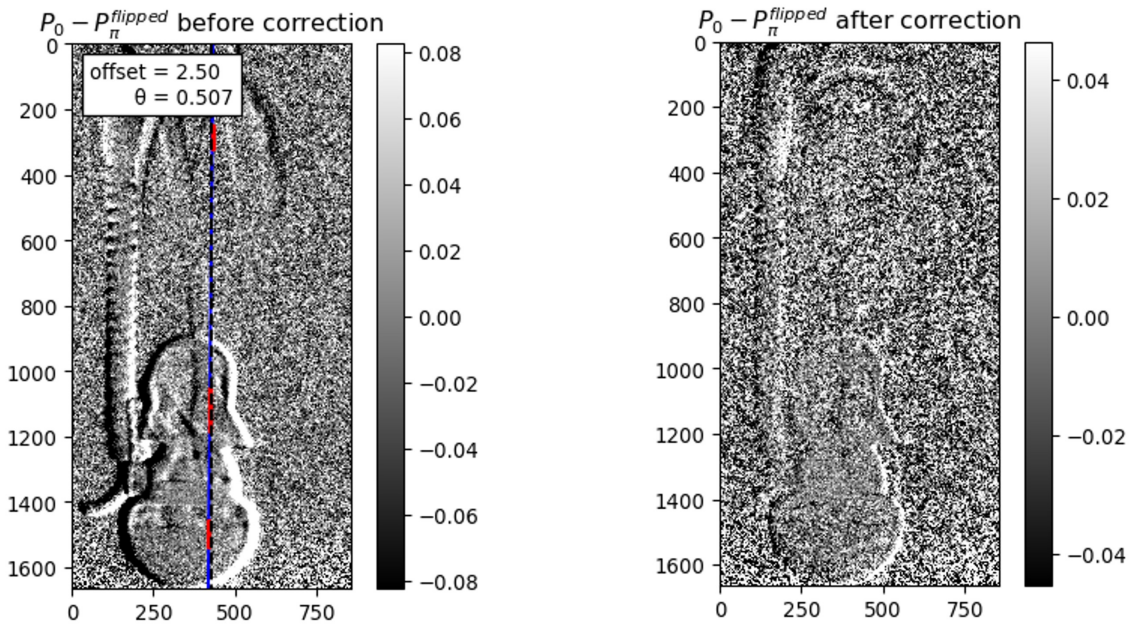

Fig. 5.13 Example of a good rotational axis correction: only the edge of the object can be slightly glimpsed in the P0° - P180°flipped image (original data acquired during CHNet-NICHE tomography experiments).

is well visible nearby the polyethylene cylinder. The second NT reconstruction is shown in Fig.5.17 and regards a possible application of NICHE imaging to archaeological artefacts. A plastic object with two metallic spirals (made of iron and bronze, respectively) and a copper-alloy tsuba (Japanese sword hand-guards) sticked together have been investigated. It is interesting to note the capability of the NICHE imaging system to highlight the plastic object with very good spatial definition despite the high incoherent scattering power of this hydrogen-rich material.

The investigations and characterisation conducted so far demonstrate the promising suitability of the NICHE imaging station for performing thermal neutron imaging with a good spatial resolution and a reasonable acquisition time for a full tomography. The new imaging beamline of the INFN-CHNet infrastructure will allow to conduct morphological and microstructural studies complementary to the more conventional X-ray imaging, with a particular focus on archaeological and Cultural Heritage objects.

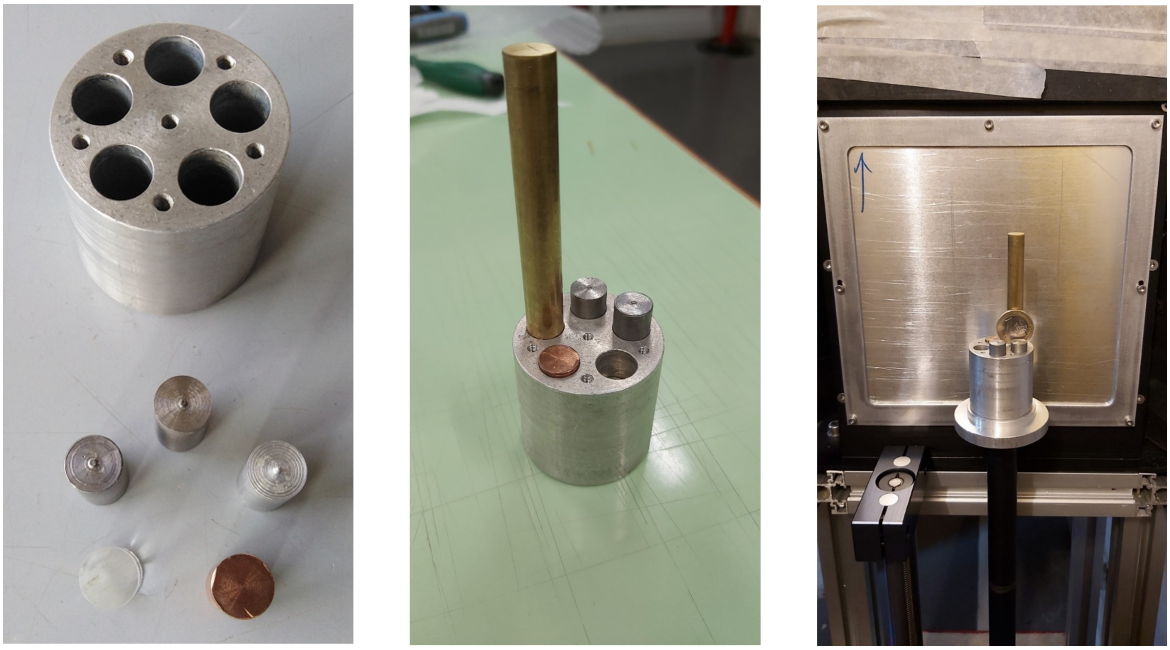

Fig. 5.14 Pictures of the 'revolver' sample, composed of an aluminium cylinder with holes filled by different cylinders made of bronze, brass, silver, polyethylene, steel and iron.

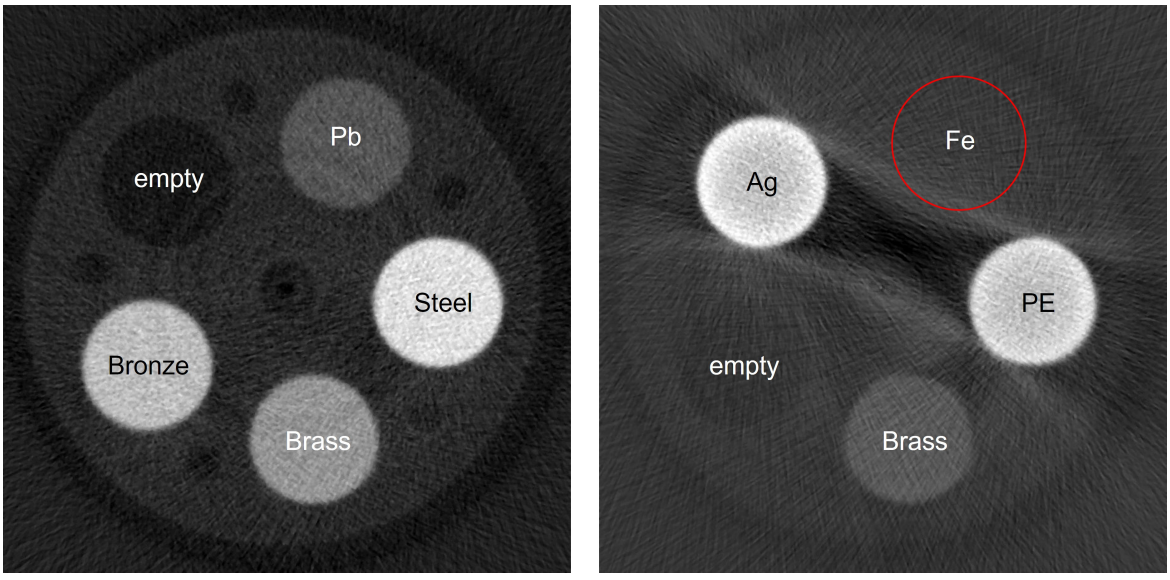

Fig. 5.15 Reconstructed slices of the revolver sample at two different depth in the volume. Materials with different neutron attenuation coefficients can be qualitative distinguished by different grey-scale values.

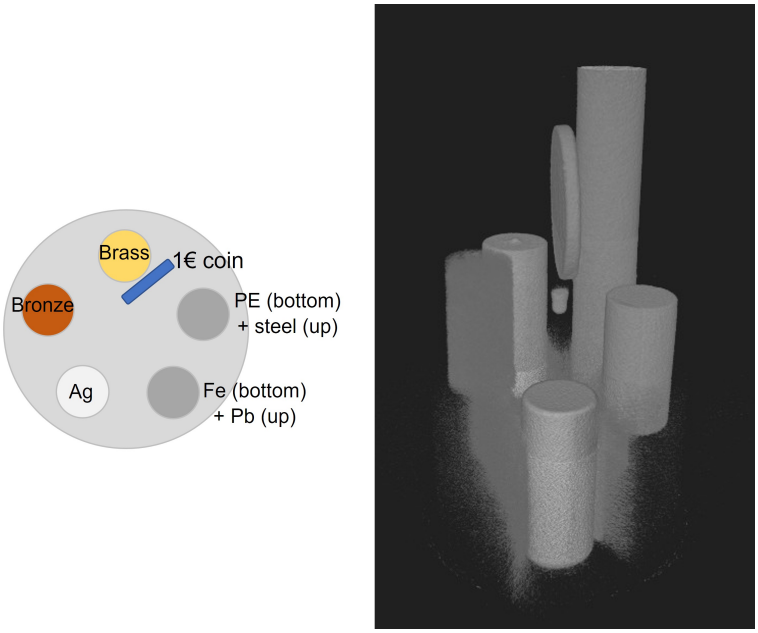

Fig. 5.16 3D reconstruction of the revolver sample obtained using the Avizo software. A schematic drawing of the position of the different cylinders inside the Al revolver is reported as a reference for the reconstruction. Noise artifacts due to neutron scattering events affect the reconstructed image, in particular in the nearby of the polyethylene cylinder rich in hydrogen.

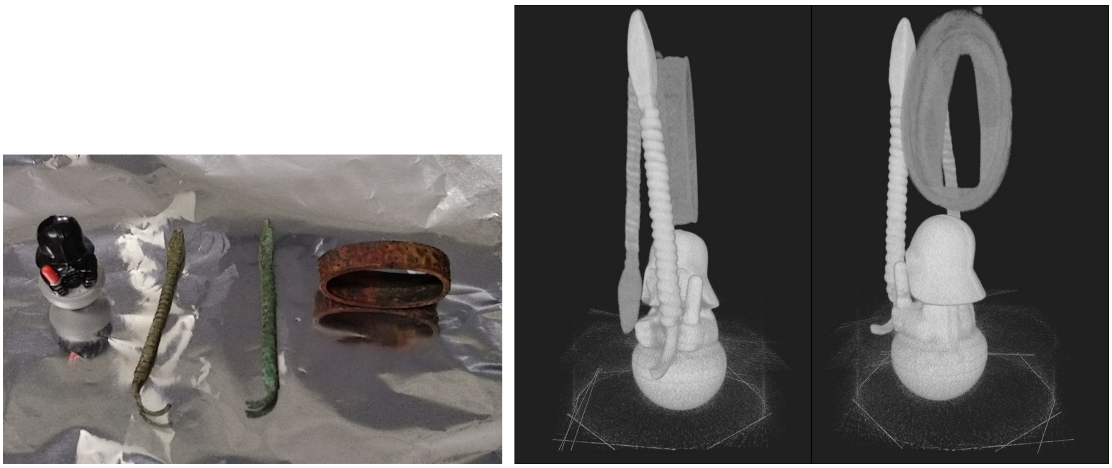

Fig. 5.17 On the left: pictures of metallic samples and a plastic object measured for tomographic reconstruction at the NICHE imaging station. On the right: 3D reconstruction of the samples obtained using the Avizo software. Even in this case, noise artifacts due to neutron scattering events affect the reconstructed image, in the nearby of the plastic object.

References

[1] Giuntini, L. et al. (2021) "Detectors and cultural heritage: The INFN-CHNet experience", *Applied Sciences*, 11(3462), pp. 3462–3462. doi: 10.3390/app11083462.

[2] Salvini, A., Alloni, D., Clemenza, M. (2019) "Design and Safety of the PGNAA Facility at the TRIGA Research Reactor of the University of Pavia – Lena", Proceedings of the International Conference Nuclear Energy for New Europe, Portorož, Slovenia, September 9-12.

[3] Gelli, N. et al. (2023) "The new INFN-CHNet neutron imaging facility", *Nuclear Inst. and Methods in Physics Research A*, 1051. doi: 10.1016/j.nima.2023.168189.

[4] Kaestner, A. P. et al. (2017) "Samples to Determine the Resolution of Neutron Radiography and Tomography", *Physics Procedia*, 88, pp. 258–265. doi: 10.1016/j.phpro.2017.06.036.

[5] Gopal, A. and Samant, S. S. (2008) "Validity of the Line-Pair Bar-Pattern Method in the Measurement of the Modulation Transfer Function (mtf) in Megavoltage Imaging", *Medical Physics*, 35(1), pp. 270–279. doi: 10.1118/1.2816108.

[6] Celli, M., Grazzi, F., and Zoppi, M. (2006) "A new ceramic material for shielding pulsed neutron scattering instruments", *Nuclear Instruments and Methods in Physics Research Section A*, 565(2), pp. 861-863. doi: 10.1016/j.nima.2006.05.234.

[7] Werner, C.J. et al. (2018) *MCNP6.2 Release Notes*, Los Alamos National Laboratory, report LA-UR-18-20808.

[8] Werner, C.J. (2017) *MCNP Users Manual - Code Version 6.2*, Los Alamos National Laboratory, report LA-UR-17-29981.

[9] Nieman, H.F., Tennant, D.C. and Dolling G. (1980) "Single crystal filters for neutron spectrometry", *Review of Scientific Instruments*, 51, 1299. doi: 10.1063/1.1136070.

[10] Stamatelatos, I.E. and Messoloras, S. (2000) “Sapphire Filter Thickness Optimization in Neutron Scattering Instruments”, *Review of Scientific Instruments*, 71, pp. 70–73.

[11] Hawari, A.I., Al-Qasir, I.I. and Mishra, K.K. (2006) "Accurate Simulation of Thermal Neutron Filter Effects In the Design of Research Reactor Beam Applications", *PHYSOR-2006, ANS Topical Meeting on Reactor Physics*, Organized and hosted by the Canadian Nuclear Society. Vancouver, BC, Canada. 2006 September 10-14.

[12] Cantargi, F., Granada, J. R. and Mayer, R. E. (2015) “Thermal Neutron Scattering Kernels for Sapphire and Silicon Single Crystals”, *Annals of Nuclear Energy*, 80, pp. 43–46. doi: 10.1016/j.anucene.2015.01.020.

[13] Micieli, D., Minniti, T. and Gorini, G. (2019) “Neutompy Toolbox, a Python Package for Tomographic Data Processing and Reconstruction”, *SoftwareX*, 9, pp. 260–264.

[14] Abramoff, M.D., Magalhaes, P.J., Ram, S.J.(2004) "Image Processing with ImageJ", *Biophotonics International*, 11(7), pp. 36-42.

[15] Micieli D et al. (2018) “A Comparative Study of Reconstruction Methods Applied to Neutron Tomography”, *Journal of Instrumentation*, 13(6). doi: 10.1088/1748-0221/13/06/C06006.

[16] Van Aarle, W., et al. (2016) “Fast and flexible X-ray tomography using the ASTRA toolbox”, *Opt. Express* 24(22), pp. 25129–25147. doi: 10.1364/OE.24.025129.

Chapter 6

Neutron Resonance Transmission Imaging (NRTI)

For well-established analytical techniques, it may be natural to extend their potentiality to imaging applications. This is the case of NRTA, which has been recently optimised for adding space-resolved information [1] resulting in the now-called Neutron Resonance Transmission Imaging (NRTI) technique.

NRTI exploits the epithermal portion of the neutron flux - not yet widely used in neutron imaging - combining the elemental/isotopic sensitivity due to the resonant absorption of neutrons with morphological details obtained by the employment of a time and space-resolved detection system. What makes NRTI different from standard neutron radiography/tomography is the possibility of not only localising specific features inside the volume of an object but also identifying and localising specific elements and isotopes with enhanced contrast with respect to others, without the need for sampling. Moreover, each detector pixel contains the full transmitted spectrum which is not integrated over the time/energy range, in contrast with neutron tomography where it is a typical process done by the neutron camera. These characteristics, combined with the non-destructiveness of the method, make NRTI a promising powerful imaging tool for application in the Cultural Heritage fields, extending the potential of neutron imaging.

NRTI measurements are conducted at the INES beamline of the ISIS Neutron and Muon Source (Chapter 2). At present, NRTI allows the qualitative recognition of the elemental composition of an object by indexing the position of the resonance dips in the transmitted spectrum. This thesis aims to start a reliable data normalisation procedure and to carry out the first calibration tests towards a quantitative composition analysis, mainly focused on archaeological copper-based materials. In bulk analyses of metallic samples, neutrons are extremely useful indeed, as this type of material cannot be easily analyzed in depth by

other most common techniques such as those based on X-rays. The following first sections will illustrate the procedure followed for the acquisition of NRTI data on standard samples (homogeneous material composed of a single element or alloy) with certified composition and their treatment for normalisation. Some examples highlighting the potentiality of NRTI for elemental and isotopic imaging will be provided, also mentioning an archaeological case study.

Finally, an attempt of a quantitative calibration of the technique is discussed, focusing on the beam hardening effect affecting the white neutron beam passing through thick and strong absorbing materials.

6.1 Measurements and instrumentation

The NRTI measurements were performed at the INES beamline thanks to the flexible layout of the experimental station. The relatively long flight path of INES (about 23 m) allows for good TOF resolution. Although the INES neutron beam is thermalized, it still provides a reasonable flux of neutrons in the epithermal region, where several elements present strong resonance peaks in the capture cross-section (Chapter 2).

The transmission measurements have been conducted by introducing a commercial neutron Gas Electron Multiplier (nGEM) [2] in the beamline. Gas Electron Multiplier detectors were initially developed at CERN [3] to achieve high rate, high accuracy detection and localization of fast charged particles in High Energy Physics. However, due to their versatility, they can be properly adapted as neutral particle detectors. The high time resolution combined with the large detection area achievable with this technology, makes nGEM detectors at least promising for high time-resolved NRTI measurements.

Generally, nGEM detectors are made of three main elements: the anode, a series of electrodes called GEM foils and the cathode. The nGEM device used in this experiment relies on the use of a $^{10}B_4C$ sheet placed perpendicularly to the incident neutron beam direction, which in turn acts as neutron-to-charged particle converters via the following reactions:

$$^{10}B + n \rightarrow ^{7}Li + \alpha \; (Q = \; 2.8\, MeV,\; BR \; = 6\%) \tag{6.1}$$

$$^{10}B + n \rightarrow ^{7}Li + \alpha \; + \gamma\,(478\, MeV\,)\; (Q = \; 2.3\, MeV,\; BR \; = 94\%) \tag{6.2}$$

The boron carbide layer is 2 μm thick. The charged reaction products (mainly the α-particles) generate the neutron detection signal through their subsequent conversion into

electrons in a gas-filled drift region. These, moved by an electric field applied in this region, reach the GEM foils where they are proportionally multiplied in cascade. The detector is sealed with an inlet and outlet hole for gas flushing. For this device, a mixture of Ar:CO_2 (70:30) was used. The active area of the commercial detector is 10×10 cm^2 and its pixel size is 0.8×0.8 mm^2. However, it is limited to the transverse size of the INES neutron beam, which is 3.2×3.2 cm^2.

The nGEM efficiency as a function of the neutron energy can be roughly estimated through the following formula:

$$\varepsilon(E) = 1 - e^{-t/\mu(E)}$$

where t is the thickness of the converter foil and $\mu(E)$ is the attenuation length as a function of neutron energy. The efficiency $\varepsilon(E)$ is displayed in Fig.6.1. The commercial nGEM is usually placed along the incident beam direction at a distance of 23.44 m from the moderator.

This detector is able to operate up to a total count rate of 10 MHz on the whole detector area. Moreover, each neutron is time stamped with a precision of 8 ns referred to the T-zero of the ISIS accelerator (signal synchronous to when the proton beam hits the target). Considering the time broadening of $\sim$400 ns affecting the initial neutron pulse due to the neutrons slowing down in the small water moderator [4, 5], the time binning of the NRTI acquisition has been set at 1 μs.

Considering the data normalization procedure introduced for Neutron Resonance Transmission analysis in Chapter 4, acquiring a sequence of measurements with and without the sample is necessary.

Furthermore, since ISIS is a spallation source, the beam could be characterized by variations in intensity due to various operating conditions of the source. Another source of intensity instability of the incident beam is the presence of the TOSCA beamline before the INES instrument: samples with strong resonances in the epithermal energy region placed at TOSCA or the closure of the TOSCA shutters can create an alteration of the intensity and quality of the beam incident to the sample placed at INES (Fig.6.2).

The frequency of these variations is not predictable during NRTI acquisitions (apart from sample changes on the TOSCA instrument). Hence, the procedure chosen for the NRTI acquisitions is an alternation of several different measurements with and without a sample lasting a few hundred of μAh (a few hours), in order to have a good statistic for the overall NRTI data of an object and a decent ability to detect and correct beam variations in each acquisition run.

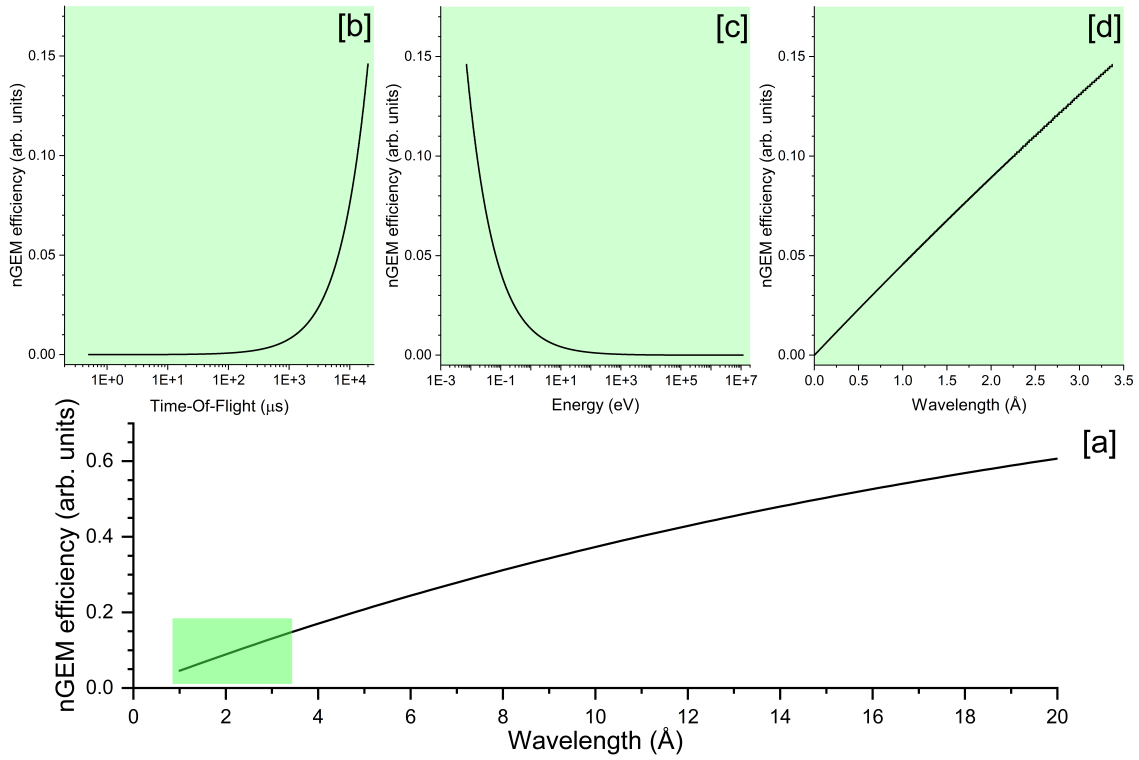

Fig. 6.1 [a] nGEM efficiency in the wavelength range 0-20 Å. The effective wavelength range exploited for NRTI measurements at INES is highlighted in the green area. [b,c,d] Enlargement of the effective nGEM efficiency in TOF, energy and wavelength units. The corresponding ranges are 0-20 ms, 0.007-1.15·10^7 eV and 0-3.4 Å.

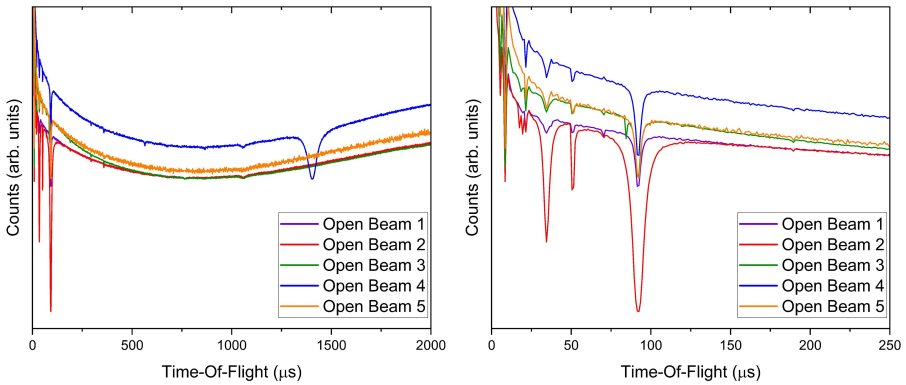

Fig. 6.2 Different Open Beam acquisitions (*i.e.*, without the sample) showing several TOF structures, which depend on the experimental conditions affecting the neutron beam incident at the INES beamline.

During the conversion from TOF to incident neutron energy or wavelength, the position of the transmission detector needs to be precisely calibrated. The nGEM detector for NRTI measurements is currently not a fixed component in the beamline, therefore after its positioning and before an NRTI experiment, its position has to be calibrated. The detector position can be accurately determined by analyzing the position of the resonance dips of gadolinium and tantalum foils (99.99% of purity and 50 μm of thickness). These two elements have well-known and rather well-separated resonances over the entire epithermal TOF range of interest for the NRTI measurements, as is evident in Fig.6.3. Fig.6.4 shows the transmission spectrum of Gd and Ta foils measured during cycle 2019/03 (Nov-Dec 2019) position calibration of the nGEM detector, which has been evaluated at 23.44 m from the moderator.

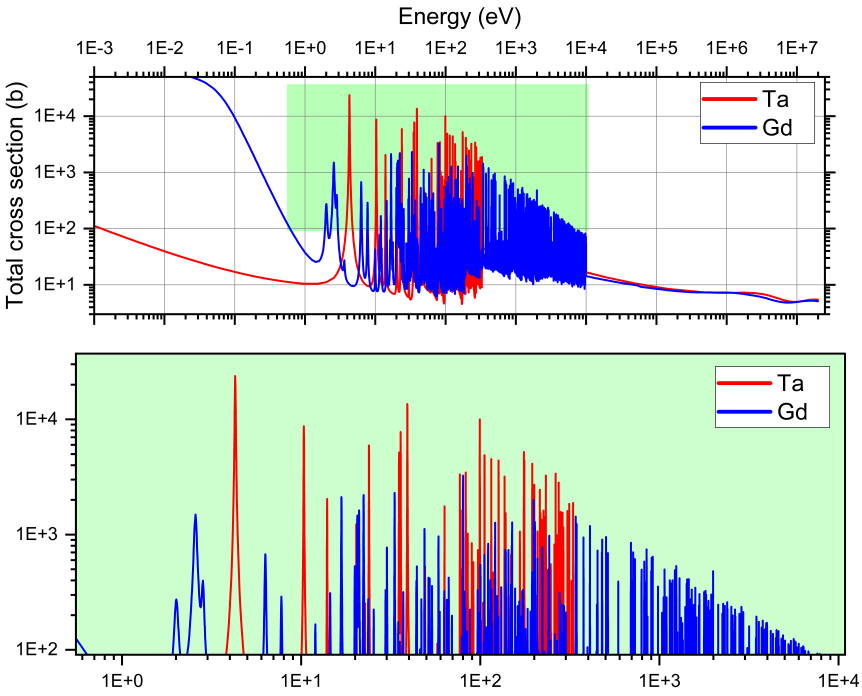

Fig. 6.3 Gd and Ta (n, total) cross sections. In the green area, the epithermal energy region is selected. Resonances are shown above the threshold of 10^2 barns, as resonances less intense are typically not visible within the INES transmission setup.

6.2 Data processing and normalisation

Since NRTI experiments are conducted at the INES beamline of the ISIS neutron source, the processing steps of the collected NRTI data are carried out using the Mantid software

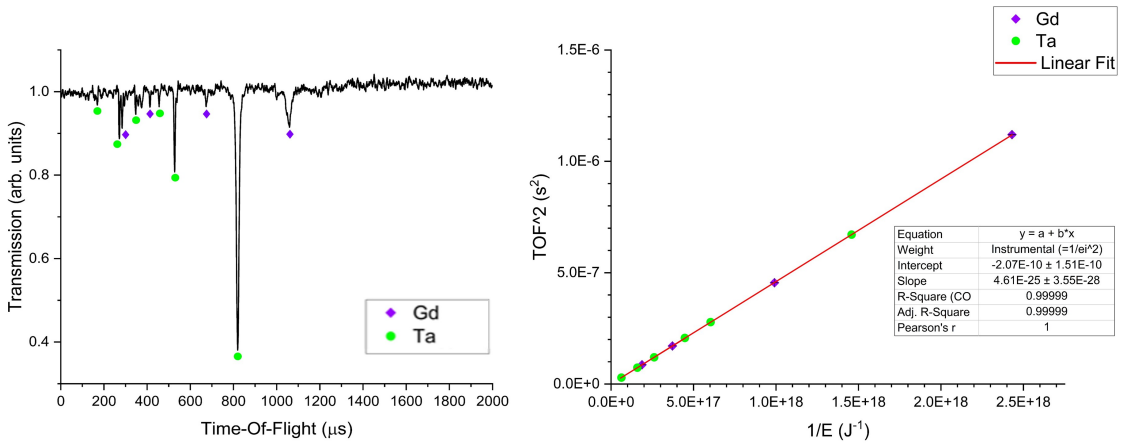

Fig. 6.4 On the left, the transmission spectrum of Gd and Ta foils. The main resonance dips used for the detector position calibration are indicated. Overlapping resonances have been not considered. On the right, the calibration curve determines the detector position (23.44 m distant from the moderator).

[6, 7], widespread in large-scale structures all over the world and used above all by ISIS instrument scientists and often by ISIS users. All the data treatment methods discussed below are performed through specific Python-based algorithms compatible with the Mantid platform and purposely created in this thesis work.

The normalization of the data was performed by using the following procedure:

- for each run pair (S,OB) associated with a specific sample, the S/OB transmission is evaluated (S and OB are the TOF-spectra of a sample-in measurement and a sample-out measurement, respectively);
- for each run pair (S,OB), the corresponding incident monitor runs measuring the irradiation current are taken into account for evaluating the current normalising factor $M = Mon_{OB}/Mon_S$;
- the overall transmission of a sample is calculated by merging together the S_i/OB_i ratios normalised by the neutron current as $T_{exp} = \frac{1}{N}\sum_{i=1}^{N}\frac{S_i}{OB_i}M_i$, where N is the total number of run associated to the same sample.

A schematic diagram of the normalisation procedure is represented in Fig.6.5. In this way, the energy-dependent shape of the spectrum is normalised with the Open Beam (OB) acquisition. Each sample-in spectrum is divided by the previous or following OB spectrum.

Usually, at ISIS the mean proton current delivered during each measurement on a beam-line, such as INES, is recorded and made available to the user. However, as previously

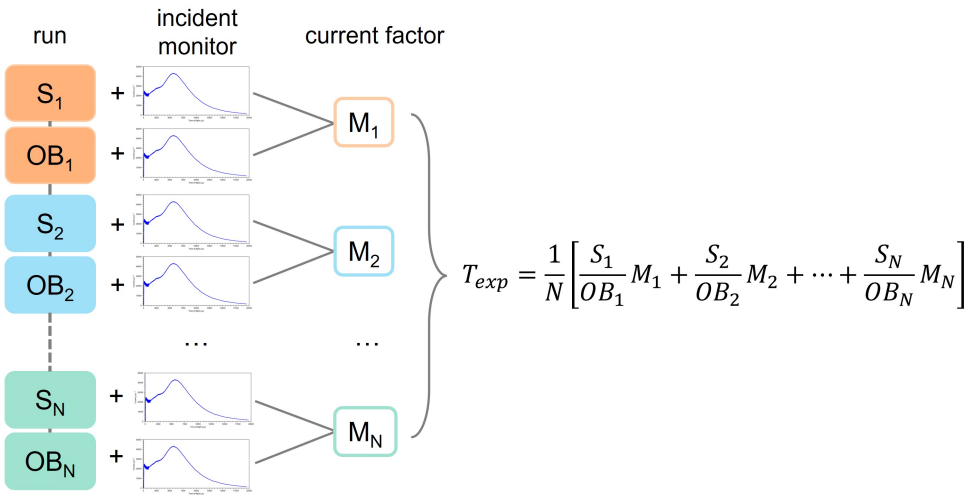

Fig. 6.5 Diagram representing the normalisation steps adopted for the NRTI data. S and OB are single transmission measurements with and without the sample, respectively. M is a constant factor which takes into account the neutron current normalisation of the ratio S/OB by dividing the monitor runs associated with S and OB.

discussed in Section 6.1 several experimental conditions may change during an NRTI acquisition. Therefore it is more reliable to evaluate the neutron flux irradiating the sample or the detector by means of the incident monitor available at INES. A typical monitor spectrum is shown in Fig.6.6. In the 0-150 μs TOF region, the monitor counts abruptly fall to zero. To avoid unreliable regions of the incident monitor and to de-link the normalisation process from the detector efficiency, the ratio between the monitor spectra associated with the sample and the open beam acquisition is evaluated in the region 250-2000 μs, assuming this ratio is constant over the entire TOF range of interest for the NRTI analysis (0-2 ms).

Fig.6.7 shows the monitor ratio for different (S,OB) pairs. Ratios that introduce non-constant dependencies with the TOF/energy due to any source of flux variation during acquisition are discarded and consequently, the associated transmission runs are not considered during the merging step of the runs associated with a sample.

6.3 The Black Resonance Method for background characterisation

To apply the Beer-Lambert law, it is necessary to adequately characterise the environmental background affecting the open beam and the sample-in measurements. B_{in} and B_{out} in Eq. 4.21 (Chapter 4) include both time-dependent and independent components. The latter can

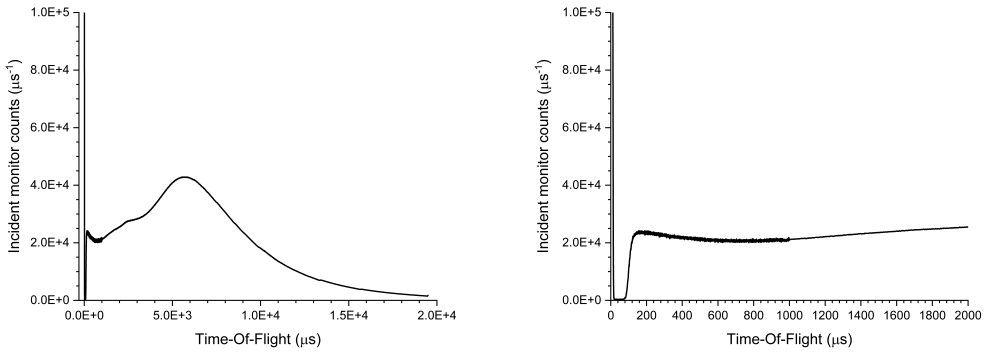

Fig. 6.6 On the left, a typical incident monitor spectrum in the TOF region 0-20 ms available at INES. On the right, the monitor spectrum enlarged in the NRTI TOF region 0-2 ms.

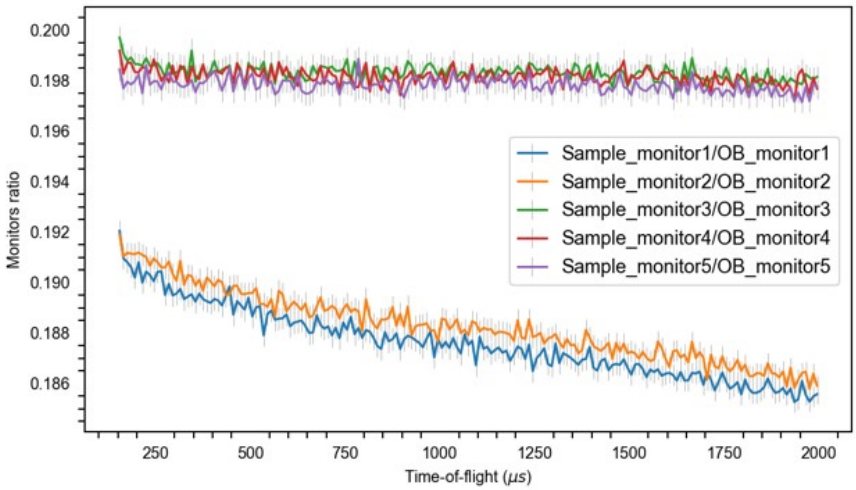

Fig. 6.7 Ratios between monitors associated with sample-in and sample-out NRTI measurements in the 250- 2000 μs TOF range.

be determined with the beam close, whilst for a moderated neutron beam the time-dependent background can be identified as the sum of the following contribution [8]:

- 2.2 MeV γ-rays produced in the target-moderator assembly. This background component (B_γ) has a time distribution related to the slowing down process of neutrons in the moderator;
- neutrons scattered inside the detector and by the instrument environment (B_{ns});
- overlap neutrons (B_{no}), *i.e.* neutrons detected but produced by the previous cycle. This source can be strongly reduced by means of a frame overlap chopper.

Table 6.1 Details of black resonances of Au, In and Havar filters measured to evaluate the background contribution affecting NRTI acquisitions.

Filter	**Thickness (mm)**	**Dark resonance position (μs)**	**Mean saturation level**
99.99% Au	0.04	763.5-766.5	$4.1 \pm 0.4\ 10^{-3}$ [1]
99.99% In	0.2	1375-1450	$3.7 \pm 0.2\ 10^{-3}$ [2]
Co42.5/Cr20/Ni13 /Fe/W/Mo/Mn	2.5	145-150	$3.4 \pm 0.1\ 10^{-3}$ [3]

Usually, the background as a function of TOF is experimentally determined as it is difficult to simulate. A typical strategy consists of the Black Resonances Method [9]: samples of elements with strong absorption resonances giving negligible transmission of neutrons at the resonance energy are employed and the background is indicated by the residual events in the resonance regions.

An ideal black resonance has a large capture-to-scattering cross-section ratio and a total width greater than the instrument resolution. To ensure saturation through the filter at resonance energy, the filter thickness should be selected to ensure that the transmission at the saturated (also called black) resonance is less than 10^{-4}. On the other hand, a thick filter will alter the background itself. Particularly, the time-dependent components $B_\gamma(t)$, $B_{no}(t)$ and $B_{ns}(t)$ are highly dependent on filters and samples absorption and scattering characteristics.

To avoid bias effects in the background, thin filters with strong resonances and low scattering power have been chosen for background characterisation. In Fig.6.8 the resonance dips observed for gold foils (0.02 and 0.04 mm thick), indium foil (0.2 mm thick), and Havar foils (2.5 mm thick) are shown. The associated 2D transmission maps are shown in Fig.6.9. According to Table 6.1, listing the mean saturation levels and the geometrical characteristics of the filters, an average value can be subtracted from the sample-in and OB spectra to correct for the background residual events. Moreover, the background seems to show an energy-independent behaviour. However, Fig.6.9 illustrates how pixel position influences saturation. Therefore, mean saturation values have to be subtracted pixel by pixel.

It is worth noting that further investigation will be needed for the following reasons:

- the black resonance filter should cover the entire active area of the detector;

[1] Evaluated from the transmission spectrum (Fig.6.8) obtained by merging all the spectra in the red region in Fig.6.9.

[2] Evaluated from the transmission spectrum (Fig.6.8) obtained by merging all the spectra in the purple region in Fig.6.9.

[3] Evaluated from the transmission spectrum (Fig.6.8) obtained by merging all the spectra in the yellow region in Fig.6.9.

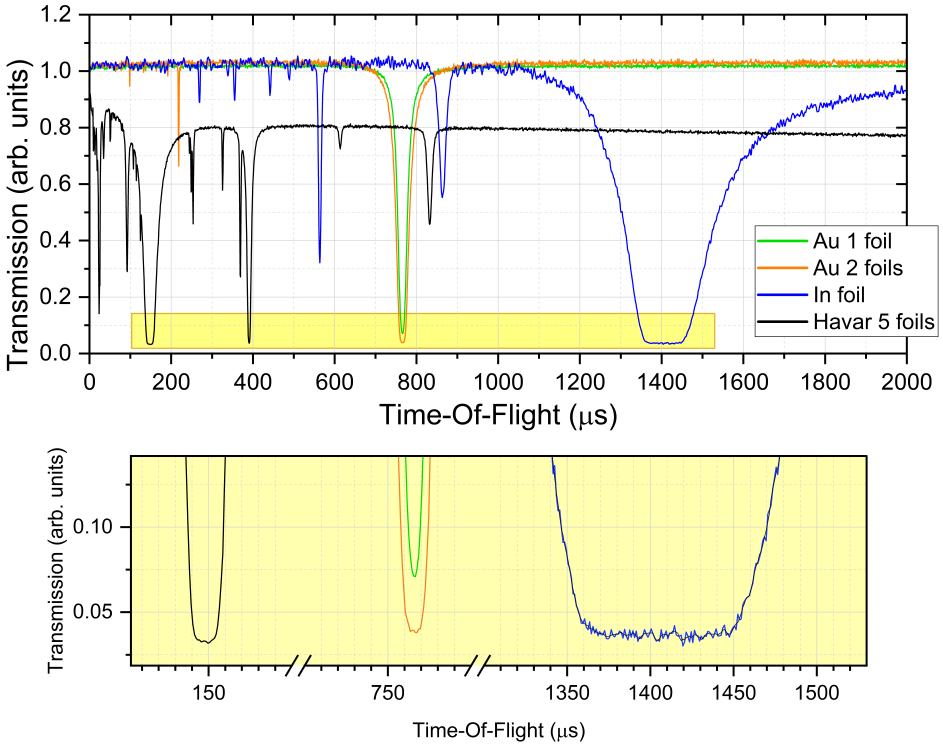

Fig. 6.8 Saturated resonances of Au, In and Havar filters.

- the black resonance should be large enough to achieve reasonable statistical (as an indication, E> 5% [10]);
- the off-resonance transmission should be 1 to avoid background contributions due to the filter itself.

Considering these requirements, the Au, In and Havar filters employed for preliminary characterisation need to be improved as they are too thin (Au) or too thick (Havar) or do not cover the entire detection area In and Havar). Moreover, the TOF region covered by the saturated resonances is too limited, therefore more filters are needed to explore the background for TOF < 100 μs and in the ranges 200-700 μs and 900-1300 μs.

6.4 Application

6.4.1 Elemental imaging

In this section, some key examples of NRTI for elemental imaging are discussed. The striking feature of NRTI to store the unintegrated transmitted spectra in each pixel of the neutron radiography permits the selection of resonances of specific elements within the irradiated

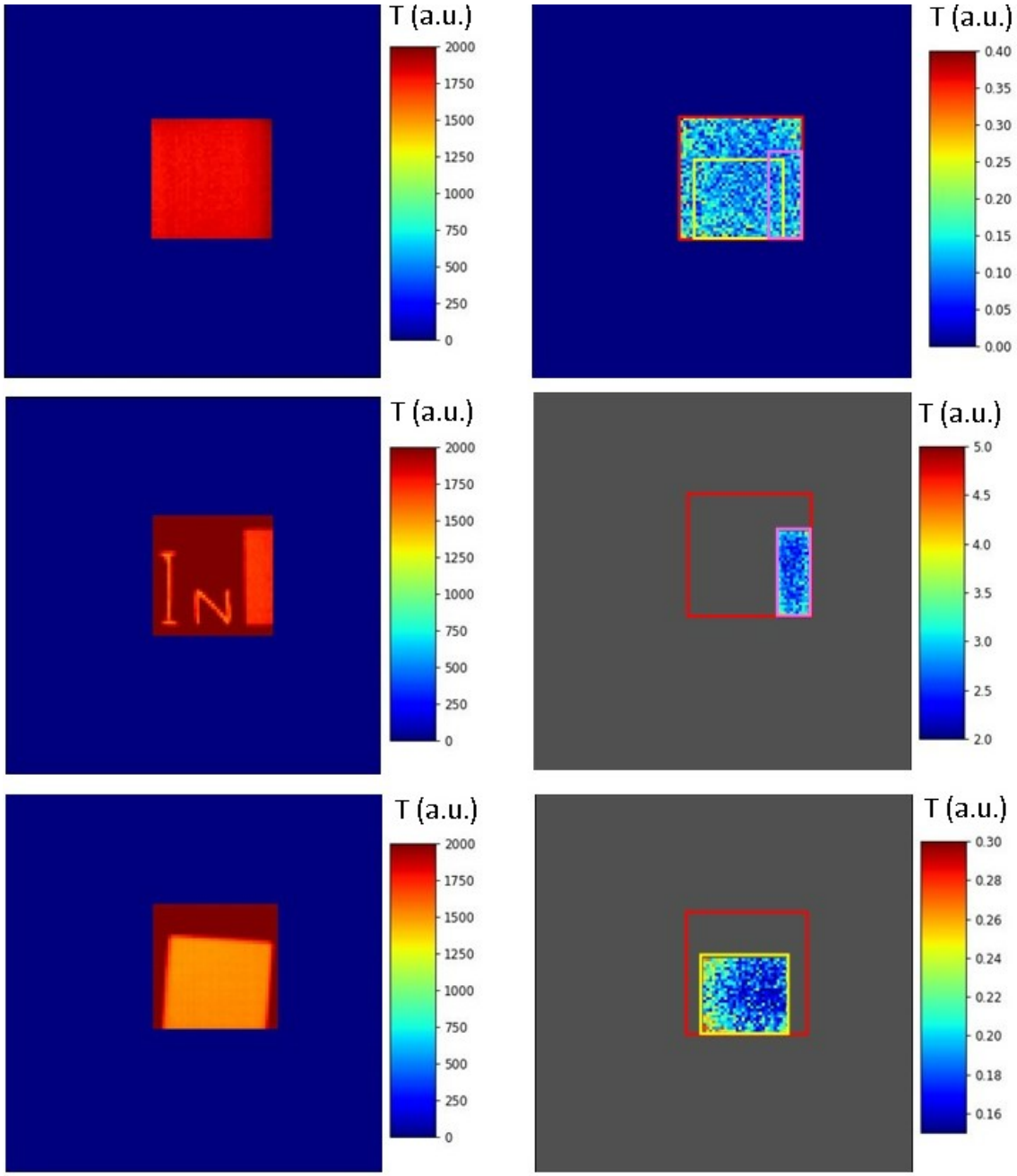

Fig. 6.9 From top to bottom: transmission map showing the Au, In and Havar filter samples. The red, pink and yellow boxes represent the selected ROI for evaluating the mean saturation level of the Au, In and Havar filters, respectively. The size of all the 2D maps is 10×10 cm^2. A mask of 3.2×3.2 cm^2 is applied to activate only the detector pixels centred within the INES transverse beam size.

object. The resonance selection enhances the contrast in regions containing the element selected with respect to the other areas without this resonance in the transmission signal. In this way, elements with similar neutron absorption coefficients can be well discriminated against each other and their localisation within the object volume can be easily visualised. This process is on the basis of the elemental and isotopic imaging that can be performed through NRTI.

The first example is reported in Fig.6.10, showing the 2D transmission map of a silver foil (0.25 mm thick) and of a silver wire (1.0 mm thick) shaped to form the letters "Ag". In this simple neutron radiography, the contrast between the silver samples and the background is low and it is simply due to the exponential dependence of the neutron transmission with the sample thickness.

By selecting a Region Of Interest (ROI) within the silver foil, *e.g.* the blue ROI in Fig.6.10, the transmission spectrum containing the Ag resonance dips can be obtained (this spectrum is the result of merging all the spectra stored in the pixels in the blue ROI). Fig.6.11(a) shows the resonance dips of the silver foil.

On the other hand, a region without any object, *e.g.* the white ROI in Fig.6.10, results in an NRTI spectrum without any resonance dips in the whole TOF range, as a consequence of a correct normalisation between sample-in and open beam acquisitions. The transmission level is, indeed, statistically around 1 as shown in Fig.6.11(b).

Through the Mantid platform, a specific resonance dip can be selected by indicating the corresponding TOF range, *e.g.* the most intense Ag resonance highlighted in the yellow box in Fig.6.11(a). Therefore the transmission map will show in each pixel the spectra "cut" in the indicated TOF range. As a result, the pixels containing the selected Ag resonance have highly enhanced contrast with respect to the others in the background.

If instead a TOF range without any resonance is selected, *e.g.* the green box in Fig.6.11(a), the contrast enhancement will be lost and the sample can only be slightly glimpsed against the background as all the pixels of the map have transmission around 1 in this TOF range, thus making the image quite uniform (Fig.6.10).

Resonance selection also permits to conduct semi-quantitative evaluation of the composition of objects. As an example, four Cu/Sb slabs with the same regular shape ($3 \times 8 \times 1$ cm^3) and different Cu/Sb content have been measured with the NRTI imaging setup. The transmission spectra related to these samples are shown in Fig.6.12, whilst their certified compositions are described in Table 7.3. The selection of the main Sb resonance in the TOF range 650-700 μs clearly indicates which slab in the 2D image (Fig.6.13) has the highest Sb content. Moreover, one sample contains 3% of arsenic and the selection of As resonance at 244.5 μs allowed to identify the position of this sample in the neutron radiography (Fig.6.13).

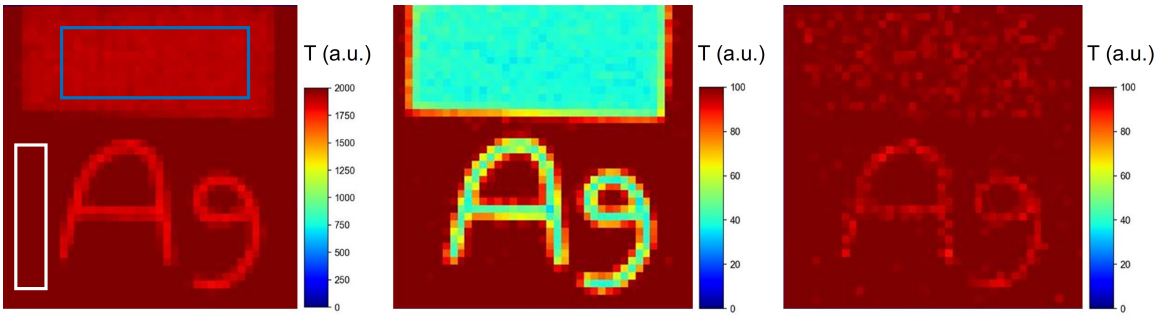

Fig. 6.10 From the left to the right: the NRTI 2D map of a silver foil and a silver wire; the 2D map after Ag resonance selection in the TOF range 700-800 μs (see Fig.6.11(a)); the 2D map after the selection of the 1400-1500 μs range containing any resonance dips (see Fig.6.11(b)). The size of all the 2D maps is 3.2×3.2 cm^2.

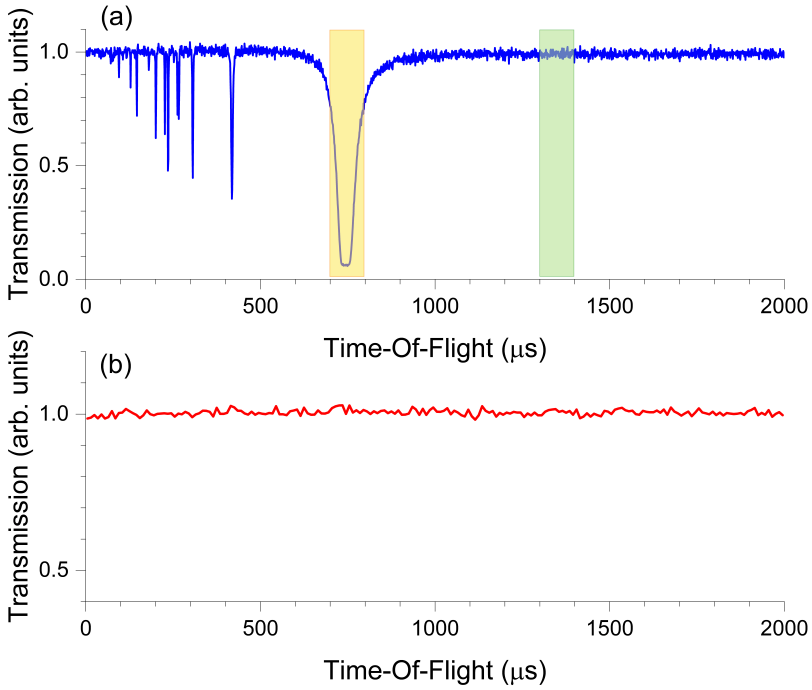

Fig. 6.11 The NRTI spectrum of the Ag foil within the blue ROI selected in Fig.6.10. The yellow area (700-800 μs) highlights the main resonance of Ag at 744.5 μs (5.19 eV), while the green area (1300-1400 μs) accentuates a TOF range without any resonance dips. (b) The NRTI spectrum of the off-sample region highlighted in the white ROI in Fig.6.10

The possibility of increasing the contrast between elements with similar neutron attenuation powers to facilitate their localization within the volume of an object provides interesting beneficial applications of the NRTI technique for non-destructive analyses on samples of archaeological interest to simultaneously determine their elemental composition and the

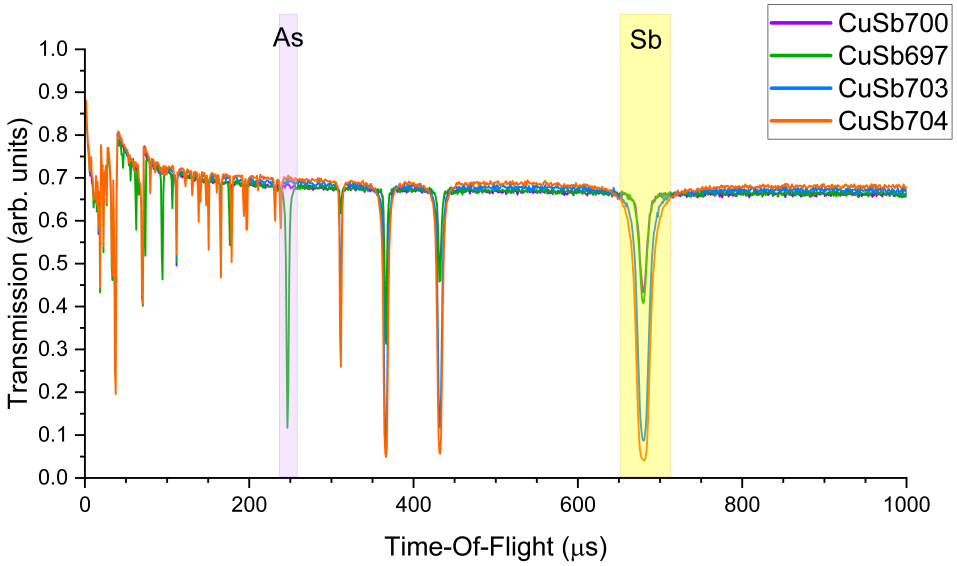

Fig. 6.12 Transmission spectra of the four Cu/Sb slabs characterised by different Cu/Sb content. Details of the composition of the slabs can be found in Table 7.3. In the image, the Sb resonance at 680 μs and the As resonance at 246.5 μs are underlined.

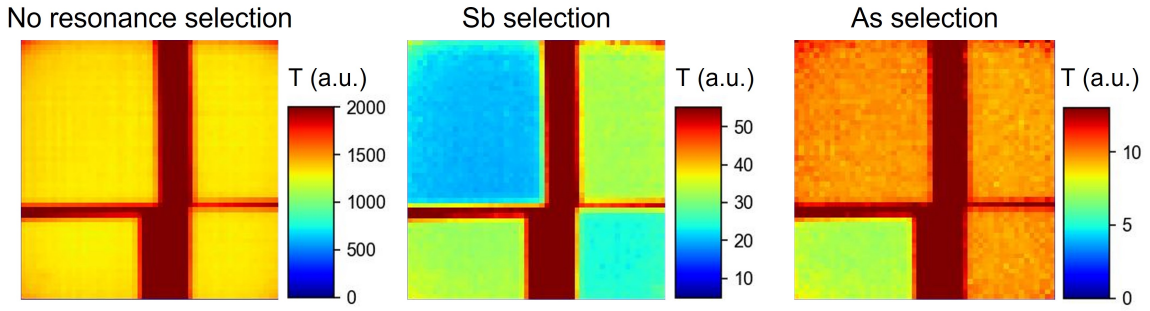

Fig. 6.13 From left to right: the NRTI radiography of four Cu/Sb slab characterised by the same thickness and different Cu/Sb compositions; the 2D transmission map after Sb-resonance selection in the TOF range 650-700 μs; the 2D transmission map after As-resonance selection in the TOF range 241-254 μs. The size of all the 2D maps is 3.2×3.2 cm^2.

morphology of the distribution of the elements, especially in materials presenting areas of inhomogeneity (despite the current limited spatial resolution of the NRTI technique, compared with the typical resolutions of the standard Neutron Tomography setups).

As a further example of elemental imaging performed with NRTI, a case study related to the Cultural Heritage filed is presented in the following paragraphs.

During 2009, the Soprintendenza Archeologia, Belle Arti e Paesaggio of Milan conducted the excavation of Corso di Porta Romana 20 in Milan (Italy) (Fig.6.14) [11]. This excavation

unearthed numerous fragments of metals and crucibles connected to bronze and brass production, datable between the end of I and the beginning of II century AD. This set of excavation finds is related to the activity of at least one workshop in the Roman city of Mediolanum.

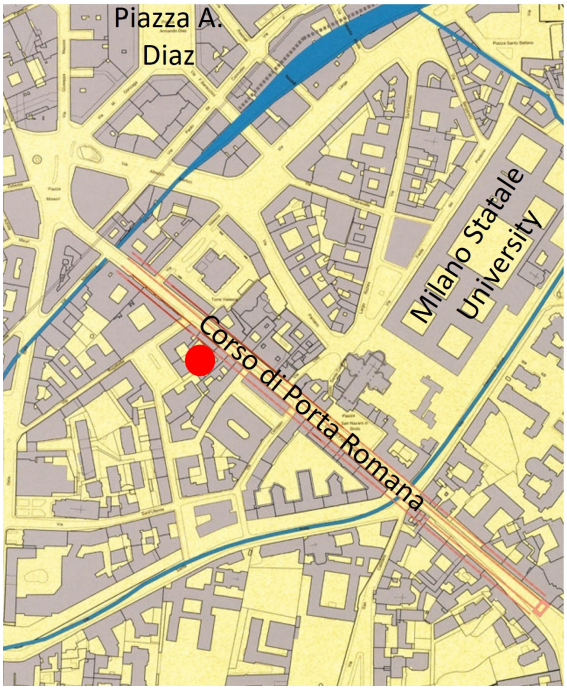

Fig. 6.14 Map of the area nearby Corso di Porta Romana, Milan, which was the site of excavation carried out in 2009 by the Soprintendenza Archeologia, Belle Arti e Paesaggio of Milan.

Brass, an alloy composed of copper and zinc, was widespread in the Roman Empire [12]. Nevertheless, up to now, the production of brass in Roman times was documented only in England, Germany, and France [13–15], but it was completely unknown in Italy. Hence, the excavation in Milan is the first testimony of brass production in Roman Italy. The crucibles consist of mass-produced terracotta pots, coated with a thick layer of refractory clay. Inside, the copper and zinc alloy were heated to high temperatures, liquefied and then thrown into moulds to make appliques for furniture and ornamental objects.

The unhearted crucible fragments contain depositions of these copper alloys, some of which are clearly visible on the fragment's surface whilst others are inside the bulk. A set of 8 crucible fragments has been investigated in a non-destructive way through Neutron Resonance Transmission Imaging (NRTI) to disclose evidence of brass casting through the composition of the alloys enclosed in the crucible fragments.

From a set of about twenty crucible fragments, six of them have been selected on the basis of their size (a few centimetres of thickness), weight (as a rough indication of the presence of metallic inclusions in the volume) and superficial morphological properties to request access to the INES beamline for NRTI analyses lasting 2 days. Each sample was irradiated for 7 hours approximately, alternating acquisitions with-in and with-out the sample.

The resulting normalised transmission maps are shown in Fig.6.15-6.18. Different transmission levels are visible without resonance selections, which are due not only to the different thicknesses of the object but also to the different absorbing materials present within its volume.

A qualitative elemental composition averaged over the whole volume of the fragments is shown in Fig.6.19. The reported transmitted spectra refer to ROI comprising the entire samples, and peak assignment reveals the presence of Cu, Zn, Sn, Sb, As and Ag in the set of fragments, linked to possible traces of metal workings inside the Mediolanum area (in particular bronze, brass and silver).

As an example of elemental imaging, the application of resonance selections to sample OT20_small shown in Fig.6.20 is discussed. Even though no metal deposits are clearly visible on the surface, the NRTI spectrum indicates the presence Cu, Zn, Sn, Sb and Ag within the fragment matrix.

Similarly to the above-discussed examples of elemental imaging with standard materials, the selection of the main resonances of Zn, Cu, Sb, Sn and Ag is performed to increase the contrast of the single element with respect to the average composition of the sample and visualise its distribution within the fragment volume. The distribution maps of these elements after their resonance selection are shown in Fig.6.21.

As a general but not mandatory rule, neutron-based analyses are often anticipated by preliminary investigations conducted with faster and less expensive -in term analytical methods (such as those conducted with X-rays as a probe) in order to request adequate time access to the neutron facility having a general idea of the type of investigation to carry out with neutrons. Following this scheme, preliminary investigations on the elemental composition of the samples have been performed by means of well-calibrated or more optimized non-destructive techniques to have a reference check for the NRTI results. In particular, PIXE analysis has been conducted at the particle accelerator Accélérateur Grand Louvre d'analyse élémentaire (AGLAE), housed by the Center for Research and Restoration of Museums of France (C2RMF) in the Louvre museum in Paris (France) [16], to assess the composition of the metallic depositions (mainly drops and small layers) present on the fragment surfaces. Details on the PIXE experimental setup and data treatment can be found in [17–19]. The bar chart in Fig.6.22 shows the quantitative composition of metallic

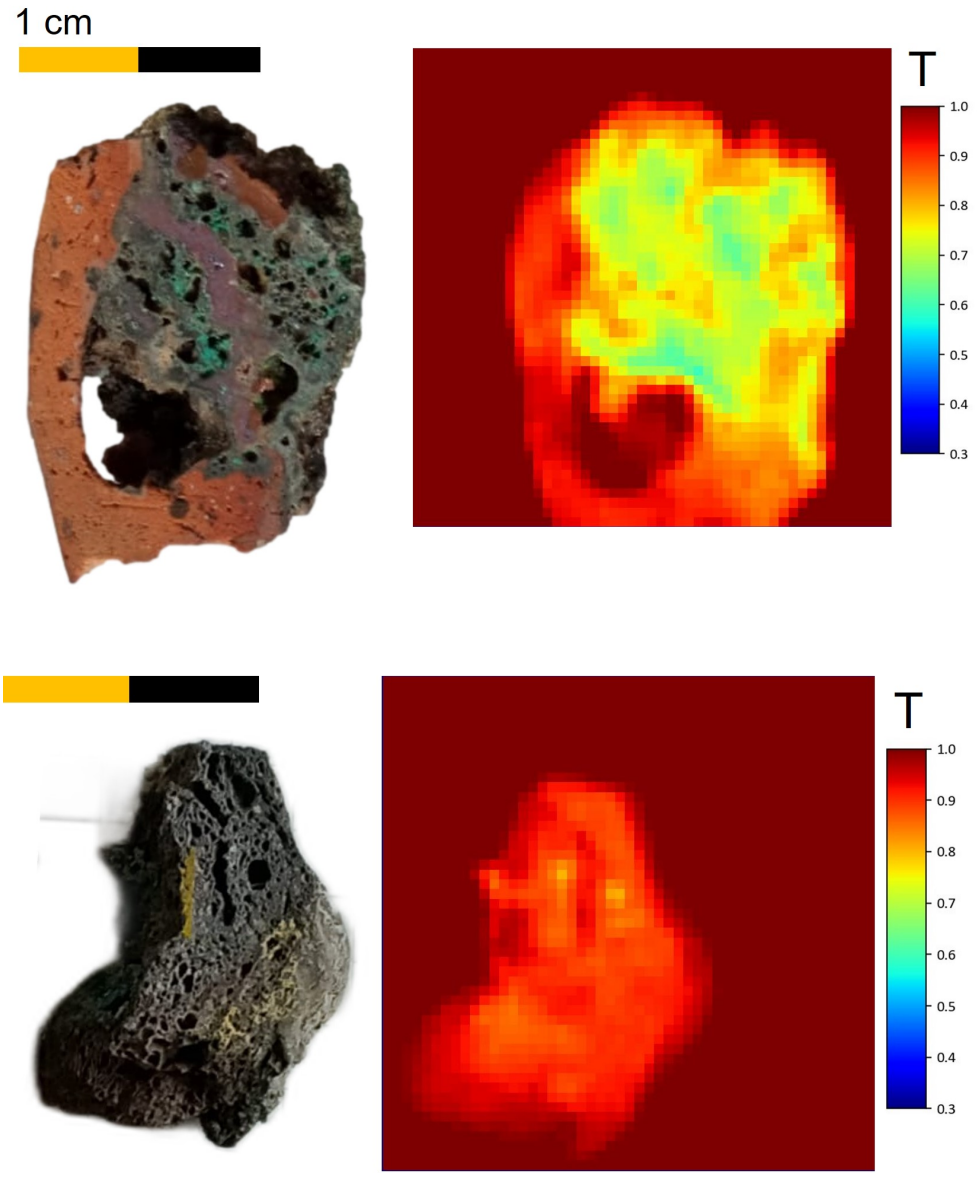

Fig. 6.15 Top: picture and transmission map of crucible fragment OT20_small. Bottom: picture and transmission map of crucible fragment OT5C. The size of all the 2D maps is 3.2×3.2 cm^2.

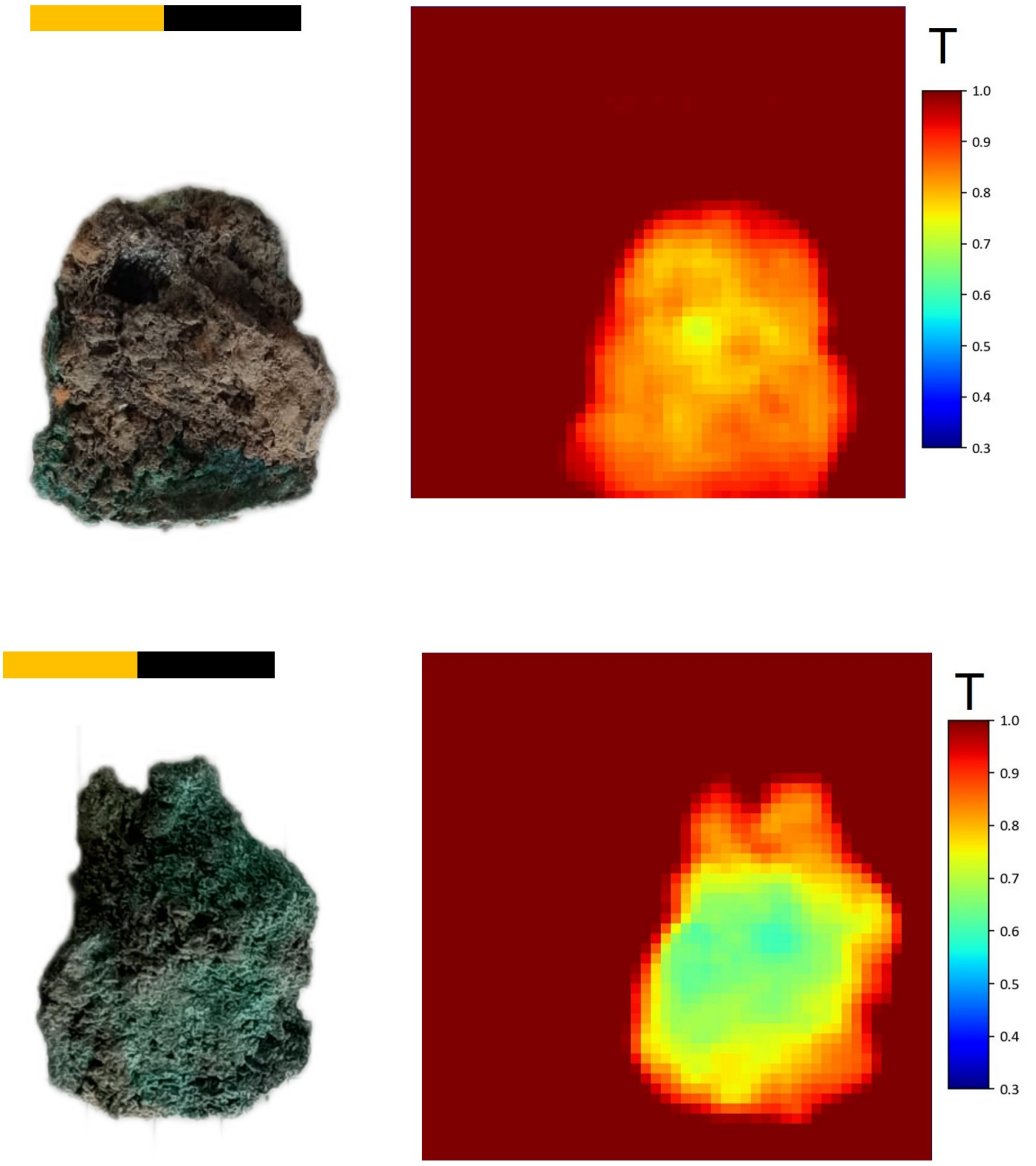

Fig. 6.16 Top: picture and transmission map of crucible fragment OTG3. Bottom: picture and transmission map of crucible fragment OTG2. The size of all the 2D maps is 3.2×3.2 cm^2.

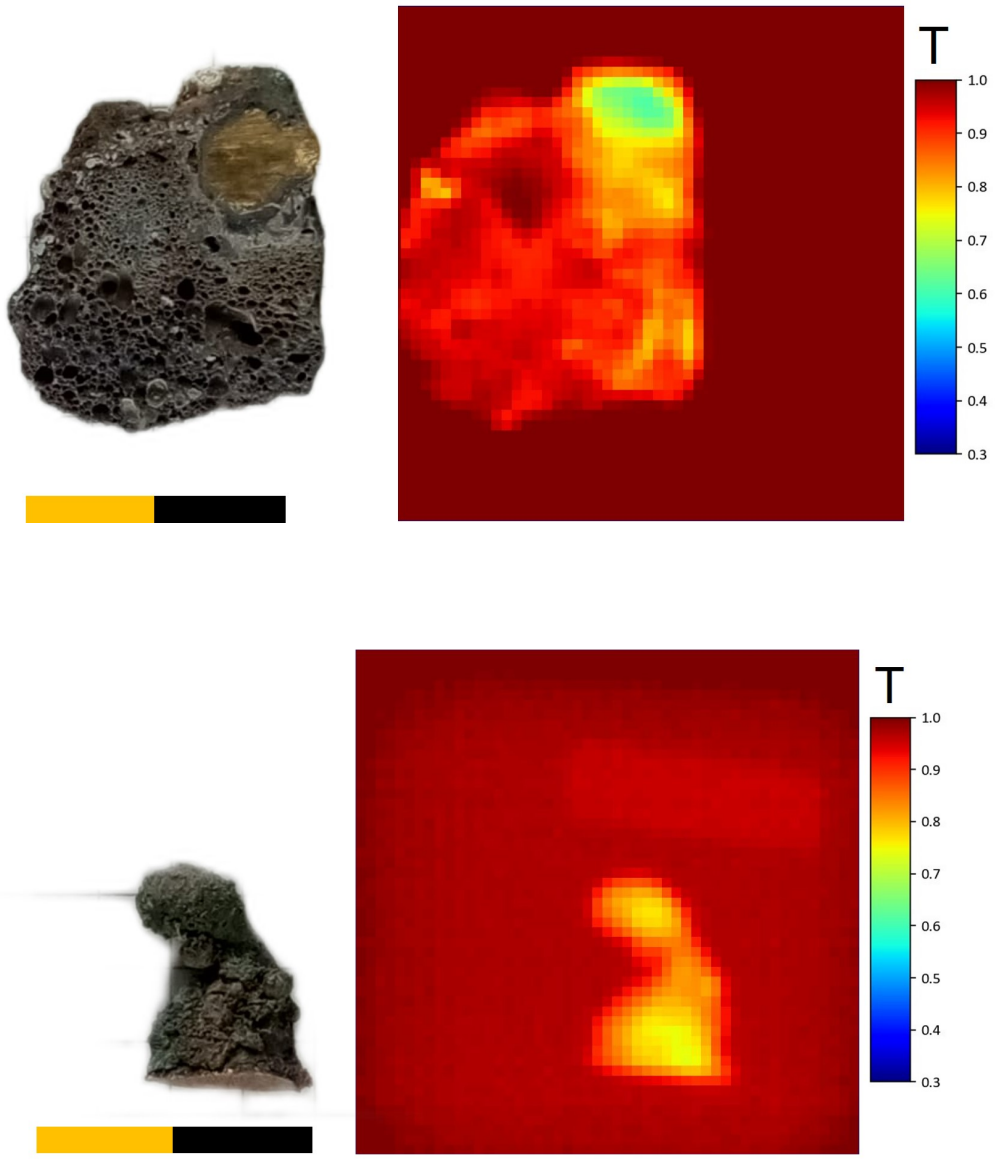

Fig. 6.17 Top: picture and transmission map of crucible fragment OT6_small. Bottom: picture and transmission map of crucible fragment OTG5. The size of all the 2D maps is 3.2×3.2 cm^2.

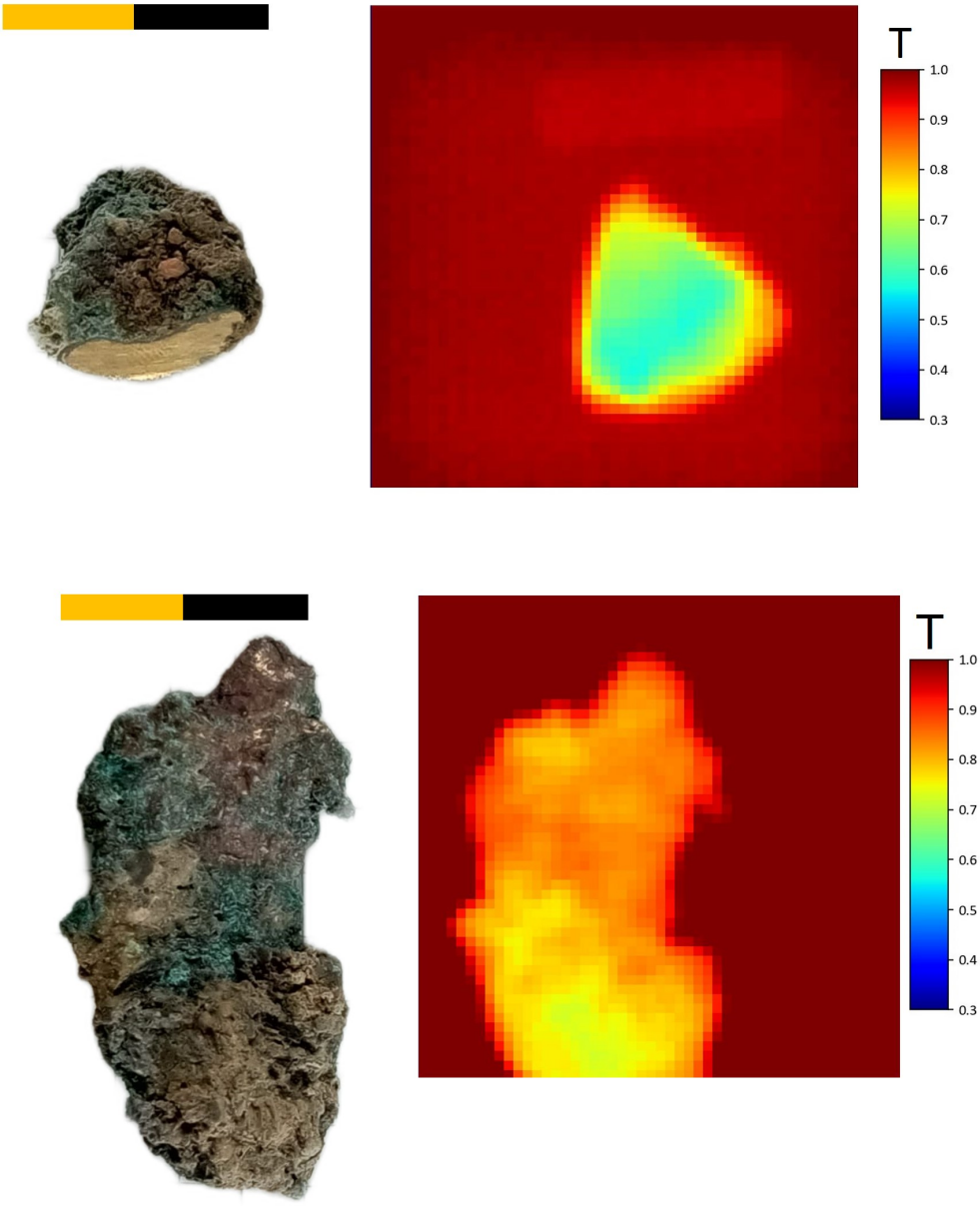

Fig. 6.18 Top: picture and transmission map of crucible fragment OT23. Bottom: picture and transmission map of crucible fragment OT21. The size of all the 2D maps is 3.2×3.2 cm^2.

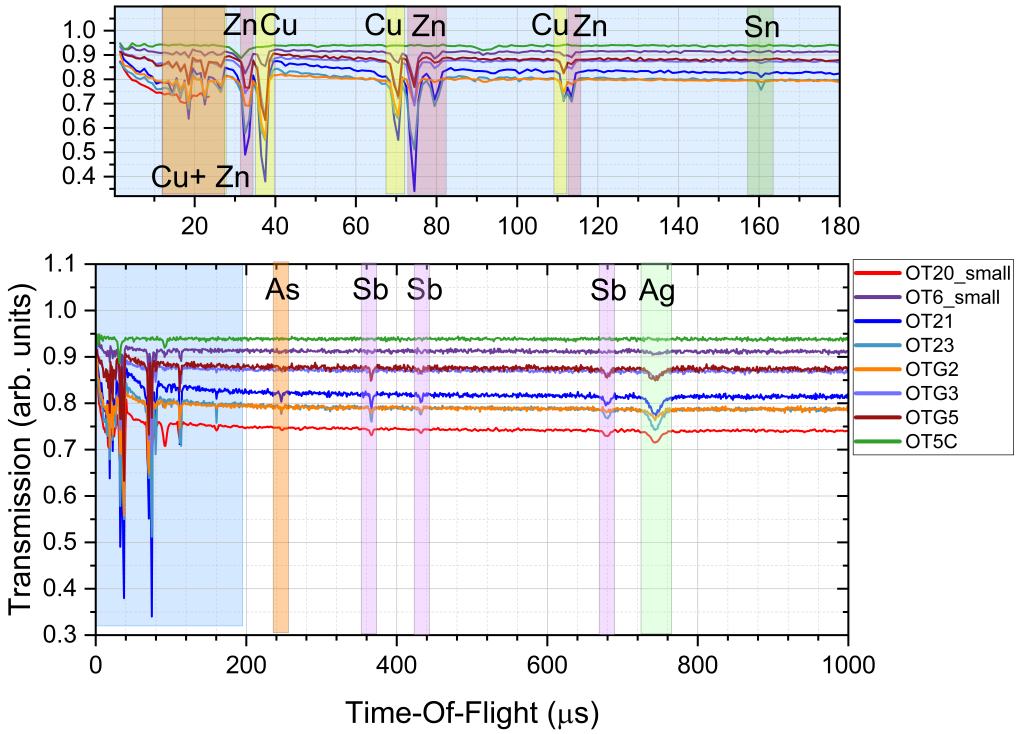

Fig. 6.19 NRTI spectra of the 8 crucible fragments shown in Fig.6.15-6.18. The qualitative composition of these fragments has been identified by indexing the resonance positions and compared them with (n,tot) cross-section libraries [20].

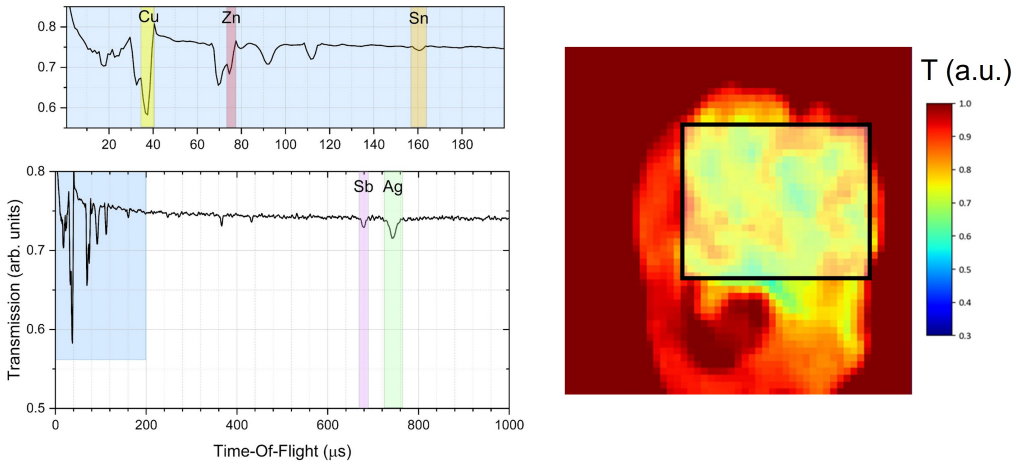

Fig. 6.20 OT20_small transmission spectrum of the ROI indicated in the neutron radiography displayed on the right. Resonances related to Cu, Zn, Sn, Sb and Ag used for elemental imaging are highlighted. The size of the 2D map is 3.2×3.2 cm^2.

depositions spread on the crucible fragment surfaces. PIXE analysis is limited to spot and surface measurements intrinsically due to the employed particle beam. Therefore, unless the

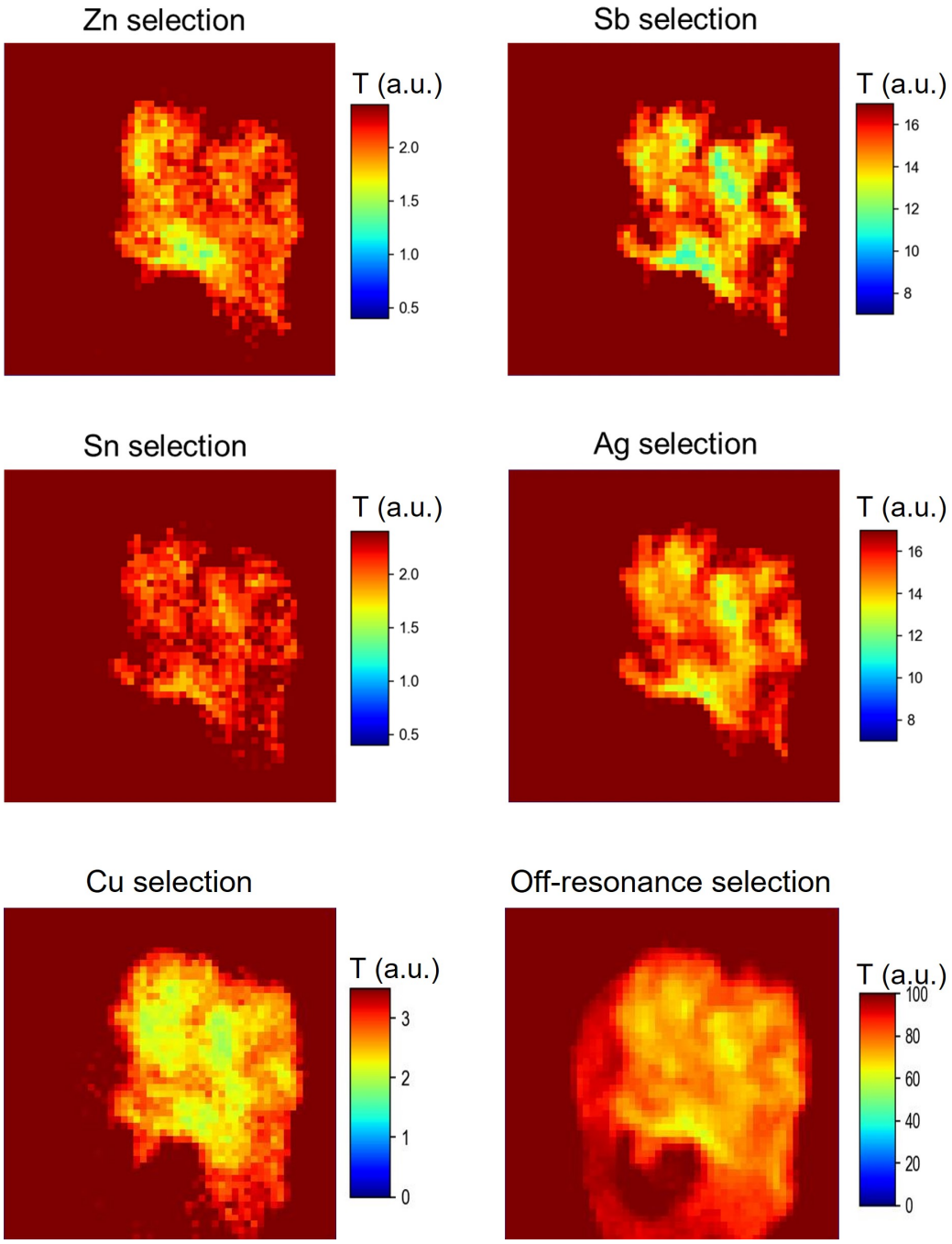

Fig. 6.21 NRTI maps after the selection of Zn, Sb, Sn, Cu and Ag resonances and of a TOF region without any absorption resonance. It is worth specifying that the 2D maps are not normalised by the sample thickness. The size of all the 2D maps is 3.2×3.2 cm^2.

metallic inclusions are on the surface, superficial techniques such as PIXE are not able to detect and localise the presence of these structures. This feature can be observed from the comparison between PIXE and NRTI (and NRCA) results. Spot measurements conducted

on sample OT20_small with the AGLAE proton beam reveal the presence of mainly copper and bronze drops, whilst Neutron Resonance Absorption analyses extend the gauge volume to the entire sample size giving clear indications of the presence of zinc, related to brass inclusions, and other metallic elements such as silver and antimony. NRTI (and NRCA) are more sensitive to even a few ppm of silver and antimony. In general, for all the crucible fragments the NRTI qualitative results are in agreement with the quantitative composition obtained through PIXE measurements.

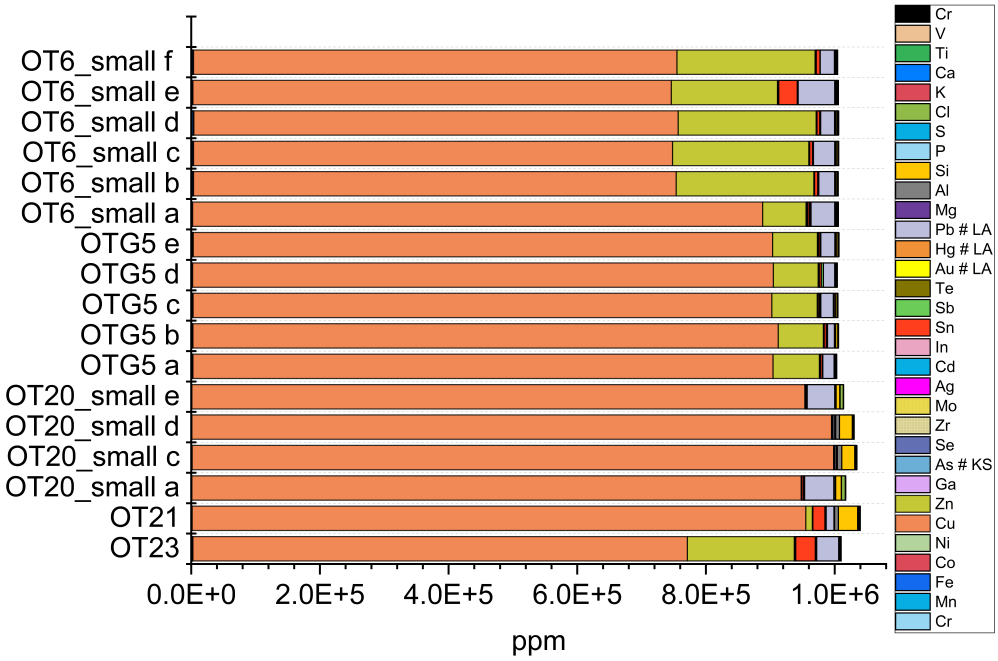

Fig. 6.22 PIXE quantitative analysis performed on metallic depositions identified on the crucible fragment surfaces.

A similar technique to NRTI based on neutron resonant absorption is NRCA (discussed in Chapter 4), which has been applied to the crucible fragments previously to the NRTI measurements. Through NRCA the qualitative bulk elemental composition averaged on the fragments volume has been obtained and can be directly compared to the NRTI results as NRCA is well-optimized and routinely applied at INES.

The NRCA spectra of the samples are shown in Fig.6.23, qualitatively confirming the elemental identification accomplished through NRTI.

To conclude this section, regardless of the limited potentiality of this kind of archaeological artefacts for elemental imaging conducted with NRTI, the achieved results demonstrate

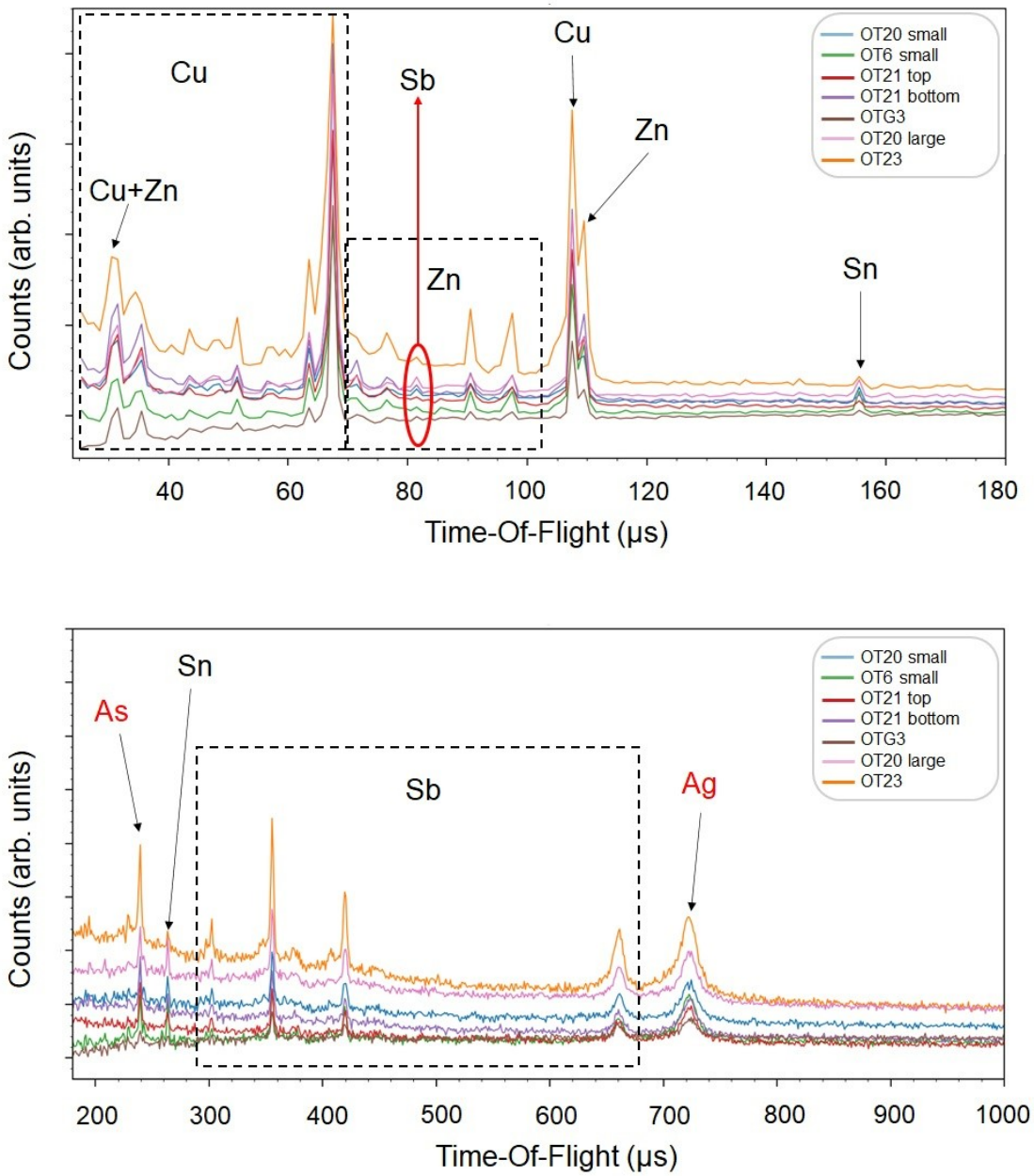

Fig. 6.23 NRCA spectra of the 8 crucible fragments investigated with NRTI and PIXE. Main peaks related to copper, zinc, tin, arsenic, antimony, and silver are highlighted. Peaks assignment is made in comparison with (n,gamma) cross-section libraries [20]

the profitability of NRTI to perform non-destructive imaging combined with elemental analyses for investigating the composition of inhomogeneous samples.

6.4.2 Isotopic imaging

The feasibility of NRTI to carry out isotopic imaging has been explored. Certified silver and lead samples with different isotopic compositions have been measured within the NRTI configuration. Details of the isotopic composition of the samples are listed in Tables 6.2 and 6.3.

Table 6.2 Composition details of silver samples enriched with Ag isotopes.

Isotope	**Enrichment (%)**	
	Ag-107	**Ag-109**
Ag-109	0.3	99.70 ± 0.1
Ag-107	99.5 ± 0.1	0.3

Table 6.3 Composition details of lead samples enriched with Pb isotopes.

Isotope	**Enrichment (%)**			
	Pb-204	**Pb-206**	**Pb-207**	**Pb-208**
Pb-204	99.94	0.04	0.01	0.01
Pb-206	< 0.02	95.90 ± 0.10	2.76	1.34
Pb-207	0.01	2.2	92.2 ± 0.2	5.59
Pb-208	< 0.01	0.4	0.7	98.90 ± 0.1

As shown in Fig.6.24 and Fig.6.25, the selection of the resonance related to the isotope Ag-107 allowed to highlight the sample mainly composed of this isotope with respect to the others. In a similar way, the selection of Ag-109 resonance accentuates the transmission signal of the sample enriched with 99.70% of this isotope.

An attempt to conduct an analogous test was made with samples made of different ratios of lead isotopes (Fig.6.26). In this case, however, the measurements were not long enough (totalling 3200 μAmps per sample) to obtain a good signal-to-noise statistic for discriminating between resonances of the different lead isotopes. Only the lead sample enriched with >90% of Pb-204 shows resonance dips related to this isotope. In general, the statistic highly depends on the (n,tot) cross-section intensity of the isotope.

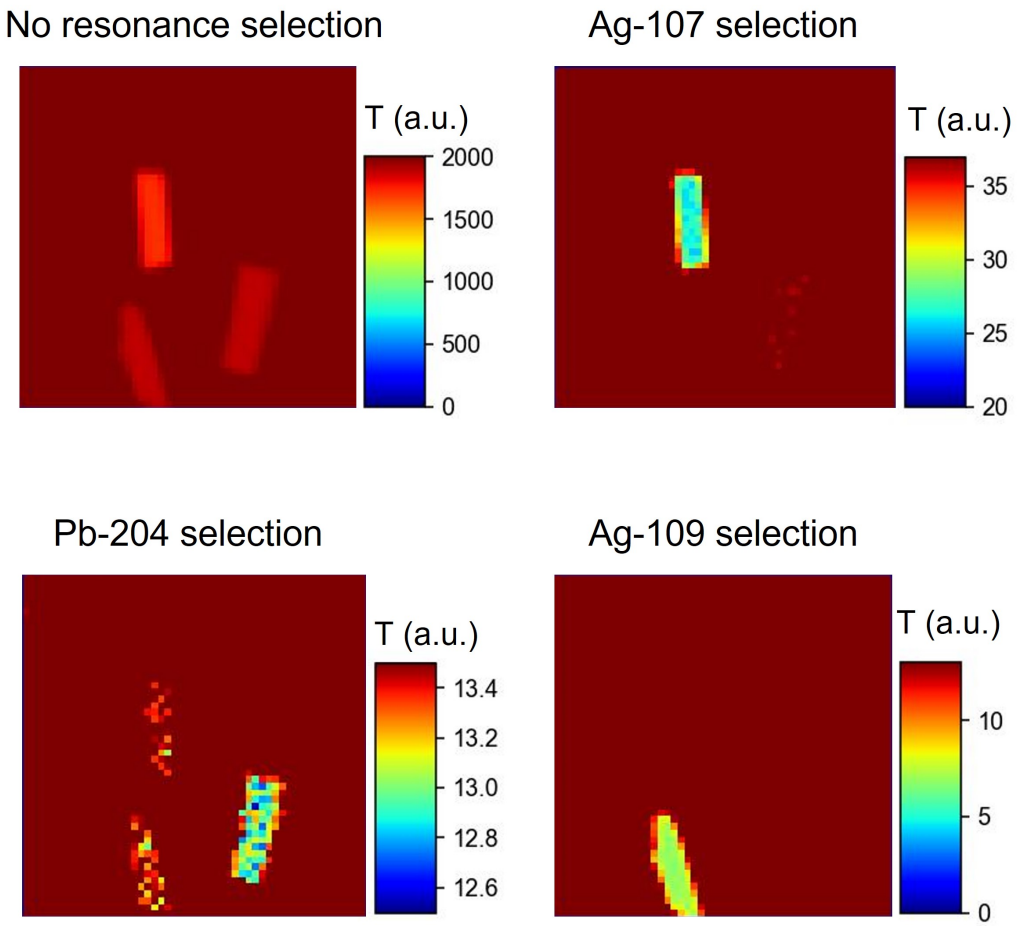

Fig. 6.24 NRTI maps after the resonance selection of isotopes Ag-107, Ag-109 and Pb-204. It is worth specifying that the 2D maps are not normalised by the sample thickness. The size of all the 2D maps is 3.2×3.2 cm^2.

Although this preliminary result, NRTI shows interesting potentiality for studies of metallic archaeological artefacts containing lead. In fact, in this kind of alloy, the distribution of lead is highly inhomogeneous being present as segregation areas separated from the alloy. By improving the detection capability of lead peaks at low TOF, NRTI may be one of the few bulk imaging techniques able to identify and localise the distribution of Pb segregation areas in an archaeological object volume. In this way, the lead segregation can be mapped with an adequate spatial resolution and this information could integrate (semi-)quantitative compositional study performed thought TOF-ND [26] and/or NRCA.

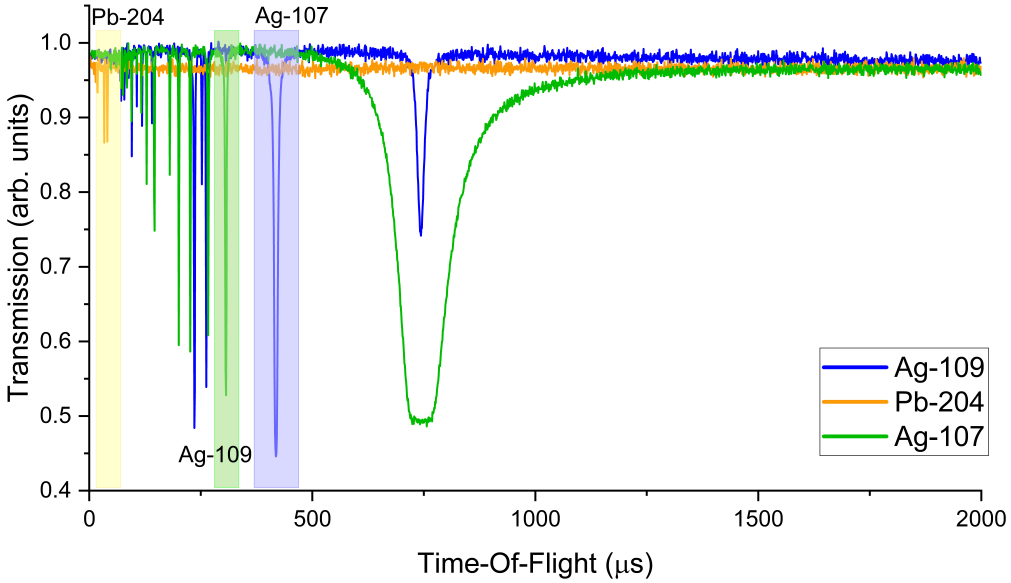

Fig. 6.25 Transmission spectra of the samples enriched with isotopes Ag-107, Ag-109 and Pb-204 as indicated in Tables 7.2 and 7.3. Resonances related to Ag-107, Ag-109 and Pb-204 used for elemental imaging are highlighted.

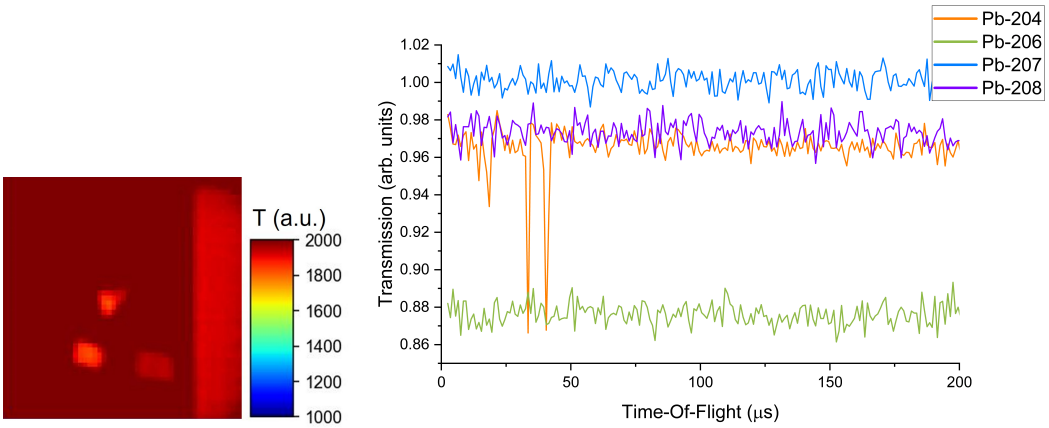

Fig. 6.26 NRTI radiography and transmission spectra of samples enriched with different lead isotopes as listed in Tables 7.2 and 7.3. The size of the 2D map is 3.2×3.2 cm^2. The sample enriched with Pb-204 is shown in Fig.6.24. The transmission spectra show resonance dips only for the sample enriched with Pb-204, whilst for the other enrichment the statistic is too low.

6.5 Towards a quantitative analysis

To calibrate the NRTI technique for quantitative elemental analysis of metallic samples of interest in the field of Cultural Heritage, several certified standard materials were measured during 2019 and 2021, the characteristics of which are listed in Table 6.4. These materials are needed as the quantitative calibration has to rely on precise values of sample density and thickness to minimize the sources of uncertainty. Within an ISIS Placement project, a Python-based database of neutron (n,γ) and (n,tot) cross-sections is being developed, providing useful interactive tools with the possibility to also upload experimental TOF spectra (such as those from NRTI measurements) for indexing resonance peak/dip positions and quantifying the elemental composition [21]. The approach followed for a first quantitative calibration

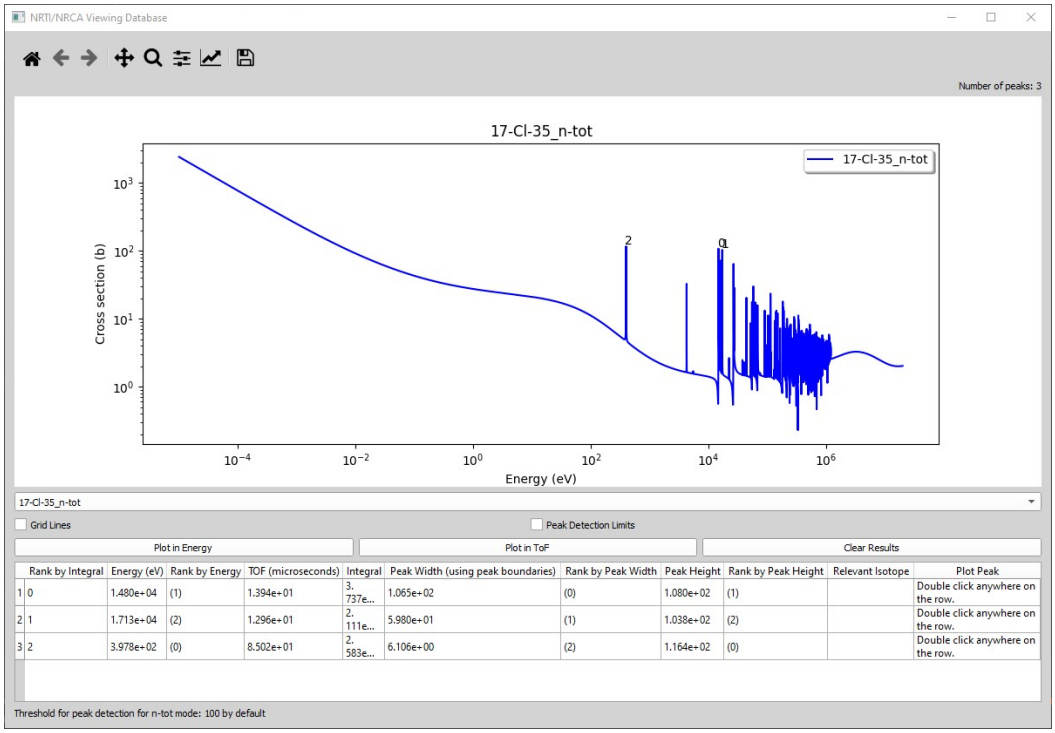

	Rank by Integral	Energy (eV)	Rank by Energy	TOF (microseconds)	Integral	Peak Width (using peak boundaries)	Rank by Peak Width	Peak Height	Rank by Peak Height	Relevant Isotope	Plot Peak
1	0	1.480e+04	(1)	1.394e+01	3.737e...	1.065e+02	(0)	1.080e+02	(1)		Double click anywhere on the row.
2	1	1.713e+04	(2)	1.296e+01	2.111e...	5.980e+01	(1)	1.038e+02	(2)		Double click anywhere on the row.
3	2	3.978e+02	(0)	8.502e+01	2.583e...	6.106e+00	(2)	1.164e+02	(0)		Double click anywhere on the row.

Fig. 6.27 GUI interface of the neutron resonance absorption database that is being developed within the ISIS Placement project [21].

test is based on the analysis of the (unsaturated) resonance dips for samples having the same composition and different thicknesses and for samples with the same thickness but variable compositions. In this way, the effects of density and thickness on the characteristics of resonance dips such as position, area and width are investigated. An example is reported in Fig.6.28, where the main antimony resonance at 679.5 μs (6.24 eV) of samples of equal thickness but variable Cu/Sb content is shown. These slab of copper-antimony has the same

Table 6.4 Details of standard materials measured with NRTI for calibration purposes.

Sample	**Shape**	**Thickness (mm)**	**Composition**
gold	foils	0.02	99.99% Au natural
gold letters	wire	0.2	99.99% Au natural
brass	foils	2.0	Cu63/Zn37
brass	foils	0.1	Cu63/Zn37
silver letters	wire	1.0	99.99% Ag natural
silver	foils	0.25	99.95% Ag natural
SrTiO3	powder	-	98.0% purity
indium	foils	0.2	99.99% In natural
indium letters	wire	1.0	99.99% In natural
havar	foils	0.5	Co42.5/Cr20/Ni13/Fe/W/Mo/Mn
phosphor bronze	sheets	2.0	Cu94/Sn6
SnPbSb	foils	0.1	Sn60/Pb39/Sb1
Stainless Steel AISI 310	foils	2.0	Fe55/Cr25/Ni20
iron	foils	0.25	99.50% Fe natural
zinc	foils	2.0	99.95% Zn natural
niobium	disks	0.25	99.90% Nb natural
tin	foils	1.0	98.8% Sn natural
Sb704	slab	1000	Cu90/Sb10
Sb703	slab	1000	Cu96/Sb4
Sb700	slab	1000	Cu99/Sb1
Sb697	slab	1000	Cu96/Sb1/As3

thickness and variable Sb content (see Table 6.4 for dimensions and composition of samples Sb679, Sb700, Sb703 and Sb704).

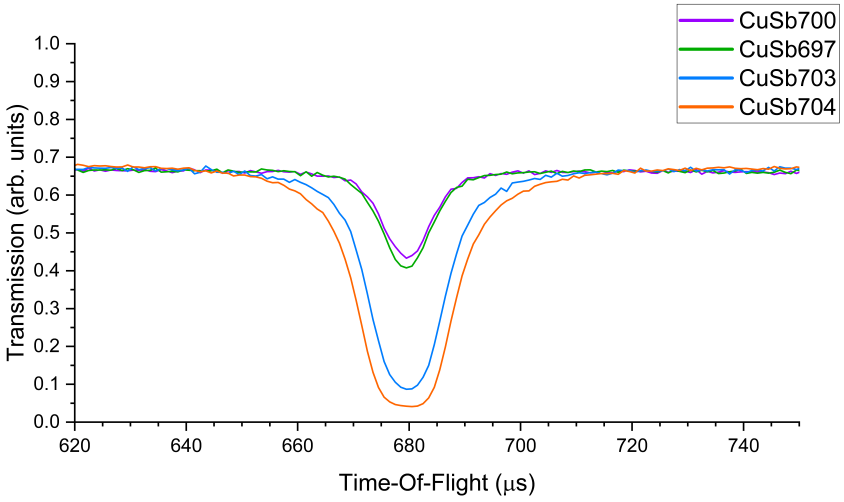

Fig. 6.28 Main resonance of antimony contained in samples Sb697, Sb700, Sb703 and Sb704.

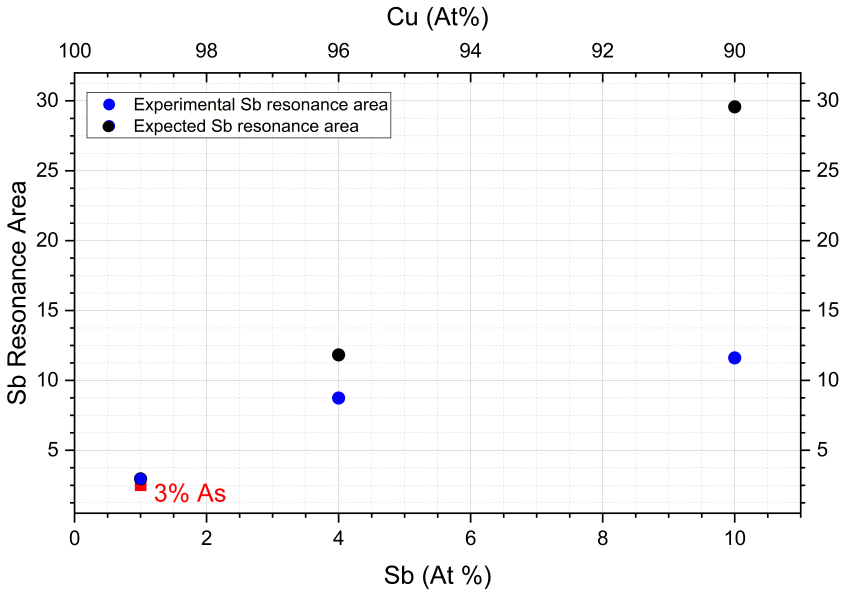

Fig. 6.29 Area under the Sb resonance shown in Fig.6.28 as a function of the Cu and Sb content in samples Sb697, Sb700, Sb703 and Sb704. The red point indicates the resonance area of sample Sb697 containing 3% of As. Blu points referred to areas evaluated from experimental data, whilst black points to the expected resonance area as a linear function of the Sb content.

In principle, the area within the resonance dip of antimony should be proportional to the Sb content, unless the resonance is saturated. However, this assumption is not yet true (see

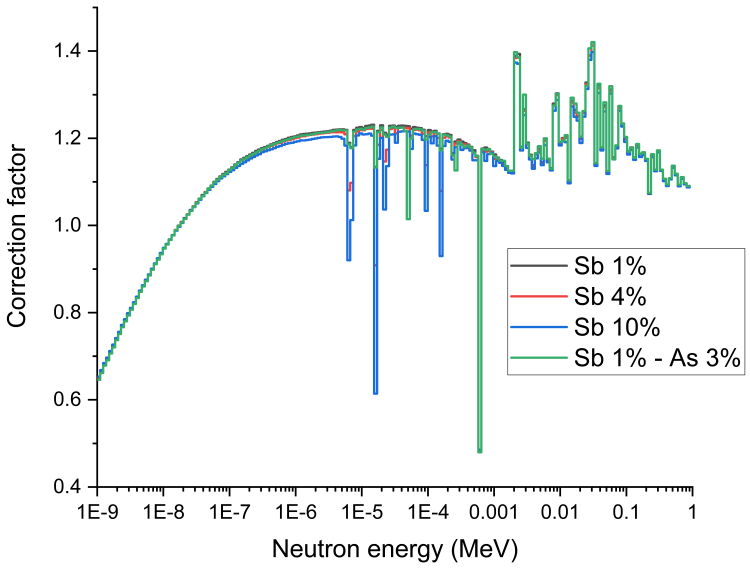

Fig. 6.30 Outcome of MCNP simulations performed to investigate the beam modification after passing through the Sb/Cu samples. Due to the presence of Sb, characterised by strong absorption resonances, the mean neutron flux in the samples has to be corrected by the factor shown in the plot, evaluated as the ratio between the simulated transmitted neutron beam and the incident neutron beam.

Fig.6.29): essentially, neutron beam modification results in major deviations from the ideal in a similar way to the beam hardening effect that can be encountered for X-rays.

Beam hardening was initially discovered and studied to explain X-ray attenuation through matter in tomography experiments [22]. Similarly to X-ray, a polychromatic neutron beam and its mean energy can be modified when it is transmitted through strong absorbing matter in some appropriate conditions and circumstances. The low-energy neutrons are more likely removed from the beam in the first thickness intervals in the absorber material, as the linear attenuation coefficient generally decreases with neutron energy increase. This effect results in a shift of the mean neutron beam energy to high energy and consequently to the rise of neutron transmission inside the sample.

As a result, the transmission or attenuation of neutrons along the different layers of the sample is not constant: the first thickness intervals attenuate neutrons differently to the rest of the material [23]. A second reason for beam hardening is the inelastic neutron collisions and multiple-scattering events within the material, which also causes the mean energy shift.

Furthermore, in presence of very intense resonances and thick samples, neutrons with the same energies of these resonances can be completely absorbed and therefore there is a

removal of specific energies in the neutron spectrum inside the sample with respect to the initial flux incident on the first thickness of the sample.

The obtained transmission spectra of copper-antimony samples are used to demonstrate the effect of the beam modification on resonances content and therefore a specific correction has to be made in order to assess the correct quantitative calibration for NRTI analysis. Monte Carlo N-Particle Transport code (MCNP) [24, 25] simulations have been performed to analyse the mean transmitted neutron beam through these Cu/Sb samples, allowing getting a correction factor (Fig.6.30) for the resonance areas in relation to the material composition.

Samples with complex geometric shapes need further imaging studies with a higher spatial resolution to reconstruct their volume and inner structures in order to define accurate simulations for beam hardening correction. Moreover, objects with unknown composition required a bayesian approach for evaluating this correction. Future studies on the quantitative calibration of the NRTI technique will focus on the definition of a bayesian protocol to extend the quantitative analysis to real archaeological objects.

References

[1] Perelli Cippo, E. et al. (2011) “Imaging of Cultural Heritage Objects Using Neutron Resonances”, *Journal of Analytical Atomic Spectrometry*, 26(5), pp. 992–999.

[2] https://www.bbtech.co.jp/en/products/ngem/

[3] Sauli, F. (2016) "The gas electron multiplier (GEM): Operating principles and applications", *Nucl. Inst. And Meth. In Physics Research A*, 805, pp. 2-24.

[4] Škoro, G., Lilley, S. and Bewley, R. (2018) “Neutronics Analysis of Target, Moderators and Reflector Design for the ISIS TS-1 Project”, *Physica B: Physics of Condensed Matter*, 551, pp. 381–385. doi: 10.1016/j.physb.2017.12.060.

[5] Schillebeeckx, P., Postma, H. (2022). "Neutron Resonance Analysis Methods for Archaeological and Cultural Heritage Applications". In: D'Amico, S., Venuti, V. (eds) *Handbook of Cultural Heritage Analysis*. Springer, Cham. doi: 10.1007/978-3-030-60016-7_7.

[6] Mantid (2013) "Manipulation and Analysis Toolkit for Instrument Data", *Mantid Project*. http://dx.doi.org/10.5286/SOFTWARE/MANTID.

[7] Arnold, O. et al. (2014) "Mantid-Data Analysis and Visualization Package for Neutron Scattering and mu-SR Experiments", *Nuclear Instruments and Methods in Physics Research Section A*, 764, pp. 156-166. doi: 10.1016/j.nima.2014.07.029.

[8] Schillebeeckx, P. et al (2012) "Determination of Resonance Parameters and their Covariances from Neutron Induced Reaction Cross Section Data", *Nucl Data Sheets*, 113:3054.

[9] Firk, F,W,K., Lynn, J.E. and Moxon, M.C. (1963) “Analysis and Interpretation of the Neutron Cross Section of Vanadium below 25 Kev”, *Proceedings of the Physical Society*, 82(4), pp. 477–487. doi:10.1088/0370-1328/82/4/301.

[10] Syme, D. B. (1982) “The Black and White Filter Method for Background Determination in Neutron Time-Of-Flight Spectrometry,” *Nuclear Instruments and Methods In Physics Research*, 198(2), pp. 357–364. doi: 10.1016/0167-5087(82)90276-9.

[11] Ceresa Mori, A. and Cucini, C. (2012) "Un'officina di bronzista e la produzione di ottone e di specchi a Mediolanum nel I-II sec. d.C.", in Cucini C (ed) *Acta mineraria et Metallurgica. Studi in onore di Marco Tizzoni, Notizie Archeologiche Bergomensi*, 20.

[12] Bayley, J. (1998) "The production of brass in Antiquity with particular reference to Roman Britain". In *Craddock PT (ed) 2000 Years of Zinc and Brass*, 7-23, BMOP 50, London.

[13] Bayley J et al, (2014), "A Saxon brass bar ingot cache from Kingsway, London". In Cotton J, Hall J, Keily J, Sherris R, and Stephenson R (eds), *Hidden Histories and Records of Antiquity. Essays on Saxon and Medieval London for John Clark, Curator Emeritus, Museum of London*. London: LAMAS, 121-28

[14] Martinón-Torres, M. and Rehren, T. (2002) "Agricola and Zwickau: theory and practice of Renaissance brass production in SE Germany", *Historical Metallurgy*, 36.

[15] Merkel, S. (2016) "Carolingian and Ottonian Brass Production in Westphalia. Evidence from the Crucibles and Slag of Dortmund and Soest", *Metalla*, 22(1), pp. 21–39.

[16] http://www.c2rmf.fr/. Accessed 6th Apr 2023.

[17] Calligaro, T. et al. (2000) "Development of an External Beam Nuclear Microprobe on the Aglae Facility of the Louvre Museum", *Nuclear Inst. and Methods in Physics Research, B*, 161, pp. 328–333. doi: 10.1016/S0168-583X(99)00899-X.

[18] Dran, J.C. et al. (2004) "Ion Beam Analysis of Art Works: 14 Years of Use in the Louvre", *Nuclear Inst. and Methods in Physics Research, B*, 219, pp. 7–15. doi: 10.1016/j.nimb.2004.01.019.

[19] Pichon, L. et al. (2015) "Programs for Visualization, Handling and Quantification of Pixe Maps at the Aglae Facility", *Nuclear Inst. and Methods in Physics Research, B*, 363, pp. 48–54. doi: 10.1016/j.nimb.2015.08.086.

[20] Evaluated nuclear data file: https://www-nds.iaea.org/exfor/endf.html.

[21] Patel, R. (2022/2023) source: https://github.com/scipatel/NRTI-NRCA-Viewing-Database.

[22] Brooks, R.A., Di. Chiro, G. (1976) "Beam Hardening in X-ray reconstructive tomography", *J. Phys. Med. Biol*. 21, pp. 390–398.

[23] Basturk, M. (2003) *Material Inspections With Low Energy Neutrons and 3D Image Reconstruction*, Thesis Dissertation, TU-Vienna, Austria, Nr. 9800103.

[24] Werner, C.J. et al. (2018) *MCNP6.2 Release Notes*, Los Alamos National Laboratory, report LA-UR-18-20808

[25] Werner, C.J. (2017) *MCNP Users Manual - Code Version 6.2*, Los Alamos National Laboratory, report LA-UR-17-29981.

[26] Cattaneo, R. at al. (2011) "Integrated X-ray and Neutron Based Analysis of Bronze Artefacts from the Ligurian Settlement of Guardamonte-Monte Vallassa", *Journal of Analytical Atomic Spectrometry*, 26(5), pp. 1024-1029. doi:10.1039/coja00259c.

Chapter 7

Conclusions

The work presented in this thesis aimed at providing new advances in the neutron imaging field. The PhD research has been carried out in two different neutron sources with the following purposes: the first is to implement a new imaging facility at a steady-state neutron source (the Triga Mark II reactor in Pavia), while the second is to further develop a time-of-flight imaging technique at a spallation source (the ISIS Neutron and Muon source) providing pulsed neutron beams.

The CHNet-NICHE thermal neutron imaging station has been successfully installed and it is currently fully operative at the LENA research reactor of the University of Pavia. I performed Monte Carlo simulations through the MCNP software to investigate the main characteristics of the B Channel. The simulations indicated good performances of the thermal Channel B in terms of the thermal-to-fast neutrons ratio and the thermalising effect of the sapphire filter present in the collimator. Different detection positions in the NICHE experimental hutch have been studied with MCNP simulations to characterise the neutron flux components among the main energy ranges. Due to the shape and size of the irradiation cabin, the effective distance between the shutter and the scintillator can range between 1100 and 1920 mm, determining a minimum and maximum nominal value for the resolution power L/D of the imaging system of 110 and 190 respectively with the pinhole diameter of 10 mm.

Two extreme distances can be selected for NT experiments depending on the imaging conditions needed: with a pinhole-to-sample distance of 140 cm the highest thermal-to-fast ratio is achieved, supported by MCNP simulation results, whilst the highest spatial resolution (125 m) has been experimentally determined at a pinhole-to-sample distance of 190 cm. The commissioning outcome shows good capabilities to perform neutron radiography and neutron tomography with a maximum field-of-view of 95 mm of diameter. With the sample positioning remote system, multiple radiographs can be made without introducing artefacts

or discontinuities to measure an object larger than the field-of-view and thus optimising the limited beam operation time of the facility.

With the NICHE neutron imaging station, case studies tailored to Cultural Heritage can be conducted, and morphological and microstructural information can be acquired that cannot be obtained with more conventional imaging methods.

At the ISIS Neutron and Muon Source, I deepened the extension of a well-established neutron time-of-flight transmission technique to imaging analysis, demonstrating the potentiality of epithermal neutrons that are not yet widely used in neutron imaging. Neutron Resonance Transmission Imaging (NRTI) is based on the epithermal portion of the white neutron beam and on a time and spatially-resolved neutron detector at the INES beamline. I addressed the definition of a reliable protocol for NRTI data normalisation on the basis of established procedures employed in neutron tomography and on background characterisation methods related to resonant absorption mechanisms available in the literature. For this purpose, I have developed ad-hoc Python codes which can be integrated into the Mantid platform, usually used for the analysis of data acquired in major neutron facilities such as ISIS. Experimental NRTI measurements on reference standard materials and archaeological artefacts allowed to demonstrate the striking performances of NRTI for elemental and isotopic imaging: the "resonance-selection" procedure performed on the un-integrated transmission spectrum, stored in each detector pixel, allowed to enhance the transmission contrast of specific elements or isotopes in the 2D map for better visualise their spatial distribution. This is a mechanism which facilitates the distinguishment between elements with similar neutron attenuation coefficients that could not be better discriminated by standard neutron tomography.

I finally defined the first steps for adding a quantitative analysis of sample compositions with the imaging inspections for the NRTI technique. An attempt of a quantitative calibration has been conducted on reference cooper-antimony samples, endorsed by MCNP simulations to focus on the beam hardening effect affecting the neutron beam passing through thick and strong absorbing materials and distorting the true information contained in the resonance dips.

Further studies will be performed in the future to better advance the quantitative calibration of NRTI, focusing on copper-based alloys which represent the most-common compositions of archaeological artefacts for which the use of neutron imaging is more convenient.

Appendix A

Published papers

Published papers related to parallel projects conducted during the PhD research are attached on the following pages and listed below:

1. **Marcucci, G.**, Scherillo, A., Cazzaniga, C., Clemenza, M., Di Martino, D. (2020). "Neutron-based techniques applied for non-destructive quantitative characterisation of ancient mosaic tesserae". In *2020 IMEKO TC-4 International Conference on Metrology for Archaeology and Cultural Heritage. International Measurement Confederation (IMEKO)*.

2. **Marcucci, G.**, Scherillo, A., Cazzaniga, C., Lemasson, Q., Lorenzi, R., Clemenza, M., et al. (2021) "Historical glass mosaic tesserae: a multi-analytical approach for their characterization", *The European Physical Journal Plus*, 136(7), doi:10.1140/epjp/s13360-021-01696-20.

3. Di Martino, D., Gagetti, E., **Marcucci, G.**, Lemasson, Q., Riccardi, M.P. (2022) "Glass-Gems from the National Archaeological Museum in Aquileia: A PIXE/PIGE Compositional Study," *Journal of Physics: Conference Series*, 2204(1). doi: 10.1088/1742-6596/2204/1/012074.

4. Rossini, R., Di Martino, D., Agoro, T., Cataldo, M., Gorini, G., Hillier, A. **Marcucci, G.**, et al. (2022) "A new multidisciplinary non-destructive protocol for the analysis of stony meteorites: gamma spectroscopy, neutron and muon techniques supported by Raman microscopy and SEM-EDS". *Journal of Analytical Atomic Spectrometry*. doi:10.1039/d2ja00263a.

5. **Marcucci, G.** et al. (2023) "Time-Of-Flight Neutron Diffraction applied to the crystalline phases identification in historical mosaic glasses", *Physics and Chemistry of Glasses: European Journal of Glass Science and Technology Part B*.

6. Gelli, N., Giuntini, L., Cantini, F., Sans-Planell, O., Magalini, M. Manetti, M., Sodi, L., Massi, M., Castelli, L., Czelusniak, C., Taccetti, F., Bella, T.E., **Marcucci, G.** et al. (2023) "The New Infn-Chnet Neutron Imaging Facility," *Nuclear Inst. and Methods in Physics Research A*, 1051. doi: 10.1016/j.nima.2023.168189.

A.1 Paper I

2020 IMEKO TC-4 International Conference on
Metrology for Archaeology and Cultural Heritage
Trento, Italy, October 22-24, 2020

Neutron-based techniques applied for non-destructive quantitative characterisation of ancient mosaic tesserae

Giulia Marcucci[1], Antonella Scherillo[2], Carlo Cazzaniga[3], Massimiliano Clemenza[4], Daniela Di Martino[5]

[1] University of Milano Bicocca and INFN - Physics Department, Piazza della Scienza 3 Milan (Italy), g.marcucci1@campus.unimib.it
[2] ISIS Neutron and Muon Source, Didcot (UK), antonella.scherillo@stfc.ac.uk
[3] ISIS Neutron and Muon Source, Didcot (UK), carlo.cazzaniga@stfc.ac.uk
[4] University of Milano Bicocca and INFN - Physics Department, Piazza della Scienza 3 Milan (Italy), massimiliano.clemenza@unimib.it
[5] University of Milano Bicocca and INFN - Physics Department, Piazza della Scienza 3 Milan (Italy), daniela.dimartino@unimib.it

***Abstract* – The conservation and preservation of cultural heritage need by now non-destructive analytical methods for the characterisation of materials, detection of degradations and authenticity assessment.**
The interaction properties of neutrons with matter make neutron-based techniques suitable for non-destructive studies of ancient artefacts since they cannot be replaced. A quantitative bulk characterisation of the chemical composition of ancient mosaic tesserae, dating from 2nd to the 11th century AD and coming from different geographical areas (Greece, Italy, and Syria) has been conducted through Neutron Resonance Capture Analysis (NRCA) combined with Neutron Activation Analysis (NAA). The NAA analysis returns the bulk composition in terms of major, minor and trace elements, while NRCA reveals the presence of particular elements, like antimony, in agreement with NAA results.

I. INTRODUCTION

Several analytical techniques are actually employed in the field of Cultural Heritage to characterize constituent materials, production methodologies, dating and provenance of the artefacts. Non-destructive analyses are generally requested.

Concerning the investigation of objects elemental composition, Laser Ablation-Inductively Coupled Plasma-Mass Spectrometry (LA-ICP-MS) and Electron Probe Microanalysis (EPMA) techniques are often performed but they are invasive. Also, X-Ray Fluorescence (XRF) is widely used for non-destructive investigation but sample preparation can be requested, and only small superficial areas are analysed. Mosaic tesserae are inhomogeneous objects, thus XRF cannot return a complete bulk characterization of the mosaic samples.

The novelty of the present study is the application of non-destructive neutron-based technique to obtain a quantitative description of the bulk composition of the mosaic tesserae. Neutron beams are a unique probe for non-destructive investigations in materials science. Neutrons sense the differences between isotopes of the same element and provide exceptional features in the penetration of many materials, making them adapt for bulk studies, while other probes can in general only cross surface layers. In contrast to other forms of radiation, they are also highly sensitive to some light elements such as hydrogen and sodium. Neutron-based techniques do not require any particular sample preparation.

We performed neutron-based analysis at the ISIS Neutron and Muon Source (UK) [1].

Elemental analyses have been conducted by Neutron Activation Analysis (NAA) [2] [3] and Neutron Resonance Capture Analysis (NRCA) [2] [4] [5].

Glass mosaic tesserae are heterogeneous materials composed of vitreous matrix and crystalline phases and produced from selected raw materials (generally minerals) with various functions, such as colorants, decolourants and opacifiers. The glass colour is mainly due to the presence

of small quantities of transition metal ions such as iron, cobalt or manganese in particular oxidation states, which cause selective absorption of electromagnetic radiation in the visible band [6]. Coloured glass is originally translucent; the opacity can be obtained through the dispersion of crystalline phases or the presence of bubbles scattered in matrix [7]. Different compounds were used through the centuries to make glass opaque such as antimony- or tin-based opacifiers.

In the current study, a set of fourteen glass tesserae (Table 1) have been analysed. The mosaic tesserae have different dating and provenance and most of them are coloured and opaque. The sample set is composed by five Greek tesserae and two Syrian tesserae dating back to I-II century AD, and seven Italian tesserae from the San Vitale basil of Ravenna, dating back to the VI century AD.

Table 1. Description of the provenance and colour of the analysed glass tesserae samples.

Sample name	Sample image	Provenance	Colour
DEL1		Delos Monastery - Greece	Opaque blue
DEL2		Delos Monastery - Greece	Opaque red
DEL3	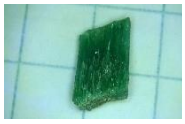	Delos Monastery - Greece	Opaque green
DEL4	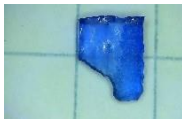	Delos Monastery - Greece	Transparent blue
DAFNI	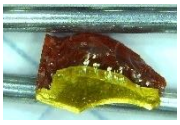	Dafni Monastery - Greece	Opaque red with a gold layer
SYG2		Syria	Opaque dark green
SYG3	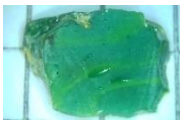	Syria	Opaque green
SVR24		Ravenna - Italy	Opaque pink
SVR25		Ravenna - Italy	Opaque green
SVR26		Ravenna - Italy	Opaque red
SVR27	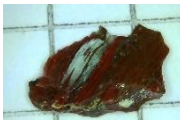	Ravenna - Italy	Opaque red/striped
SVP27		Ravenna - Italy	Opaque green
SVP46	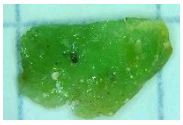	Ravenna - Italy	Opaque green
SVP57		Ravenna - Italy	Opaque black

II. NEUTRON-BASED TECHNIQUES AT INES

As mentioned in the previous section, all mosaic tesserae have been irradiated at the INES beamline at ISIS, which provide a thermal-epithermal neutron flux in the order of 10^6 n/s cm^2. During irradiation, NRCA spectra have been recorded through a Yttrium–Aluminum–Perovskite (YAP) scintillator performing Time-Of-Flight measurements [8]. For each sample, a qualitative analysis of NRCA spectra is conducted by indexing the observed resonances and comparing the centre of each to tabulated libraries [9]. Correction for background contributions has been applied to the experimental data by the subtraction of an “empty” measurement (i.e., without the samples in the INES

station).

After the neutron irradiation, the samples were placed in front of a High Purity Germanium (HPGe) detector to measure the induce radioactivity. Each irradiated sample has been placed at contact, at the centre of the HPGe active surface. The HPGe was housed in a lead shielding to limit the background and placed at ChipIr beamline of ISIS.

During irradiation, the beam status has been monitored by recording the current of the ISIS accelerator and by the INES beam monitor. This allows to calculate the net irradiation time and to correctly estimate the activation rate in case of beam OFF for some time intervals.

In most cases, especially when several isotopes with different half-lives were produced, the radioactivity of the samples has been measured a few times. The first measurements after irradiation have been needed to detect the γ-rays of isotopes with relatively short half-life, while measurements after the decay of short-lived isotopes have allowed higher sensitivity to isotopes with lower activity and longer decay time. For each sample, three measurements of few minutes have been performed, followed by several measurements of one hour. A prior calibration of the detector has been performed with radioactive sample of ^{137}Cs, ^{241}Am, ^{60}Co and ^{40}K.

During the neutron irradiation, the variation of the number of radioactive nuclei is given by:

$$dN = Rdt - \lambda N dt$$

where λ is the decay constant, N the number of radioactive nuclei and R is the activation rate:

$$R = \mathcal{N} \int \sigma(E)\varphi(E)dE$$

and $\sigma(E)$ the activation cross section, $\mathcal{N}$ the number of precursor isotope atoms and φ the neutron flux. The activity after irradiation (t_{irr}) is given by:

$$A(t) = R\left(1 - e^{-\lambda t_{irr}}\right)e^{-\lambda t}$$

Thus, the decays expected to occur during the measurement are:

$$n_{decay} = \frac{R}{\lambda}\left(1 - e^{-\lambda t_{irr}}\right)e^{-\lambda t_{wait}}\left(1 - e^{-\lambda t_{meas}}\right)$$

where t_{wait} is the delay between the end of the irradiation and the start of the measurement.

The net area under a specific peak gives the number of counts recorded by the detector, which is related to the number of decay events.

Finally, the number of precursor isotope atoms are derived as:

$$\mathcal{N} = \lambda n_{decay} \frac{1}{(1 - e^{-\lambda t_{irr}})e^{-\lambda t_{wait}}(1 - e^{-\lambda t_{meas}})} \frac{1}{\int \sigma(E)\varphi(E)dE}$$

III. RESULTS

Fig.1 shows the average quantitative elemental composition of the mosaic tesserae obtained by NAA. Since a thermal and epithermal neutron spectrum have been employed for the sample's irradiation, elements with a high cross-section in this energy range have been observed. Na, Mn, Sb, As, Au and Cu isotopes radioactivity have been detected by a HPGe detector and the related elemental concentrations have been evaluated.

Samples DEL4, DAFNI, SVP57 and SYG2 show the highest concentration of sodium (from 10% to 20%) while samples SVR25 and SYG3 only 2%. Sample SVP57 has the highest magnesium content among the other tesserae.

Sample	Weight (mg)	Irradiation time (h)	Na	Mn	As	Sb	Au	Cu
DEL1	24,98	22,2	7,1% ± 0,2%	0,196% ± 0,007%	n.d.	4,70% ± 0,01%	n.d.	n.d.
DEL2	29,25	5,3	7,4% ± 0,2%	0,093% ± 0,002%	0,015% ± 0,001%	0,057% ± 0,002%	n.d.	8,6% ± 0,5%
DEL3	6,91	4,8	7,2% ± 0,2%	0,128% ± 0,004%	n.d.	1,9% ± 0,1%	n.d.	n.d.
DEL4	5,71	17,0	10,3% ± 0,3%	0,014% ± 0,002%	0,870% ± 0,006%	0,42% ± 0,01%	n.d.	n.d.
DAFNI	3,56	12,6	11,1% ± 0,3%	0,35% ± 0,01%	n.d.	n.d.	0,032% ± 0,001%	n.d.
SVR24	4,01	6,9	7,4% ± 0,2%	0,086% ± 0,006%	0,38% ± 0,02%	8,3% ± 0,3%	0,007% ± 0,001%	n.d.
SVR25	22,5	21,0	2,4% ± 0,1%	0,025% ± 0,001%	0,052% ± 0,002%	0,65% ± 0,01%	n.d.	n.d.
SVR26	1,80	18,4	8,3% ± 0,2%	0,45% ± 0,02%	0,036% ± 0,003%	0,055% ± 0,004%	n.d.	n.d.
SVR27	7,25	5,3	9,2% ± 0,2%	0,240% ± 0,007%	0,032% ± 0,002%	0,074% ± 0,004%	n.d.	n.d.
SVP27	18,48	22,8	5,1% ± 0,1%	0,012% ± 0,001%	0,0032% ± 0,0004%	0,0031% ± 0,0003%	n.d.	n.d.
SVP46	1,63	17,0	9,4% ± 0,3%	0,133% ± 0,007%	n.d.	0,0450% ± 0,004%	n.d.	n.d.
SVP57	4,95	18,2	19,2% ± 0,5%	2,88% ± 0,06%	n.d.	4,1% ± 0,1%	n.d.	n.d.
SYG2	14,70	7,5	15,5% ± 0,4%	0,019% ± 0,001%	n.d.	n.d.	n.d.	n.d.
SYG3	34,36	5,0	2,0% ± 0,1%	0,00557% ± 0,0003%	0,0036% ± 0,0003%	0,005% ± 0,001%	n.d.	n.d.

Fig. 1. Table of the chemical composition of the mosaic tesserae (weight %) obtained by NAA. (n.d.=under detection limit).

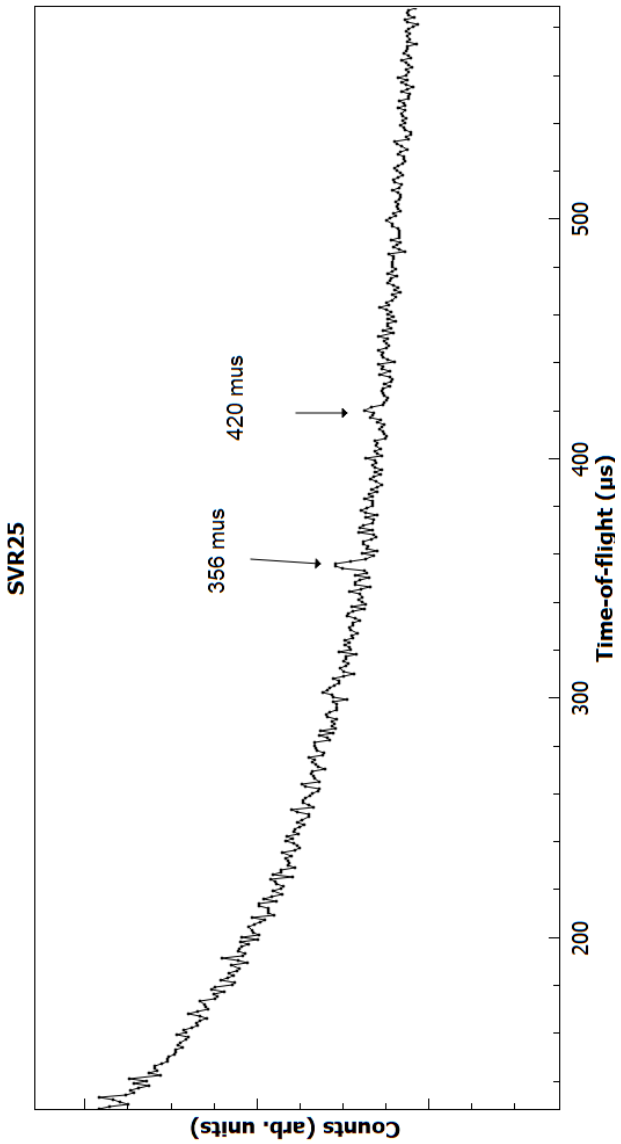

Fig. 2. NRCA spectrum of sample SVR25 showing the Sb peaks at 356 and 420 µs.

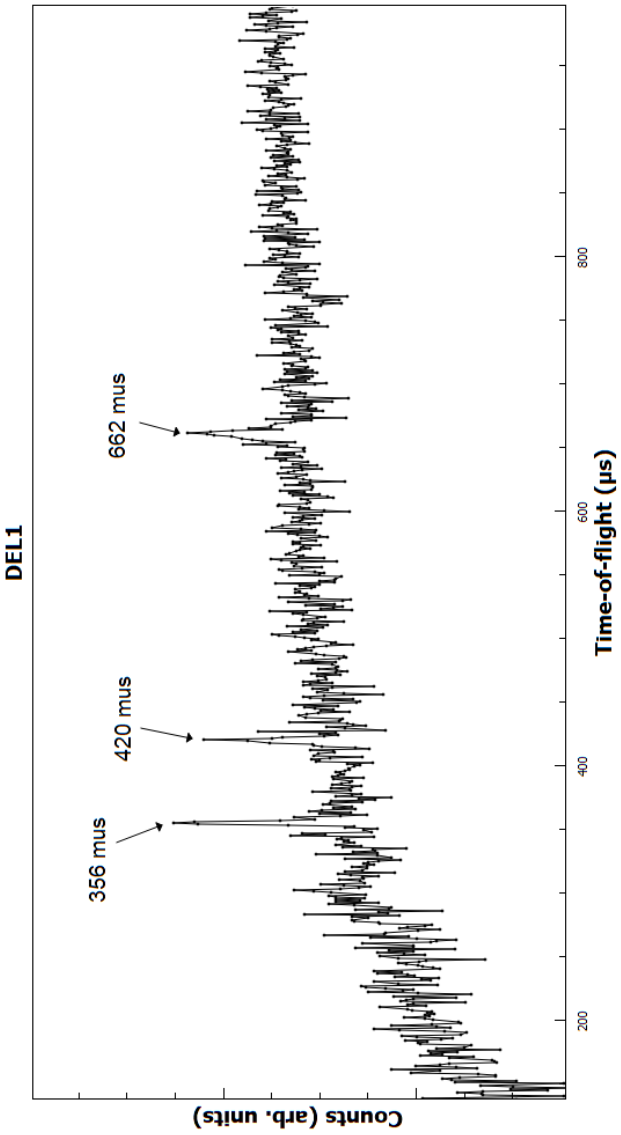

Fig. 3. NRCA spectrum of sample DEL1 showing the Sb peaks at 356, 420 and 662 µs.

High concentration of antimony has been found in samples DEL1 and SVP57 (4,7% and 4,1% respectively) and SVR24 (8,3%). In the other glass tesserae, antimony is present in low concentrations, except in sample DAFNI and sample SYG2. In these cases, the Sb signal is lower than the detection limit of the experimental system. Presence of Au has been detected and evaluated in samples DAFNI (where a gold layer is visible on the surface) and in SVR24.

The red tessera DEL2 shows a high content of copper (8,6%) accordingly to the colourant function of Cu oxides in glasses.

NRCA analysis shows the presence of antimony in samples SVR25 and DEL1 (Fig.2 and Fig.3, respectively). NRCA at the moment allows only qualitative indications of the presence of elements in the samples. NRCA spectra of the glass tesserae are characterised by a high background in the TOF range between 25 and 120 μs, due to the vitreous matrix. Therefore, resonance peaks of copper - or any other elements with NRCA signal in this range - cannot be distinguished.

IV. CONCLUSIONS

In this study, the quantitative bulk elemental composition of glass mosaic tesserae is determined in a non-destructive way by means of neutron-based techniques. Through NAA a quantitative description in terms of Na, Mn, As, Sb, Au and Cu elements is provided. It is worth mentioning that elements with high thermal end epithermal cross-section can be detected by irradiating the samples with a thermal-epithermal neutron flux. NRCA analysis encountered the vitreous matrix background issue in resonance peaks detection. Presence of antimony was detected in samples irradiated for more than twenty hours and for which NAA returns an Sb concentration around 4%.

Further investigation on the application of these neutron-based techniques to glass samples will help to understand the optimum way to obtain detectable signals for quantitative study.

V. REFERENCES

[1] https://www.isis.stfc.ac.uk
[2] N. Kardjilov, G. Festa (Editors), “Neutron Methods for Archaeology and Cultural Heritage, Neutron Scattering Applications and Techniques”, Springer, Berlin, 2007.
[3] M.D. Glascock, H. Neff, “Neutron activation analysis and provenance research in archaeology”, Meas. Sci. Technol., vol.14, No.9, 2003, pp.1516-1527.
[4] H. Postma et al., “Neutron resonance capture analysis of materials”, J. Radioanal. Nucl. Chem., vol.248, 2001, pp.113–120.
[5] H. Postma et al., “Neutron resonance capture analysis and applications”, J. Radioanal. Nucl. Chem., vol.271, 2007, pp.95–99.
[6] K. Nassau, “The Physics and Chemistry of Color. The Fifteen Causes of Color”, John Wiley & Sons, 1983.
[7] E. Basso et al., “Characterization of colorants and opacifiers in roman glass mosaic tesserae through spectroscopic and spectrometric techniques”, J. Raman Spectrosc., vol.45, 2014, pp.238–245.
[8] A. Pietropaolo et al., “A Neutron Resonance Capture Analysis Experimental Station at the ISIS Spallation Source”, Applied Spectroscopy, vol. 64, No.9, 2010, pp. 1068-1071.
[9] http://atom.kaeri.re.kr/nuchart

A.2 Paper II

Eur. Phys. J. Plus (2021) 136:738
https://doi.org/10.1140/epjp/s13360-021-01696-2

THE EUROPEAN PHYSICAL JOURNAL PLUS

Regular Article

Historical glass mosaic tesserae: a multi-analytical approach for their characterization

Giulia Marcucci[1,a], **Antonella Scherillo**[2,b], **Carlo Cazzaniga**[2,c], **Quentin Lemasson**[3,4,d], **Roberto Lorenzi**[5,e], **Massimiliano Clemenza**[1,f], **Maria Pia Riccardi**[6], **Daniela Di Martino**[1,g]

[1] Dipartimento di Fisica "G. Occhialini", Università Milano-Bicocca, and INFN, Piazza della Scienza 3, 20126 Milan, Italy
[2] ISIS, Neutron and Muon Source, Rutherford Appleton Laboratory, Chilton-Didcot OX11 0QX, UK
[3] Centre de Recherche Et de Restauration Des Musées de France, 14 quai François Mitterrand, 75001 Paris, France
[4] FR3506 NewAGLAE, Ministère de La Culture/Chimie ParisTech, 14 quai François Mitterrand, 75001 Paris, France
[5] Dipartimento di Scienza dei Materiali, Università Milano-Bicocca, via Cozzi 55, 20125 Milan, Italy
[6] Dipartimento di Scienze della Terra e dell'Ambiente and Arvedi Laboratorio–sede di Pavia, Università degli Studi di Pavia, Via Ferrata 9, 27100 Pavia, Italy

Received: 14 April 2021 / Accepted: 23 June 2021

Abstract We present a completely non-destructive approach to analyse a set of historical glass mosaic tesserae. Aim of the study is to obtain a qualitative and quantitative characterization of the glass matrix in terms of elements and mineralogical phases. Several non-destructive techniques have been applied like Particle-Induced X-ray Emission, Particle-Induced Gamma-ray Emission, micro-Raman spectroscopy, neutron resonance capture analysis and neutron activation analysis in order to combine different technique strengths and to explore the effect of different range sizes for the analysis. Yet, best practices require the use of combined analysis and different skills. The paradigm of a non-destructive multi-analytical approach is suggested for a comprehensive investigation in non-homogeneous real samples, like historical glass mosaic tesserae.

1 Introduction

Glass production in antiquity has followed different recipes in different chronological periods, depending on the availability of raw materials and on glass manufacturing techniques. As a matter of fact, glass was a widespread material from late Egypt to modern times, and many

[a] e-mail: giulia.marcucci@unimib.it
[b] e-mail: antonella.scherillo@stfc.ac.uk
[c] e-mail: carlo.cazzaniga@stfc.ac.uk
[d] e-mail: quentin.lemasson@culture.gouv.fr
[e] e-mail: roberto.lorenzi@unimib.it
[f] e-mail: massimiliano.clemenza@unimib.it
[g] e-mail: daniela.dimartino@unimib.it (corresponding author)

Published online: 10 July 2021

archaeological studies discriminate provenance, manufacturing techniques and chronological issues of glass specimens on the basis of different elemental and mineralogical compositions [1]. In general, a mosaic glass is a silica-based material with many fining, colouring and opacifying agents. Just to give an example of the complexity of glass composition, mediaeval and post-mediaeval glass was categorized in four types based on its alkali concentration: (a) Na-rich glass, with $Na_2O > 12$ wt% and $K_2O < 5$ wt%; (b) K-rich glass, with K_2O between 10 and 15 wt% and $Na_2O < 5$ wt%; (c) mixed alkali glass, with intermediate relatively high values for both sodium and potassium; and (d) high-lime low-alkali HLLA glass, where $Na_2O + K_2O < 10$ wt% [2]. Similar categories exist for colourants and opacifying agents (like calcium antimonate, lead antimonate and cassiterite or their allotropes to cite a few). Thus, the search for specific elements, but also mineralogical phases (for the colouring and opacifying agents), is very important, and the use of completely non-destructive techniques is highly desirable. In the literature, the study of archaeological glass composition is based on consolidated techniques, like inductively coupled plasma-optical emission spectrometry (ICP-OES) [3] and electron microprobe analysis (EMPA) [4–6]. Yet, ICP-OES requires sampling, which is not acceptable for many archaeological artefacts, and EMPA is often invasive. Moreover, due to the limited areas investigated, the results obtained by these techniques not always return a comprehensive description of inhomogeneous samples. Other techniques could be applied, and we tried to explore different types of analysis in different size ranges (from microns to centimetres spatial ranges of examination). In fact, mosaic glasses are archaeological glasses whose beauty is connected to their many hues, colours and transparencies, which derive from the composition and location of different mineralogical phases and chromophore ions modifying the starting glass structure. Therefore, the samples cannot be considered homogeneous, and depending on the areas examined, different results could be obtained due to the different spatial distribution of modifying ions and phases.

We carried out an in-depth study by different techniques, in order to obtain the composition of a set of historical mosaic tesserae. Ion beam analyses (IBA), like Particle-Induced X-ray Emission (PIXE) and Particle-Induced Gamma-ray Emission (PIGE), micro-Raman spectroscopy and neutron-based experiments were performed to check the presence of specific elements and mineralogical phases. However, we stress that not all analyses can describe the bulk of the specimens. IBA can hardly penetrate the surface layers, does not discriminate among allotropes and has a limited region of acquisition (spot measurements). Micro-Raman spectroscopy can inspect the inner parts of the specimens only when transparent samples are analysed. Moreover, the investigated area that a single measurement can reach is micrometric in size (about 25 μm^2, for a 20$\times$ enlargement, in our experimental set-up).

We thus propose, in order to have a non-destructive bulk characterization, a new multi-analysis route studying a set of historical mosaic tesserae by a wide number of surface techniques. Finally, the combination with neutron-based techniques, like neutron resonance capture analysis (NRCA) and neutron activation analysis (NAA), will allow for a comprehensive elemental bulk characterization in a non-destructive way.

The combined use of surface (like IBA and Raman) and bulk (NRCA and NAA) techniques will provide the elemental and mineralogical phases composition. The results suggest the use of a multidisciplinary approach to have a comprehensive quantitative description of mosaic glasses, evidencing the most appropriate non-destructive technique for the study of different glass characteristics.

2 Materials and methods

In this study, a set of 18 glass tesserae have been chosen as specimens to be tested for a multi-analytical study as part of an ongoing methodological research [7–10]. The mosaic tesserae (described and displayed in Table 1) have different dating and provenance, and most of them are coloured opaque tesserae. The sample set is composed by four Greek tesserae dating back to I–II century AD and one to the XI century AD, three Syrian tesserae dating back to the VIII century AD, and ten Italian tesserae coming from Basilica di San Vitale in Ravenna dating back to the VI century AD. The samples do not present any visible patina or alteration layer on their surface. The protocol is a combination of non-destructive analytical techniques described below, including PIXE/PIGE, micro-Raman spectroscopy and neutron-based analysis. As it will be detailed, PIXE/PIGE measurements cannot be described as bulk ones. In general, micro-Raman spectroscopy, for non-transparent samples, allows only single-spot and surface analysis. In order to have a quantitative bulk analysis of the samples, neutron-based techniques have been applied, exploiting the neutrons penetration depth of the order of several centimetres, even in dense material. This property relies on the different nature of radiation–matter interaction that distinguishes neutrons with respect to charged particles. Therefore, neutrons allow both surface and bulk properties to be measured in a non-destructive manner.

2.1 Particle-Induced X-ray Emission and Particle-Induced Gamma-ray Emission

Ion beam PIXE/PIGE analyses were performed at AGLAE facility (Centre de Recherche et Restauration des Musées de France—C2RMF), based in the Palais du Louvre in Paris (France). A 3 MeV proton beam, extracted through a 0.1 μm thick Si_3N_4 window (surface 1 mm^2), hits the samples with a beam spot about 50 μm wide. For PIXE analysis, four 50 mm^2 silicon drift detectors (SDDs) were used with a 50 μm aluminium filter to enhance the detection of high-energy X-rays, while one SDD with a smaller solid angle was used in a helium atmosphere to enhance the response to low-energy X-rays. In this configuration, it is possible to identify the elements with $Z > 11$ and to measure their concentrations with a lower limit of detection for higher atomic number and depending on irradiation conditions. An ultrapure germanium detector was used to detect in parallel the γ-rays from 60 keV to 2 MeV for PIGE analysis, fundamental for the measurement of sodium concentration. In order to reduce the effects of sampling inhomogeneities, each measurement was taken on a wider area (500×500 μm^2). Moreover, each sample was measured in two or more different points. This was necessary since the surface could display heterogeneities at a micrometric scale. Though we used a larger analysis spot, with respect to the micrometric beam spot, reaching a sub-millimetre area, other problems can affect the measurements, like non-planar surface or the presence of inclusions.

PIXE data analysis was performed following the procedures described in [11]. PIGE normalization is needed to reach an inner part of the samples. In fact, though the estimated range of proton penetration in the analysed material is of the order of about a hundred μm, the effective depth of analysis depends on the element. For sodium, the X-ray information comes from the first microns, whereas for γ-rays, being of much higher energy, the information comes from a bigger volume upper than 30 μm [12]. Precise quantitative measurements of element concentrations were taken and controlled by regularly using a set of calibration references, in particular standard glasses like BRILL A, B, D. Errors can be estimated as in [13], with values ranging from 1 to 10%, depending on the concentrations.

Table 1 Glass tesserae samples listed by codes, pictures, weight, provenance, dating and colour

Sample code	Sample image	Weight (mg)	Provenance and dating	Colour
DEL1	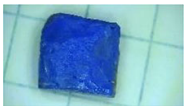	24.98	Delos Monastery—Greece, 1st–2nd AD	Opaque blue
DEL2		29.25	Delos Monastery—Greece, 1st–2nd AD	Opaque red
DEL3	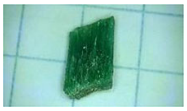	6.91	Delos Monastery—Greece, 1st–2nd AD	Opaque green
DEL4	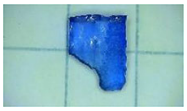	5.71	Delos Monastery—Greece, 1st–2nd AD	Transparent blue
DAFNI	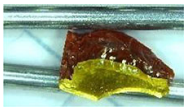	3.56	Dafni Monastery—Greece, 11th AD	Opaque red with a golden layer
SYG1	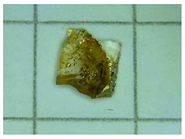	1.17	Syria, 8th AD	Transparent with golden inclusions
SYG2		14.70	Syria, 8th AD	Opaque dark green
SYG3		34.36	Syria, 8th AD	Opaque green
SVC12	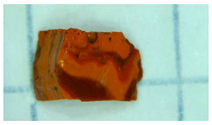	2.85	Ravenna—Italy, 6th AD	Opaque red
SVP27	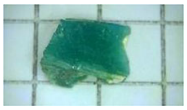	8.48	Ravenna—Italy, 6th AD	Opaque green
SVP46	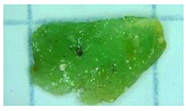	1.63	Ravenna—Italy, 6th AD	Opaque green
SVP59	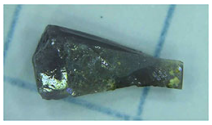	2.83	Ravenna—Italy, 6th AD	Opaque black
SVP58	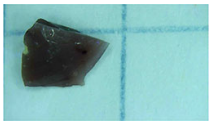	1.44	Ravenna—Italy, 6th AD	Opaque black

Table 1 continued

Sample code	Sample image	Weight (mg)	Provenance and dating	Colour
SVP57	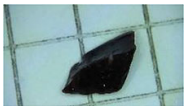	4.95	Ravenna—Italy, 6th AD	Opaque black
SVR24		4.01	Ravenna—Italy, 6th AD	Opaque pink
SVR25		22.50	Ravenna—Italy, 6th AD	Opaque green
SVR26	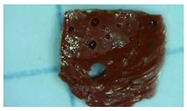	1.80	Ravenna—Italy, 6th AD	Opaque red
SVR27	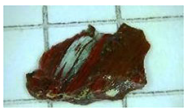	7.25	Ravenna—Italy, 6th AD	Opaque red/striped

Sample sizes can be derived by sample images, superimposed on a square background (side of 0.5 cm)

2.2 Raman spectroscopy

A micro-Raman spectroscopy study has been applied, which allowed the identification of mineralogical phases used as opacifiers dispersed in the glass matrix as well as the characterization of some of the glass matrices themselves. The Raman spectrometer used to analyse the glass tesserae is a LabRam HORIBA Jobin Yvon. The spectrometer works in backscattered configuration and is coupled to an optical microscope to selectively analyse components of heterogeneous samples on a micrometre scale. Three objectives are available to change the dimension of the sample area under investigation: 20×, 50× and 100×, which corresponds to spot sizes of about 10 μm, 5 μm and 2 μm in diameter, respectively. The sample holder consists of a motorized XY stage, characterized by a spatial resolution of 0.1 μm. The spectral resolution of the Raman spectrometer is about 2 cm^{-1}. Two different lasers have been used: He–Ne at 633 nm and Ar^+ at 488 nm, whose choice was related to the possible presence of photoluminescence signals.

The spectral position of the detection system was calibrated with a standard of crystalline silicon before any measurement.

The attribution of the Raman signatures of the crystalline inclusions has been made by comparison with data in the literature as well as in the RRUFF database [14], while the assignment of the glass matrix by comparison with the literature only.

2.3 Neutron-based techniques

Neutron resonance capture analysis (NRCA) and neutron activation analysis (NAA) have been conducted at the ISIS Neutron and Muon Source (UK). NRCA and NAA return isotopic and elemental composition of the samples in major, minor and trace elements. NRCA measurements were taken at the INES (Italian Neutron Experimental Station) beamline of ISIS, which is characterized by a white pulsed neutron beam moderated by a water moderator at 295 K, and a sample-to-moderator distance $L_0 \approx 22.8$ m [15]. Being ISIS a pulsed neutron

source, time-of-flight (ToF) spectroscopy measurements, such as NRCA, are possible. This means that the energy of the absorbed neutrons is directly related to their time of flight, which is the actual physical quantity measured.

The presence of resonance structures in neutron-induced reaction cross sections is the basis of the NRCA technique. For each nuclide, resonances appear at specific energies; thus, these sharp peaks are fingerprints of nuclides and can be used to determine the elemental and isotopic composition of materials [16].

All mosaic tesserae were singularly packed in aluminium foils without pre-treatment and then irradiated with the INES neutron flux. During irradiation, neutron capture reactions occur in the sample and prompt γ radiation is emitted. The γ-rays' arrival time on the detectors is recorded using three yttrium aluminium perovskite (YAP) crystals coupled with photomultipliers. The arrival time of the γ cascade following the neutron capture reaction corresponds to the time of flight (and therefore energy) of the neutron captured by the sample.

Each NRCA spectrum has been acquired alternating measurements with and without the sample to correct the data from background contributions. The NRCA data were processed using the Mantid software [17].

NAA measurements were taken by transferring each sample at the ChipIR beamline after irradiation on INES and by measuring the induced radioactivity with a high-purity germanium (HPGe) detector [18]. The HPGe is housed in a lead shielding to limit the background signal. Each irradiated tessera has been placed at contact, at the centre of the HPGe active surface. In most cases, especially when several isotopes with different half-lives were produced, the measurement of the radioactivity of the samples has been repeated a few times. The first measurements after irradiation have been needed to detect the γ-rays of isotopes with relatively short half-life, while measurements after the decay of short-lived isotopes have allowed higher sensitivity to isotopes with lower activity and longer decay time. For each sample, three measurements of a few minutes have been taken, followed by several measurements of one hour. However, it required about 10 min to transfer samples from the INES beamline to the HPGe detector. Isotopes with short half-lives cannot readily be detected. A prior energy calibration of the detector has been performed using radioactive samples of ^{137}Cs, ^{241}Am, ^{60}Co and ^{40} K.

We highlight that neutron-based techniques were seldom used, though being a non-destructive technique very useful in heritage science studies. Some interesting applications were shown in [16], though NRCA was never applied to mosaic samples.

3 Results and discussion

3.1 PIXE and PIGE

Table 2 reports PIXE results, after PIGE normalization, obtained by the procedure described in Sect. 2.1. Elemental composition is first obtained by PIXE, and the oxide concentration can be derived by PIGE. We can note that all elements (starting from sodium oxide) have been detected, when above the detection limit.

Most of the samples display the same sodium oxide concentration, within 10% uncertainty. This can be an indicator of the same glass matrix, while other oxide content can differ too.

On the contrary, four samples (SVP57/SVR25/DEL4/DAFNI) show different concentrations for sodium at least in 2 of the 4 points analysed. While one sample is clearly a multilayer sample (DAFNI), other samples did not show higher heterogeneities typical of a multilayer structure. Careful attention should be paid when composition data are discussed for man-

Table 2 Oxides' concentrations derived by PIXE/PIGE. The concentrations are in wt%

Sample code	Na_2O (PIGE)	MgO	Al_2O_3	SiO_2	P_2O_5	SO_3	Cl	K_2O	CaO	TiO_2	MnO	Fe_2O_3	CuO	ZnO	As_2O_5	SnO_2	Sb_2O_5	PbO # LA
SVP46	15.9	0.86	2.57	59.1			1.06	0.73	8.65	0.15	0.27	1.01	1.21	0.01		0.98		6.98
	16.1	0.96	2.46	59.2	0.16		1.08	0.71	8.55	0.13	0.25	0.84	1.03	0.01		1.03		6.98
SVP59	11.6	2.62	3.48	63.2	0.2	1.97	1	1.14	6.15	0.12	3.14	0.77	0.1	0.04			3.99	0.09
	13.5	1.66	2.77	62.1	0.25	1.28	0.83	0.85	8.2	0.12	3.42	0.64	0.1	0.03			3.7	0.1
SVP58	10.1	1.39	3.65	68.5	0.17	1.07	0.79	0.88	6.83	0.14	2.11	0.73	0.03	0.02			3.29	0.07
SVP57	14.4	0.59	2.31	64.6		0.64	0.69	0.87	6.58	0.12	3.91	0.65	0.09	0.01			3.85	0.16
	13.4	0.61	2.39	66.5		0.72	0.79	0.92	7.15	0.12	3.08	0.51	0.07	0.01			3.18	0.12
SVP27	20	0.57	2.27	62.9			1.3	0.42	5.52	0.11	0.02	0.53	0.99	0.24		0.51		4.2
	20.2	0.56	2.42	62.6			1.27	0.36	5.5	0.1	0.02	0.55	1.02	0.24		0.5		4.08
SVC12	9.51	1.05	3.95	37.9	0.46		0.51	1	7.53	0.33	0.23	4.79	6.65	0.31			0.35	24.4
	9.25	1.12	3.85	39.2	0.48		0.57	0.92	8.12	0.33	0.22	4.67	5.66	0.29			0.38	23.9
SVR27	17.9	1.03	2.64	60.8	0.23		1.27	0.86	5.37	0.53	0.56	2.56	0.93	0.96		1.94		2.04
	12.7	1.3	2.96	47.4	0.6		0.7	1.74	7.8	0.54	0.32	5.08	2.28	3.85		6.58		5.74
SVR26	14.9	0.92	2.22	54.5	0.33		0.71	1.01	7.82	0.2	1.1	3.1	2.39	0.88		2.61		6.95
	14.6	0.98	2.33	55.4	0.3		0.7	0.95	7.54	0.19	1.05	2.96	2.28	0.84		2.85		6.73
SVR25	12.7	0.54	0.5	62.1			0.38	3.14	4.05		0.11	0.53	2.04	0.02		1.41	2.17	9.95
	13.1	0.63	0.54	62.3	0.15		0.38	3.25	4.23		0.11	0.54	2.07	0.02		0.75	1.91	9.76
	6.04	0.69	0.38	23.7	0.19		0.58	1.01	3.05		0.04	0.42	1.21	0.05		29.7	6.57	26
	1.2	0.34	0.23	5.04			0.22				0.01	0.12	0.26	0.04		63.7	8.39	18.6
SVR24	12.5	0.78	0.57	56.1			0.43	5.45	7.24		0.21	0.63	0.05	0.05	0.67		4.43	9.55

Table 2 continued

Sample code	Na_2O (PIGE)	MgO	Al_2O_3	SiO_2	P_2O_5	SO_3	Cl	K_2O	CaO	TiO_2	MnO	Fe_2O_3	CuO	ZnO	As_2O_5	SnO_2	Sb_2O_5	PbO # LA
	12.3	0.64	0.54	55.8			0.37	5.51	7.47		0.22	0.65	0.05	0.05	0.68	0.69	4.58	9.91
SYG3	14.5	1.09	7.7	63.9	0.26	0.23	0.72	1.34	3.43	0.28	0.03	1.32	2.89	0.16		0.4		1.6
	14.9	1.05	6.59	65	0.34	0.22	0.81	1.13	3.42	0.32	0.04	1.23	2.98	0.17		0.35		1.41
SYG1	17.3	0.86	2.58	67.1		0.38	0.88	0.75	6.54	0.17	1.97	1.1	0.01	0				0.01
	17.6	0.78	2.52	65.6		0.41	0.89	0.76	7.61	0.17	2.14	1.17	0.01	0.01				0.01
SYG2	12.3	0.46	2.28	52.8			0.9	0.82	8.03	0.09	0.02	0.42	1.76	0.01		2.5		17.2
	12.6	0.4	2.38	53.3			0.93	0.85	7.77	0.08	0.02	0.42	1.86	0.01		2.36		16.7
DEL4	15	0.51	2.88	56.3			0.18	1.24	2.86		0.02	0.42	0.3	0.11	1.41		0.39	18
	13.9	0.46	1.79	56.7			0.17	1.31	3.29		0.02	0.34	0.29	0.11	1.59		0.47	19.2
DEL3	11.8	0.79	2.45	61.1	0.23		1.02	0.86	7.82		0.23	0.56	1.57	0.01			0.84	10.3
	10.9	0.64	2.4	49.1			0.93	0.95	21.3	0.07	0.22	0.76	1.44	0.01			0.74	9.96
DEL2	10.1	0.3	1.47	42.3			0.58	0.55	3.81	0.07	0.14	2.44	6.39					31.4
	9.98	0.35	1.43	43			0.57	0.49	3.72	0.08	0.14	2.58	6.33	0.01			0.3	30.6
DEL1	13.4	0.87	4.21	57.7			0.5	0.64	6.7	0.09	0.54	1.46	0.45	0.02			5.39	7.17
	14	0.75	3.78	58.7			0.49	0.6	6.43	0.07	0.5	1.37	0.43	0.02			5.19	6.87
DAFNI	14.5	0.39	0.77	48.3			0.38	3.46	6.4		0.57	3.09	0.83	0.02			0.24	20.8
	15.6			60.7							0.19	1.07	0.34	0.01				10.4
SYG1	17.9	0.84	2.55	66.9		0.38	0.91	0.77	6.53	0.16	1.73	0.96	0.01	0.01				0.01
DAFNI	13.9	0.49	0.51	58.7			0.33	4.25	6.7		0.52	0.44	0.03	0.01				13.8

Missing values are quantities below the detection limits

ufacturing and provenance attributions. For example, SVR25 has one measured point with a very low silica content and a very high Sn-oxide content, maybe due to the presence of some Sn-based crystalline phase. On the other hand, for SVP57 similar contents of silica are measured in the two spots analysed, while different contents of S-, Mn-, Fe- and K-oxides are obtained, maybe due to a different glass matrix.

3.2 Raman spectroscopy

Raman scattering can provide different information on glass tesserae depending on the investigated area and its magnification. Raman spectra of glass mosaic tesserae generally exhibit broad bands due to the vibration of the amorphous glass network. Instead, the presence of narrow Raman peaks is due to crystalline phases acting as opacifiers.

The Raman spectrum of the amorphous matrix of the mosaic tessera DAFNI is an example of the Raman signature of the network of our glasses (see supplementary materials S1). Two main regions can be distinguished: one between 300 and 600 cm^{-1} associated with the stretching and bending vibration of the glassy structure, and a region between 900 and 1200 cm^{-1} associated with the stretching vibration of species containing non-bridging oxygens. The basic unit of silicates (glassy or crystalline) is the SiO_4 tetrahedron. Pure amorphous silica can be described as a 3D network of SiO_4 tetrahedra sharing their oxygen atoms and forming Si–O–Si bridges [19]. However, glass mosaic tesserae were produced by using different raw materials and intentionally adding glass modifiers mainly to reduce the melting point. Impurities replace the Si^{4+} covalent bounded atoms decreasing the Si–O bridges and the connectivity of the glassy network and creating different tetrahedra species, known as Q^n configuration, where n denotes the number of bridging oxygens. The small band around 800 cm^{-1} is assigned to the motion of Si against its tetrahedral oxygen cage [20]. Previous Raman spectroscopy studies of the Si–O stretching and bending component of the glassy network have shown the possibility to differentiate between compositional families e.g. lead-based and alkali-based glasses [21–23]

Following the literature [21–23], an attempt of spectral deconvolution has been carried out with the aim of separating the different vibrational species [24] (see supplementary materials S1 and S2). The relative intensity of the Q^n components (calculated as the ratio between the Gaussian area and the total area of the stretching region) and their corresponding wavenumbers are shown in Fig. 1. Samples DEL3, DEL4 and SYG3 show similar characteristics, while DAFNI Q^n components suggest a different composition from the others as DAFNI Q^3 intensity is the lowest, while its Q^1 and Q^2 intensities are the highest. This result implies two possible conclusions: the DAFNI mosaic tessera has more modifiers than the Sirian and Delos tesserae, or its modifiers are based on heavy elements, such as lead, which break the network bounds more invasively.

A further consideration can be made on the reproducibility of the Raman measurements. Depending on the investigated region of the glasses, the same samples show different Raman spectra and wavenumber positions of the Q^n components due to the heterogeneous structure of the glass tesserae. Thus, Raman spectroscopy analysis should be conducted on several sections of the tesserae to obtain a more comprehensive description about the structure.

The polymerization index [25] has been derived for samples DAFNI and SYG3, and the results are in accordance with PIXE/PIGE results. In fact, the polymerization index of DAFNI ranges between 0.46–0.48, and according to [19], it reflects a high-lead concentration in the glass and a low melting temperature, while the SYG3 sample shows higher values of the polymerization index (0.54–0.59), and therefore, the two types of mosaic tessera belong to different compositional families.

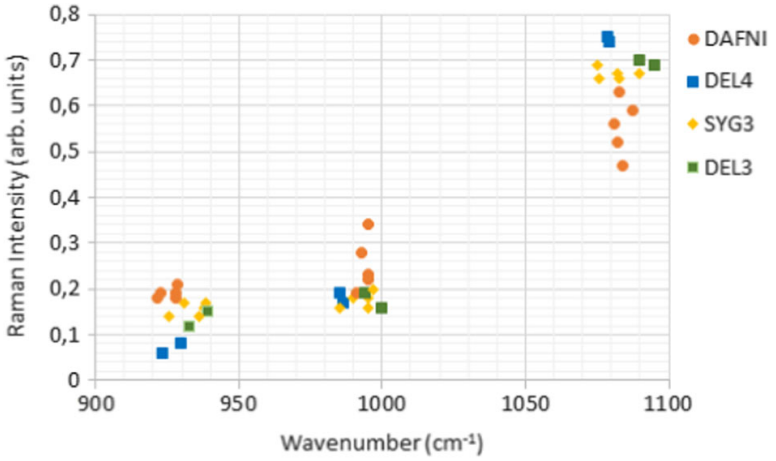

Fig. 1 Area of the different Q^n species as a function of their corresponding wavenumber (centre of the Gaussian peak). See supplementary materials for details

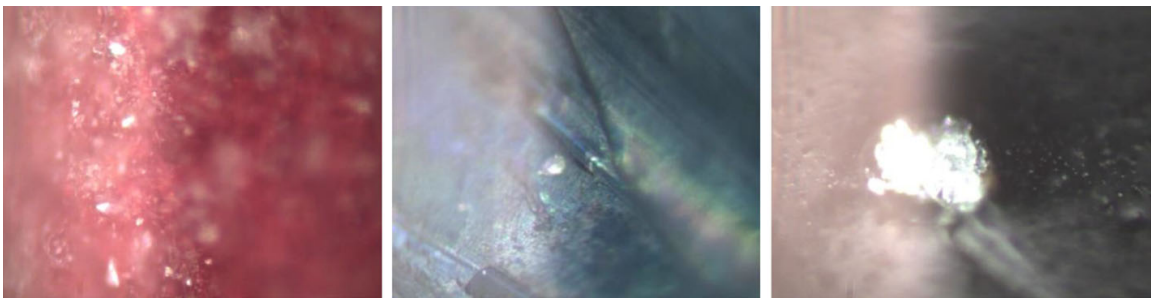

Fig. 2 From the left: view of sample DEL2, DEL4 and SVP57 at the microscope camera. The crystalline phases detected in these regions are cuprite, diopside and thenardite, respectively. The image dimensions are 0.37×0.55 mm^2

By selecting with the microscope camera a particular area of the sample where a defined structure attributable to a crystalline phase was morphologically visible (Fig. 2), it was often possible to associate mineralogical phases to the Raman spectra of these structures. In fact, Raman spectra (see Fig. 3) gave evidence of the presence of crystal structures that could often be associated with phases both related to the production history of the artefact and to its use. These structures are quite similar to those of mineralogical phases, of which the Raman spectra are well known.

In our set of samples, we detected several phases listed in Table 3. The Raman signatures of calcium-antimonates have quite recently been recognized in the scientific literature on mosaic tesserae [26]. In this case, the assignment of the Ca-antimonate phase has been made through reference spectra found in the literature. Concerning sample SVR25, the Sn-based crystalline phase suggested by PIXE/PIGE results could be assigned to cassiterite. All acquired spectra of sample SYG2 were characterized by strong luminescence; thus, it does not present any useful Raman signal for phases identification.

3.3 Neutron resonance capture analysis

NRCA relies on the analysis of resonance capture spectra obtained by detecting prompt γ-rays emitted after a neutron capture reaction in the sample. A qualitative analysis of the NRCA spectra has been conducted by indexing the observed resonances and comparing the centre of each measured peak to tabulated libraries [27]. Only four mosaic tesserae show

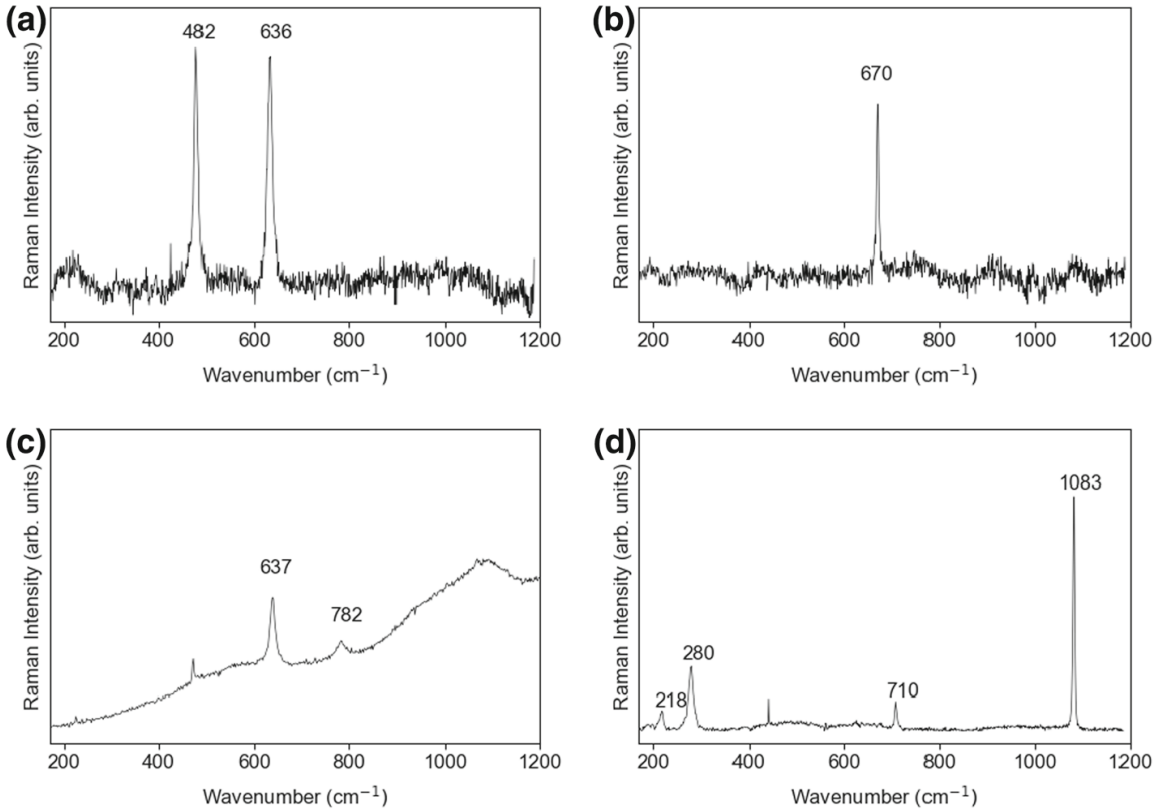

Fig. 3 **a** Representative Raman spectrum of the crystalline phase $Ca_2Sb_2O_7$ identified within DEL1. **b** Representative Raman spectrum of the crystalline phase $CaSbO_6$ identified within SVP57. **c** Representative Raman spectrum of the crystalline phase SnO_2 identified within SYG3. **d** Representative Raman spectrum of the crystalline phases $Sn_3O_2(OH)_2$ and $CaCO_3$ identified within DEL2. The spectra were acquired using the 632.8 nm HeNe laser line with 5 mW of power at the source. Other Raman spectra, according to Table 3, are available as supplementary materials (S3)

NRCA spectra with resonance peaks (Figs. 4, 5). Samples SVR25, SVR24 and DEL1 show peaks at 302 μs, 356 μs, 418 μs and 660 μs that can be assigned to antimony.

The presence of copper in sample DEL2 was derived assigning the two peaks at 36.5 and 68.5 μs, which correspond to the most intense resonances of the copper cross section for neutron capture reactions. One peak related to lead is also visible at low time of flight (30 μs) in the NRCA spectrum of sample DEL2.

This result obtained by NRCA is consistent with the opaque red colour of the sample DEL2: from the literature [28, 29] it is known that the combination of these two elements was employed by the craftsmen to obtain the red tint, given by copper oxides and copper ions, whose precipitation is facilitated by the presence of lead (see [28], pages 105–128).

In the other cases, we can conclude that NRCA signal of expected elements is not visible due to their amount lower than the corresponding detection limit, which is not constant among the elements, but it depends on the neutron capture cross section of the single element.

Moreover, the INES set-up is not yet optimized to perform quantitative NRCA, and thus, only qualitative information can be obtained through this technique at present. Therefore, the NRCA technique is suitable for detecting antimony and thus for deducing the presence of Sb-based opacifiers on a larger investigation area compared to Raman spectroscopy and ion beam analysis. The same consideration can be made for copper, which is related to colouring functions in the glass. Another advantage of NRCA is the capability of detecting the presence of lead as opposed to neutron activation analysis (as will be explained in Sect. 3.4).

Table 3 Raman phase assignments of inclusions

Sample	Peak position (cm^{-1})	Phase assignment	
DEL1	482, 636	$Ca_2Sb_2O_7$	Ca-antimonate
DEL2	218 280, 710, 1083 200, 220	$Sn_3O_2(OH)_2$ $CaCO_3$ Cu_2O	Hydroromarchite R090060 Calcite R040070 Cuprite R050374
DEL3	280, 710, 1083	$CaCO_3$	Calcite R040070
DEL4	320, 390, 664, 1013	$MgCaSi_2O_6$	Diopside R040009
SYG3	637, 782	SnO_2	Cassiterite R060563
SVP27	281, 712	$CaMn_2 + (CO_3)_2$	Kutnohorite R060473
SVP46	286, 717, 1090	$CaMg(CO_3)_2$	Dolomite R050129
SVP57	670 450, 466, 621, 633, 650, 893, 1101, 1133, 1153	$CaSbO_6$ Na_2SO_4	Ca-antimonate Thenardite R040183
SVR24	203, 337, 481, 510, 636 334,507	$Ca_2Sb_2O_7$ $Pb_2Sb_2O_7$	Ca-antimonate Lead antimonate
SVR25	476, 540, 634, 777 340, 456, 506	SnO_2 $Pb_2Sb_2O_7$	Cassiterite R060563 Lead antimonate

Where a numerical code beginning with "R" is given, reference spectra are taken from the RRUFF database [14]

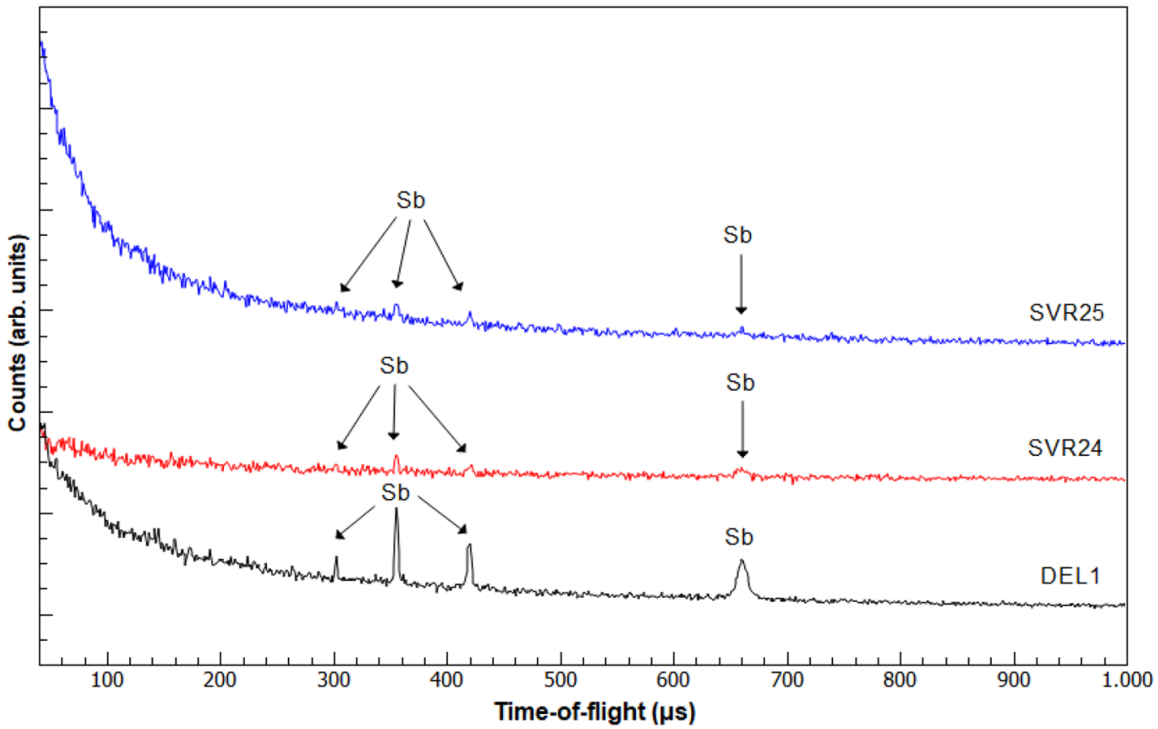

Fig. 4 Neutron resonance capture analysis spectra with elements assignment of mosaic samples SVR25, SVR24 and DEL1. Four peaks related to antimony are visible in each spectrum

3.4 Neutron Activation Analysis

For each tessera, elemental composition obtained by NAA is presented in Table 4.

Table 4 Concentration (wt%) of elements identified by NAA, compared with respective PIXE oxides' concentrations (wt%) and NRCA results

	Na (wt%)			Mn (wt%)			As (wt%)			Sb (wt%)			Cu (wt%)			Au (wt%)		
Sample	NAA	PIGE (Na_2O)	NRCA	NAA	MnO PIGE	NRCA	NAA	As_2O_5 PIGE	NRCA	NAA	Sb_2O_5 PIGE	NRCA	NAA	CuO PIGE	NRCA	NAA	PIGE	NRCA
DEL1	7.1 ± 0.2	13.4		0.196 ± 0.007	0.54					4.70 ± 0.01	5.39	X		0.45				
		14.0			0.50						5.19			0.43				
DEL2	7.4 ± 0.2	10.1		0.093 ± 0.002	0.14		0.015 ± 0.001			0.057 ± 0.002			8.6 ± 0.5	6.39	X			
		9.98			0.14						0.3			6.33				
DEL3	7.2 ± 0.2	11.8		0.128 ± 0.004	0.23					1.90 ± 0.10	0.84			1.57				
		10.9			0.22						0.47			1.44				
DEL4	10.1 ± 0.3	15.0	n.a	0.014 ± 0.002	0.02	n.a	0.75 ± 0.02		n.a	0.41 ± 0.01	0.39	n.a		0.30				n.a
		13.9	0.02						0.47			0.29						
DAFNI	11.1 ± 0.3	14.5		0.352 ± 0.011	0.54						0.24			0.83		0.0318 ± 0.0014		
		15.6			0.50									0.34				
SYG2	15.5 ± 0.4	12.3		0019 ± 0.011	0.02									1.76				
		12.6			0.02									1.86				

Table 4 continued

	Na (wt%)			Mn (wt%)			As (wt%)			Sb (wt%)			Cu (wt%)			Au (wt%)		
Sample	NAA	PIGE (Na_2O)	NRCA	NAA	MnO PIGE	NRCA	NAA	As_2O_5 PIGE	NRCA	NAA	Sb_2O_5 PIGE	NRCA	NAA	CuO PIGE	NRCA	NAA	PIGE	NRCA
SYG3	1.96 ± 0.05	14.5		0.0057 ± 0.0003	0.03		0.0036 ± 0.0003			0.0049 ± 0.005				2.89				
		14.9			0.04									2.98				
SVP27	5.38 ± 0.15	20.0		0.012 ± 0.001	0.02		0.0032 ± 0.0004			0.0030 ± 0.0003				0.99				
		20.2			0.02									1.02				
SVP46	9.4 ± 0.3	15.9	n.a	0.133 ± 0.007	0.27	n.a			n.a	0.045 ± 0.004		n.a		1.21				n.a
		16.1			0.25									1.03				
SVP57	19.2 ± 0.5	14.4		2.88 ± 0.06	3.91					4.10 ± 0.12	3.85			0.09				
		13.4			3.08						3.18			0.07				
SVR24	7.1 ± 0.2	12.5		0.092 ± 0.006	0.21		0.362 ± 0.014			8.1 ± 0.3	4.43			0.05		0.0068 ± 0.0007		
		12.3			0.22						4.58			0.05				
SVR25	2.37 ± 0.06	12.7		0.025 ± 0.001	0.11		0.052 ± 0.002			0.654 ± 0.012	2.17			2.04				
		13.1			0.11						1.91			2.07				
		6.04			0.04						6.57			1.21				
		1.20			0.01						8.39			0.26				
SVR26	8.1 ± 0.2	14.9		0.45 ± 0.02	1.10		0.036 ± 0.003			0.054 ± 0.004				2.39				
		14.6			1.05									2.28				
SVR27	8.7 ± 0.2	17.9		0.234 ± 0.007	0.56		0.030 ± 0.002			0.070 ± 0.004				0.93				
		12.7			0.32									2.28				

Missing values are quantities below the detection limits. Samples not analysed by NRCA are labelled as n.a. (n.a. = not available), while elements detected through NRCA among the samples are marked with X. We note that PIGE standard and calibrated results are referred to the oxides

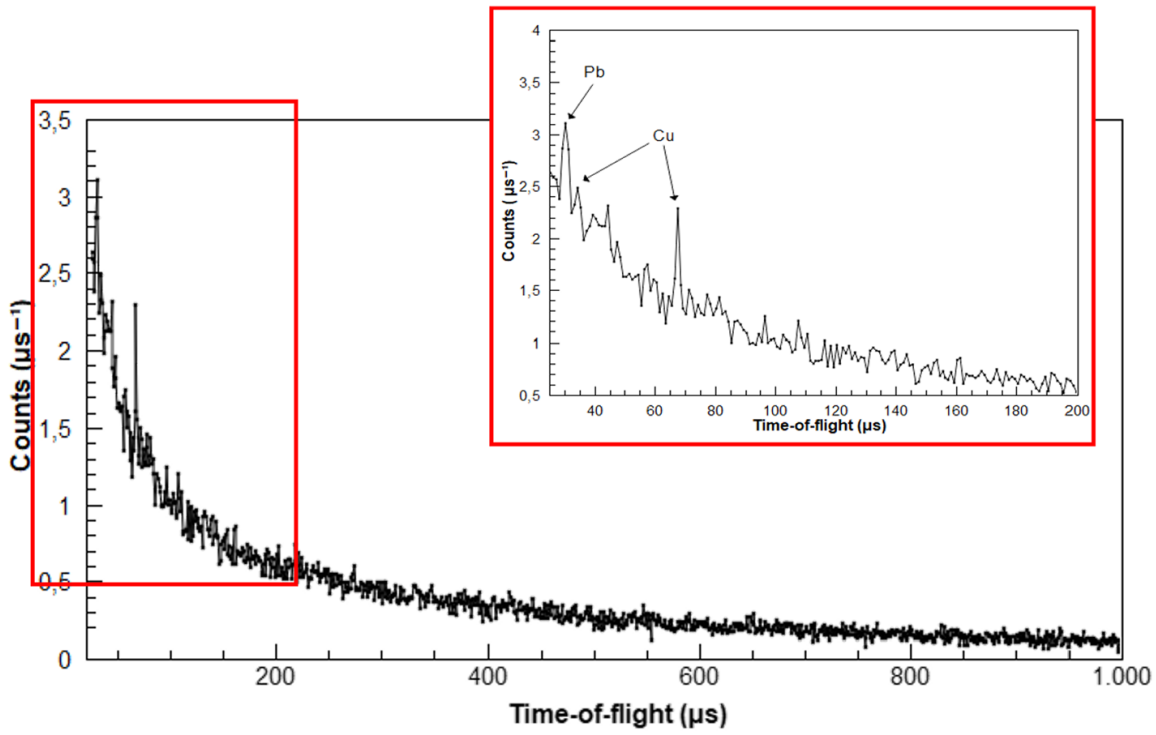

Fig. 5 Neutron resonance capture analysis spectra with elements assignment of mosaic sample DEL2. Two peaks related to copper are visible (enlarged in the inset)

We can note that not all the elements can be measured by NAA in our set-up. The detection limit of the neutron activation technique is not easy to derive as it is different for each element**.** In fact, several element characteristics affect its detection limit. First, the neutron capture cross section: elements with very high neutron capture cross sections can be detected in part per million, such as gold or arsenic (Fig. 6). Other elements are quite difficult to detect due to very low probability of interaction with neutrons, such as lead. The half-life of the radioactive isotopes is also crucial. Very fast decay times (compared to the waiting time between sample irradiation and activity measurements) lead to loss of the possibility of detecting such isotopes. As an example, the radioisotope Mg-27 produced by thermal neutron activation has a half-life of about ten minutes that is comparable with our waiting time. Thus, we cannot detect the presence of magnesium in our samples, although it is a typical element constituting glass mosaic tesserae.

Other important parameters are the γ energy compared to the background and interferences due to sample activation.

In Table 4, NAA results are compared with the corresponding ones obtained by PIGE, and there is a good agreement (within errors) for many samples. We can also observe that the quantitative analysis provided by NAA is representative of the bulk composition, while PIXE values are often lower or higher, depending on the morphology of the investigated area. Regarding antimony and arsenic, NAA is more sensitive with respect to PIXE while we have the opposite situation for copper. Moreover, through NAA we could quantify the Au content, while to get the same information through PIXE, a priori calibration with a metallic reference standard is needed.

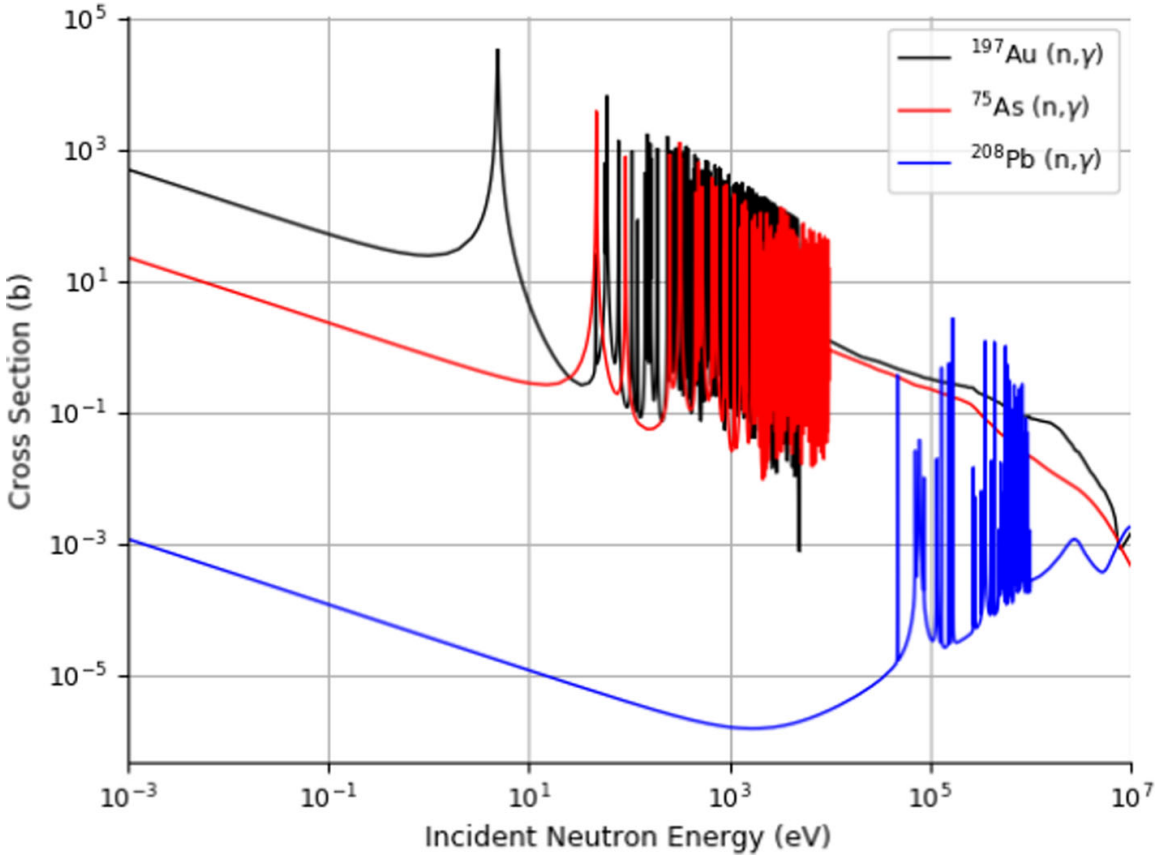

Fig. 6 Neutron capture cross section of As-75, Au-197 and Pb-208 [27]

4 Conclusions

Results obtained by a multi-analytical approach have evidenced that there is not a technique of choice if the aim is to study mosaic tesserae by a completely non-destructive analysis. In fact, all the considered techniques have advantages and limitations, as explained below. A summary of the major features of these analytical methods is reported in Table 5.

Ion beam PIXE/PIGE analyses return compositional information in terms of a wide range of oxides and elements. With PIGE analysis, low-Z elements, such as sodium, can also be detected. On the other hand, this technique does not provide bulk information as the investigated area is limited to tens of micrometres in thickness. It is worth mentioning that PIXE/PIGE results cannot always reflect the mean composition of the tesserae. In fact, being a surface and spot analysis, it can be affected by an alteration layer or the composition can be altered by the presence of a micro-crystal cluster in the investigated section.

Raman spectroscopy is a well-known technique for micrometric analysis of heterogeneous compounds. Its major advantages include crystal specificity and non-destructiveness, the first very appreciated for univocal phases identification and the latter mandatory for studies on archaeological and precious artefacts. A related characteristic to consider is the high spatial and spectral resolution. Moreover, spectra measured on the glass matrix and within inclusions were in agreement with PIXE/PIGE analysis as far as lead glasses analysis and microcrystalline phases detection. For our studies, another remarkable advantage is the possibility to conduct analysis by benchtop instrumentation. However, Raman spectroscopy is a single-spot technique and limited to qualitative information regarding opacifiers and glass matrix composition. Databases of minerals Raman spectra are very useful for phase identification, and the availability of a large number of compositional studies of glasses and mosaic tesserae in the literature allows to have a good statistic for differentiating between glass fam-

Table 5 Major features of the non-destructive techniques applied for the characterization of the mosaic tesserae

Technique	Area of investigation	Information	Quantitative analysis	Remarkable limitations
Raman spectroscopy	Spot size 10/5/2 μm wide, depending on the selection of the objective (10×/20×/50×). At 633 nm, the wavelength of the HeNe laser, the penetration depth is about few micrometres	Qualitative information on the glass matrix and the crystalline phases	NO	Superficial and spot analysis. Intrinsic weakness of the Raman scattering phenomenon, which can be overwhelmed by natural fluorescence of the sample. It is not suitable for assaying elemental fingerprints, and nearly all pure metals are Raman silent
PIXE/PIGE	Spot size 50 μm wide, but it is possible to perform mapping measurements on a wider area. Effective depth of analysis depends on the element (upper than 30 μm for sodium with PIGE)	Composition in terms of element and oxides	YES	Superficial and spot analysis. PIGE measurements are needed to exclude external layers (like degradation or alteration layers). Different detectors are needed to determine a very large number of elements
NRCA	Beam size can be shaped by means of a jaws system. The maximum beam size is 40×40 mm^2	Elemental and isotopic composition of the bulk	NO (with present set-up at INES)	Detection limits depend on the neutron capture cross section of each isotope. Long measuring time compared with Raman spectroscopy or PIXE/PIGE analysis
NAA	Beam size can be shaped by means of a jaws system. The maximum beam size is 40×40 mm^2	Elemental and isotopic composition of the bulk	YES	Detection limits depend on the neutron capture cross section of each isotope. Low neutron flux intensity of the INES beamline compared with typical reactor flux, where NAA is a consolidated technique [30]

ilies. By examining different areas of the same glass tessera with Raman spectroscopy, the heterogeneity of this kind of sample is highlighted, as well as by the PIXE and PIGE results.

On the contrary, neutron-based techniques provide compositional information of the whole bulk of the mosaic tesserae in terms of elements, overcoming effects of potential alteration layer and the heterogeneity of historical glasses. In fact, neutrons are a high penetrating probe and the small size of our samples compared to the dimension of the INES neutron beam allows them to be irradiated in the whole volume.

Thus, NRCA and NAA can be considered non-destructive analyses complementary to the previous superficial ones. However, they are mainly limited by the neutron reactions' cross sections of the elements present within the glasses, and consequently, not all elements can be detected with our experimental conditions (neutron energy, irradiation time and measure time).

Therefore, in the archaeometric search for the best characterization route to be used for the glass mosaic tesserae composition determination, we can conclude that when limited to the use of non-destructive techniques it is necessary to consider a multi-analytical approach. Only exploring different methodologies, different spatial resolutions and inner parts can be reached and an in-depth characterization of the tesserae can be obtained.

Supplementary Information The online version contains supplementary material available at https://doi.org/10.1140/epjp/s13360-021-01696-2.

Acknowledgements This work was partially supported within the CNR-STFC Agreement 2014–2020, concerning collaboration in scientific research at the spallation neutron source ISIS (UK). Financial support by the Access to Research Infrastructures activity in the Horizon 2020 Programme of the EU (IPERION CH Grant Agreement n. 654028) is gratefully acknowledged (FIXLAB: AGLAE, France).

Authors' contributions D.D. and G.M. conceived the idea of a new protocol for mosaic glass samples. Q.L, M.P.R., G.M. and D.D. performed PIXE/PIGE experiments, G.M. carried out Raman measurements in collaboration with R.L., G.M., C.C. and A.S. performed the neutron experiments. All authors gave contributions in the data analysis and results discussion. D.D. and G. M. wrote the manuscript in consultation with all authors.

Funding Open access funding provided by Università degli Studi di Milano - Bicocca within the CRUI-CARE Agreement. Partial fundings have been received as explained in the acknowledgement section.

Data Availability Statement This manuscript has associated data in a data repository. [Authors' comment: The raw/processed data required to reproduce these findings are available from the corresponding author on reasonable request.]

Code availability Not applicable.

Declarations

Conflict of interest The authors declare no conflicts or competing interests.

References

1. J. Henderson, *Ancient Glass: An Interdisciplinary Exploration* (Cambridge University Press, New York, 2013)
2. D. Dungworth, T. Cromwell, D. Ashurst, C. Cumberpatch, D. Higgins, H. Willmott, Post Mediev. Archaeol. **40**(1), 160–190 (2006)
3. R. Arletti, S. Quartieri, G. Vezzalini, Period. Mineral. **75**, 25–38 (2006)
4. R. Arletti, C. Fiori, M. Vandini, Archaeometry **52**(5), 796815 (2010)
5. A. Silvestri, S. Tonietto, G. Molin, P. Guerriero, J. Archaeol. Sci. **39**(7), 2177–2190 (2012)
6. A. Silvestri, F. Nestola, L. Peruzzo, Microchem. J. **124**, 811–818 (2016)
7. D. Di Martino, A. Galli, M. Martini, J. Raman Spectrosc. **43**, 18241827 (2012)
8. C.B. Azzoni, D. Di Martino, V. Marchesi, B. Messiga, M.P. Riccardi, Archaeometry **47**, 381388 (2005)
9. C.B. Azzoni, D. Di Martino, C. Chiavari, M. Martini, E. Sibilia, M. Vandini, Archaeometry **44**, 543–554 (2002)
10. C.B. Azzoni, D. Di Martino, B. Messiga, M.P. Riccardi, Period. Mineral. Vol. Spec. Archaeom. Cult. Herit. **71**, 73–85 (2002)
11. L. Pichon, T. Calligaro, Q. Lemasson, B. Moignard, C. Pacheco, Nucl. Instrum. Methods Phys. Res. Sect. B Beam Interact. Mater. Atoms **363**, 48–54 (2015). https://doi.org/10.1016/j.nimb.2015.08.086
12. I. Biron, S. Beauchoux, Meas. Sci. Technol. **14**(9), 15641578 (2003). https://doi.org/10.1088/0957-0233/14/9/308
13. M. Radepont, Q. Lemasson, L. Pichon, B. Moignard, C. Pacheco, Measurement **114**, 501–507 (2018). https://doi.org/10.1016/j.measurement.2016.07.005
14. B. Lafuente, R.T. Downs, H. Yang, N. Stone, The power of databases: the RRUFF project, in *Highlights in Mineralogical Crystallography*. ed. by T. Armbruster, R.M. Danisi (W De Gruyter, Berlin, 2015), pp. 1–30
15. A. Pietropaolo, G. Festa, F. Grazzi, E. Barzagli, A. Scherillo, E.M. Schooneveld, F. Civita, EPL **95**, 48007 (2011). https://doi.org/10.1209/0295-5075/95/48007
16. N. Kardjilov, G. Festa, *Neutron Methods for Archaeology and Cultural Heritage* (Springer, Berlin, 2017)
17. O. Arnold et al., Nucl. Instrum. Methods Phys. Res. Sect. A **764**, 156–166 (2014)
18. C. Cazzaniga, A. Scherillo, A. Fedrigo, D. Raspino, F. Grazzi, C.D. Frost, Neutron activation analysis of archaeological artefacts using the ISIS pulsed neutron source. AIP Advances (2021). https://doi.org/10.1063/5.0043935
19. P. Colomban, A. Tournie, L. Bellot-Gurlet, J. Raman Spectrosc. **37**, 841–852 (2006)
20. F.L. Galeener, A.E. Greissberger, Phys. Rev. B **27**(10), 6199–6204 (1983)
21. P. Colomban, F. Treppoz, J. Raman Spectrosc. **32**, 93102 (2001)
22. P. Colomban, G. Sagon, X. Faurel, J. Raman Spectrosc. **32**, 35160 (2001)
23. P. Colomban, I. Robert, C. Roche, G. Sagon, V. Milande, Rev. Archeom. **28**, 153–167 (2004)
24. E. Radice, *Analysis of Raman Spectra of Mosaic Glasses*. Bachelor Thesis, Physics Degree, University of Milano Bicocca (2019)
25. P. Colomban, J. Non Cryst. Solids **323**, 180187 (2003)
26. E. Basso, C. Invernizzi, M. Malagodi, M.F. La Russa, D. Bersani, P.P. Lottici, J. Raman Spectrosc. **45**, 238245 (2014)
27. http://atom.kaeri.re.kr/nuchart. Accessed 9th Mar 2021
28. R.H. Brill, The Corning Museum of Glass (1970), pp. 105–128
29. S. Fiorentino et al., Archaeol. Anthropol. Sci. **11**, 337–359 (2019)
30. https://www.nist.gov/laboratories/tools-instruments/instrumental-neutron-activation-analysis-inaa. Accessed 9 Mar 2021

A.3 Paper III

Glass-gems from the National Archaeological Museum in Aquileia: a PIXE/PIGE compositional study

Glass-gems from the National Archaeological Museum in Aquileia: a PIXE/PIGE compositional study

D Di Martino[1], **E Gagetti**[2], **G Marcuccci**[1], **Q Lemasson**[3] **MP Riccardi**[4]

[1] Dipartimento di Fisica "G. Occhialini", Università degli Studi di Milano Bicocca and INFN, Sezione di Milano Bicocca.
[2] Dipartimento di Beni Culturali e Ambientali (docente a contratto), Università degli Studi di Milano "La Statale".
[3] FR3506 NewAGLAE, Ministère de la Culture/Chimie ParisTech, 14 quai François Mitterrand, 75001 Paris, France.
[4] Dipartimento di Scienze della Terra e dell'Ambiente and Arvedi Laboratorio– sede di Pavia, via Ferrata 9, Università degli Studi di Pavia, 27100 Pavia, Italy

mariapia.riccardi@unipv.it

Abstract. A total of 100 investigated coloured/colourless opaque and transparent glass-gems of the National Archaeological Museum of Aquileia (Italy) have been analyzed with a non-invasive approach, at the AGLAE facility (Centre de Recherche et Restauration des Musées de France - C2RMF), located at the Palais du Louvre in Paris (France).
The collection represents a "unicum" in terms of number of finds and richness of typologies. Almost all the glass-gems were discovered in the Roman site of Aquileia, known as an important center of glass working, and are dated between the 2nd century BCE to the 2nd century CE. Their safe provenance from the city and cemeteries of Roman Aquileia, and their number, offer an unparalleled statistical sample.
Most of the objects belong to the natron-glass group. The families of HIMT glass and glass made from plant ashes are also represented. This compositional variety of glass supports the hypothesis that Aquileia was an important glass working center in the Roman age.

1. Introduction

In antiquity, glasses were produced also for imitation purposes, for example for reproducing several varieties of colored marbles [Journal of Cultural Heritage, 42 (2020), 202-212] and in gemology [1]. Ancient glass-gem makers were constantly looking for new recipes to mime gemstones: opaque coloured glasses could be obtained (and tuned) with careful insertion of some elements, likely forming microcrystalline phases (as calcium or lead antimoniate). The coloration of glass is the result of complex interactions between structural and chemical effects. In particular, the presence and the relative concentration of transition metals play a fundamental role, acting as chromophores in the glass base [2]. The whole composition of the specimens thus reflects the progress reached by the manufacturer's workshop and it can be used as an archaeological marker of production times and geographical area. Roman glass skilfully achieved the control over colour, mixing colourizers and decolourizers [3]. A unique sample is offered by the collection of the National Archaeological Museum in Aquileia [4], consisting of more than 1,300 pieces, dating from the 2nd century BCE to the 2nd century CE. Its uniqueness is given from the fact that almost all of the glass-gems were discovered on the site of the Roman site of Aquileia, which is known as an important centre of glass-making. The city was destroyed by Attila in the mid-5th century, and rebuilt south-west in the Middle Ages. Its largest part is still unexcavated beneath the fields constituting an invaluable archaeological reserve, today listed in the UNESCO World Heritage. Even if only a minority of the glass-gems in the National Archaeological Museum of Aquileia comes from controlled and/or stratigraphic excavations, their safe provenance from the city and the cemeteries of Roman Aquileia, and their number offer an unparalleled statistic sample

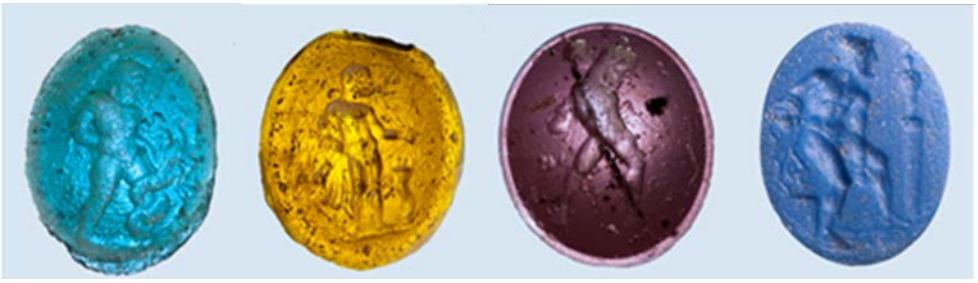

Fig. 1 Examples of glass-gems samples, coming from the National Archaeological Museum of Aquileia (real size about 2cmx1cmx0.5cm), dating from the 2nd century BCE to the 2nd century CE.

2. Materials and methods

After a preliminary typological and glyptic study, in collaboration with the National Archaeological Museum of Aquileia (Italy), we selected about 100 significant glass gems (representative for color, style and gemological criteria), from the 1300 specimens of glass gems enriching its collections [1, 5]. The aim of the project was to determine the composition of the glass, for major, minor and trace components. Therefore, both light and heavy elements were analyzed.

Particle Induced X-ray Emission/ Particle Induced Gamma Ray Emission (PIXE/PIGE) analyses were performed at the AGLAE facility (Centre de Recherche et Restauration des Musées de France - C2RMF), located at the Palais du Louvre in Paris, France, (see for example [6, 7]).

In order to have an indication of the uniformity of the bulk material, checking composition, presence of segregation or distribution of impurities (non-homogeneous stains may be a consequence of different processing techniques), several acquisitions were collected on an area of 500x500µm². In addition, when samples are produced by the superposition of different glass layers, PIXE/PIGE mapping was performed to return the different elemental spatial localization. More than 400 analyses were collected, defining the relative abundances of major and minor elements, including chromophores or opacifying agents. Quantitative measurements of element concentration have been obtained, also using a set of calibration references (Brill A, Brill C and Brill D, Corning Museum of Glass).

3. Results

A preliminary processing of the data-set has allowed us to identify the compositional 'families glass' attested in the collection of Roman glass gems of the National Archaeological Museum of Aquileia.

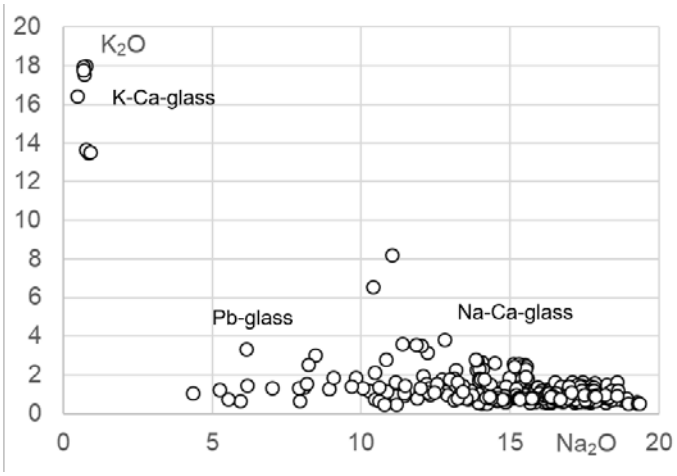

Fig. 2 The Na_2O vs K_2O binary diagram shows the main compositional groups. The fluxes used are both mineral fluxes (natron) and plant ash (both sodium and potash). A separate group is that of lead glass.

The chemical composition, in terms of major elements, shows that almost all of the artefacts belong to the Na-Ca-glass group (Fig. 2), in agreement with literature data on contemporary blown glass artefacts [8, 9, 10]. Only two artefacts were made with K-Ca-glass and a small group of artefacts was made with lead glass.

Considering some elements, such as K_2O and MgO (Fig. 3A), it is evident that the chemical formula of the Na-Ca-glasses is that characteristic of Roman glass made with natron; a minority group, mainly traceable to glass-gems imitating nicolo, can be attributed to the use of Na-plant ash as a flux.

The TiO_2, Fe_2O_3 and MnO contents also identify, in the Na-Ca-glasses, the presence of compositions referable to the HIMT glass group (Fig. 3B).

These preliminary results are very interesting because they were obtained on a large number of specimens of glass gems. The compositional differences obtained show how Aquileia represented an important and active center of glass working in the Roman age.

These first results will be further discussed and analysed in a transdisciplinary context, integrating the chemical composition with the archaeological and stylistic aspects of the artefacts.

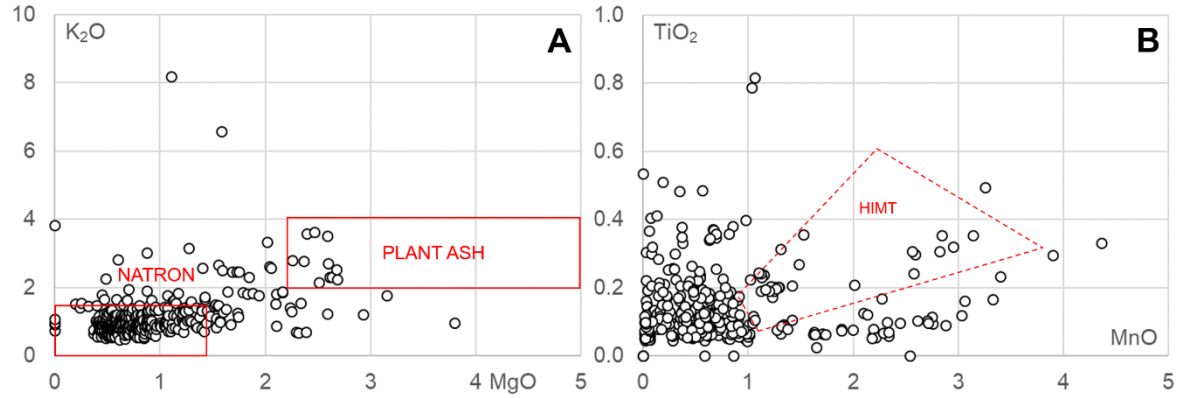

Fig. 3 The distribution of some minor components defines different compositional sub-groups. **A**. MgO vs K_2O distinguishes natron-glass from plant ash-glass; **B**. MnO vs TiO_2 defines which artefacts belong to the HIMT glass group.

References

[1] Sena Chiesa, G., 2010, Pallas 83, 225.
[2] Sanderson, D.C.W., and Hutchings, J.B., 1987, Glass Technology 28, 99.
[3] Jackson, C.M. 2005 Archaeometry 47, 763.
[4] Sena Chiesa, G., 1966, Gemme del Museo Nazionale di Aquileia, Padova.
[5] Sena Chiesa, G., Gagetti, E., 2009, Aquileia e la glittica di età ellenistica e romana, Trieste, Editreg
[6] Pichon, L., Moignard, B., Lemasson, Q., Pacheco C., Walter, P., 2014, Development of a multi-detector and a systematic imaging system on the AGLAE external beam, Nuclear Instruments and Methods in Physics Research B 318, 27–31
[7] Marcucci, G., Scherillo, A., Cazzaniga, C., Lemasson, Q., Lorenzi, R., Clemenza, M., ... & Di Martino, D. (2021). Historical glass mosaic tesserae: a multi-analytical approach for their characterization. The European Physical Journal Plus, 136(7), 1-19.
[8] Gallo, F., Marcante, A., Silvestri, A., & Molin, G. (2014). The glass of the “Casa delle Bestie Ferite”: a first systematic archaeometric study on Late Roman vessels from Aquileia. Journal of Archaeological Science, 41, 7-20.

[9] Boschetti, C., Mantovani, V., & Leonelli, C. (2016). Glass coloring and recycling in Late Antiquity: a new case study from Aquileia (Italy). Journal of Glass Studies, 58, 69-86.
[10] Maltoni, S., Silvestri, A., Marcante, A., & Molin, G. (2016). The transition from Roman to Late Antique glass: new insights from the Domus of Tito Macro in Aquileia (Italy). Journal of Archaeological Science, 73, 1-16.

A.4 Paper IV

JAAS

ROYAL SOCIETY OF CHEMISTRY

PAPER

View Article Online
View Journal

Cite this: DOI: 10.1039/d2ja00263a

A new multidisciplinary non-destructive protocol for the analysis of stony meteorites: gamma spectroscopy, neutron and muon techniques supported by Raman microscopy and SEM-EDS

Riccardo Rossini, [abcd] Daniela Di Martino, *[ab] Toluwalase Agoro, [d] Matteo Cataldo,[abd] Giuseppe Gorini,[ab] Adrian D. Hillier,[d] Matthias Laubenstein, [e] Giulia Marcucci, [abd] Maya Musa, [af] Maria Pia Riccardi,[gh] Antonella Scherillo[d] and Massimiliano Clemenza[ab]

Received 28th July 2022
Accepted 15th November 2022

DOI: 10.1039/d2ja00263a

rsc.li/jaas

The physical and chemical characterisation of meteorites is of paramount importance in the study of the formation of the Solar System. In this work we show the feasibility of a complete set of non-destructive measurements to perform such a characterisation using a stony meteorite as a mock-up sample. The identification of the sample as a meteorite was performed by means of gamma ray spectrometry, which identified the presence of cosmogenic ^{26}Al. Time-of-Flight Neutron Diffraction (ToF-ND) enabled the mineralogical phase quantification and the analysis of the presence of strains and substitutions in each mineral. Neutron Resonance Capture Analysis (NRCA), Neutron Resonance Transmission Imaging (NRTI) and Muonic Atom X-Ray Spectroscopy (MAXRS) allowed a study of the presence and the space distribution of certain elements. Furthermore, micro-Raman Spectroscopy (μRS) and Scanning Electron Microscopy with Energy-Dispersive X-ray Spectroscopy (SEM-EDS) were also considered in order to validate the protocol.

1 Introduction

The non-destructive characterisation of valuable samples like meteorites is of paramount importance in terms of sample conservation and measurement repeatability. Meteorites are a heterogeneous class of samples which are typically classified by means of average destructive quantification and petrological observation. The latter ones, despite being technically non-destructive, require the extraction of a thin section, which is a destructive procedure. In general, the dominant physical characterisation techniques used to analyse meteorites make use of probes with a small depth of penetration in materials (<1 mm), such as X rays and electrons. We refer to them as surface techniques. The aim of this study is to make use of physical characterisation techniques based on radiation with a long average range in materials (centimeters) to study the volume of the sample instead of its surface. Examples of such radiation are neutrons, muons and gamma rays. These bulk techniques enable to study also the internal part of the sample without causing major damage to the specimen. Meteorites are important for their scientific-cultural meaning, but their characterisation could also entail relevant implications on the knowledge on the cosmogenesis and the formation of the Solar System.

In this framework, a completely non-destructive protocol is presented, which makes use of bulk techniques to characterise the elemental, mineral and radio-isotopic composition of the sample.[1,2] Passive techniques, such as the collection of the radiation emitted by the sample, were also considered (in particular the collection of gamma rays, which is a bulk technique).

The first important procedure to carry out is to determine whether or not a received sample is a meteorite. On this purpose, gamma ray spectrometry is used to look for the presence of certain radionuclides which are formed by nuclear reactions involving primary cosmic rays and which have half-life smaller than the time of existence of the Earth atmosphere (around 10^9 years).[3] The presence of such nuclides confirms the fact that the sample spent long periods of time outside the Earth atmosphere and therefore it may prove its meteoric origin. The main cosmogenic radionuclides with these

[a]Department of Physics G. Occhialini, University of Milano-Bicocca, Milan, Italy. E-mail: daniela.dimartino@unimib.it
[b]Milano-Bicocca Division, INFN, Milan, Italy
[c]Department of Physics, University of Pavia and Pavia Division, INFN, Pavia, Italy
[d]ISIS Neutron and Muon Source, STFC, Didcot, UK
[e]Laboratori Nazionali del Gran Sasso (LNGS), INFN, Assergi - L'Aquila, Italy
[f]Department of Earth and Environmental Sciences (DISAT), University of Milano-Bicocca, Milan, Italy
[g]Department of Earth and Environmental Sciences, University of Pavia, Pavia, Italy
[h]Arvedi Laboratory, CISRiC, University of Pavia, Pavia, Italy

characteristics, ordered by decreasing half-life, are:[1] ^{26}Al ($t_{1/2}$ = 7.6 × 10^5 years), ^{60}Co ($t_{1/2}$ = 5.27 years), ^{22}Na ($t_{1/2}$ = 2.6 years), ^{54}Mn ($t_{1/2}$ = 312 days), ^{46}Sc ($t_{1/2}$ = 84 days) and ^{48}V ($t_{1/2}$ = 16 days). If the sample fall is recent (for instance, a time less than 5τ of ^{22}Na has passed, about 10 years, where $t_{1/2} = \tau \ln 2$) one could perform standard gamma ray spectrometry. Otherwise, high-sensitivity and low-background gamma ray spectrometry is needed, as the long half-life of ^{26}Al (the only one left in this latter case) implies it has a small activity. This is also required whenever the sample is just too small to have an acceptable activity for standard gamma ray spectrometry.

It is then important to characterise the mineral and elemental composition of the sample. The former analysis is carried out by exploiting the Time-of-Flight (ToF) technique to perform Neutron Diffraction (ND) from a pulsed thermal-epithermal neutron beam. ToF-ND enables mineralogical phase characterisation and quantification in the bulk of the sample, due to the long range of neutrons in most materials, with respect to other particles.

A qualitative bulk elemental characterisation is made possible thanks to the analysis of the absorbed neutron spectrum during the exposition of the sample into a thermal-epithermal pulsed neutron beam. Neutron Resonance Capture Analysis (NRCA)[4] consists in the study of the captured neutron spectrum by timing the gamma rays promptly emitted after each beam spill. This technique returns a bulk information on the whole analysed area. On the other hand, Neutron Resonance Transmission Imaging (NRTI)[5,6] consists in the acquisition of a space-resolved Time-of-Flight neutron spectrum in transmission by means of a neutron beam monitor. As a consequence, NRTI allows elemental mapping. Therefore, NRCA and NRTI spectra are complementary and they return consistent information. Furthermore, in the case of NRTI, information is space-resolved, whereas in NRCA it is averaged on all the part of the sample crossed by the neutron beam. Neutron techniques were applied to meteorites a few times.[7,8] A combined ToF-ND and neutron-capture imaging protocol has already been applied to chondrites, particularly to the Chelyabinsk meteorite.[9]

Muonic atom X-ray Emission Spectroscopy (μXES), a novel technique for elemental characterization, is also exploited. μXES is a method based on the detection of high energy X-rays emitted by the sample after negative muon irradiation. This irradiation causes the formation of muonic atoms, whose characteristic X-ray emission allows the elemental characterisation of the sample. The shape of the muon energy loss curve dE/dx (the Bragg peak) enables such measurements at different depth into the material, by tuning the muon beam momentum.[10–14] Even though the sensitivity to trace elements is still not optimised, this technique enables the non-destructive quantification of major elements in the bulk of a sample, and it is therefore a unique quantitative probe of the internal elemental composition of a sample.

It has been decided to introduce two consolidated surface techniques, such as Raman spectroscopy and Scanning Electron Microscopy, in order to validate the protocol. Furthermore, these methods allowed a more complete overview on the sample, enabling space-resolved mapping measurements. These techniques should be applied on a thin section (R003, see next section), which is typically available for many meteorites as it is used for petrological observation. Micro-Raman Spectroscopy (μRS) is used to identify the main mineral phases present in the sample in a space-sensitive way, even though the technique is basically qualitative. By Scanning Electron Microscopy in BackScattered Electrons (BSE-SEM) imaging it is possible to characterise the morphology of a surface by mapping the local average atomic number Z in greyscale. In this way, it is possible to identify different structures in order to study their elemental composition with the EDS microprobe. The space-sensitive quantitative elemental characterisation in this protocol is performed on the thin section R003 by means of Energy Dispersive X-ray Spectroscopy (EDS), consisting in the collection of the X-ray spectrum emitted while Scanning Electron Microscopy (SEM) is running.

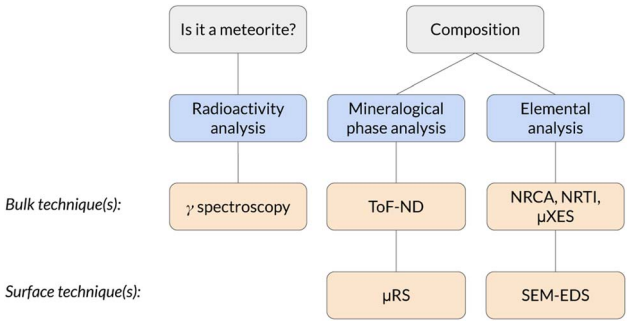

Fig. 1 Scheme of the analysis protocol described in this work.

The whole protocol, schematised in Fig. 1, has been tested for the first time on a supposed meteorite coming from a private collection. This is the first time a completely non-destructive bulk and surface analysis protocol is applied to a meteorite.

2 Materials and methods

2.1 Samples

The analysis protocol has been applied on an supposed meteorite, coming from the Middle East desert, which has belonged to a private collection for more than 20 years. During this period, the sample was cut into 2 massive pieces in order to extract a standard petrological (thickness 30 μm) thin section for transmitted light observations, which was used to identify the sample as a chondrite, a class of stony meteorites.[15]

These samples, which are shown in Fig. 2, have the following features:

- Sample R001 is a 12.61(36) g tip of the chondrite, with size 22.23 × 33.11 × 13.17 mm^3;
- Sample R002 is a 14.65(14) g central slice of the chondrite, with size 26.95 × 35.97 × 6.41 mm^3;
- Sample R003 is a standard petrological thin section (30 μm thick) obtained from sample R002.

The average density, measured on samples R001 and R002, is (2.1 ± 0.1) g cm^{-3}. From the thin section analysis we identified the presence of aluminium in cracks and fissures, a clear

Fig. 2 The three samples from the same meteorite studied in this work: R001 and R002 are bulk samples, whereas R003 is a standard petrological thin section.

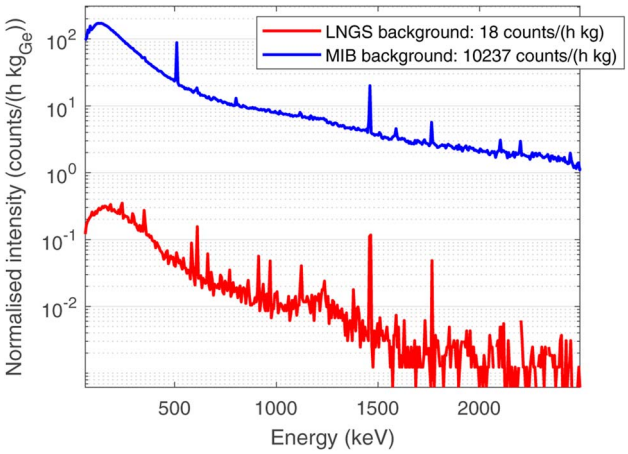

Fig. 3 Comparison between the normalised background at LNGS (lower curve, red), with a depth of 3400 mwe, and the background at the radioactivity laboratory at the University of Milano-Bicocca MIB (upper curve, blue), at sea level. Spectra are normalised in time of measurement and mass of germanium in each detector.

evidence of the fact that the thin section polishing was made with alumina. As it was not possible to quantify aluminium, which is a key element in this sample, from the thin section. As a consequence, one of the two surfaces of sample R002 has been polished in order to perform EDS on it. The polishing was carried out with SiC with grain size 18 μm and 15 μm and with diamond paste with grains of 3–6 μm, 1–3 μm and finally 0.25 μm.

2.2 Low-background gamma ray spectrometry

In order to optimise the bulk characterisation of the radioisotopes present in the sample, a low-background High-Purity Germanium detector (HPGe) was used, located at the STELLA (SubTErranean Low Level Assay) laboratory[16] within the subterranean Laboratori Nazionali del Gran Sasso (LNGS) underneath the Gran Sasso mountain, at a depth of 3800 mwe (meters of water equivalent). In particular, it is a p-type coaxial low-background HPGe detector from ORTEC (the relative efficiency at the 1332.52 keV peak of ^{60}Co is 84%, the energy resolution 1.9 keV).

Fig. 3 shows the comparison between the gamma ray background at the STELLA facility at LNGS (lower curve) and the one measured at sea level in the radioactivity laboratory of the University of Milano-Bicocca (MIB, upper curve). Both spectra are normalised to count rate and detector mass, which is approximately proportional to the efficiency. The gamma ray background at LNGS is about two or three orders of magnitude lower than the one at MIB. The huge difference between these spectra results from the great depth of LNGS under the Gran Sasso mountain, but also from the choice of low-radioactivity materials in the construction of the detector and the LNGS facility itself.

In order to obtain the activity of ^{26}Al, the Monte Carlo (MC) simulation code Arby, based on the CERN software package Geant4,[17] was used to calculate the Full Energy Peak (FEP) efficiency of the ^{26}Al emission, taking into account the sample geometry and composition, the detector geometry and the absorption of radiation by the detector dead layers and the sample itself. As the MC is carried out by simulating single-isotope decays, considering all electromagnetic, strong and weak processes which may occur, it returns the value of efficiency weighed by the branching ratio of the selected peak (εBR). The sample composition used in the MC simulation is the same obtained by means of the EDS campaign described in the previous section. The FEP efficiencies are used to obtain the activity from the count rate of each peak, which is calculated by Gauss-fitting.

2.3 Time-of-flight neutron diffraction (ToF-ND)

The INES diffractometer at the ISIS Neutron and Muon Source in Didcot (UK) has been used.[18] It is endowed with a completely motorised and programmable sample holder (x–y–z–ω) and 9 neutron detection banks, featured with 16 ^{3}He detectors each. In addition, it also hosts the instrumentation for the neutron resonance measurements, as described in the next section.

The 50 Hz pulsed neutron beam is produced by the spallation of 800 MeV protons (supplied by a synchrotron having total current 210 μA) against a tungsten target. As slow neutrons are required for Tof-ND and many other applications, a water-based moderator is used to thermalise the neutron beam, obtaining a quasi-Maxwell distribution with $kT = 25$ meV, corresponding to room temperature.

For each investigated spot, 9 histograms were acquired, one for each detection bank, and standard Rietveld refinement procedure has been applied to extract the required information. In order to perform these analyses, the GSAS software has been used.[19] In particular, the analysis was divided into two parts:

- Phase analysis, a multi-spectral refinement on all banks excluding the one at smallest 2θ angle (forward scattering) with the objective of identifying and quantifying the phases present in the sample;
- Peak shape analysis, a refinement on the highest-2θ bank only (back scattering) in order to extract information about the peak shape and the crystal structure. The reason for the choice

of this spectrum for this task relies both on its optimal spectral resolution and the minimised sensitivity to the thickness of the sample, provided it is approximately below 1 cm, as in this case. These considerations are made particularly for the INES geometry and might not hold in general.[18]

ToF-ND measurements were applied on two 2 × 2 cm^2 regions for each sample, in order to verify the uniform distribution of mineral phases in the whole sample. The neutron beam of irradiation for each spot corresponds to an integrated proton current of 1500 μAh on the spallation target, totalling around 8 h 30 min of measurement for each of the 4 regions.

2.4 Neutron resonance capture analysis (NRCA) and neutron resonance transmission imaging (NRTI)

The neutron-based qualitative elemental characterisation is carried out while performing ToF-ND at INES. In particular, NRCA is performed by means of three time-resolved YAP detectors positioned below the INES detection banks, outside the neutron beam. Typically, the three spectra are consistent with each other and they are merged. As the resulting spectrum is relative to the whole inspected area, it does not allow elemental mapping. The low-ToF region of the spectrum, around 30 μs after the beam spill, is saturated by the noise and therefore it does not contain crucial information. On the other hand, NRTI is made possible at INES by a n-GEM (neutron Gas Electron Multiplier) detector[20] in transmission with respect to the beam. The resulting information can be visualised by means of bi-dimensional maps, but the space resolution is limited by the current space resolution of n-GEM detectors (around 0.75 mm). In this case, as the n-GEM detector has a good neutron/gamma discrimination, all the ToF interval between two beam spills (25 ms) is usable, even the first 30 μs. In principle, the quantification of some elements may be possible, but further simulation and calibration on the INES setup is needed and it is scheduled to be carried out in the next years.

2.5 Muonic atom X-ray emission spectroscopy (μXES)

The μXES measurement is performed at the RIKEN facility at the ISIS Neutron and Muon Source, UK. The technique consists of two sets of measurements at different momentum of the non-collimated negative muon beam: one at 20 MeV per c and one at 40 MeV per c. In this work, this technique was applied only to sample R001. The sample was wrapped in an aluminium foil, to facilitate the positioning on the sample holder, and placed 10 cm after the beam exit, with two HPGe detectors positioned 15 cm from the meteorite. Aluminium is also a reference for the depth selection during the measurements, since it acts as an interface between the interior and the exterior of the sample.

The analysis procedure consists in peak identification and quantification of the related count rate by Gauss-fitting for each peak and each value of beam momentum. At this point, each peak is weighed according to the efficiency curve of the detection system in that configuration, obtained by MC simulation on the Arby interface for Geant4.[17]

In order to understand at which depth is released the energy of the muon beam at the various values of the beam momentum, MC simulation on SRIM[21] are also carried out, taking into account a 3% momentum spread. Both values of momentum were simulated (10 k events each) obtaining the Bragg curve $\frac{dE}{dx}(x)$. The depth interval in which most energy is released corresponds to the area analysed by the technique, since most muonic atoms are formed in that depth interval. The results, reported in Fig. 4, show that in the 20 MeV per c run the measurement is sensitive to the aluminium foil and the surface of the sample (few μm), whereas the bulk of the sample (~1.5 mm) is being investigated in the 40 MeV per c run.

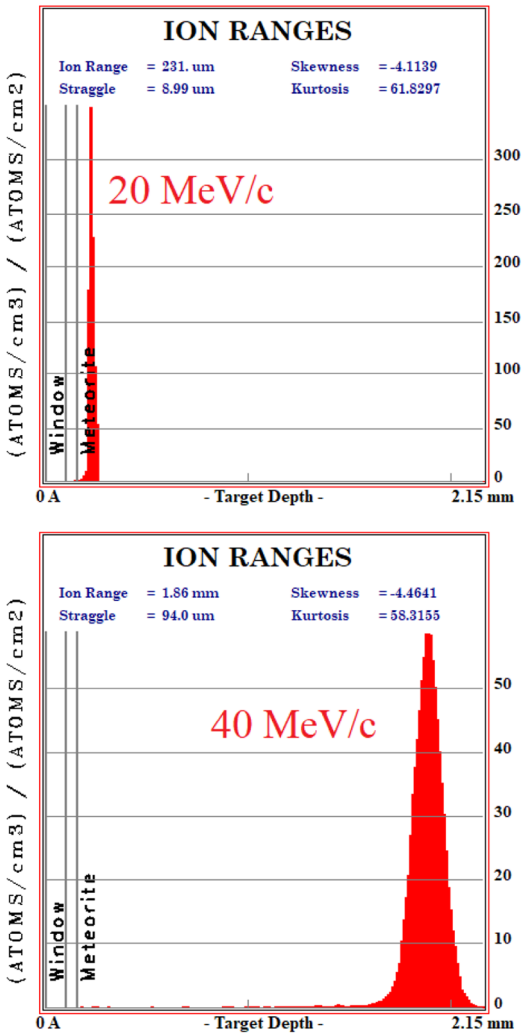

Fig. 4 Monte Carlo simulation on SRIM of the beam penetration into the sample (10 k events). Upper: 20 MeV per c run, lower: 40 MeV per c run. The drawn bands show the depth of the Al layer (0.10 to 0.15 mm) and the meteorite (over 0.15 mm).

2.6 Micro-Raman spectroscopy (μRS)

A Renishaw in-*via* reflex μ-spectrometer coupled in confocality with a Leica optical microscope has been used. It is endowed with two laser sources: a 632.8 nm, 25 mW He–Ne laser and a 514.5 nm, 100 mW solid state laser. The detection system consists in a Charged Coupled Device (CCD) and two different

motorised diffraction gratings with 1800 lines per mm and 3200 lines per mm. The microscope is featured with 3 long working distance objectives, 5 × (0.12 numerical aperture – NA), 50 × (0.75 NA), 100 × (0.75 NA), and 2 short working distance objectives, 20 × (0.40 NA), 50 × (0.50 NA). Further details on the experimental setup are available in ref. 22.

2.7 Scanning electron microscopy in backscattered electrons (BSE-SEM) with energy dispersive X-ray spectroscopy (EDS)

The instrument used for this purpose is a Tescan FE-SEM Mira 3XMU-series equipped with an EDAX spectrometer based on an Apollo XL Silicon Drift Detector (SDD). The instrument has been set to work at 15.8 mm working distance with a 20 kV accelerating voltage and 12 mA beam current. The relative elemental quantification is calculated from the EDS spectrum by the ZAF method. This technique is based on the comparison of the area under Kα emission peaks with standards, correcting the effect given by average atomic number (*Z*), self-absorption (A), and fluorescence excitation (F) on the X-ray emission. Details on the EDS measurements can be found in ref. 22.

3 Results and discussion

3.1 Low-background gamma ray spectrometry results

The choice of using low-background gamma ray spectrometry in an underground laboratory as LNGS was made due to the expected age of the sample, as described in Section 2.2.

Aluminium-26 is a β^+ emitter,[23] which decays on a 1808 keV excited state of ^{26}Mg as a main decay channel (Branching ratio BR 82%).[24] This state promptly de-excites to the ground state of ^{26}Mg by emitting a single 1808 keV gamma ray. As a consequence, the presence of ^{26}Al is marked by the 1808 keV gamma peak, the 511 keV e^+e^- annihilation peak and the 2319 keV sum peak, as the excited state of ^{26}Mg has a negligible half-life ($4.76 \cdot 10^{-13}$ s). The time-normalised gamma spectra of background and of the two bulk samples (R001 and R002) are shown in Fig. 5. The background acquisition lasted 30 days, whereas the measurements of the samples lasted 16 days each. All other peaks correspond to primordial radioactivity normally present in Earth rocks too (^{40}K, ^{232}Th chain, ^{238}U chain).[25]

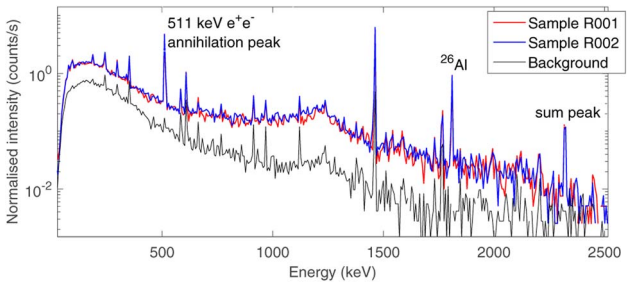

Fig. 5 Time-normalised gamma spectra of the source-uncorrelated background (lower curve, black, 30 days of measurement) and the two meteorite bulk samples (upper curves, blue & red, 16 days of measurement each). The three-peak signature of the presence of ^{26}Al is highlighted: 511 keV annihilation peak, 1808 keV γ emission and 2319 keV sum peak.

The activity of ^{26}Al was estimated from both the 1808 keV and the 2319 keV peak, as the probability of random 511 keV and 1808 keV coincidences can be neglected due to the low activity of the sample.

The resulting values for the specific activity of ^{26}Al are reported in Table 1 (efficiencies are simulated as specified in Section 2.2). These values are *t*-Student confident with each other and their weighted value returns an estimation for the specific activity of ^{26}Al in the whole sample:

$$A = (0.92 \pm 0.06)\ \text{Bq kg}^{-1}$$

A rough estimation of the amount of ^{26}Al in Earth rocks can be given by the concentration of this isotope in ground-level dust,[26] *i.e.* 0.07 ± 0.03 particles per m^3. Calculating the concentration of ^{26}Al in our samples we get $(9.5 \pm 0.8) \cdot 10^{14}$ particles per m^3, and the difference between these values is around 13 standard deviations (calculated by *t*-Student test). As a consequence, this value is not consistent with the typical amount of ^{26}Al contained in Earth rocks[27] and one can conclude that the sample is a meteorite. The slight difference in the values of *A* for the two samples, which can be observed in Table 1, is also present in the quantification of all the measurable fossil radioisotopes in the samples, which is reported in a previous work.[28] However, the uncertainty introduced by MC systematics makes these values consistent with each other.

3.2 ToF-ND results

In this section, the analysis of one spot in sample R002 is presented, as the four diffractograms are consistent with each other.

The fitted spectrum of bank 6 ($2\theta = 73.1°$) coming from the multi-spectral fit for phase analysis is depicted in Fig. 6. The main mineral phases identified in this sample are forsterite (olivine, Mg_2SiO_4), enstatite (pyroxene, $Mg_2(Si_2O_6)$ and magnetite (cubic Fe_3O_4). Furthermore, troilite (FeS) and kamacite (Fe–Ni alloy with Fe : Ni ratio around 95 : 5, originating from Ni

Table 1 Estimation of the activity of ^{26}Al for the two samples using 1808 keV and 2319 keV peaks

Sample	Mass (g)	Isotope	Peak (keV)	Counts/h	Activity (mBq)	Specific activity (Bq kg^{-1})
R001	12.61(36)	^{26}Al	1808	0.90 ± 0.05	12.2 ± 1.4	0.97 ± 0.09
R001	12.61(36)	^{26}Al	2319	0.22 ± 0.02	12.2 ± 1.8	0.97 ± 0.17
R002	14.65(14)	^{26}Al	1808	0.97 ± 0.05	12.6 ± 1.4	0.86 ± 0.10
R002	14.65(14)	^{26}Al	2319	0.21 ± 0.02	12.6 ± 1.9	0.86 ± 0.14

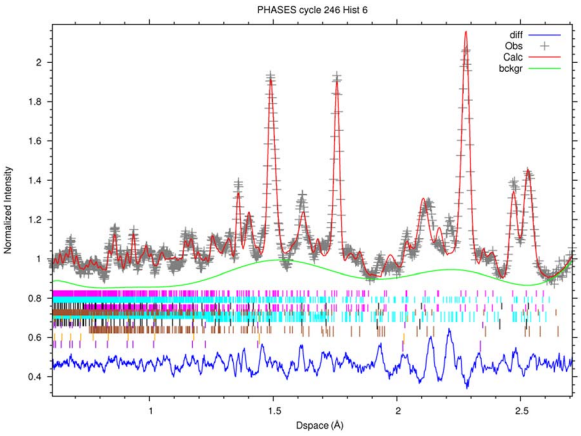

Fig. 6 Rietveld-refined multi-spectral ToF-ND measurement for phase analysis, spectrum of Bank 6 (2θ = 73.1°). Phases: forsterite (pink), enstatite (light blue), magnetite (black), troilite (brown), kamacite (orange), plus the aluminium (violet) of the sample holder. Experimental points are shown in gray, the background fit in green, the refined spectrum fit in red and the residuals in blue. Colors refer to the online version. Reduced $\chi^2 = 7.31$.

Table 2 Results of the phase analysis on the ToF-ND pattern on R002

Phase	% wt over crystalline component
Forsterite	56.0 ± 0.5
Enstatite	30.2 ± 0.5
Magnetite	5.89 ± 0.14
Troilite	6.1 ± 0.3
Kamacite	0.80 ± 0.03

substitutions) have also been found. As the sample was contained in an aluminium holder during the measurements, Al has also been added in the refinement, but it was subtracted from the mineral phase quantification. The quantitative results of phase analysis are reported in Table 2, where each phase is reported in % wt over the total crystalline component.

In peak shape analysis only the three major phases were added and the cells were refined in order to extract cell parameters a, b and c, which are presented in Table 3. In particular, the value of a for forsterite resulted to be (4.7703 ± 0.0002) Å, which lies in between the nominal values for forsterite Mg_2SiO_4 (4.7540 Å) and fayalite Fe_2SiO_4 (4.8211 Å). As these two phases share the same lattice structure, the Vegard law[29,30] can be applied, which assumes that the value of the cell

Table 3 Results of peak-shape analysis on the ToF-ND pattern on R002

Phase	a (Å)	b (Å)	c (Å)
Forsterite	4.7703 ± 0.0002	10.2323 ± 0.0006	5.9967 ± 0.0003
Enstatite	18.2515 ± 0.0017	8.8631 ± 0.0009	5.1970 ± 0.0005
Magnetite	8.3994 ± 0.0005	8.3994 ± 0.0005	8.3994 ± 0.0005

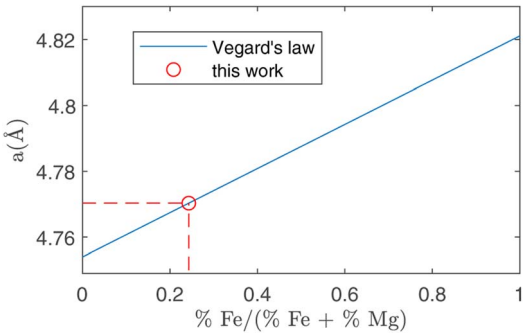

Fig. 7 Running of the a crystal cell parameter as a function of the relative amount of Fe substitutions. The two extremes in this plot are forsterite (without Fe, abscissa = 0) and fayalite (without Mg, abscissa = 1). Using the value for a obtained in forsterite with ToF-ND (circle, see Table 3) it is possible to estimate the amount of Fe substitutions using the Vegard law (solid line).

parameter grows linearly from the forsterite to the fayalite value as the ratio of Fe substitutions increases. This procedure is depicted in Fig. 7. In this way, it was possible to estimate the amount of Fe substitutions as (24.3 ± 0.3)%.

It is typically possible to estimate the amount of Ni in kamacite with a similar procedure. However, it was not possible in this case due to the negligible amount of kamacite, which did not allow this quantification. As a consequence, we manually set a 95 : 5 ratio between Fe and Ni, later confirmed by EDS measurements as reported in Section 3.6. Nevertheless, the described procedure of kamacite calibration by means of the Vegard's law may be interesting in the study of iron meteorites, where the major phases are typically kamacite and taenite.[7]

It is also possible to study the texture and strains in the crystals, on a few specific neutron beamlines.[31] Indeed, the lattice alterations can give information about the extreme conditions withstood by the sample during its formation and its fall in the atmosphere.

3.3 NRCA and NRTI results

The NRCA measurements were carried out together with the ToF-ND data acquisition. The interesting 40–160 μs region in time-of-flight of the NRCA spectrum is presented in Fig. 8 together with the peak identification performed with the ENDF/B-VIII.0 database of neutron-capture cross sections.[32] No other relevant structures were visible in the full 30–1000 μs time-of-flight NRCA spectrum. It was obtained by merging the four sampled spectra as they were all consistent with each other. The region of interest is below 3 keV, *i.e.* over 30 μs, in order to avoid the gamma ray background promptly generated during spallation and moderation. This technique allowed to identify the presence of Fe, Mn and Co. The fact that Mn and Co peaks are larger than the Fe one is not due to energy resolution, but it is a direct consequence of the shape of the resonance in the cross section around the peak energy.

Regarding NRTI, the analysis on the sole sample R002 is here presented, as no difference has been identified between R001 and R002. Furthermore, having sample R002 constant

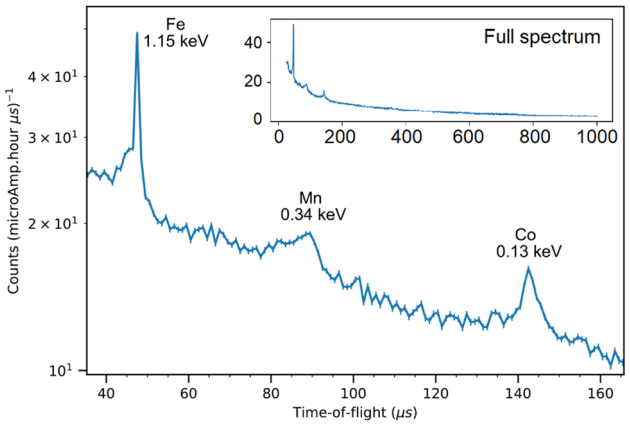

Fig. 8 The 40–160 keV zoom of the NRCA spectrum on sample R002 with peak identification by means of the ENDF/B-VIII.0 database, accessed through the KAERI website.[32] In the inset the full NRCA spectrum is displayed, with the same axes.

thickness, no further corrections are needed, which should be applied to sample R001 as it has a more complex geometry. The main results of NRTI applied to sample R002 are reported in Fig. 9. The total transmission coefficient, calculated on the integrated spectrum, shows that the sample has a uniform neutron absorption within the space resolution of the detector in use (750 μm). The neutron transmission spectrum is also presented in the same figure with peak attribution. It is important to notice that the NRTI spectrum in the (40–160) μs range is complementary to the NRCA spectrum in the same range, as one would expect. This technique allows the identification of Fe, Mn and Co, enabling the investigation of all the neutron energy range as the n-GEM discriminated gamma rays from neutrons. As a consequence it makes possible the study of the time-of-flight spectrum from 0 to 30 μs too, which was excluded by NRCA.

Unlike the ToF-ND and neutron-capture analysis of the Chelyabinsk meteorite,[9] whose inhomogeneities made it interesting to perform Neutron Tomography (NT), in this case the sample proved to be homogeneous at mm scale inspected by NRTI. We therefore decided not to further analyse these data.

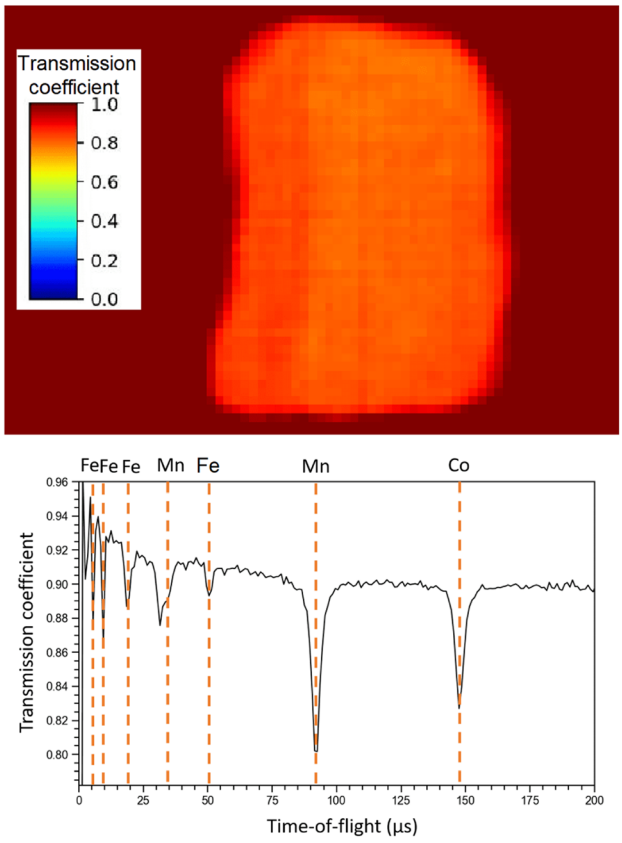

Fig. 9 NRTI integrated transmission coefficient on sample R002 (up), showing the uniformity of the sample, and NRTI spectrum on R002 (down) with peak identification by means of the ENDF/B-VIII.0 database, accessed through the KAERI website.[32]

3.4 μXES results

The four main elements have been quantified in the bulk on the 40 MeV per c run data, *i.e.* investigating around 1–2 mm under the surface (as one can derive from Fig. 4). The % wt of the main elements are: O (30.6 ± 0.9)%, Si (23.6 ± 0.1)%, Mg (23.2 ± 0.1)% and Fe (22.6 ± 0.1)%. These elements are the main constituents of the mineral phases observed by ToF-ND, as a consequence these two techniques return consistent results. In Section 3.6 these results are discussed and compared to the results of EDS.

3.5 μRS results

The μ-Raman mapping spectroscopy confirms the predominance of forsterite and enstatite on the thin section, which can be considered representative of the whole sample. This is because many portions of the thin section were analysed, returning consistent results. The μRS spectra of these two phases, obtained on sample R003, are reported in Fig. 10 with the band attribution.[33] In addition, traces of diopside (pyroxene, $CaMg(Si_2O_6)$), hematite (iron oxide) and quartz (tectosilicate, SiO_2) were identified, along with traces of laser-induced anhydrite.[34] In particular, the Raman signal is visible only in

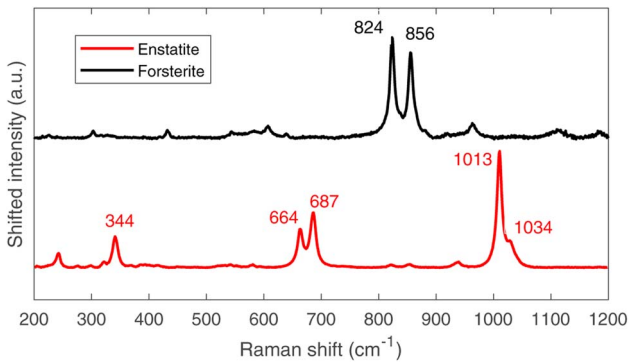

Fig. 10 Raman spectra of forsterite (up, black) and enstatite (down, red), with peak identification.[33]

chondrules, whereas the inter-chondrular matrix appears almost completely Raman-inactive. Fig. 14 shows an overview on the chondrules cross-mapped with μRS and EDS: two chondrules have been studied with both techniques (A and B), whereas two different chondrules were used as mock-ups to understand the main mineral phases (chondrule C, studied with μRS) and the difference in the composition of glass and forsterite (chondrule D, studied with EDS). Detailed results from μRS and EDS mapping can be found in a previous work.[22]

It is crucial to make use of μRS for phase identification as the identification of phases can be cumbersome in ToF-ND and therefore μRS may lead in the ToF-ND data analysis.

3.6 BSE-SEM and EDS results

It has been decided to study with these techniques the same structures in sample R003 investigated with μRS, but other Raman-inactive portions have also been analysed, like the intra-chondrular glass and the metallic relics. For example, the study of chondrule D (see Fig. 14) allowed to identify the richness of the intra-chondrular glass in certain elements such as Si, O, Ca, Na & Al, whereas the surrounding forsterite contains Mg, O & Si above all. The BSE-SEM and EDS mapping measurements are extensively presented in a previous work.[22]

The EDS elemental composition, obtained by repeating the EDS measurement on 20 spots identified as made of forsterite or enstatite (10 spots each) by μRS, is reported in standard box plots in Fig. 11. It is important to observe the different amount of Si, O and Mg, the three main constituents of these two minerals. Furthermore, one can observe the presence of Fe substitutions in both minerals. The amount of substitutions in forsterite can be estimated as $\mathrm{Fe}/(\mathrm{Fe}+\mathrm{Mg}) = (23 \pm 5)\%$, which is t-Student consistent ($t = 0.29$) with the estimation that can be obtained with the ToF-ND applying the Vegard law (24.3 ± 0.3)%. The amount of Fe substitutions in enstatite has not been calculated due to the big relative uncertainty on the amount of Fe.

Some Fe-based relics have been studied too. This part of the probing resulted in the identification of two classes of metallic structures: a Fe–Ni alloy and a Fe–S mineral. An example of the aspect of these relics at BSE-SEM can be seen in Fig. 12. All these relics were surrounded by an iron-based oxidised material. The elemental quantification of these two classes of iron-based

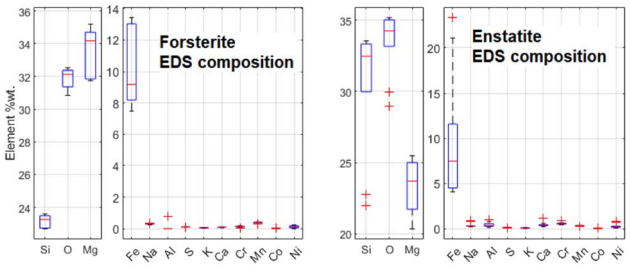

Fig. 11 Comparison between the elemental composition of forsterite and enstatite crystals, obtained by means of 10 EDS measurements for each mineral.

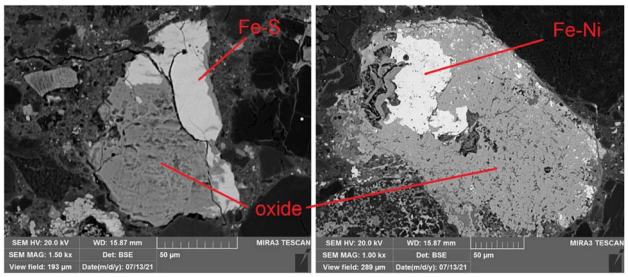

Fig. 12 Example of two iron-based relics (Fe–S left and Fe–Ni right) as seen by BSE-SEM with same level of contrast. The Fe–Ni relic appears brighter (higher atomic number Z) than Fe–S and both are surrounded by a gray area, corresponding to the oxidised metal.

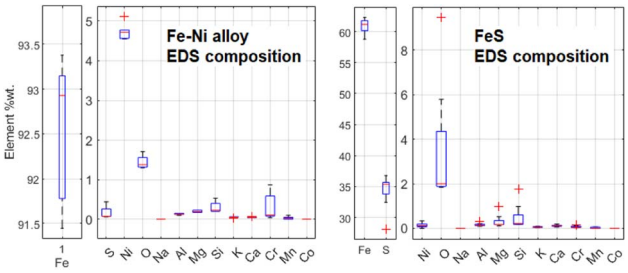

Fig. 13 Comparison between elemental composition of Fe–Ni and Fe–S structures, obtained by means of 5 EDS measurements for Fe–Ni and 8 ones for Fe–S.

structures is reported in Fig. 13. This analysis is consistent with ToF-ND in identifying relevant quantities of magnetite (iron oxide) together with iron compounds with sulfur (troilite) and nickel (kamacite). Those latter phases can be considered Raman-inactive, which is the reason why the inter-chondrular matrix is totally black when observed by μRS. The Fe : Ni ratio in the left box in Fig. 12 has been used in defining the kamacite atomic composition for the ToF-ND data analysis.

In order to have a complete elemental composition on the sample avoiding the overestimation of aluminium due to the thin section treatment method, repeated wide-range EDS measurements were carried out on the polished surface of sample R002. In particular, 100 s EDS measurements were carried out on 5 × 6 mm non-intersecting areas in standard SEM conditions, returning the composition reported in Table 4. The results on the first four phases (normalised totalling 100%) are all consistent within 3σ with the values obtained by μXES (evaluation made with the t-Student test).

A great effort is being made in trying to make these NRCA and NRTI quantitative techniques and μXES more sensitive to low-concentration elements. This would be useful in order to skip the use of a statistically-relevant EDS campaign for elemental quantification. In fact, EDS still requires a polished surface, obtained with a destructive procedure, which can also alter the microstructure of the sample.

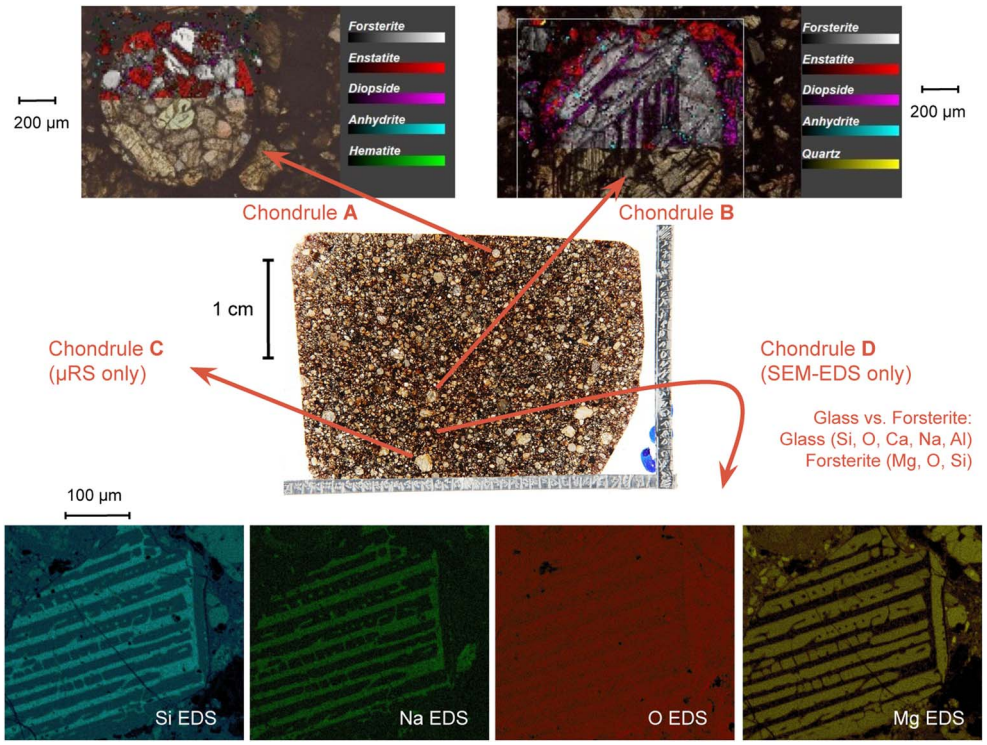

Fig. 14 Combined µRS and SEM-EDS mapping study on four chondrules on the thin section R003. Further details can be found in a previous work.[22]

Table 4 EDS average composition of sample R002, obtained by means of 20 measurements on 5 × 6 mm areas on a polished surface

Element	% wt	Element	% wt
O	28.1 ± 0.6	Ni	1.44 ± 0.11
Si	23.0 ± 0.4	Na	0.51 ± 0.04
Fe	22.5 ± 0.7	Cr	0.46 ± 0.04
Mg	18.7 ± 0.3	Mn	0.29 ± 0.05
Al	1.66 ± 0.08	K	0.145 ± 0.016
Ca	1.65 ± 0.05	P	0.04 ± 0.02
S	1.5 ± 0.3	Co	

4 Conclusions

In conclusion, this multidisciplinary protocol enables the characterisation of the sample in a non-destructive way. In particular, gamma ray spectrometry allows to identify the sample as a meteorite by searching for the presence of cosmogenic radionuclides. If the sample fall is recent (less than about ten years), standard gamma ray spectrometry can be performed, whereas in case of an older fall, low-background gamma ray spectrometry is required. In this case, the presence of ^{26}Al is a marker of the meteoric origin of the studied sample.

It is of crucial importance to notice that the overlapping of surface and bulk techniques is not only a cross-check, because they all return significant information which help the interpretation of other data and contribute to the characterisation of the sample.

In fact, ToF-ND enables the user to perform mineral phase quantification and lattice analysis, provided a hint on the present phases which can be given by a few µRS measurements. We also gave an estimation for the amount of Fe substitutions is forsterite which proved to be consistent with the EDS elemental quantification. However, a thorough mapping of the sample surfaces by means of µRS can yield a precise mineral phase spatial distribution, which can not be obtained with ToF-ND. In some minor phases such as kamacite, the amount of Ni substitutions had to be extracted from a SEM-EDS campaign.

Finally, NRCA and NRTI return a marker of the presence of certain elements (in this case Co, Fe, Mn) while µXES quantifies the weight ratio among the main elements in the sample (O, Si, Mg, Fe). However, a consolidated technique such as SEM-EDS is still required for a trusted, complete and quantitative elemental characterisation, even though it requires a thin section or a polished surface.

Above all, this analysis protocol would enable to insert a meteoric sample into the standard meteorite classification framework without any destructive measurement. This sample proved to be a good mock-up for testing this protocol, whereas more tests are expected to be applied on catalogued meteorites from various classes. Furthermore, research and development is being carried out in order to be able to extract quantitative information on the elemental composition from NRCA and NRTI at INES.

Author contributions

D. D., G. G., M. M., M. P. R. A. S. and M. Cl. conceived the idea of a new methodology for the characterisation of meteorite samples based on a completely non-destructive protocol. M. M. and R. R. performed Raman experiments and data analysis. M. P. R. and R. R. carried out SEM measurements and data analysis. M. Cl., M. L. and R. R. carried out gamma ray measurements, performed MC simulation and analysed data. A. S. carried out neutron measurements, whereas data analysis was carried out by R. R. and A. S. (ToF-ND and NRCA) and G. M. and A. S. (NRTI). A. H., T. A. and M. Ca. carried out muon experiments and data analysis. All authors gave contributions in the results discussion. R. R. wrote the manuscript in consultation with all authors. All authors have read and approved the published version of the manuscript.

Conflicts of interest

There are no conflicts to declare.

Acknowledgements

This work was partially supported within the CNR-STFC Agreement 2021–2027, in particular regarding the activity at the ISIS Neutron and Muon Source. The neutron measurements were carried out at ISIS within the experiment number RB 2000255. The INFN – Laboratori Nazionali del Gran Sasso (Italy) and the Gulf Institute of Gemology (Oman) are thankfully acknowledged for the analytical support.

References

1 R. Hutchinson, *Meteorites: a Petrologic, Chemical and Isotopic Synthesis*, 1st edn, 2004.
2 W. Van Schmus and J. Wood, *Geochim. Cosmochim. Acta*, 1967, **31**, 747–765.
3 V. Alexeev, M. Laubenstein, P. Povinec and G. Ustinova, *Adv. Space Res.*, 2015, **56**, 766–771.
4 H. Postma and P. Schillebeeckx, *Encyclopedia of Analytical Chemistry*, 2009.
5 G. Festa, E. Perelli Cippo, D. Di Martino, *et al.*, *J. Anal. At. Spectrom.*, 2015, **30**, 745–750.
6 A. Fedrigo, D. Raspino, F. Grazzi and A. Scherillo, *J. Anal. At. Spectrom.*, 2019, **34**, 2420–2427.
7 F. Grazzi, A. Scherillo, V. Moggi Cecchi, M. Morelli, G. Pratesi and S. Caporali, *Minerals*, 2018, **8**, 19.
8 K. Podurets, S. Kichanov, *et al.*, *Crystallogr. Rep.*, 2021, **66**, 254–266.
9 S. Kichanov, D. Kozlenko, A. Kirillov, *et al.*, *SN Appl. Sci.*, 2019, **1**, 1563.
10 A. D. Hillier, D. McK Paul and K. Ishida, *Microchem. J.*, 2016, **125**, 203–207.
11 M. Cataldo, M. Clemenza, K. Ishida and A. Hillier, *Appl. Sci.*, 2022, **12**, 4237.
12 M. Clemenza, M. Bonesini, M. Carpinelli, *et al.*, *J. Radioanal. Nucl. Chem.*, 2019, **322**, 1357–1363.
13 M. Clemenza, G. Baldazzi, G. Ballerini, *et al.*, *Nucl. Instrum. Methods Phys. Res., Sect. A*, 2019, **936**, 27–28.
14 S. D'Amico and V. Venuti, *Handbook of Cultural Heritage Analysis*, 1st edn, 2022.
15 M. Grady, G. Pratesi, V. Moggi Cecchi, *Atlas of Meteorites*, 2014.
16 M. Laubenstein, *Int. J. Mod. Phys. A*, 2017, **32**, 1743002.
17 A. S. Agostinelli, J. Allison, K. Amako, *et al.*, *Nucl. Instrum. Methods Phys. Res., Sect. A*, 2003, **506**, 250–303.
18 S. Imberti, W. Kockelmann, *et al.*, *Meas. Sci. Technol.*, 2008, **19**, 34003–34010.
19 A. Larson and R. Von Dreele, *Los Alamos National Laboratory Report LAUR*, 2004, pp. 86–748.
20 F. Sauli, *Nucl. Instrum. Methods Phys. Res., Sect. A*, 2016, **805**, 2–24.
21 J. Ziegler, M. Ziegler and J. Biersack, *Nucl. Instrum. Methods Phys. Res., Sect. B*, 2010, **268**, 1818–1823.
22 M. Musa, R. Rossini, D. Di Martino, M. Riccardi, M. Clemenza and G. Gorini, *Materials*, 2021, **14**, 7585.
23 J. Parrington, H. Knox, *et al.*, *Nuclides and Isotopes: Chart of the Nuclides*, 1996.
24 C. M. Lederer, J. M. Hollander and I. Perlman, *Table of Isotopes*, 6th edn, 1967.
25 M. Eisenbud and T. Gesell, *Environmental Radioactivity from Natural, Industrial and Military Sources*, 4th edn, 1997.
26 M. Auer, D. Wagenbach, E. Wild, *et al.*, *Earth Planet. Sci. Lett.*, 2009, **287**, 453–462.
27 R. Middleton and J. Klein, *Philos. Trans. R. Soc. London, Ser.*, 1987, **323**, 121–143.
28 R. Rossini, M. Clemenza and D. Di Martino *et al.*, *Low-background Gamma Spectroscopy and Neutron Diffraction in the Study of Stony Meteorites*, submitted to Applied Radiation and Isotopes, 2022.
29 L. Vegard, *Z. Phys.*, 1921, **5**, 17–26.
30 R. Cattaneo, C. Chiaramonte Trerè, L. Mordeglia, *et al.*, *J. Anal. At. Spectrom.*, 2011, **26**, 1024.
31 S. Nagler, A. Stoica, *et al.*, *J. Anal. Methods Chem.*, 2019, 6164058.
32 *Evaluated Nuclear Data File ENDF/B-VIII.0*, **https://atom.kaeri.re.kr/nuchart/**, last accessed on 23rd of November, 2022.
33 H.-J. Schubnel and M. Pinet *et al.*, in *Utilité de la microsonde Raman pour l'identification non-destructive des gemmes*, ed. A. F. de Gemmologie, 1st edn, 1992.
34 R. Fogel, *Meteorit. Planet. Sci.*, 1997, **32**, 577–591.

A.5 Paper V

Time-Of-Flight Neutron Diffraction applied to the crystalline phases identification in historical mosaic glasses

Giulia Marcucci,[1,2] Antonella Scherillo[2], Ronald I. Smith[2], and Daniela Di Martino[1]

[1] *Dipartimento di Fisica "G. Occhialini", Università degli Studi di Milano Bicocca and INFN Sezione di Milano Bicocca, IT*
[2]*ISIS Facility Rutherford Appleton Laboratory, Chilton, Didcot, Oxon OX11 0QX, UK*
Corresponding Author e-mail: Antonella.Scherillo@stfc.ac.uk

Abstract. We present a completely non-destructive study of the crystalline phases present in the vitreous matrix of ancient mosaic glass tesserae, based on the application of the time-of-flight neutron diffraction (ToF-ND) technique. In contrast, standard phase analysis techniques may involve a sample preparation step, which is not compatible with the requirement of damage prevention of archaeological artefacts. Moreover, superficial or spot investigation by standard methods may not provide a complete description of the samples, especially in the case of inhomogeneous materials such as mosaic glasses, whereas ToF-ND can investigate the whole glass composition at the centimetre scale. The present study aims to obtain a bulk characterization of the glasses in terms of their mineralogical phase composition. Six glass specimens of ancient mosaic glass tesserae, that had been previously analysed with other non-destructive techniques to obtain their chemical and phase composition, were investigated by ToF-ND. These tesserae come from archaeological excavations or mosaics under restoration from different archaeological sites and geographical areas (Italy, Greece, and Syria) and date from the 1st to the 11th century AD. Several crystalline phases based on Ca, Sb, Sn, Cu and Pb minerals were identified, confirming the mineralogical phases identified with Raman spectroscopy in previous analyses. In addition, several other phases were identified for five of the samples. It is concluded that ToF-ND is an extremely important complementary tool for non-destructive bulk investigations of mosaic glass tesserae, which can overcome the heterogeneity of this kind of archaeological material.

Introduction. The study of opacifiers in glass mosaic tesserae plays a key role into the determination of important historical and archaeological information regarding glass manufacturing technology and its evolutions in ancient times, the provenance of the raw materials and the possible trade routes.

Generally, the opacity was obtained by adding small mineral particles or bubbles diffused in the vitreous matrix. The characterisation of opacifiers is usually achieved through easily accessible and widespread techniques like (micro-) Raman spectroscopy [1-3], X-ray Powder Diffraction (XRPD) [2-4] or synchrotron-based XRPD [5, 6] and Scanning Electron Microscopy-Energy Dispersive Spectroscopy (SEM-EDS) analysis [2, 4, 6].

However, mosaic glasses are rather heterogeneous materials: depending on the area under examination, different results could be obtained due to the different spatial distributions of the modifying ions and crystalline phases present. Therefore, spot analysis like Raman spectroscopy may not detect all the crystalline phases dispersed in the mosaic bulk and/or give inaccurate measurements of the glass composition. Furthermore, in the archaeological field, the prevention of artefact damage is a crucial issue and destructive techniques or sample preparation (as required by SEM-EDS and XRDP) should be avoided.

Following these considerations, it is necessary to account for non-destructive methods which allow bulk analysis in terms of mineralogical phases, like Time-Of-Flight Neutron Diffraction (ToF-ND). Neutrons can penetrate deep into the sample (a few centimetres, even in metallic objects), and they can be used in the same way as photon radiation to determine, via quantitative phase analysis, the crystalline phase composition in the entire bulk of a sample. Despite ToF-ND being a widespread technique for the study of both the mineral phase composition and the microstructure of polycrystalline materials such as metals, alloys, ceramics and stones, no previous neutron diffraction studies applied to mosaic glass tesserae could be found in the literature.

The present paper investigates the potential of ToF-ND as an alternative non-destructive approach to XRPD and as a complementary investigation to Raman spectroscopy for the characterisation of opacifiers in glass mosaic tesserae. The method of choice has been applied at the POLARIS time-of-flight, high intensity, medium resolution powder diffractometer [7] of the ISIS pulsed spallation neutron source, at the Rutherford Appleton Laboratory in the UK. On a pulsed source, the incident beam is not monochromatic and energy-dispersive techniques are employed instead. A pulsed polychromatic "white" beam is incident on the sample and the scattered neutrons are wavelength sorted by measuring their total times-of-flight to fixed detectors, and the d-spacings calculated according to $d = ht/2mLsin\theta$ as it is explained for example in [8].

Six mosaic tesserae were analysed to assess the potential of ToF-ND in investigating this kind of glass artefact. Previous PIXE investigation allows to determine the composition of these glasses, which are typical soda-lime matrixes. Crystalline phase identification was achieved confirming the mineralogical phases identified with Raman spectroscopy. PIXE and Raman results can be found in [9]. In addition, several other phases were identified for five samples as discussed in the Results section, confirming the ToF-ND to be an extremely important complementary tool for non-destructive bulk investigations of mosaic glass tesserae.

Materials and Methods. The current investigation involved the analysis of six mosaic tesserae with different colours, provenance and dating (described in Table 1) to measure the crystalline phases present in the bulk as mentioned in the previous section. No additional sample preparation was required for the diffraction experiment at the POLARIS beamline (ISIS Neutron and Muon Source, Didcot - UK).

At ISIS, neutrons are produced in short pulses by a spallation process involving high-energy protons (800 MeV) striking a tungsten target with a frequency of 50 Hz, generating neutrons having a spectrum of energies in the MeV range, whereas the instruments for looking at the structure of materials require neutrons with meV – eV energies. For this reason, neutrons are slowed down by using moderators made from low-atomic-number material in which neutron absorption is small. For the specific case of the POLARIS instrument station, a moderation made of water at ambient temperature (316 K) is used to achieve the necessary reductions in the neutrons energy. The POLARIS diffractometer with its five large ZnS scintillator-based detector banks covering an angular range of $6° \leq 2\theta \leq 168°$ allows for the collection of data from very small samples, such as the mosaic tesserae, in only a few hours (in our case ~15 hours each). The $\Delta d/d$ resolution varies from ~2.7% in the very low angle bank (which can measure d-spacings up to 40Å) to the highest resolution of ~0.3% in the backscattering bank [7].

Neutrons are diffracted according to Bragg's law and ToF-ND measurements have been carried out as described in [8]. All the tesserae were loaded into thin-walled cylindrical vanadium sample cans

(8 mm of diameter) for collection of the neutron diffraction data. Vanadium is often used for sample containers in neutron experiments because of its high-temperature stability, low reactivity and minimal contribution to the neutron scattering measurements which generally results in vanadium Bragg reflections with very low intensities compared to the peaks of the sample. The measurements were performed in vacuum condition.

The mineralogical phases present in each of the tesserae samples were confirmed using the GSAS code [10] and the EXPGUI interface [11] to calculate the resulting diffraction pattern. For this purpose, Crystal Information Files (CIF) of pure single-phase fingerprints from Crystallography Open Database (COD) [12-14] were used as a reference for the comparison with the experimental data.

Table 1. List of the analysed mosaic glass tesserae. Information regarding the colour, provenance and dating are provided. Sample sizes can be derived by sample images, superimposed on a square background (side of 0.5 cm). The mass range of the tesserae is 3.5-30 g.

Sample name	**Sample image**	**Colour**	**Provenance**	**Dating**
DEL1		Opaque blue	Delos Monastery, Greece	1^{st}–2^{nd} AD
DEL2		Opaque red	Delos Monastery, Greece	1^{st}–2^{nd} AD
DEL3	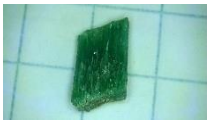	Opaque green	Delos Monastery, Greece	1^{st} - 2^{nd} AD
DAFNI	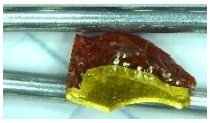	Red with a golden layer	Dafni Monastery, Greece	11^{th} AD
SVP57	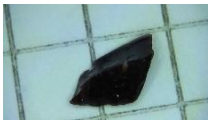	Opaque black	Ravenna, Italy	6^{th} AD
SVR24		Opaque pink	Ravenna, Italy	6^{th} AD

Results and discussion. The obtained diffraction patterns show several peaks according to the Bragg's law. The peak positions are directly related to the crystal lattice dimensions of the different phases present in the bulk of the mosaic glasses. Time-Of-Flight diffraction spectra can be easily converted in d-spacing scale (or even in wavelength or Q scales) to have a direct correspondence between the main intense peaks and the associated crystalline phases. A multi-phase analysis has been

conducted merging the diffraction patterns coming from each detector bank to consider the full d-spacing range available on the POLARIS instrument (0.2-12.6 Å). However, no peaks associated with crystalline phases are present above 4 Å for all the samples.

Figures 1-6 give the association between measured diffraction peaks with calculated or observed positions of pure single-phases considered as references from the COD database. For each tessera, the diffraction pattern of the high-resolution bank (0.2-2.6 Å) is reported and in some cases also the subsequent bank where significative peaks are present in the region 2.6-3.8 Å. Some minor peaks of the diffractograms (e.g. at 1.86 Å in Figure 1) could not be possible to identify considering the likely crystalline phase present in the sample based on the elemental composition measured with the other techniques described in [9].

Through the previously cited Rietveld refinement, Ca-antimonate opacifiers ($CaSb_2O_6$ and/or $Ca_2Sb_2O_7$) have been identified in the bulk of samples DEL1, SVP57 and SVR24. Calcite $CaCO_3$ has been recognized in the tesserae DEL1, DEL2 and DEL3. Moreover, tin-based opacifiers have been detected in both the form of Cassiterite (SnO_2) and Romarchite (SnO) in the blue sample DEL1. Cassiterite peaks have been identified also in DEL3.
In the red tesserae, copper in the form of Cu ion and Cuprite crystals Cu_2O has been found. This composition is compatible with common red colourants found in ancient glass tesserae.
Mineral inclusions of Pyrolusite MnO_2 and Covellite CuS are present in the SVP57, probably with a colouring function associated with the dark appearance of the tessera.

The reported results indicate that ToF-ND is a powerful non-destructive technique for investigating the bulk mineralogical phase composition in order to not only determine the opacifiers but also the oxides and other phases related to colouring function in mosaic glasses.

The identified phases are consistent with previous Raman spectroscopy investigations [9] as listed in Table 2. Moreover, Tof-ND reveals the presence of further phases due to the larger area of analysis which comprehends the entire volume of the tesserae (while the investigated area that a single Raman measurement can reach is micrometric in size – from 2 μm to about 10 μm in diameter). As an example, in sample DEL1 only the phase $Ca_2Sb_2O_7$ was detected with Raman Spectroscopy. On the other hand, both types of calcium-antimonates ($CaSb_2O_6$ and $Ca_2Sb_2O_7$) have been identified in the neutron diffraction pattern as well as both types of tin-oxides, Cassiterite and Romarchite, and the Calcite opacifiers.

The chemical structure of the additional phases detected through neutron diffraction is consistent with the elemental composition of each tessera obtained by previous PIXE analyses published in [9].

Another advantage is the possibility to identify metallic inclusions, such as copper in DEL2, whereas Raman spectra of metals are silent. Because of this feature, the DAFNI tessera has been chosen to be analysed with neutron diffraction to identify the composition of the golden layer on one side of the sample. Even though the ToF-ND has high sensitivity to metals, no peaks related to gold or other metals are present in the diffraction pattern. Instead, the only signal detected is due to the vanadium sample cell. This can be due to a very low phase content compared to the detection limit of the instrument and a longer measuring time may be required to see a significant signal.

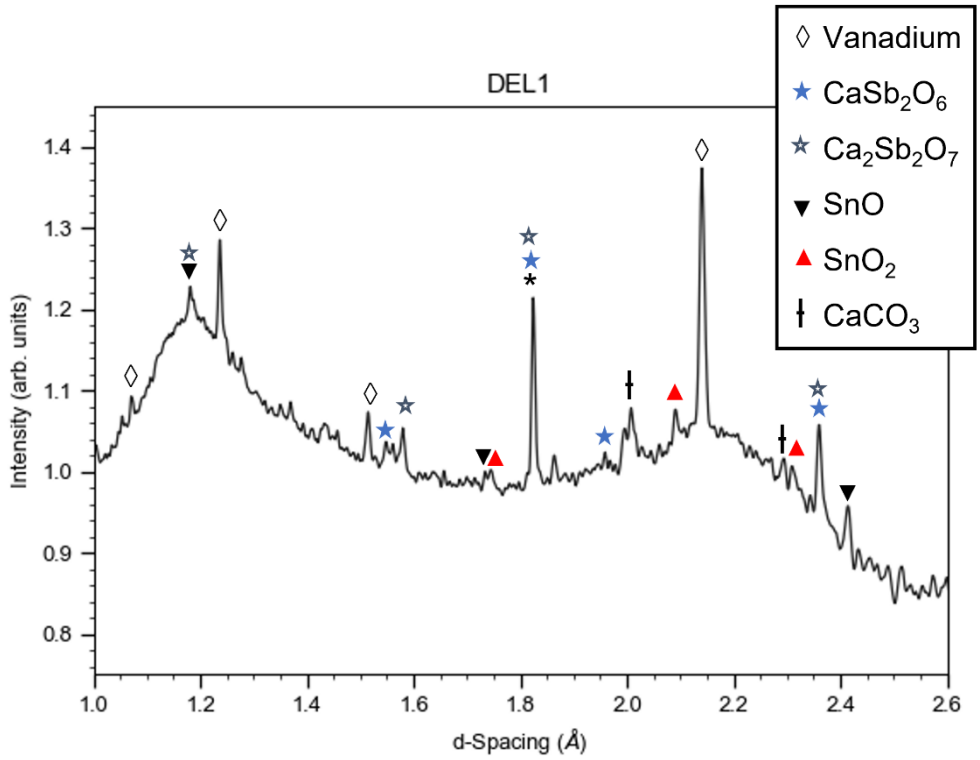

Figure 1. Phases identification for the opaque blue mosaic tessera DEL1 in the d-spacing range 1.0-2.6 Å of the high-resolution bank of the POLARIS beamline. Below 1.0 Å, signal related to vanadium is only present. The vanadium peaks are related to the sample container used to perform the diffraction measurements.

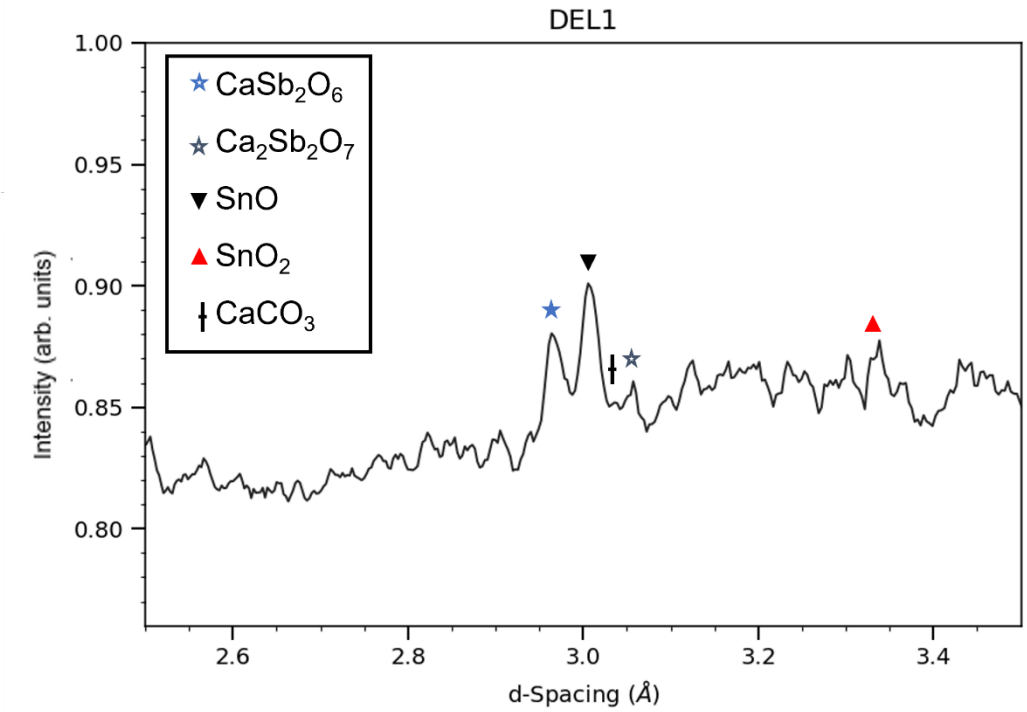

Figure 2. Diffraction pattern of the opaque blue mosaic tessera DEL1 in the d-spacing range 2.5-3.5 Å. This region is reported to highlight the identification of the main peaks of the mineralogical phases present in the sample

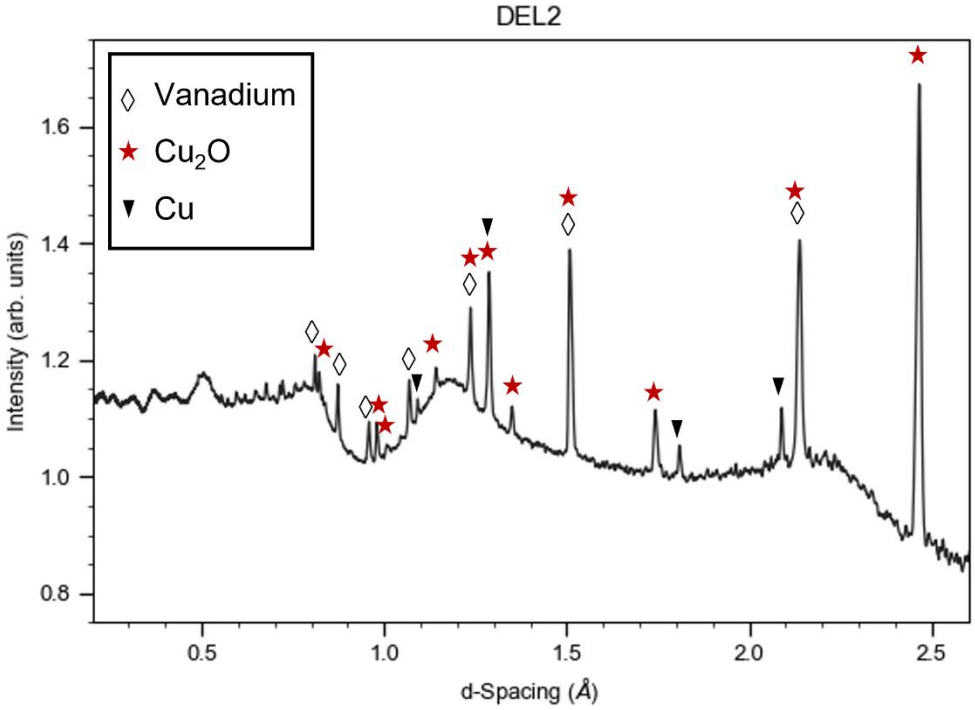

Figure 3. Diffraction pattern of the opaque red mosaic tessera DEL2 in the d-spacing range 0.2-2.6 Å of the high-resolution bank of the POLARIS beamline. The vanadium peaks are related to the sample container used to perform the diffraction measurements.

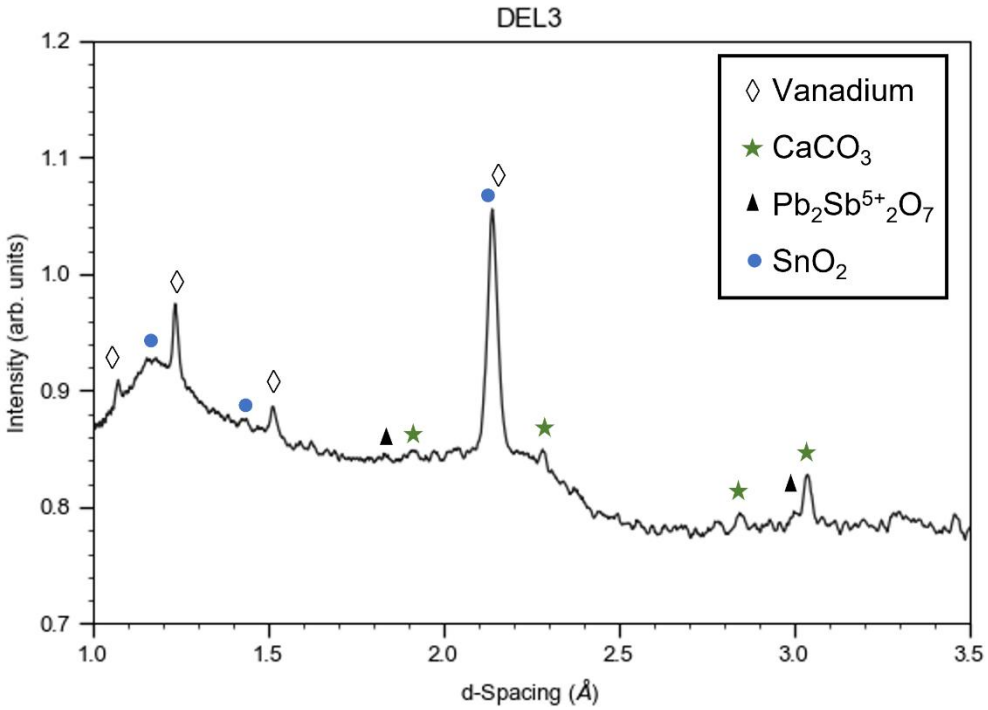

Figure 4. Diffraction pattern of the opaque green mosaic tessera DEL3 in the d-spacing range 1.0-3.5 Å. In this region, the main peaks of $CaCO_3$, $Pb_2Sb_2O_7$ and SnO_2 have been identified. The vanadium peaks are related to the sample container used to perform the diffraction measurements.

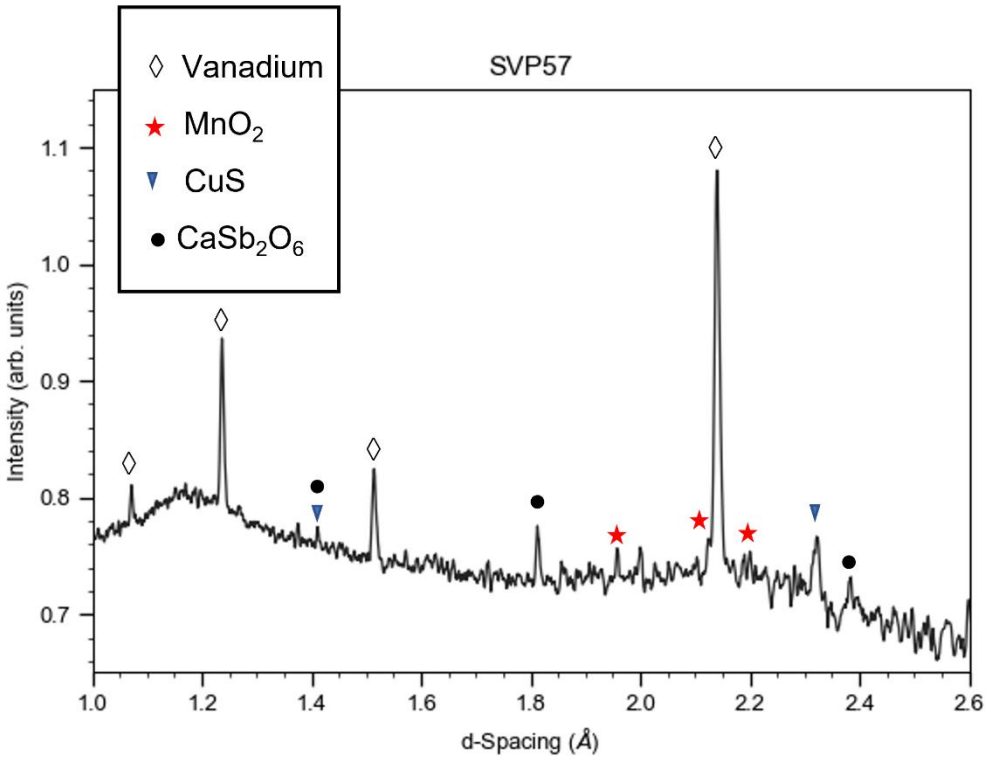

Figure 5. Diffraction pattern of the black mosaic tessera SVP57 in the d-spacing range 1.0-2.6 Å of the high-resolution bank of the POLARIS beamline. The vanadium peaks are related to the sample container used to perform the diffraction measurements.

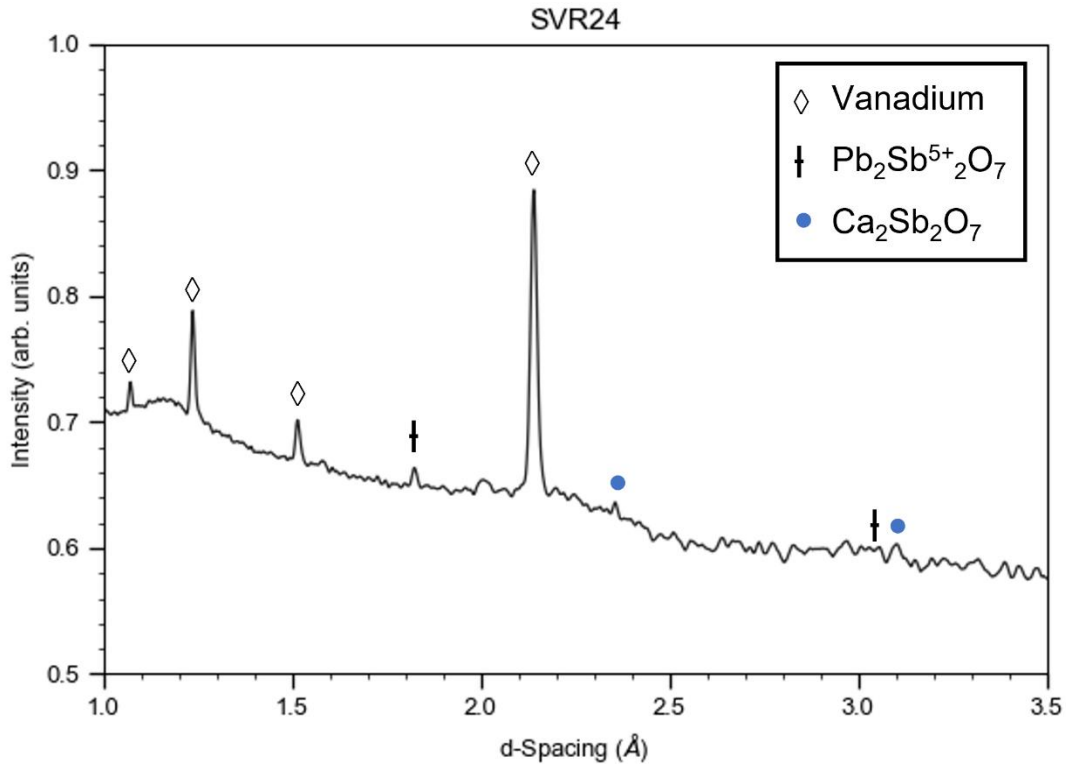

Figure 6. Phases identification for the pink mosaic tessera SVR24 in the d-spacing range 1.0-3.5 Å. In the region below 1.0 Å, signal related to the vanadium sample container is only present.

Table 2. List of crystalline phases and oxides detected through Raman spectroscopy and Time-Of-Flight Neutron Diffraction.

Sample	Raman spectroscopy	Time-Of-Flight Neutron Diffraction
DEL1	$Ca_2Sb_2O_7$	$Ca_2Sb_2O_7$, $CaSb_2O_6$, SnO, SnO_2, $CaCO_3$
DEL2	$CaCO_3$, Cu_2O	Cu, Cu_2O
DEL3	$CaCO_3$	$CaCO_3$, $Pb_2Sb_2O_7$, SnO_2
SVP57	$CaSb_2O_6$, Na_2SO_4	$CaSb_2O_6$, MnO_2, CuS
SVR24	$Ca_2Sb_2O_7$, $Pb_2Sb_2O_7$	$Ca_2Sb_2O_7$, $Pb_2Sb_2O_7$

Conclusions. Prior studies on mosaic glass tesserae usually employed invasive or spot/superficial techniques to characterise the crystalline phases acting as opacifiers and colourants in the vitreous matrixes.

In this paper we explore a new approach for the investigation of the mineralogical phases in this kind of archaeological sample, focusing on the choice of a non-destructive method which can provide information on the entire sample volume. For this reason, ToF-ND was chosen as it is already widely applied for the study of phases and oxides in other types of objects in the Cultural Heritage field.

The application of ToF-ND on six ancient mosaic tesserae yielded a successful determination of calcium- and lead-antimonates opacifiers, tin-oxides opacifiers, and colourants in the form of copper, copper oxides and sulphide and manganese oxides.

The comparison between neutron diffraction data and previous Raman analyses highlights the ability of ToF-ND to determine the overall mineralogical composition of the tesserae and its advantage of obtaining information on both crystalline and metallic phases in a single measurement. Hence, ToF-ND is a valuable alternative to destructive methods and complementary to Raman spectroscopy, which can be used as a preliminary analysis to identify some phases useful for the neutron diffraction data refinement.

Acknowledgements. This work was partially supported within the CNR-STFC Agreement 2014–2020, concerning collaboration in scientific research between the spallation neutron source ISIS (UK)

and CNR (Italy). We acknowledge ISIS Neutron and Muon Source for beamtime on POLARIS. Data is available here: 10.5286/ISIS.E.RB1910332.

References

1. Basso, E., Invernizzi, C., Malagodi, M., La Russa, M.F., Bersani, D. & Lottici P.P. Characterization of colorants and opacifiers in roman glass mosaic tesserae through spectroscopic and spectrometric techniques. *Journal of Raman Spectroscopy*, 2014, **45**, 238-245.
2. Vandini, M. & Fiorentino, S. From Crystals to Color: A Compendium of Multi-Analytical Data on Mineralogical Phases in Opaque Colored Glass Mosaic Tesserae. *Minerals*, 2020, **10**, 609.
3. Bersani, D., Saviane, L., Morigi, A., Mantovani, L., Aceto, M. & Fornasini, L. Multi-technique characterization of glass mosaic tesserae from Villa di Teodorico in Galeata (Italy). *Journal of Raman Spectroscopy*, 2021, **52**, 2234–2245.
4. Silvestri, A., Tonietto, S., Molin, G. & Guerriero, P. Multi-methodological of paleo-Christian glass mosaic tesserae of St.Maria Mater Domini (Vicenza, Italy). *Eur. J. Mineral.*, 2015, **27**, 225-245.
5. Lahlil, S., Biron, I., Cotte, M. & Susini, J. New in-situ crystallization of calcium antimonate opacified glass during the Roman period. *Appl. Phys. A*, 2010, **100**, 683–692.
6. Casas, L., Di Febo, R., Boix, C., Egea, A., Vallcorba, O., Queralt, I., Anglisano, A., Moreno, I. & Andino, L. The Colors of the Circus Mosaic from Barcino (Roman Barcelona): Characterization, Provenance, and Technology Issues. *Minerals*, 2021, **11**, 746.
7. Smith, R.I., Hull1, S., Tucker, M.G., Playford, H.Y., McPhail, D.J., Waller, S. P., Norberg, S.T. The Upgraded Polaris Powder Diffractometer at the ISIS Neutron Source. *Rev. Sci. Instrum.*, 2019, **90**, 115101.
8. Willis, B.T.M. Crystallography with a pulsed neutron source. *Z. Kristallogr.*, 1994, **209**, 385. doi:10.1524/zkri.1994.209.5.385
9. Marcucci, G., Scherillo, A., Cazzaniga, C., Lemasson, Q., Lorenzi, R., Clemenza, M., Riccardi, M.P. & Di Martino, D. Historical glass mosaic tesserae: a multi-analytical approach for their characterization. *Eur. Phys. J. Plus*, 2021, **136**, 738.
10. Larson, A.C., Von Dreele, R.B. General Structure Analysis System (GSAS). *Los Alamos National Laboratory Report LAUR*, 2004, 86-748.
11. Toby, B.H. EXPGUI, a graphical user interface for GSAS. *J. Appl. Crystallogr.*, 2001, **34**, 210-213
12. Gražulis, S., Daškevič, A., Merkys, A., Chateigner, D., Lutterotti, L., Quirós, M., Serebryanaya, N. R., Moeck, P., Downs, R. T. & LeBail, A. Crystallography Open Database (COD): an open-access collection of crystal structures and platform for world-wide collaboration. *Nucleic Acids Research*, 40, D420-D427. doi: 10.1093/nar/gkr900
13. Gražulis, S., Chateigner, D., Downs, R. T., Yokochi, A. T., Quiros, M., Lutterotti, L., Manakova, E., Butkus, J., Moeck, P. & Le Bail, A. (2009). Crystallography Open Database – an open-access collection of crystal structures. *J. Appl. Crystallogr.*, 42, 726-729. doi: 10.1107/S0021889809016690
14. https://www.crystallography.net/cod/ Accessed 9th Sept 2022

A.6 Paper VI

Nuclear Inst. and Methods in Physics Research, A 1051 (2023) 168189

Contents lists available at ScienceDirect

Nuclear Inst. and Methods in Physics Research, A

journal homepage: www.elsevier.com/locate/nima

Full Length Article

The new INFN-CHNet neutron imaging facility

N. Gelli [a], L. Giuntini [a,b], F. Cantini [a,b,c], O. Sans-Planell [d,e], M. Magalini [d,e], M. Manetti [a], L. Sodi [a], M. Massi [a], L. Castelli [a], C. Czelusniak [a], F. Taccetti [a], T.E. Bella [f], G. Marcucci [g,h,i], M. Clemenza [g,h], D. Di Martino [g,h], M. Morigi [j,k], M. Bettuzzi [j,k], L. Vigorelli [d,e,l], A. Re [d,e], A. Lo Giudice [d,e], D. Alloni [m,n], M. Prata [m,n,p], S. Altieri [m,o], A. Salvini [m,n], F. Grazzi [a,c,*]

[a] INFN Sezione di Firenze, Italy
[b] Dipartimento di Fisica e Astronomia, Università degli Studi di Firenze, Italy
[c] Consiglio Nazionale delle Ricerche, Istituto di Fisica Applicata "Nello Carrara", Sesto Fiorentino, Italy
[d] INFN, Sezione di Torino, Torino, Italy
[e] Dipartimento di Fisica, Università degli Studi di Torino, Italy
[f] Independent researcher
[g] INFN Sezione di Milano Bicocca, Milano, Italy
[h] Dipartimento di Fisica "G. Occhialini", Università di Milano Bicocca, Milano, Italy
[i] ISIS Facility, UKRI-STFC, Rutherford Appleton Laboratory, Didcot, UK
[j] INFN Sezione di Bologna, Italy
[k] Dipartimento di Fisica ed Astronomia "Augusto Righi", Università di Bologna, Italy
[l] Dipartimento di Elettronica e Telecomunicazioni, Politecnico di Torino, Italy
[m] INFN Sezione di Pavia, Italy
[n] Laboratorio Energia Nucleare Applicata (LENA), Pavia, Italy
[o] Dipartimento di Fisica, Università di Pavia, Italy
[p] European Commission, Joint Research Centre, Ispra (VA), Italy[1]

ARTICLE INFO

Keywords:
Neutron imaging
Neutron tomography
Thermal neutron
Morphological analysis
Cultural heritage application

ABSTRACT

In this paper, NICHE (Neutron Imaging for Cultural HEritage), the new neutron imaging facility of the Italian National Institute of Nuclear Physics (INFN) is shortly presented. We report on the main features of the beamline, the specifications of the detection set-up, and the performances of the imaging system. NICHE is installed at the TRIGA reactor of LENA (Laboratorio Energia Nucleare Applicata) Pavia University laboratory (Italy). The imaging facility was designed during 2020, installed in the spring 2021, and has been in operation since May 2021. NICHE is the first Italian neutron imaging station open to national external users through the INFN-CHNet network application system. NICHE allows users to obtain neutron radiographies and tomographies, thus allowing for morphological characterisation of samples. First results to highlight the potential of the facility are reported. In particular, we show the first results about spatial resolution measurement and 3D reconstruction to provide morphological analysis capabilities.

1. Introduction

The Cultural Heritage Network INFN-CHNet is a research infrastructure, widespread all over Italy, of the Istituto Nazionale di Fisica Nucleare (INFN) dedicated to the development and the applications of analytical techniques to perform advanced diagnostic on materials and artefacts related to Cultural Heritage (CH) [1]. It is based on several research centres, both in Italy and abroad, where cutting-edge technologies are developed and optimised in order to address the needs of Cultural Heritage researchers, such as archaeologists, historians, art historians, restorers, and conservators, as regards diagnostic features [2].

Within CHNet, many complementary analytical techniques are available whose scientific output quality is continuously improved and upgraded. The use of different analysis and diagnostic technologies provides complementary information aiming at facilitating the application of the best practices for restoration/conservation. Analyses are also useful for characterising materials and manufacturing techniques, studying the provenance of the raw materials, and giving indications about material authenticity.

* Corresponding author at: Consiglio Nazionale delle Ricerche, Istituto di Fisica Applicata "Nello Carrara", Sesto Fiorentino, Italy.
E-mail address: f.grazzi@ifac.cnr.it (F. Grazzi).
[1] Present address.

https://doi.org/10.1016/j.nima.2023.168189
Received 17 January 2023; Accepted 5 March 2023
Available online 8 March 2023

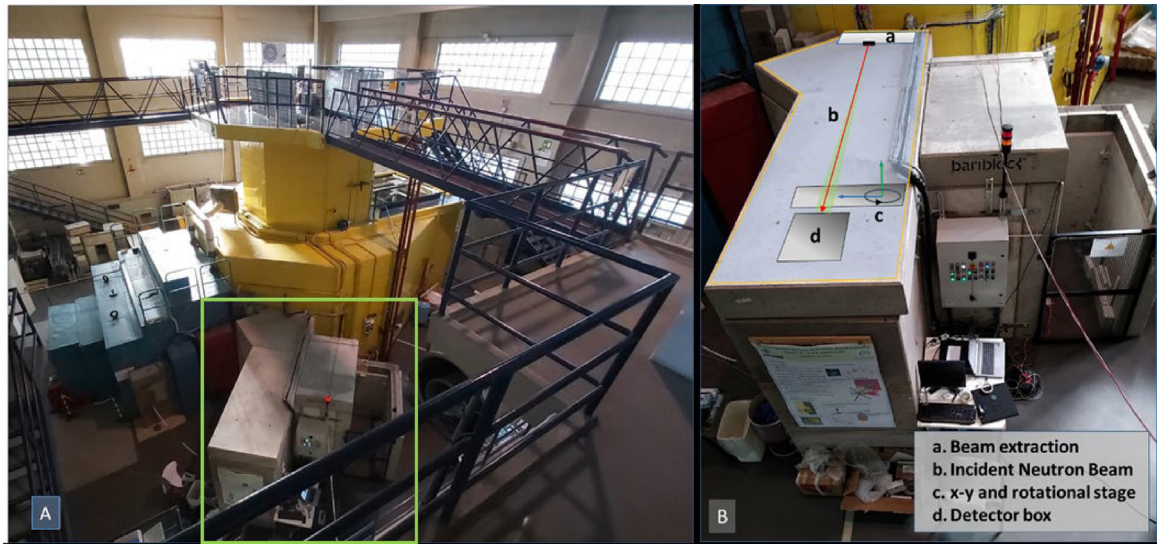

Fig. 1. A: panoramic view of the TRIGA reactor at LENA laboratory, including the port B experimental hutch (highlighted in green) where the NICHE set-up is host. B: superimposed schematic diagram of the NICHE set-up main components and aerial view of the experimental hutch.

Until 2021, neutron imaging (NI) was not available within CHNet, notwithstanding its tailored features for non-destructively evaluating sample morphology. NI integrates/complements results from well-known and widely-used X-ray radiography and tomography.

NI is a well-established election technique in the study of various metal composite samples [3–11], as different metals cannot be penetrated or measured with a relevant contrast factor in X-ray imaging while they exhibit reasonable transparency and relevant contrast in neutron radiography. Analogously, organic materials containing hydrogen can be visualised using NI, although surrounded by metal, a result very hard to achieve using X-rays [4].

These are the main reasons that led to the conception and implementation of the INFN-CHNet NICHE facility, described in this paper. The new NI station, developed in the framework of the NICHE experiment, was installed at the thermal beam port channel B of the TRIGA reactor of Laboratorio Energia Nucleare Applicata (LENA), in Pavia (Italy).

2. NICHE: presentation and overview

In recent years, the efficiency of digital imaging systems as well as the light yield of scintillator-based neutron detectors improved in sensitivity, dynamic range and linearity thus it makes possible to perform imaging analysis even at weak neutron sources. This allows to exploit small neutron sources, such as low-power research reactors (e.g. the TRIGA type [12]) and accelerator driven sources [13] to perform good quality NI.

The quality of NI data depends on the beam properties, such as neutron flux, collimation, beam size, and background noise (environmental and detector related). Concerning the TRIGA reactor available at LENA, simulations and preliminary tests, aiming at the neutron beam characterisation, showed promising results, notwithstanding the limited reactor power (250 kW) and the limited daily working duty-cycle (6 h, four days a week) [14].

The beam-port B of the TRIGA reactor (radial port, facing on the moderator) has the best potential for thermal NI applications, as it exhibits the highest ratio of thermal neutron with respect to the total neutron flux. The flight tube contains 70 mm bismuth and 100 mm sapphire filters to lower gamma and epithermal flux. The Monte Carlo N-Particle (MCNP) radiation transport code [15] was used to simulate the flux at the shutter beam position which turned out to be 1.6×10^7 cm^{-2} s^{-1} for the thermal component, 3.5×10^5 cm^{-2} s^{-1} for the epithermal component, and 2.1×10^5 cm^{-2} s^{-1} for the fast component. The evaluated gamma flux is $\sim 10^6$ cm^{-2} s^{-1} MeV^{-1} in the range 1–5 MeV [14]. These results make this beam port potentially suitable for thermal NI. The neutron shutter is located at the external wall of the TRIGA reactor monolith, approximately at 4.12 m from the reactor core.

3. Instrumental setup

An experimental hutch was already built around the B port shutter with constraints related to the available space and the multiple use of such port for other experimental activities, as shown in the aerial view of Fig. 1A. The size and shape are: 2.5 m length, 0.6 m minimum width, 2.1 m height, entrance area with double corner labyrinth. These imposed constraints imply strict limitations to the mechanical design of the imaging experimental station.

Beam collimation for imaging purposes is based on the use of removable and interchangeable cartridges (830 mm away from the shutter external wall) made of borated ceramic tiles [16] with variable pin-hole diameter (5, 10, 20, 30, 40, and 50 mm size).

The sample position area allows for its horizontal and vertical translation (orthogonal to the beam) and rotation around a vertical axis. Two linear stages using precision stepper-motors allow the horizontal and vertical translation, while rotation is made by a PI M-060 stage. All translation and rotation stages are remotely controlled.

The imaging camera box is composed by a 300 μm-thick ^{6}LiF/ZnS(Ag) scintillator screen 200 × 200 mm wide, followed by a 45° mirror, a 35 mm focusing lens and a ZWO ASI 2600 MM pro CMOS camera (16 bit). Lens focusing and camera operation are both remotely controlled. Pixel size corresponds to 30×30 μm^2 on the scintillator in the current configuration, allowing for a field of view (FOV) of 180×120 mm^2. The 45° mirror is used to limit the radiation damage induced by the neutron beam to the CMOS camera. A light-tight camera box houses the whole system. Remote control of the sample positioning, the lens focusing and the camera system is operated via ARDUINO Mega, using an in-house developed software in the LabView 2018 SP1 environment. The code is designed to perform multiple command sequence, allowing the execution of sequential radiographies in different areas of the sample and the acquisition of tomographic projections, if necessary.

A scheme of the neutron imaging set-up components is shown in Fig. 1B.

A few pictures of the inner area of the NICHE experimental hutch are shown in Fig. 2A and B. The details of the camera box components are shown in Fig. 2C.

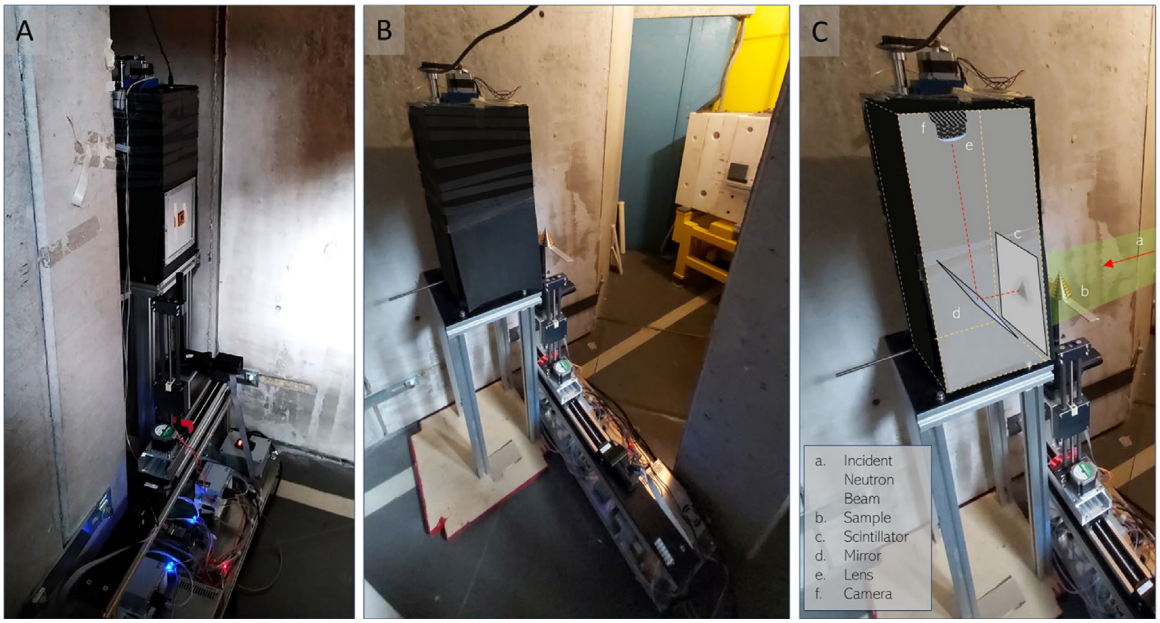

Fig. 2. A–B: Pictures showing sample translation and rotation stages, and the detector camera box. C: Picture and sketch of the optical components within the camera box.

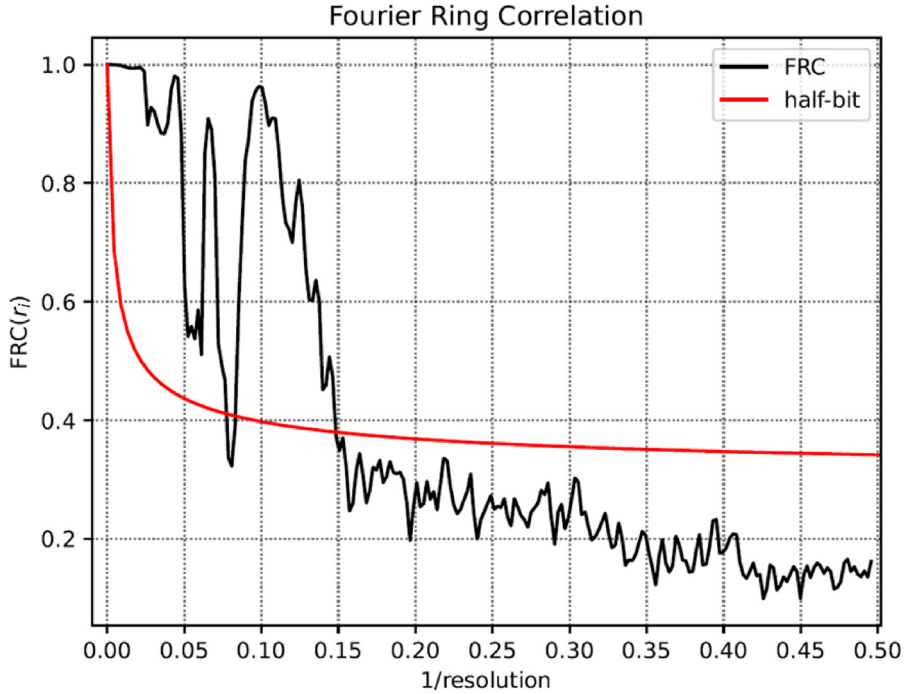

Fig. 3. FRC analysis of Siemens star sample at 50 mm distance from scintillator (L/D = 140) providing a resolution of 30/0.15 μm.

4. Characteristics and performances

In order to maximise the flexibility of the NICHE imaging station, we selected two extreme working positions exhibiting, respectively, the highest flux and the highest spatial resolution. These two configurations correspond to the minimum (position A Table 1) and maximum (position B Table 1) possible distance between the sample and the pin-hole. The L/D ratio (L is the distance between the pin-hole and the sample; D is the diameter of the pin-hole) is the parameter commonly used to define the resolution power of an imaging system. We decided to provide specifications for the 10 mm-diameter pin-hole because it maintains a reasonably short exposure time together with an acceptable resolution, while the improvement in flux of larger pin-hole configurations does not compensate for the reduction in resolution.

The resolution of the radiographs has been estimated in the different working conditions by using several spatial resolution reference samples, such as the "bar pattern" and "Siemens star" produced and distributed by the Paul Scherrer Institut (PSI) [17]. The best resolution was measured by sticking a Gd reference sample, based on bar pattern grid, directly on the scintillator.

An accurate evaluation of the resolution can be achieved by applying the Fourier Ring Correlation (FRC) method to a set of two twin images taken on the same sample in the same experimental configuration and performing a frequency analysis [18]. An example of FRC application is shown in Fig. 3, where a set of images of a Siemens

Table 1
Basic imaging parameters in two different experimental configuration maximising flux (A) or resolution (B). The best resolution was measured by sticking a Gd reference sample, based on bar pattern grid, directly on the scintillator; D = diameter of the full brightness area of the neutron beam, and S = side of the inscribed square.

A: pin-hole to sample distance 140 cm	B: pin-hole to sample distance 190 cm
L/D ≈ 140	L/D ≈ 190
Field of view: D = 65 mm, S = 45 mm	Field of view: D = 95 mm, S = 65 mm
Best spatial resolution: 150 μm	Best spatial resolution: 125 μm
Radiography Acquisition time: 300 s	Radiography Acquisition time: 600 s

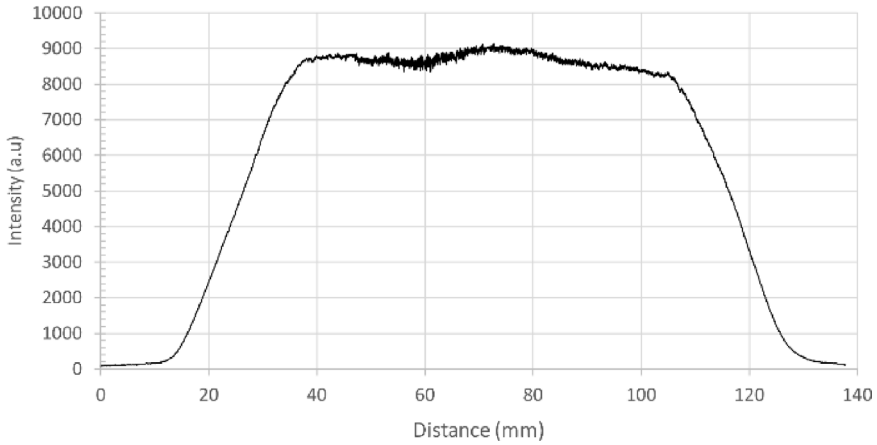

Fig. 4. Beam intensity profile at its horizontal diameter, showing good uniformity in the central area. It also allows for the measurement of the full brightness field of view, which results to be about 9 cm FWHM at 190 cm from the pin-hole.

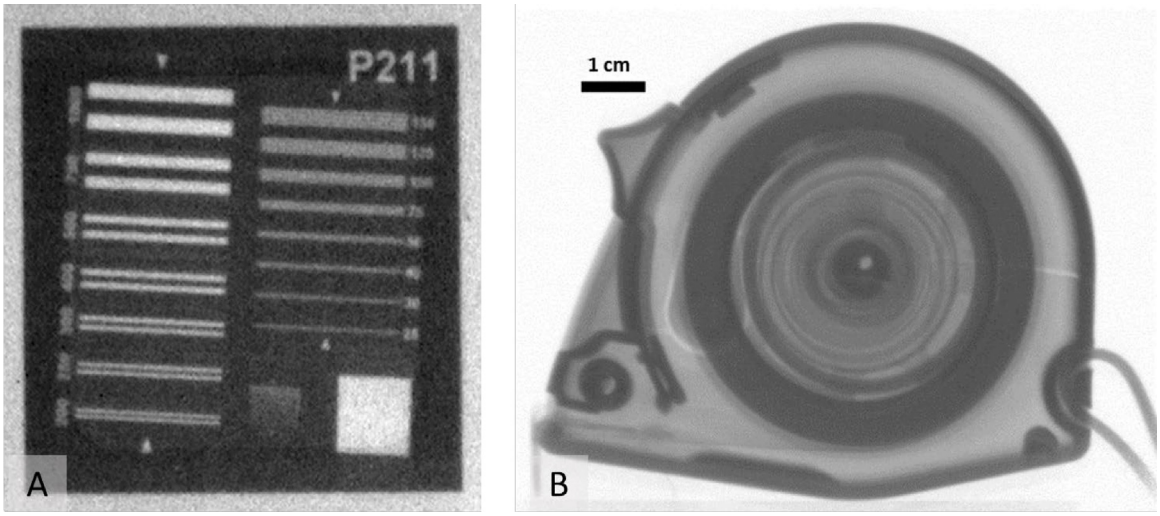

Fig. 5. Neutron radiographs collected at L/D = 190, integration time 300 s, sample-to-scintillator distance 40 mm. A: the PSI bar pattern (25 mm side length) devoted to spatial resolution estimation; B: rolled metal tape with plastic case.

star [17] was acquired at NICHE at 50 mm sample-to-scintillator distance (L/D = 140), a typical working distance for a complex geometry sample, and exhibiting an intersection point between data and half bit function threshold [19] at 0.15 unit/resolution. The resolution value is obtained by dividing the pixel size by such a parameter, thus providing an effective resolution of 200 μm for samples in the typical measuring position (50 mm distance from scintillator).

In Fig. 4, the beam intensity profile is reported, showing good uniformity in the central area. The analysis of sample image raw data was performed by using the free software package ImageJ [20]. As a first step, we apply on every image a "spot filter" to remove the pixels that "shoot" anomalously due to gamma radiation; after that, it is always necessary to subtract the "dark" image from the raw intensity data: in this way we can take into account the CMOS dark current. The background-subtracted sample image is then normalised dividing it by applying open beam image normalisation to erase effects related to variations in incident intensity.

In the following part of the paper, we report some selected examples of neutron radiographs acquired with NICHE, showing the potential of the facility in terms of field of view, contrast, and spatial resolution for a large variety of flat and 3D samples, made up of different combinations of materials. In this way, it is possible to evaluate the capability of morphological analysis in composite objects, and the ability to differentiate among various constituents.

Fig. 5 shows two open beam corrected (normalised) radiographs taken with L/D = 190 and the samples positioned at 40 mm from the scintillator screen, using 300 s integration time.

Fig. 5A shows the PSI bar pattern radiography, that allows to estimate the spatial resolution of the system by mapping which of the tilted lines are visible and well-resolved according to their size

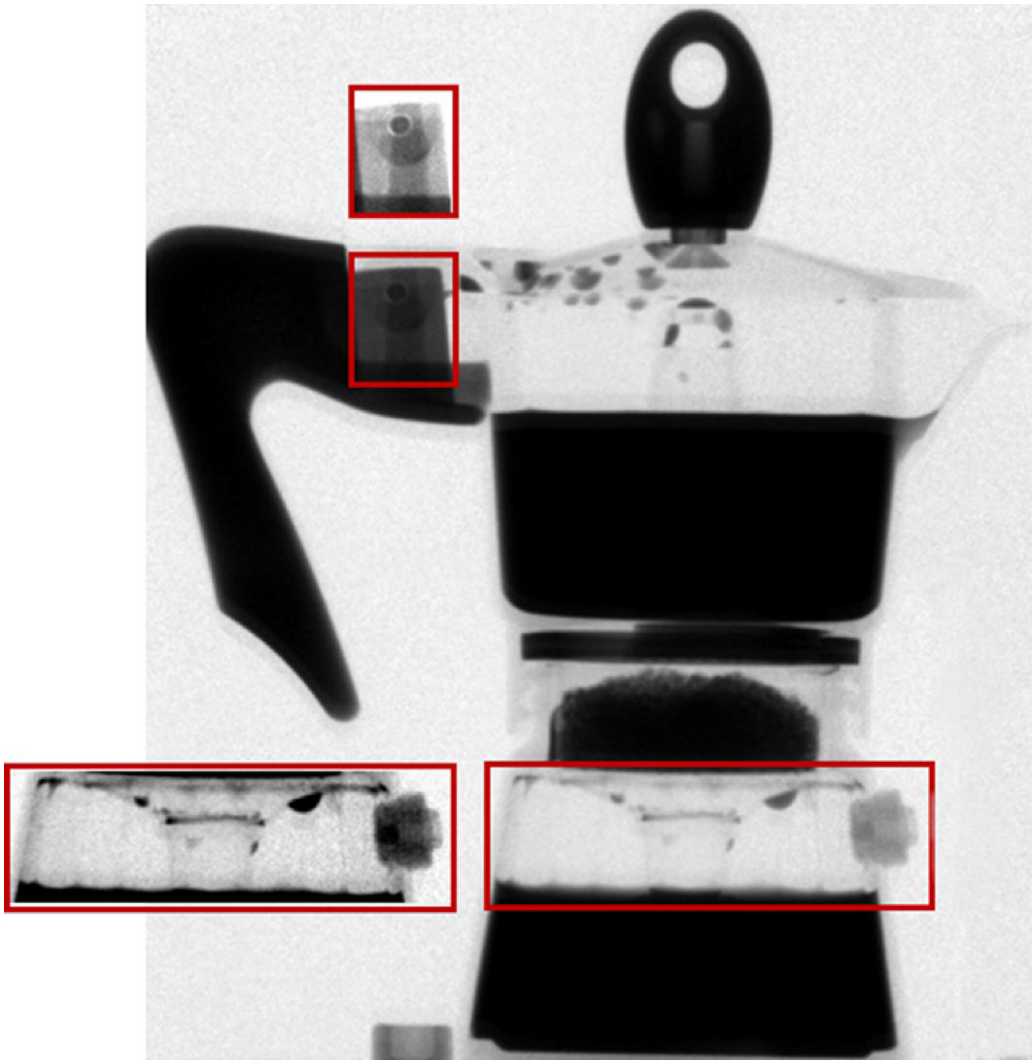

Fig. 6. Composite radiograph of a moka pot, obtained as a mosaic of 2 × 2 neutron images, stitched together. The insets show inner structure and connecting parts of the machine case.

and inter-spacing, 150 μm in this case. The radiograph of a rolled tape metre (Fig. 5B) shows the assembled structure containing a metal tape encased within a plastic frame. Different grey tones reveal the arrangement of the rolled tape and of the mechanical joints of the case.

It is possible to perform neutron radiographs of samples larger than the neutron beam spot size by using the horizontal and vertical translations stages. We can move the sample to take partial radiographs in different positions and later recombine them. However, present spatial constraints in the experimental hutch do not allow full coverage of objects larger than 25 cm.

In order to test the stitching procedure, we choose to cover the whole area occupied by a moka pot (inspired by A. Kaestner [21]) by taking four radiographs arranged in a 2 × 2 grid. The composite normalised image, obtained by using pairwise stitching ImageJ tool [22] is shown in Fig. 6, where it is evident that no stitching artefacts are visible. In the image it is possible to observe several interesting features, such as the different attenuation power of coffee powder, the aluminium case, the water reservoir and also the water droplets dispersed in the upper chamber of the coffee machine and on the lid. Red-squared insets highlight selected areas in which further details are pointed out by adjusting brightness and contrast.

Neutron tomography was performed by exploiting the sample rotating stage. Because of the large number of projection images (minimum 300 according to pixel size and imaging station spatial resolution) and the minimum time needed for each of them in order to have an acceptable signal to noise ratio (120 s), a tomography requires at least two operational days at LENA to be completed.

As an example, we show, in Fig. 7, the tomographic reconstruction of a plastic figure. Data were processed using Octopus [23] for reconstruction and different ImageJ spatial linear and radial filters [20] to preliminary process the projections. The 3D rendering was performed by using 3D Slicer 4.11 [24].

It is interesting to note the capability of the system to highlight the plastic parts with very good spatial definition, notwithstanding the high incoherent scattering power of such hydrogen-rich material.

5. Conclusions

The commissioning of the new Neutron Imaging facility is completed and the NICHE station is currently fully operative at the TRIGA reactor of the LENA laboratory.

NICHE is integrating the diagnostic instrumentation already owned by the INFN-CHNet and widening the range of available technologies of the network.

It allows the acquisition of single radiographs with good spatial resolution (up to 125–150 μm) and a maximum field of view of about 9 cm (diameter).

The sample positioning remote system allows carrying out measurements even on objects larger than the field of view, by making

Fig. 7. Example of results of neutron tomography on a plastic model (approx. 3.5 cm height). 3D rendering and sectioning show the inner structure.

multiple radiographs and stitching them without introducing artefacts or discontinuities.

The system also allows the acquisition of tomographies, still with effective spatial resolution (better than 250 μm) and contrast suitable for material science analysis.

The NICHE neutron imaging station will allow to perform case studies of interest in the field of CH, providing morphological and microstructural information not obtainable with the more conventional X-ray imaging.

CRediT authorship contribution statement

N. Gelli: Project management and organization, Equipment project construction and testing, Data acquisition and treatment. **L. Giuntini:** Equipment project construction and testing. **F. Cantini:** Instrument install and commissionin, Sample preparation, Data acquisition and treatment, Data analysis. **O. Sans-Planell:** Instrument install and commissioning, Data acquisition and treatment. **M. Magalini:** Instrument install and commissioning, Data acquisition and treatment, Data analysis. **M. Manetti:** Equipment project construction and testing. **L. Sodi:** Equipment project construction and testing. **M. Massi:** Equipment project construction and testing. **L. Castelli:** Equipment project construction and testing. **C. Czelusniak:** Equipment project construction and testing. **F. Taccetti:** Project management and organization. **T.E. Bella:** Sample preparation, Data analysis. **G. Marcucci:** Data acquisition and treatment, Data analysis. **M. Clemenza:** Project management and organizatio, Instrument install and commissioning. **D. Di Martino:** Data analysis. **M. Morigi:** Project management and organization, Sample preparation. **M. Bettuzzi:** Instrument install and commissioning, Data acquisition and treatment. **L. Vigorelli:** Sample preparation, Data acquisition and treatment, Data analysis. **A. Re:** Project management and organization, Sample preparation. **A. Lo Giudice:** Sample preparation. **D. Alloni:** Project management and organization, Instrument install and commissioning, Reactor management. **M. Prata:** Reactor management. **S. Altieri:** Reactor management. **A. Salvini:** Reactor management. **F. Grazzi:** Equipment project construction and testing, Instrument install and commissioning, Sample preparation, Data acquisition and treatment, Data analysis.

Declaration of competing interest

The authors declare that they have no known competing financial interests or personal relationships that could have appeared to influence the work reported in this paper.

Data availability

Data will be made available on request.

Acknowledgements

This work has been funded by INFN, Italy, via the CHNet-NICHE CSN 5 experiment, and by INFN-CHNet network.

The support of A. Catelani, N. Pasqualetti and M. Leporatti of the Mechanical Workshop of the Department of Physics and Astronomy of the University of Firenze is acknowledged with gratitude.

The authors would like to thank the LENA personnel, who have provided great support to the experimental work well beyond their possibilities.

References

[1] L. Giuntini, L. Castelli, M. Massi, M. Fedi, C. Czelusniak, N. Gelli, L. Liccioli …, F. Taccetti, Detectors and cultural heritage: The INFN-CHNet experience, Appl. Sci. 11 (2021) 3462, https://www.mdpi.com/2076-3417/11/8/3462/pdf.

[2] F. Taccetti, L. Castelli, C. Czelusniak, N. Gelli, A. Mazzinghi, L. Palla, C. Ruberto ., L. Giuntini, A multipurpose X-ray fluorescence scanner developed for in situ analysis, Rend. Lincei 30 (2) (2019) 307–322, http://dx.doi.org/10.1007/s12210-018-0756-x, http://www.springerlink.com/content/120941/.

[3] Eberhard H. Lehmann, Eckhard DESCHLER-ERB, A. Ford, Neutron tomography as a valuable tool for the non-destructive analysis of historical bronze sculptures, Archaeometry 52 (2) (2010) 272–285, http://dx.doi.org/10.1111/j.1475-4754.2009.00480.x.

[4] Eberhard H. Lehmann, Stefan Hartmann, Markus O. Speidel, Investigation of the content of ancient tibetan metallic Buddha statues by means of neutron imaging methods, Archaeometry 52 (3) (2010) 416–428, http://dx.doi.org/10.1111/j.1475-4754.2009.00488.x.

[5] Fedrigo Anna, et al., Neutron imaging study of 'pattern-welded'swords from the Viking age, Archaeol. Anthropol. Sci. 10 (6) (2018) 1249–1263.

[6] Francesco Grazzi, et al., Characterization of two Japanese ancient swords through neutron imaging. 波紋 25(3) (2015): 206-213.

[7] K. Kino, et al., Analysis of crystallographic structure of a Japanese sword by the pulsed neutron transmission method, Physics Procedia 43 (2013) 360–364, http://dx.doi.org/10.1016/j.phpro.2013.03.043.

[8] A. Depalmas, et al., Neutron-based techniques for archaeometry: characterization of a Sardinian boat model, Archaeol. Anthropol. Sci. 13 (6) (2021) 1–9, http://dx.doi.org/10.1007/s12520-021-01345-w.

[9] Filomena Salvemini, et al., Non-invasive characterization of ancient Indonesian Kris through neutron methods, Eur. Phys. J. Plus 135 (5) (2020) 1–25.

[10] F. Salvemini, F. Grazzi, A. Fedrigo, et al., Revealing the secrets of composite helmets of ancient Japanese tradition, Eur. Phys. J. Plus 128 (2013) 87, http://dx.doi.org/10.1140/epjp/i2013-13087-y.

[11] F. Salvemini, et al., On the use of neutron imaging methods to identify microstructural features in ancient Indian swords and armour, Microchem. J. 159 (2020) 105397, http://dx.doi.org/10.1016/j.microc.2020.105397.

[12] M. Prata, et al., Italian neutron sources, Eur. Phys. J. Plus 129 (2014) 255, http://dx.doi.org/10.1140/epjp/i2014-14255-3.

[13] I.S. Anderson, et al., Research opportunities with compact accelerator-driven neutron sources, Phys. Rep. 654 (2016) 1–58, http://dx.doi.org/10.1016/j.physrep.2016.07.007.

[14] A. Salvini, et al., Design, implementation and future utilization of the PGNAA facility at the university of Pavia–Lena laboratory, in: Research Reactors: Addressing Challenges and Opportunities To Ensure Effectiveness and Sustainability. Summary of an International Conference. Supplementary Files, 2020.

[15] Werner, Christopher John, et al., MCNP Version 6.2 Release Notes, No. LA-UR-18-20808, Los Alamos National Lab.(LANL), Los Alamos, NM (United States), 2018.

[16] M. Celli, F. Grazzi, M. Zoppi, A new ceramic material for shielding pulsed neutron scattering instruments, Nucl. Instrum. Methods Phys. Res. A 565 (2) (2006) 861–863, http://dx.doi.org/10.1016/j.nima.2006.05.234.

[17] Trtik Pavel, et al., Improving the spatial resolution of neutron imaging at paul scherrer institut–the neutron microscope project, Physics Procedia 69 (2015) 169–176.

[18] Marin Van Heel, Similarity measures between images, Ultramicroscopy 21 (1) (1987) 95–100.

[19] Marin Van Heel, Michael Schatz, Fourier shell correlation threshold criteria, J. Struct. Biol. 151 (3) (2005) 250–262.

[20] Michael D. Abràmoff, Paulo J. Magalhães, Sunanda J. Ram, Image processing with imagej, Biophoton. Int. 11 (7) (2004) 36–42.

[21] https://www.psi.ch/.

[22] S. Preibisch, S. Saalfeld, P. Tomancak, Globally optimal stitching of tiled 3D microscopic image acquisitions, Bioinformatics 25 (11) (2009) 1463–1465.

[23] Dierick Manuel, Bert Masschaele, Luc Van Hoorebeke, Octopus, a fast and user-friendly tomographic reconstruction package developed in labview®, Meas. Sci. Technol. 15 (7) (2004) 1366.

[24] Uday Patil Abhishek, Naiknimbalkar Digvijay, J.B. Jeeva, Pre-operative brain tumor segmentation using SLICER-3D, in: 2014 International Conference on Green Computing Communication and Electrical Engineering, ICGCCEE, IEEE, 2014.